Towards a Better Understanding of Attitude Oscillations Experienced by Quadcopters In Axial Descent

MSc Thesis

Charlie B. Bogaerts [1]
Supervised by Coen C. de Visser [2]

July, 2023

[1]MSc student, Faculty of Aerospace Engineering, Delft University of Technology
[2]Assistant Professor, Faculty of Aerospace Engineering, Delft University of Technology

Contents

How to read this document iv

I Thesis Report 1

List of Tables 2

List of Figures 3

List of Symbols 5

List of Abbreviations 10

1 Introduction 11

2 Model Derivation 15
2.1 General model definitions and assumptions . . . 15
2.2 Flight controller and mixer . . . 18
2.3 Motor dynamics . . . 19
2.4 Rotor control forces and moments . . . 20
2.5 Quadcopter dynamics . . . 24
2.6 Input and outputs in the frequency domain . . . 28

3 Experimental Setup 30
3.1 Quadcopter specifications . . . 30
3.2 Isolated rotor in wind tunnel . . . 31
3.3 Actuator transient response . . . 33
3.4 PID gain measurements . . . 33
3.5 Mass and MMOI measurement . . . 33
3.6 Gimbal tests with elastic bands . . . 34
3.7 Structural vibration tests . . . 34
3.8 Gimbal tests with controller . . . 35
3.9 Flight tests with ballast . . . 35

4 Data Processing and Experimental Results 37
4.1 Isolated rotor wind tunnel data . . . 37
4.1.1 Average thrust and torque . . . 38
4.1.2 Variation in thrust and torque . . . 40
4.1.3 Derivatives with respect to wind speed and rotation speed . . . 42
4.1.4 Difference between rotors . . . 46

4.2 Actuator transient response . . . 50
4.3 PID gain measurement . . . 52
4.4 Mass and MMOI measurement . . . 53
4.5 Gimbal tests with elastic bands . . . 54
4.6 Structural vibration tests . . . 60

5 Evaluation of the Complete Model 62
5.1 Analyses of model characteristics . . . 62
5.2 Comparison of model output with flight data . . . 68
5.3 The diverging rotor speed effect . . . 74

6 Conclusion 79

7 Recommendations 85

II Scientific Paper: Assessing the Contribution of Isolated Rotor Aerodynamics to Quadcopter Attitude Oscillations in Axial Descent 86

8 Introduction 88

9 General definitions and rotor operational states 90

10 Experimental Setup 93
10.1 Quadcopter specifications . . . 93
10.2 Isolated rotor in wind tunnel . . . 94
10.3 Gimbal tests with elastic bands . . . 95

11 Data Processing and Experimental Results 96
11.1 Isolated rotor average thrust and torque . . . 96
11.2 Isolated rotor variation in thrust and torque . . . 98
11.3 Derivatives with respect to wind speed and rotation speed . . . 99
11.4 Gimbal tests with elastic bands . . . 104

12 Conclusion 111

III Literature study: Nonlinear Control of High Performance Quadcopters 113

13 Introduction 114

14 The quadcopter as MAV 116
14.1 The birth and rise of the quadrotor . . . 116
14.2 Quadrotor applications . . . 117
14.3 Basic functionality . . . 119

15 General quadcopter dynamics **123**
15.1 Reference frames . . . 123
15.2 Translational and rotational equations of motion . . . 125
15.3 Forces and moments generated by the propellers . . . 127
15.3.1 Isolated propeller operating in steady conditions . . . 127
15.3.2 Isolated propeller operating in the vortex ring state and beyond . 130
15.3.3 Rotor Interaction . . . 132
15.3.4 Gyroscopic rotor effects . . . 134
15.4 Forces and moments generated by the fuselage . . . 136

16 Advanced quadcopter control **138**
16.1 Robust and adaptive control . . . 139
16.2 Nonlinear quadcopter control . . . 141
16.2.1 Gain Scheduling and Linear Parameter Varying control . . . 141
16.2.2 Feedback linearization . . . 143
16.2.3 Lyapunov functions . . . 146
16.2.4 Backstepping . . . 147
16.2.5 Sliding mode control . . . 148
16.3 Quaternions . . . 150
16.4 Fault tolerant control . . . 153
16.4.1 Types of actuator failures . . . 153
16.4.2 Control strategies . . . 154

17 Contributing to quadcopter control research **156**
17.1 Identifying gaps in current literature . . . 156
17.2 Research proposal . . . 158

A Isolated Rotor Wind Tunnel Data **160**

Bibliography **179**

How to read this document

This document contains a thesis report, a scientific paper and a literature study which were made as part of a thesis project performed to finalize the master program Control & Simulation at the faculty of Aerospace Engineering of the TU Delft. The literature study was performed first and served as a basis to formulate a research problem, a research objective and a set of research questions. After completion of the research project itself, a report was made to document all used methods and found results. Due to insights gained over time, the report includes a different set of research objectives and questions, although they are very similar to, and derived from, the ones presented in the literature study. Complementary to this report, a scientific paper has been made which covers two of the most important experiments that were performed during the thesis. Documentation of these experiments are also included in the report. The scientific paper can thus be seen as shortened and simplified version of the report, which gives it an appropriate length for potential publication.

The report, a scientific paper and literature study correspond to Part I, Part II and Part III, respectively, These three parts can all be read as stand alone texts as this was the way they were originally written. However, this inherently causes some duplication when considering this document as a whole. For example, many subsections covering the experimental results of Part II can also be found in Part I. Finally, in Appendix A some very detailed plots are included that cover experimental results discussed both Part I and Part II.

Part I

Thesis Report

List of Tables

3.1 Betaflight settings. 31
3.2 Betaflight configurator controller gains. 31
3.3 BLHeli32 ESC settings. 31

4.1 Controller gains estimations. 52
4.2 Masses and MMOIs. 53

5.1 Flight test center and peak frequencies. 72
5.2 Wind tunnel center and peak frequencies. 74

List of Figures

2.1 Body frame drawn on a Parrot Bebop quadcopter. (from [1], modified) . 16
2.2 Flow diagram of linearized quadcopter dynamics. 17
2.3 Schematic of a single winding circuit of a DC motor. 19
2.4 Operating states of a rotor 21

3.1 Test setup of wind tunnel tests. 32
3.2 Quadcopter with 5x4.5x3 rotors, battery and ballast weights. 35

4.1 Estimated thrust data for the 5x4.5 isolated rotor. Positive speeds refer to the rotor in axial descent. 39
4.2 Estimated torque data for the 5x4.5 isolated rotor. Positive speeds refer to the rotor in axial descent. 40
4.3 Estimated thrust standard deviation for the 5x4.5 isolated rotor. Positive speeds refer to the rotor in axial descent. 41
4.4 Estimated torque standard deviation for the 5x4.5 isolated rotor. Positive speeds refer to the rotor in axial descent. 42
4.5 Change in thrust w.r.t rotor rotational speed for the 5x4.5 isolated rotor. Positive speeds refer to the rotor in axial descent. 43
4.6 Change in thrust w.r.t descent speed for the 5x4.5 isolated rotor. Positive speeds refer to the rotor in axial descent. 44
4.7 Change in torque w.r.t rotor rotational speed for the 5x4.5 isolated rotor. Positive speeds refer to the rotor in axial descent. 45
4.8 Change in torque w.r.t descent speed for the 5x4.5 isolated rotor. Positive speeds refer to the rotor in axial descent. 46
4.9 Increase in thrust of the 5x5x3 rotor w.r.t the 5x4.5x3 rotor. Positive speeds refer to the rotor in axial descent. 47
4.10 Increase in torque of the 5x5x3 rotor w.r.t the 5x4.5x3 rotor. Positive speeds refer to the rotor in axial descent. 48
4.11 Increase in σ_f of the 5x5x3 rotor w.r.t the 5x4.5x3 rotor. Positive speeds refer to the rotor in axial descent. 49
4.12 Increase in σ_n of the 5x5x3 rotor w.r.t the 5x4.5x3 rotor. Positive speeds refer to the rotor in axial descent. 49
4.13 A part of the measured rotor speed samples used to estimate a_0. 50
4.14 Linear and quadratic models of the dependency of α_0 on the rotor speed. 51
4.15 Example comparison between measurements and simulation of the gimbal oscillation. 55

4.16 PSDs of single rotor thrust $f(t)$ based on the reconstructed roll moment $L_d(t)$ and pitch moment $M_d(t)$. The damped natural frequency of the gimbal is indicated with ω_{gim}. Dashed lines indicate the rotational speed of the rotors in Hz, and match in color with their respective PSD. 57
4.17 Rotor thrust standard deviation. The black line represents isolated rotor thrust data. Purple and orange triangles represent thrust standard deviations reconstructed from the measured roll rate and measured pitch rate, respectively, which are corrected for gyroscope noise. The purple and orange dashed lines correspond to gyroscope noise only along the roll and pitch axis, respectively. 59
4.18 PSD of attitude rates as a result of an impact test. 60

5.1 Poles and zeros of each attitude axis and of the full model. 64
5.2 Change of roll model poles as a function of rotor speed. 65
5.3 Change of yaw model poles as a function of rotor speed. 67
5.4 Flight speed and ω_h combinations corresponding to used experiment data. 70
5.5 PSD's according to the model and flight data with $V = 20.4\,\mathrm{m\,s^{-1}}$ and a mean rotor speed of 5.7 krpm. 71
5.6 PSD's according to the model and wind tunnel data with $V = 15\,\mathrm{m\,s^{-1}}$ and a mean rotor speed of 5.7 krpm. 73
5.7 The ratio of the total estimated model power over flight test total power. 74
5.8 The ratio of the total estimated model power over wind tunnel total power. 75
5.9 Test run 3 as example revealing the diverging rotor speed effect. 76
5.10 Measured rotor speed divergence as function of throttle setting. 77

List of Symbols

α_i	i'th parameter used to describe LPF behaviour of the electric motor.
β	Constant related to the aerodynamic drag of a rotor.
δ	Throttle setting as number between zero and one.
$\Delta\omega_N$	Metric for quantifying the diverging rotor speed effect.
Δf	Difference in thrust between the 5x5x3 and 5x4.5x3 rotor.
Δn	Difference in drag torque between the 5x5x3 and 5x4.5x3 rotor.
$\Delta\sigma_f$	Difference in thrust STD between the 5x5x3 and 5x4.5x3 rotor.
$\Delta\sigma_n$	Difference in drag torque STD between the 5x5x3 and 5x4.5x3 rotor.
ζ_{gim}	Estimated damping ratio of the gimbal with elastic bands.
θ_i	i'th parameter used to describe LPF behaviour of the gimbal with elastic bands.
λ_a	Estimated Kalman filter accelerometer bias.
ρ	Air density.
$\boldsymbol{\sigma}$	Vector containing the four rotor rotation speeds w.r.t the surrounding air.
$\sigma_f^{5\times5}$	Thrust force STD generated by the 5x5x3 rotor.
$\sigma_f^{5\times4.5}$	Thrust force STD generated by the 5x4.5x3 rotor.
$\sigma_n^{5\times5}$	Drag torque STD generated by the 5x5x3 rotor.
$\sigma_n^{5\times4.5}$	Drag torque STD generated by the 5x4.5x3 rotor.
σ_f	STD of the thrust force of a rotor.
$\hat{\sigma}_f$	STD of the thrust force of a rotor as logarithm..
σ_{f_i}	STD of the thrust force of the i'th rotor.
σ_i	Rotation speed of the i'th rotor w.r.t the surrounding air.
σ_{L_d}	STD of L_d.
σ_n	STD of the drag torque of a rotor.
$\hat{\sigma}_n$	STD of the drag torque of a rotor as logarithm.
σ_{n_i}	STD of the drag torque of the i'th rotor.
ϕ	Roll angle of the quadcopter.
$\overline{\Omega}$	Laplace transform of ω.
$\boldsymbol{\omega}$	Vector containing the four rotor rotation speeds w.r.t the quadcopter.
ω	Rotor rotation speed or general notation for angular frequency.
$\boldsymbol{\Omega}_d$	Rotational velocity of the quadcopter w.r.t the inertial frame.
ω_{gim}	Estimated natural frequency of the gimbal with elastic bands.
ω_h	Equivalent hover rotor speed as measure for throttle setting.
ω_i	Rotation speed of the i'th rotor w.r.t the quadcopter (always positive).
ω_i^*	Linearization rotation speed of the i'th rotor.
$\boldsymbol{\Omega}_r^i$	Rotational velocity of the i'th rotor w.r.t the inertial frame.
$\boldsymbol{\Omega}_{rd}^i$	Rotational velocity of the i'th rotor w.r.t the quadcopter.
$\overline{\omega}_i$	Deviation of rotation speed of the i'th rotor w.r.t the linearization point.
$\tilde{\omega}_i$	Rotation speed of the i'th rotor along the z-axis of the body frame.

ω_{nq}	Nyquist rate angular frequency.
ω_s	Sample rate angular frequency.
$\boldsymbol{\omega}_{tar}$	Vector containing the target rotation speeds for each rotor.
A	Actuator disk area of a rotor.
a	Cut off frequency of the HPF used to construct the pseudo derivative.
a_m	Body frame z-axis acceleration measured by the accelerometer.
B_p	Transfer function of the PID controller of the roll rate.
c_p	Output of the controller that controls the roll axis.
c_q	Output of the controller that controls the pitch axis.
c_r	Output of the controller that controls the yaw axis.
D	Rotor diameter.
d_g	Effective damping constant of the gimbal with elastic bands.
e	Back EMF generated by one of the motor windings.
F	Body frame z-axis force due to changing rotor speeds and other disturbances.
f	Thrust force of a rotor in the negative body frame z-axis direction.
$f^{5\times5}$	Thrust force generated by the 5x5x3 rotor.
$f^{5\times4.5}$	Thrust force generated by the 5x4.5x3 rotor.
f_σ	Derivative of a rotor thrust force w.r.t rotation speed σ.
f_{σ_i}	Derivative of the i'th rotor thrust force w.r.t rotation speed σ_i.
F^*	Linearization point of F.
f_i^*	Linearization point of f_i.
$\overline{F}$	Deviation of F from the linearization point F^*.
f_c	Center frequency of a PSD.
F_d	Disturbance force on the quadcopter along the z-axis of the body frame.
f^{data}	Either the center or peak frequency according to the recorded data.
f_i	Thrust force of the i'th rotor in the negative body frame z-axis direction.
$\boldsymbol{F}_i^b$	Thrust vector of the i'th rotor expressed in the body frame.
F_m	Body frame z-axis force generated by rotors due to quadcopter motion.
f^{model}	Either the center or peak frequency according to the model.
F_p	Sensitivity of body frame z-axis force to roll rate.
f_p	Peak frequency of a PSD.
F_q	Sensitivity of body frame z-axis force to pitch rate.
F_r	Sensitivity of body frame z-axis force to yaw rate.
f_{t1}	Rotor thrust at the boundary of the TWS and windmilling state.
f_{t2}	Rotor thrust at the boundary of the VRS and normal operating state.
$F_{\overline{V}}$	Sensitivity of body frame z-axis force to a change in speed.
f_v	Derivative of a rotor thrust force w.r.t descent speed v_i.
f_{v_i}	Derivative of the i'th rotor thrust force w.r.t descent speed v_i.
$f_{v=0}$	Rotor thrust generated with no external airspeed.
g	Gravity constant.
G_D^p	D gain of the roll rate PID controller.
G_I^p	I gain of the roll rate PID controller.
G_P^p	P gain of the roll rate PID controller.
G_D^q	D gain of the pitch rate PID controller.
G_I^q	I gain of the pitch rate PID controller.
G_P^q	P gain of the pitch rate PID controller.
G_D^r	D gain of the yaw rate PID controller.
G_I^r	I gain of the yaw rate PID controller.

G_P^r	P gain of the yaw rate PID controller.
G_D	D gain of a PID controller.
G_I	I gain of a PID controller.
G_P	P gain of a PID controller.
h	Estimated Kalman filter altitude.
h_m	Altitude measured by the barometer.
H_{pL}	Transferfunction relating the roll moment to roll rate.
H_{pM}	Transferfunction relating the pitch moment to roll rate.
H_{pN}	Transferfunction relating the yaw moment to roll rate.
H_{pF}	Transferfunction relating the total force to roll rate.
H_{qL}	Transferfunction relating the roll moment to pitch rate.
H_{qM}	Transferfunction relating the pitch moment to pitch rate.
H_{qN}	Transferfunction relating the yaw moment to pitch rate.
H_{qF}	Transferfunction relating the total force to pitch rate.
H_{rL}	Transferfunction relating the roll moment to yaw rate.
H_{rM}	Transferfunction relating the pitch moment to yaw rate.
H_{rN}	Transferfunction relating the yaw moment to yaw rate.
H_{rF}	Transferfunction relating the total force to yaw rate.
$H_{\overline{V}L}$	Transferfunction relating the roll moment to descent speed.
$H_{\overline{V}M}$	Transferfunction relating the pitch moment to descent speed.
$H_{\overline{V}N}$	Transferfunction relating the yaw moment to descent speed.
$H_{\overline{V}F}$	Transferfunction relating the total force to descent speed.
i	Induced velocity of a rotor.
i_{arm}	Armature current of one of the motor windings.
I_{xx}^d	MMOI around the body frame x-axis without rotors and ballast.
I_{yy}^d	MMOI around the body frame y-axis without rotors and ballast.
I_{zz}^d	MMOI around the body frame z-axis without rotors and ballast.
I_{xx}^f	MMOI around the body frame x-axis with rotors but without ballast.
I_{yy}^f	MMOI around the body frame y-axis with rotors but without ballast.
I_{zz}^f	MMOI around the body frame z-axis with rotors but without ballast.
I^g	Generic notation of MMOI of the quadcopter and gimbal.
I_{xx}^g	MMOI around the body frame x-axis of the quadcopter and gimbal.
I^r	MMOI matrix of a rotor and motor bell in the body frame.
I_{xx}^r	MMOI of a rotor and motor bell along the body frame x-axis.
I_{xy}^r	Off-diagonal MMOI term of a rotor and motor bell in the body frame.
I_{xz}^r	Off-diagonal MMOI term of a rotor and motor bell in the body frame.
I_{yy}^r	MMOI of a rotor and motor bell along the body frame y-axis.
I_{yz}^r	Off-diagonal MMOI term of a rotor and motor bell in the body frame.
I_{zz}^r	MMOI of a rotor and motor bell along the body frame z-axis.
I_{xx}	MMOI around the body frame x-axis of the quadcopter with rotors and ballast.
I_{yy}	MMOI around the body frame y-axis of the quadcopter with rotors and ballast.
I_{zz}	MMOI around the body frame z-axis of the quadcopter with rotors and ballast.
$i_{v=0}$	Induced velocity with no external airspeed (often denoted by i_h).
j	Amount of intervals of rotor rotation speeds used for triangulation.
K	Motor back EMF constant.
k	Amount of intervals of rotor descent speeds used for triangulation.
k_d	Effective stiffness of the gimbal with elastic bands.
L	Roll moment due to changing rotor speeds and other external disturbances.

L^*	Linearization point of L.
$\overline{L}$	Deviation of L from the linearization point L^*.
L_d	Disturbance roll moment.
L_g	Total gyroscopic roll moment generated by all rotors.
L_g^i	Gyroscopic roll moment exerted on the airframe by the i'th rotor.
L_m	Additional roll moment generated by rotors due to quadcopter motion.
L_p	Sensitivity of roll moment to roll rate.
L_q	Sensitivity of roll moment to pitch rate.
L_r	Sensitivity of roll moment to yaw rate.
$L_{\overline{V}}$	Sensitivity of roll moment to a change in speed.
l	Smoothness parameter for the simplex B-spline.
l_x	Distance of the rotor rotation axis to the CG along the body frame x-axis.
l_y	Distance of the rotor rotation axis to the CG along the body frame y-axis.
M	Pitch moment due to changing rotor speeds and other external disturbances.
m	Total mass of the quadcopter including ballast.
M^*	Linearization point of M.
$\overline{M}$	Deviation of M from the linearization point M^*.
$\dot{m}$	Generic notation for mass flow.
m_d	Mass of the quadcopter without rotors and ballast.
m_f	Total mass of the quadcopter with rotors but without ballast.
m_r	Mass of a single rotor.
m_{bal}	Mass of the ballast added to the quadcopter.
$\dot{m}_{no}$	Mass flow through the rotor in the normal operating state.
$\dot{m}_{wm}$	Mass flow through the rotor in the wind milling state.
M_d	Disturbance pitch moment.
M_g	Total gyroscopic pitch moment generated by all rotors.
$\boldsymbol{M}_g^i$	Gyroscopic moment exerted on the airframe by the i'th rotor.
M_g^i	Gyroscopic pitch moment exerted on the airframe by the i'th rotor.
M_p	Sensitivity of pitch moment to roll rate.
M_q	Sensitivity of pitch moment to pitch rate.
M_r	Sensitivity of pitch moment to yaw rate.
M_m	Additional pitch moment generated by rotors due to quadcopter motion.
$M_{\overline{V}}$	Sensitivity of pitch moment to a change in speed.
N	Yaw moment due to changing rotor speeds and other external disturbances.
n	Drag torque generated by a rotor.
$n^{5\times5}$	Drag torque generated by the 5x5x3 rotor.
$n^{5\times4.5}$	Drag torque generated by the 5x4.5x3 rotor.
n_σ	Derivative of a rotor drag torque w.r.t rotation speed σ_i.
n_{σ_i}	Derivative of the i'th rotor drag torque w.r.t rotation speed σ_i.
N^*	Linearization point of N.
n_i^*	Linearization point of n_i.
$\overline{N}$	Deviation of N from the linearization point N^*.
n_a	Random variable capturing noise of the accelerometer measurements.
N_d	Disturbance yaw moment.
N_g	Total yaw reaction torque generated by all rotors.
n_h	Random variable capturing noise of the barometer measurements.
n_i	Aerodynamic drag torque generated by the i'th rotor.
N_g^i	Gyroscopic yaw moment exerted on the airframe by the i'th rotor.

N_m	Additional yaw moment generated by rotors due to quadcopter motion.
N_p	Sensitivity of yaw moment to roll rate.
N_q	Sensitivity of yaw moment to pitch rate.
N_r	Sensitivity of yaw moment to yaw rate.
$N_{\overline{V}}$	Sensitivity of yaw moment to a change in speed.
n_v	Derivative of a rotor drag torque w.r.t descent speed v.
n_{v_i}	Derivative of the i'th rotor drag torque w.r.t descent speed v_i.
p	Roll rate of the quadcopter.
q	Pitch rate of the quadcopter.
R	Equivalent electrical resistance of one of the motor windings.
r	Yaw rate of the quadcopter.
s	Laplace variable.
s_{esc}	Estimated ESC input signal.
S_{pp}	PSD of the roll rate.
S_{qq}	PSD of the pitch rate.
S_{rr}	PSD of the yaw rate.
$S_{\overline{VV}}$	PSD of the total thrust force along the body frame z-axis.
T	Torque generated by the motor.
t	Time.
u_b	Speed of the quadcopter along the x-axis of the body frame.
u_{in}	Voltage applied to one of the BLDC motor windings.
U_{vir}	Laplace transform of u_{vir}.
u_{vir}	Dummy variable related to motor armature voltage.
V	Absolute value of the quadcopters velocity vector in the body frame.
$\boldsymbol{v}$	Vector containing the four individual rotor descent speeds.
$\overline{\boldsymbol{v}}$	Vector containing the four individual rotor descent speed deviations.
v	Descent speed of an individual rotor.
V^*	Linearization descent speed of the quadcopter.
$\overline{V}$	Deviation of quadcopter speed w.r.t the linearization point.
V_E	Speed of the quadcopter along the y-axis of the inertial frame.
$\boldsymbol{V}^b$	Velocity vector of the quadcopter expressed in the body frame.
v_b	Speed of the quadcopter along the y-axis of the body frame.
V_D	Speed of the quadcopter along the z-axis of the inertial frame.
$\boldsymbol{V}^I$	Velocity vector of the quadcopter expressed in the inertial frame.
v_i	Descent speed of the i'th rotor.
$\overline{v}_i$	Deviation of the i'th rotor speed w.r.t the linearization point.
V_N	Speed of the quadcopter along the x-axis of the inertial frame.
w	Change of flow speed in the far wake of a rotor.
w_b	Speed of the quadcopter along the z-axis of the body frame.
W_{F_d}	White noise intensity level of F_d.
W_{L_d}	White noise intensity level of L_d.
W_{M_d}	White noise intensity level of M_d.
W_{N_d}	White noise intensity level of N_d.

List of Abbreviations

BLDC	Brushless Direct Current
CCW	Counterclockwise
CG	Center of gravity
CW	Clockwise
EMF	Electromagnetic force
ESC	Electronic speed controller
HPF	High pass filter
IMU	Inertial measurement unit
LPF	Low pass filter
MMOI	Mass moment of inertia
OLS	Ordinary least squares
STD	Standard deviation
TWS	Turbulent wake state
UAV	Unmanned aerial vehicle
VRS	Vortex ring state
WMS	Windmilling state

Chapter 1

Introduction

In the past decade the popularity of small scale quadcopters as UAVs has drastically increased. These quadcopters distinguish themselves from other UAVs by their ability of vertical take off and landing, their ability to hover efficiently [2] and above all their potential for incredible maneuverability. Their parts are cheap, making them in their entirety cheap to manufacture and service [3, 4]. The inherent flexibility, robustness and accessibility allows these rotorcraft to be effective tools in surveying, transportation, research, disaster risk management, humanitarian work [5] and many more.

This surge in popularity has continuously been mirrored by the amount of research that has been done on the topic of improving flight characteristics of quadcopters. Many quadcopters use a simple PID controller that is optimized for the hover condition. Since effects such as aerodynamic interaction between the rotors are small during hover [6], this type of controller is generally quite effective as long as the speed of the quadcopter remains small. However, when speeds do increase, a variety of complex aerodynamic effects become more dominant [7, 8]. This makes the system nonlinear and causes a linear controller with fixed gains to be an inadequate solution to retain the stability and maneuverability that the quadcopter can theoretically have at these speeds [9]. One area of research is therefore the design of more advanced control of quadcopters. Consequently, this raises the need for better models of system dynamics at these speeds.

Given enough power and an appropriate trajectory, a quadcopter can theoretically reach high speeds in any direction. One rather special direction is the downward direction where the air approaches the underside of the quadcopter. The most basic and perhaps the most common encounter with this part of the flight envelope is when the quadcopter descents in a straight vertical line while maintaining a level altitude. However, an infinite amount of trajectories can be realised that cause the airspeed velocity vector to point towards the bottom of the quadcopter.

What makes this part of the flight envelope remarkable is that the rotors operate under negative inflow. This means the rotor is set up in a way to blow against the direction of the external airflow. The behavior of an isolated rotor in this flight condition has been extensively researched, especially in relation to helicopter flight [10, 11]. As downward speed is increased, isolated rotors generally encounter the VRS (vortex ring state), TWS (turbulent wake state) and WMS (windmilling state), and in that order. The VRS, and to a degree the TWS, are known to be related to excessive vibration, thrust fluctuation

and severe control issues for helicopters. Standard procedure for most rotorcraft has therefore been to avoid this VRS where possible [12, 13].

Unsurprisingly, these severe oscillations during downward velocities are also commonly encountered during quadcopter flight, especially during the performance of more aggressive flight manoeuvres. Analogous to the strategy for helicopters, multiple studies have focused on motion planning algorithms to avoid this part of flight envelope [12, 13]. These algorithms use models predicting in which flight states the VRS can occur [14]. For example, instead of descending in a straight vertical line, the quadcopter can descent using a spiral trajectory [15]. The interesting option of giving the quadcopter a high yaw rate during a vertical descent has also been shown to be effective in avoiding the VRS [14], because this way all rotors have an edgewise velocity component.

Since quadcopters usually have an abundance of excess power compared to helicopters, it is likely that a quadcopter in the VRS is mostly difficult to control due to a lack of adequate flight control. To make a quadcopter more stable and controllable in this state, and thereby expand its flight envelope considerably, it is necessary to get a better understanding of what exactly happens during this VRS from a system modelling perspective. Since a quadcopter has four fixed pitch rotors, dynamics may be very different than found for helicopters that have a single variable pitch rotor. Some research has been performed on the interaction effects of two small scale rotors operating in each others vicinity. Here attention is given to the behaviour of the flow [16], and its impact on thrust forces [17, 18]. In these studies the two rotor rotational speeds are kept equal and constant. Quadcopter flight is likely much more complicated than this as there are four rotors which rotational speeds are continuously varied by the controller. Since rotor interaction affects quadcopter attitude, the controller and aerodynamics are coupled in a complex feedback loop.

The study documented in this report aims to shed more light on the underlying mechanics of the oscillations found for quadcopter flight specifically. Not only is this interesting from a theoretical standpoint, having a better understanding of this flight condition can also serve as a foundation for developing controllers that can effectively handle this part of the flight envelope. From a general perspective this would significantly increase the possible flight conditions of the quadcopter which extends its performance in a very concrete way. Since the overall goal is to support future flight controller design, this study takes a more system modelling oriented approach, rather than diving into the more complex relevant aerodynamics. More precisely, it is investigated whether the oscillatory behaviour can be quantified as function of several basic parameters such as rotor rotational speed and flight velocity, rather than tying to understand the detailed interaction between rotors, airframe and the surrounding air. This latter option is deemed to big of a step based on the current state of scientific knowledge on the subject.

To avoid confusion around term VRS, which refers to the the operating state of a rotor where large vortices develop, this document will from now on refer to the manifestation of roll, pitch and yaw oscillations during downward velocities as the 'propwash' effect. This allows for analysing properties of oscillations without actually having to consider the aerodynamic behaviour around the rotors. After all, as of writing this report it has not been quantified how this propwash effect is influenced by rotors operating in the VRS. In fact, it has not been shown that propwash effect only occurs when rotors operate in

the VRS, and not in the TWS and WMS. This study aims to shed more light on these subjects as well.

The approach of this study is to make a model of the quadcopter experiencing the propwash effect, and comparing simulations of this model with experimentally obtained flight data. This model consist of several subsystems that are modelled individually using either a theoretical derivation or system identification technique. The model is based on the major simplifying assumption that there is no rotor-rotor interaction. This allows for obtaining individual rotor behaviour in a wind tunnel, and calculating how much this behaviour would influence the severity of the propwash effect. Comparing the model simulations and flight data can then be used to verify how much of this propwash effect is actually due to these individual rotor properties. Since the model also includes gyroscopic effects, reaction torque effects, varying motor transient responses and the influence of rotor downward velocity due to roll and pitch rates, the significance of these can also be quantified by comparing the model with flight data.

Based on the above, the following research problem is formulated which is used to derive a research objective:

> *Controllers used for quadcopters use propeller force models that are inaccurate during axial descent. This gives rise to instability or the need for conservatively tuned controllers.*

From this identified problem the following research objective is formulated:

> *The objective is to support the development of flight controllers that have high performance for quadcopters in axial descent by measuring isolated rotor thrust and torque in a wind tunnel to make and analyse an attitude dynamics model relevant for this flight condition.*

The research objective is considered to be completed once the following research questions have been answered.

1. What selection of the rotor forces and moments are worth measuring, considering practical limitations of the test stand?
2. What variables need to be measured during isolated rotor experiments that are not forces or moments?
3. Given the available resources, what test stand is appropriate to measure the selected variables?
4. Given the available resources, what wind tunnel test setup would allow for measuring the stochastic nature of the rotor forces and moments to an extent that is relevant for quadcopter control?
5. What independent variables need to be varied during the isolated rotor experiment and over what range?
6. What model structure is best suited to implement in simulation of the rotor dynamics?

7. Could a the controller use the rotor model as a static mapping from required force to required rotor rotational speed?

8. What sensor data would be needed by the controller to function properly?

9. How can knowledge of the estimated model potentially be used in the design of quadcopter controllers?

This report is structured as follows. In chapter 2 the used model will be derived and described. In chapter 3 all the test setups of the relevant experiments are presented. The results of these experiments are discussed in chapter 4. Most of these results serve to quantify parameters of the constructed model. In chapter 5 the characteristics of the fully developed model are discussed and compared to flight data and wind tunnel data of the actual quadcopter. The final section of the latter chapter discusses an interesting phenomenon that was encountered during flight testing, which is, for a lack of a better name, referred to as the 'diverging rotor speed' effect. Finally, a conclusion is presented in chapter 6.

Chapter 2

Model Derivation

A model will be created which behaviour can be compared with real life flight data in order to gain insight into sources of oscillation during the propwash effect. This chapter covers the theoretical background of this model. The focus lies on what assumptions are made, how the model is derived from a mathematical standpoint and how the model is used to simulate the propwash effect.

In section 2.1 the general structure of the model will be discussed together with the major assumptions that are made. In section 2.2, modelling the flight controller and mixer will be discussed. The combination of an ESC, electric motor and rotor are from now on referred to as an actuator. How an actuator dynamically responds to an input is treated in section 2.3. In section 2.4 some theoretical background is given on rotor aerodynamics and how rotor thrust and torque can be modelled. Gyroscopic moments and reaction torques are also covered here. In section 2.5 the more general dynamics of the quadcopter are treated. Finally, in section 2.6, it is shown what kind of input is given to the model in order to make the output of the model a potential estimation of the quadcopter motions during the propwash effect.

2.1 General model definitions and assumptions

The model that is derived in this chapter is based on two distinct reference frames. The first reference frame is the inertial frame where Newton's second law of motion holds in its basic form. For this frame the x-axis points north, the y-axis points east and the z-axis is aligned with the local gravity vector. The second reference frame is the body frame, as is shown in Figure 2.1, which rotates as if attached to the quadcopters airframe. The x-axis of this frame points towards the front of the quadcopter, the y-axis to its right side and the z-axis towards its bottom. The orientation of the body frame with respect to the inertial frame is described by the yaw, pitch and roll angles. For properties of individual rotors, such as their MMOI, the body frame is used as well.

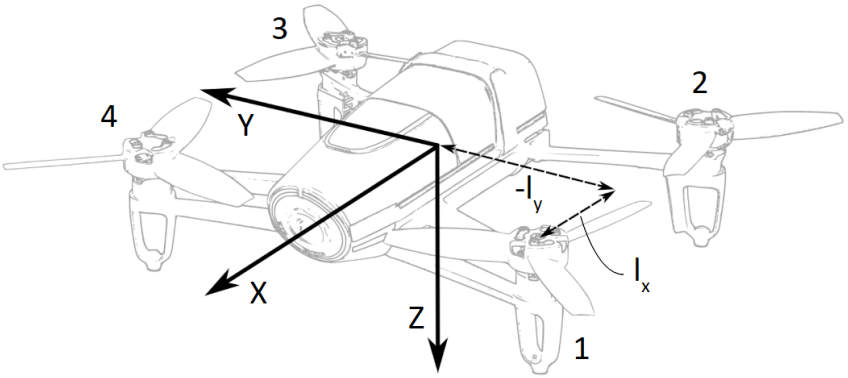

Figure 2.1: Body frame drawn on a Parrot Bebop quadcopter. (from [1], modified)

It is assumed that all four rotor planes coincide and that the CG (center of gravity) of the quadcopter lays in this common rotor plane. Furthermore, it is assumed that the distance of the rotation axis of any rotor to the CG is equal. The distance from the rotation axis of any rotor to the CG along the x-axis of the body frame is equal to l_x, and along the y-axis equal to l_y. The (x, y) position of rotors one, two, three and four in the xy-plane of the body frame are thus $(l_x, -l_y)$, $(-l_x, -l_y)$, $(-l_x, l_y)$ and (l_x, l_y), respectively.

All forces and moments that work on the airframe, such as lift and drag forces, are not taken into account as a source of propwash oscillations. Furthermore, the rotors are assumed to operate in the air stream as if the were in isolation. This means no interaction effects are considered between the rotors or between any rotor and air frame.

The propwash effect tends to occur when the external airflow is approaching the quadcopter from below. The model focuses on the flight condition where the angle between the velocity vector and the body frame z-axis remains small, say smaller than 10°. If $\boldsymbol{V}^b = [u_b \quad v_b \quad w_b]$ is the velocity vector of the quadcopter with respect to the air, expressed in the body frame, then it can be stated that $||\boldsymbol{V}|| \approx w_b$. Because the effects of forward and sideways speeds u_b and v_b are assumed to be zero for the remainder of this report, w_b is simply written as V. Note that positive values for V correspond to the quadcopter in axial descent.

To constrict the scope of the model even more, it is assumed that the change in direction of the velocity vector in the inertial frame $\boldsymbol{V}^I = [V_N \quad V_E \quad V_D]$ is small. That implies the quadcopter travels along a relatively straight path. Strictly speaking only one flight scenario exists that can fulfill all mentioned assumptions for a period of time. This scenario is where the quadcopter has a close to level attitude and vertically descends with speed V. However, it can be shown that the straight path requirement does not impact the results of the model drastically, meaning that the used model should also give insight in the behaviour of more general flight manoeuvres for which the propwash effect is encountered.

The model derived in this chapter is linear due to the many tools available for analysing such systems. This is achieved by linearizing several effects that are in fact nonlinear according to measured data or derived equations. The model is linearized around a constant rotation speed for each rotor, ω_1^*, ω_2^*, ω_3^* and ω_4^*, and an airspeed V^*. A particular set of values for these five parameters is from now on referred to as a 'flight condition'. Each

flight condition can thus be captured by a particular realisation of the linear model. For each realisation of the model only small deviations in ω_1, ω_2, ω_3, ω_4 and V are allowed, where these deviations are referred to as $\overline{\omega}_1$, $\overline{\omega}_2$, $\overline{\omega}_3$, $\overline{\omega}_4$ and $\overline{V}$. In other words, $\omega_i = \omega_i^* + \overline{\omega}_i$ and $V = V^* + \overline{V}$.

In Figure 2.2 a schematic representation of the model is shown. The input to this model are disturbance moments to the quadcopter around the x, y, and z-axis, referred to as L_d, M_d and N_d, respectively, and a disturbance force along the body frame z-axis referred to as F_b . Of course these could be realized by external forces such as wind gusts or contact with other objects. However, in this report these are actually realized by unmodeled fluctuations in thrust and torque produced by the rotors. The output of the model consist of the states of the 'quadcopter dynamics' block. These are the roll rate p, pitch rate q, yaw rate r and deviation in speed $\overline{V}$ from the linearization speed V^*. The feedback path in Figure 2.2 covers the PID controller, the mixer, the four low pass filters to model the transient response of the actuators, the rotor aerodynamics and the inertial effects of the rotor.

The model contains 13 states. Four of these come from the quadcopter dynamics block itself. The PID controller adds two states for roll control, two for pitch control and one for yaw control. The reason the PID controller for roll and pitch introduces two states rather than one is due to the fact that a pseudo derivative is used for the derivative term, which is discussed in section 2.2. Finally, the LPF blocks add one state each. Blocks that add a state are marked as being 'dynamic' rather than 'static'. Furthermore, many blocks indicate between brackets whether they depend on a linearization value such as ω_1^*, ω_2^*, ω_3^*, ω_4^* or V^*. Note that the quadcopter dynamics block is also dependent on m_{bal}, which is mass of the ballast added to the quadcopter during flight testing.

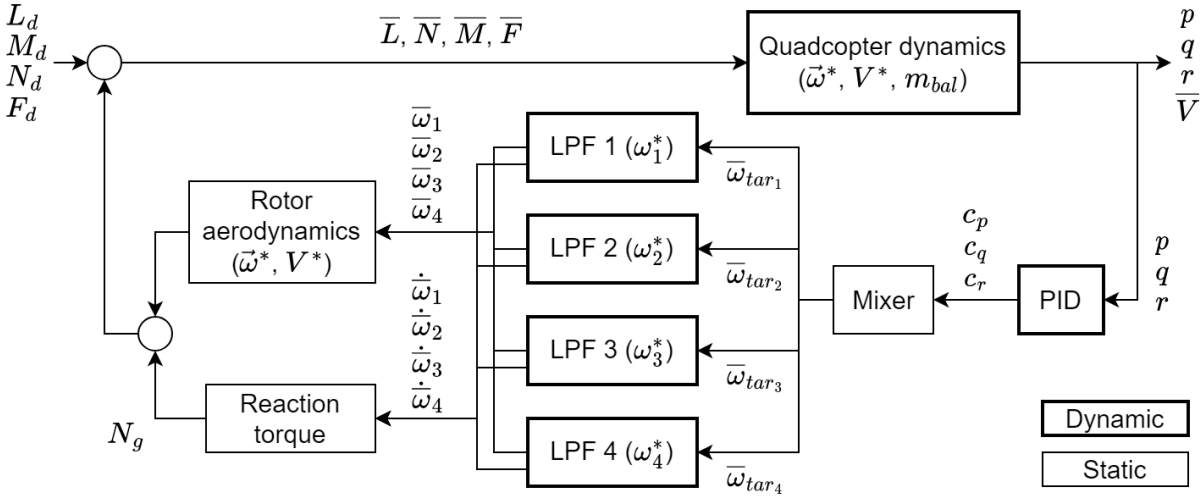

Figure 2.2: Flow diagram of linearized quadcopter dynamics.

The fact that the air velocity vector is assumed to be close to parallel to the quadcopters z-axis makes it a very symmetric problem from an aerodynamic perspective. Therefore, it seems reasonable to expect that all rotor speeds will be very similar during such a descent manoeuvre, as they are with other symmetric flight conditions such as hover. One might then wonder why it is necessary to model each individual rotor with its

own rotational speed since this increases the model complexity significantly. Strangely enough, experiments showed that during these descent manoeuvres the rotors speeds can in fact be very different. Exactly why this is remains unclear, but in section 5.3 this effect is discussed in more detail.

2.2 Flight controller and mixer

For this research project Betaflight was used as flight control firmware. Besides a number of features, Betaflight controls the quadcopters attitude rates using a PID controller for the roll and pitch axes, and a PI controller for the yaw axis. This set of three controllers is indicated by the 'PID' block in Figure 2.2. The outputs of this controller block are the control signals c_p, c_q and c_r for the roll, pitch and yaw axis, respectively, which is then fed to the mixer block. The mixer distributes each control signal over the four rotors so that an appropriate response is generated.

Besides the mentioned mixer and PID controller, Betaflight offers a load of settings that influence the flight behaviour of the quadcopter. For this project, as many of these options were turned off to simplify making the model for the complete system. A couple of features could not be completely turned of however due to practical limitations. One of these features are the filters that filter the measured attitude rates p, q and r. The filters that were used are some LPFs and notch filters. All these filters were set to only have effect on frequencies higher than 80 Hz. It had been noticed in early test flights that the propwash effect mainly consist of frequencies that are much lower than this. The filters are therefore very unlikely to influence the attitude oscillations that occur during the propwash effect. It was therefore decided to not include these filters in the model as shown in Figure 2.2, causing the model to be invalid to analyse oscillations with a frequency higher than 80 Hz.

Due to issues with modeling a noncausal system, the derivative terms in the 'PID' block were implemented using pseudo derivatives. This pseudo derivative is equal to a HPF (high pass filter) with a sufficiently large cut off frequency. As an example, if $B_p(s)$ denotes the transfer function of the PID controller of the roll rate, it is implemented as shown in Eq. 2.1. Here G_D, G_P and G_I are the real gains of the controller. The parameter a dictates the cut of frequency of the HPF and is set to a value of 1.591×10^{-4}, resulting in a cut off frequency of 100 Hz. This frequency is higher than the frequencies of interest for the propwash effect. Implementing the PID controller using a pseudo derivative should therefore not influence the accuracy of the model at these lower frequencies.

$$B_p(s) = G_D \frac{s}{1+as} + G_P + G_I \frac{1}{s} \tag{2.1}$$

There are various types of mixers that can be activated in Betaflight. The default mixer is a linear one, and is described by the matrix as is shown in Eq. 2.2. This matrix is only accurate if the actuators do not run into their limits, which means the rotor rotational speeds should be between the minimum and maximum values. Once one of the actuator hits its limits, the matrix is severely altered in a dynamic way, which would

make the whole system nonlinear and the model from Figure 2.2 would be inaccurate.

$$\boldsymbol{\omega}_{tar} = \begin{bmatrix} 1 & 1 & -1 \\ 1 & -1 & 1 \\ -1 & -1 & -1 \\ -1 & 1 & 1 \end{bmatrix} \begin{bmatrix} c_p \\ c_q \\ c_r \end{bmatrix} \tag{2.2}$$

In reality the mixer does not not directly output a target rotor speed as is implied in Figure 2.2. In fact the mixer gives an input to the ESCs which in turn control the motors. This ESC mapping from the mixer output to the motor input is assumed to be linear. Although not discussed further in this report, this assumption was later verified to hold up quite well. The signal gain that is added by the ESC is included in the 'PID' control block, removing the need to have separate ESC model blocks.

2.3 Motor dynamics

The motion of the quadcopter is controlled by its four actuators. Once an input is given to the ESC, it takes some time for the rotor actually reach the commanded rotational speed. This is due to the MMOI of the rotor and the motor bell, and due to the electrical behaviour of the motor. This lag behaviour is captured by the LPF blocks in Figure 2.2.

The motors used on the quadcopter are BLDC electric motors which, in contrast to brushed motors, are electrically commutated. In case trapezoidal commutation is used, the motors characteristics are pretty much identical to a standard brushed DC motor [19]. The dynamics of a DC motor can be modelled as the interaction between its electrical components and the mechanics of the load applied to the motor.

The electrical representation for one of the armatures of the motor is shown in Figure 2.3. Here u_{in} is the voltage applied to the armature and R is the resistance of the winding. The variable $e(t)$ is the back EMF generated by the windings that experience a changing magnetic field due to the permanent magnets passing by the windings. Note that adding an inductor in series with the resistor would result in a more accurate representation of the motor armature. However, since its influence on the transient response of the motor is usually small, it is not included here.

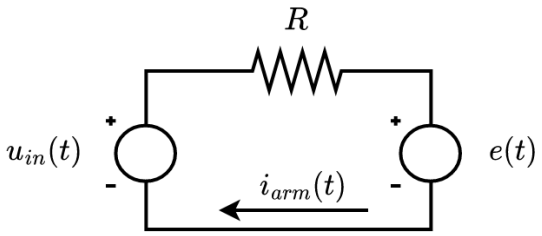

Figure 2.3: Schematic of a single winding circuit of a DC motor.

It can be shown that the torque $T(t)$ divided by the armature current $i_{arm}(t)$ is equal to the back EMF $e(t)$ divided by the rotational speed of the motor, and also equal to some constant K. This is shown in Eq. 2.3 and Eq. 2.4.

$$T(t) = K i_{arm}(t) \tag{2.3}$$

$$e(t) = K\omega(t) \tag{2.4}$$

It is assumed that the load on the motor consists of the MMOI of the rotor and motor bell, I^r_{zz}, as well as aerodynamic drag, $T_d(\omega) = \beta\omega^2$, where β is some constant. Applying Newton's second law and Kirchhoff's law then results in Eq. 2.5 and Eq. 2.6, respectively.

$$I^r_{zz}\dot{\omega} = Ki_{arm}(t) - \beta\omega^2 \tag{2.5}$$
$$0 = u_{in} - K\omega - Ri_{arm}(t) \tag{2.6}$$

Eliminating $i_{arm}(t)$ from those equations results in Eq. 2.7.

$$I^r_{zz}R\dot{\omega} = u_{in}K - K^2\omega - \beta\omega^2 R \tag{2.7}$$

This equation can be linearized around a certain rotor rotational speed ω^* by stating that $\omega^2 \approx \omega^{*^2} + 2\omega^*\overline{\omega}$. Substituting this approximation into Eq. 2.7 results in Eq. 2.8.

$$\begin{aligned} I^r_{zz}R\dot{\overline{\omega}} &= u_{in}K - K^2\overline{\omega} - \beta(\omega^{*^2} + 2\omega^*\overline{\omega})R \\ &= u_{in}K - K^2\overline{\omega} - \beta\omega^{*^2}R - 2\beta\omega^*\overline{\omega}R \\ u_{in}K - \omega^{*^2}R &= I^r_{zz}R\dot{\overline{\omega}} + \overline{\omega}(2\beta\omega^*R + K^2) \end{aligned} \tag{2.8}$$

It can be noticed that Eq. 2.8 can be written in the form shown in Eq. 2.9, where α_0 to α_2 are shorthand notations of the actual coefficients from Eq. 2.8. Introducing a virtual input voltage $u_{vir} = u_{in} + \alpha_2/\alpha_1$ results in the the transfer function shown in Eq. 2.10. This equation shows that the response of the rotor can be modelled by a certain gain multiplied with an LPF. The LPF has a cut off frequency which is equal to α_0. The transformation of u_{in} to u_{vir} only influences the total gain, not the LPF cut off frequency. This change in gain is not relevant here since this is taken care of by the other blocks from Figure 2.2 and their linearizations.

$$\alpha_1 u_{in} + \alpha_2 = \dot{\overline{\omega}} + \alpha_0\overline{\omega} \tag{2.9}$$
$$\alpha_1 u_{vir} = \dot{\overline{\omega}} + \alpha_0\overline{\omega}$$
$$\frac{\overline{\Omega}(s)}{U_{vir}(s)} = \frac{\alpha_1}{s + \alpha_0} \tag{2.10}$$

In conclusion, considering the assumptions made in this section, the transient response of each actuator can be modelled as a first order LPF with a cut off frequency that is dependent on the linearization rotation speed ω^*. That is, $\alpha_0 = \alpha_0(\omega^*)$. In fact, if only linear and quadratic drag forms are applied to the motor, the cut off frequency should be a linear function of linearization rotation speed since $\alpha_0(\omega^*) = 2\beta R\,\omega^* + K^2$.

2.4 Rotor control forces and moments

According to literature a rotor can operate in a couple of different states that each have different aerodynamic characteristics. These states are the normal operating state, the VRS , the TWS and the WMS, which are presented schematically in Figure 2.4. These figures reveal that a rotor thrust force f pointing up is defined as positive. That is, $\boldsymbol{F}^b_i = [0 \quad 0 \quad -f_i]$, where $\boldsymbol{F}^b_i$ is the force generated by the i'th rotor expressed in the body frame. The local rotor speed v is defined positive when blowing in opposite direction with respect to the rotors induced velocity i.

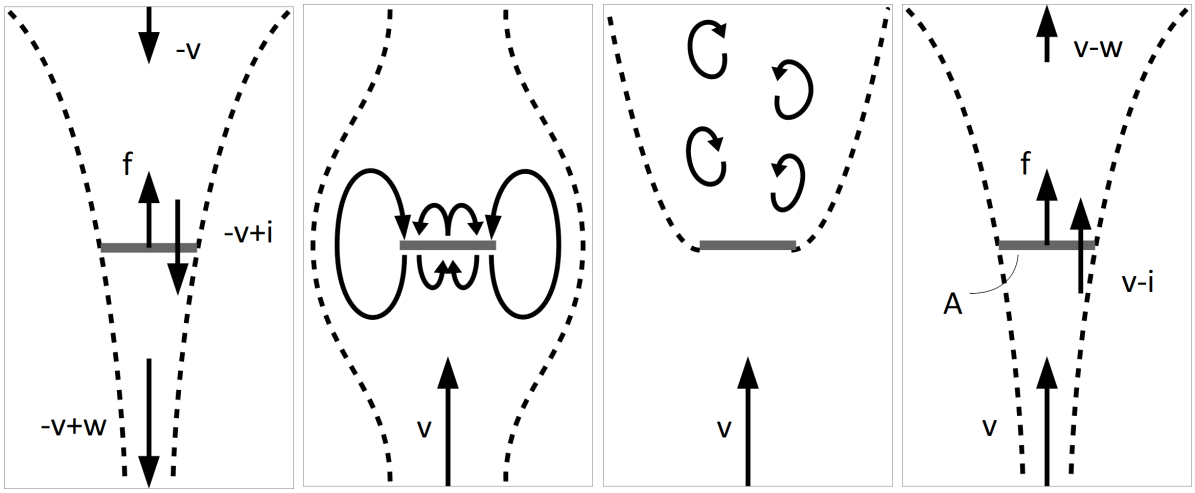

(a) Normal state (b) VRS (c) TWS (d) WMS

Figure 2.4: Operating states of a rotor

When the speed v is negative, the rotor is in its normal operating state, as is shown in Figure 2.4a. The other three states only occur when the local speed v is positive. As one would increase this speed starting at a speed of $0\,\mathrm{m\,s^{-1}}$, one would encounter the VRS as is shown in Figure 2.4b, the TWS as is shown in Figure 2.4c and the WMS as is shown in Figure 2.4d, and in that order. There is somewhat of a grey area when the speed is just slightly negative but small with respect to the induced velocity i. Technically the rotor does not operate in its normal state in this region due the negative inflow, but the large vortices that give the VRS its name are also not yet present. This gray area is from now on referred to as the 'pre-VRS'.

Momentum theory can be used to find the relations between the thrust of the rotor and the velocities in the airflow around it. Unfortunately, this is only possible when there is a well defined airflow as is the case for the normal operating state and the WMS. However, momentum theory an give some insight into when the transition between normal state and VRS and the transition between TWS and WMS occurs. In subsequent chapters this can then be used to interpret recorded rotor wind tunnel data.

Taking Figure 2.4d as a reference, the mass flow during windmilling, $\dot{m}_{wm}$, through the rotor with area A can be expressed as shown in Eq. 2.11, where ρ is the density of the air. The speed of the flow through the rotor is the sum of the external flow speed v, and the induced velocity i. Note that v is in general not equal to the overall speed of the quadcopter, V, due to roll and pitch rates. Furthermore, comparing the flow properties way below the rotor with the flow way above the rotor by applying the laws of conservation of momentum and energy results in Eq. 2.12 and Eq. 2.13, respectively. Here w is how much the air in the far wake has slowed down.

$$\dot{m}_{wm} = \rho A(v - i) \tag{2.11}$$

$$f = \dot{m}v - \dot{m}(v - w) = \dot{m}w \tag{2.12}$$

$$f(v - i) = \frac{1}{2}\dot{m}v^2 - \frac{1}{2}\dot{m}(v - w)^2 \tag{2.13}$$

Combining Eq. 2.12 and Eq. 2.13 gives $w = 2i$. Its not difficult to see that the higher the thrust f, the more the air is slowed down and thus the higher w. However, its not

possible for w to become larger then v, since then the air speed in the far wake would reverse and the flow model no longer holds. At the thrust f where $v = w$, the rotor transitions from the WMS to the TWS. At this point $f = f_{t1}$. Filling in $v = w$ into Eq. 2.12 results in Eq. 2.14.

$$\begin{aligned} f &= \dot{m}_{wm} w \\ &= \rho A (v - \frac{1}{2} w) w \\ f_{t1} &= \rho A (v - \frac{1}{2} v) v \\ &= \frac{1}{2} \rho A v^2 \end{aligned} \tag{2.14}$$

For the normal operating state, Eq. 2.12 and Eq. 2.13 are exactly the same if the sign conventions shown in Figure 2.4a are used. However, the mass flow is now positive in the opposite direction. That is $\dot{m}_{no} = -\dot{m}_{wm}$, where $\dot{m}_{no}$ is the mass flow for the normal operating state.

As mentioned, the transition between the normal state to the pre-VRS happens when the airflow v becomes positive. In this pre-VRS state the flow model of Figure 2.4a is technically incorrect, but in practice the model equations hold up quite well when $v < i_{v=0}/2$ [11], where $i_{v=0}$ is the induced velocity the rotor would generate at the same thrust level but with zero external airspeed $v = 0$. The thrust at $v = 0$, $f_{v=0}$, can be related to $i_{v=0}$ using Eq. 2.12, as is shown in Eq. 2.15.

$$\begin{aligned} f &= \dot{m}_{no} w \\ &= 2\rho A (i - v) i \\ f_{v=0} &= 2\rho A i_{v=0}^2 \\ i_{v=0} &= \sqrt{\frac{f_{v=0}}{2\rho A}} \end{aligned} \tag{2.15}$$

The rotor transitions from the pre-VRS to the VRS once f reaches a value as is shown in Eq. 2.16, where the result of Eq. 2.15 is substituted into $v = i_{v=0}/2$. At this point $f = f_{t2}$.

$$\begin{aligned} v &= i_{v=0}/2 \\ v &= \frac{1}{2} \sqrt{\frac{f}{2\rho A}} \\ f_{t2} &= 8\rho A v^2 \end{aligned} \tag{2.16}$$

Momentum theory does not say anything about what happens to the thrust and induced velocity in the VRS and the TWS. Assuming a constant air speed v, its therefore only possible to state the following.

- Starting in the WMS and increasing rotor rotational speed, a mathematically defined TWS is reached when the thrust increases to a value of $f_{t1} = \rho A v^2/2$.
- Starting in the pre-VRS and decreasing rotor rotational speed, a mathematically defined VRS is reached when the thrust decreases to a value of $f_{t2} = 8\rho A v^2$.

Based on the momentum theory discussion above, the forces and moments generated by each individual rotor are assumed to be a static function of the rotor rotational speed ω_i and the local external air speed v seen by the rotor. It is assumed that forces and moments that work on a single rotor are the sum of aerodynamic forces and moments, and inertial rotor effects. The latter refers to gyroscopic effects and reaction torques.

Due to the restrictions set in section 2.1, it is assumed that only the aerodynamic thrust and torque produced by the rotor are of significant value. Aerodynamic forces and moments that are parallel to the rotor plane are thus assumed to be zero.

Variation in aerodynamic thrust and torque due to change in a rotor speed $\overline{\omega}_i$ is captured by the 'rotor aerodynamics' block in Figure 2.2. On the other hand, variation in aerodynamic thrust and torque due to a change in quadcopter states, such as the attitude rates p, q, r or the change in airspeed $\overline{V}$, is captured by the 'Quadcopter dynamics' block, as is explained in section 2.5. The 'rotor aerodynamics' block consist of a multiplication matrix which entries are dependent on the rotor rotational speeds ω_i^* and speed V^* that linearization is performed around.

Because the each rotor and motor bell combination has a certain MMOI, it can generate both gyroscopic and reaction moments. Moments can be derived using the Euler equation of rotation, as is shown in Eq. 2.17. Here $\boldsymbol{M}_g^i = [L_g^i \quad M_g^i \quad N_g^i]^T$ is the moment exerted on the quadcopters air frame by the i'th rotor due to the inertial properties of the rotor, $\boldsymbol{\Omega}_r^i$ is the rotational velocity with respect to the inertial frame of the i'th rotor, and I^r is the MMOI of the rotor and motor bell. Since the preceding vectors are expressed in the body frame, the axis system for I^r is taken to be the body frame as well. In this case it can be shown that for three bladed rotors, the cross terms I_{xy}^r, I_{yz}^r and I_{xz}^r are zero irrespective of the rotation angle of the rotor. Therefore I^r is a diagonal matrix and constant in time, as shown in Eq. 2.18.

$$-\boldsymbol{M}_g^i = I^r \dot{\boldsymbol{\Omega}}_r + \boldsymbol{\Omega}_r^i \times I^r \boldsymbol{\Omega}_r^i \tag{2.17}$$

$$I^r = \begin{bmatrix} I_{xx}^r & -I_{xy}^r & -I_{xz}^r \\ -I_{xy}^r & I_{yy}^r & -I_{yz}^r \\ -I_{xz}^r & -I_{yz}^r & I_{zz}^r \end{bmatrix} = \begin{bmatrix} I_{xx}^r & 0 & 0 \\ 0 & I_{yy}^r & 0 \\ 0 & 0 & I_{zz}^r \end{bmatrix} \tag{2.18}$$

The rotation of the rotor in the inertial frame is equal to the sum of the rotation of the quadcopter in the inertial frame $\boldsymbol{\Omega}_d$, and the rotation of the rotor with respect to the quadcopters air frame $\boldsymbol{\Omega}_{rd}^i$, as shown in Eq. 2.19. The latter vector is expressed as $\boldsymbol{\Omega}_{rd}^i = [0 \quad 0 \quad \tilde{\omega}_i]^T$ with $\tilde{\omega}_i = (-1)^{i-1}\omega_i$. Substituting this sum into Eq. 2.17 results in Eq. 2.20, which after working out gives Eq. 2.21.

$$\boldsymbol{\Omega}_r^i = \boldsymbol{\Omega}_d + \boldsymbol{\Omega}_{rd}^i \tag{2.19}$$

$$
\begin{aligned}
-\boldsymbol{M}_g^i &= I^r(\dot{\boldsymbol{\Omega}}_d + \dot{\boldsymbol{\Omega}}_{rd}) + (\boldsymbol{\Omega}_d + \boldsymbol{\Omega}_{rd}) \times I^r(\boldsymbol{\Omega}_d + \boldsymbol{\Omega}_{rd}) \qquad (2.20)\\
&= I^r\dot{\boldsymbol{\Omega}}_d + I^r\dot{\boldsymbol{\Omega}}_{rd} + [\boldsymbol{\Omega}_d \times I^r\boldsymbol{\Omega}_d] + [\boldsymbol{\Omega}_d \times I^r\boldsymbol{\Omega}_{rd}] + [\boldsymbol{\Omega}_{rd} \times I^r\boldsymbol{\Omega}_d] + [\boldsymbol{\Omega}_{rd} \times I^r\boldsymbol{\Omega}_{rd}]\\
&= \begin{bmatrix} 0 \\ 0 \\ I^r_{zz}\dot{\tilde{\omega}}_i \end{bmatrix} + \begin{bmatrix} I^r_{xx}\dot{p} \\ I^r_{yy}\dot{q} \\ I^r_{zz}\dot{r} \end{bmatrix} + \begin{bmatrix} p \\ q \\ r \end{bmatrix} \times \begin{bmatrix} I^r_{xx}p \\ I^r_{yy}q \\ I^r_{zz}r \end{bmatrix} + \begin{bmatrix} p \\ q \\ r \end{bmatrix} \times \begin{bmatrix} 0 \\ 0 \\ I^r_{zz}\tilde{\omega}_i \end{bmatrix} + \begin{bmatrix} 0 \\ 0 \\ \tilde{\omega}_i \end{bmatrix} \times \begin{bmatrix} I^r_{xx}p \\ I^r_{yy}q \\ I^r_{zz}r \end{bmatrix}\\
&\quad + \begin{bmatrix} 0 \\ 0 \\ \tilde{\omega}_i \end{bmatrix} \times \begin{bmatrix} 0 \\ 0 \\ I^r_{zz}\tilde{\omega}_i \end{bmatrix}\\
&= \begin{bmatrix} I^r_{xx}\dot{p} \\ I^r_{yy}\dot{q} \\ I^r_{zz}(\dot{r} + \dot{\tilde{\omega}}_i) \end{bmatrix} + \begin{bmatrix} I^r_{zz}qr - I^r_{yy}qr \\ I^r_{xx}pr - I^r_{zz}pr \\ I^r_{yy}pq - I^r_{xx}pq \end{bmatrix} + \begin{bmatrix} qI^r_{zz}\tilde{\omega}_i \\ -pI^r_{zz}\tilde{\omega}_i \\ 0 \end{bmatrix} + \begin{bmatrix} -I^r_{yy}q\tilde{\omega}_i \\ I^r_{xx}p\tilde{\omega}_i \\ 0 \end{bmatrix}\\
&= \begin{bmatrix} I^r_{xx}\dot{p} \\ I^r_{yy}\dot{q} \\ I^r_{zz}(\dot{r} + \dot{\tilde{\omega}}_i) \end{bmatrix} + \begin{bmatrix} I^r_{zz}qr - I^r_{yy}qr + qI^r_{zz}\tilde{\omega}_i - I^r_{yy}q\tilde{\omega}_i \\ I^r_{xx}pr - I^r_{zz}pr - pI^r_{zz}\tilde{\omega}_i + I^r_{xx}p\tilde{\omega}_i \\ 0 \end{bmatrix}\\
&= \begin{bmatrix} I^r_{xx}\dot{p} \\ I^r_{yy}\dot{q} \\ I^r_{zz}(\dot{r} + \dot{\tilde{\omega}}_i) \end{bmatrix} + \begin{bmatrix} q(I^r_{zz} - I^r_{yy})(r + \tilde{\omega}_i) \\ p(I^r_{xx} - I^r_{zz})(r + \tilde{\omega}_i) \\ 0 \end{bmatrix} \qquad (2.21)\\
&\approx \begin{bmatrix} q(I^r_{zz} - I^r_{yy})\tilde{\omega}_i \\ p(I^r_{xx} - I^r_{zz})\tilde{\omega}_i \\ I^r_{zz}\dot{\tilde{\omega}}_i \end{bmatrix} \qquad (2.22)
\end{aligned}
$$

In general it can be assumed that $\tilde{\omega}_i$ is much larger than the attitude rates p, q, r and their derivatives. This results in a simplified expression for gyroscopic moment as shown in Eq. 2.22. Summing this moment for all four rotors results in the gyroscopic roll and pitch moments generated as are shown in Eq. 2.23 and Eq. 2.24, respectively, and the yaw reaction torque as shown inEq. 2.25.

$$
\begin{aligned}
L_g &= q(I^r_{zz} - I^r_{yy})(-\omega_1 + \omega_2 - \omega_3 + \omega_4) \qquad (2.23)\\
M_g &= p(I^r_{xx} - I^r_{zz})(-\omega_1 + \omega_2 - \omega_3 + \omega_4) \qquad (2.24)\\
N_g &= I^r_{zz}(-\dot{\omega}_1 + \dot{\omega}_2 - \dot{\omega}_3 + \dot{\omega}_4) \qquad (2.25)
\end{aligned}
$$

As expected, it can be seen that the gyroscopic effect of all rotors cancel if all rotors rotate with the same speed. Linearization around the four rotor speeds ω_i^* and speed V^* results in Eq. 2.26 to Eq. 2.28.

$$
\begin{aligned}
L_g &= q(I^r_{zz} - I^r_{yy})(-\omega_1^* + \omega_2^* - \omega_3^* + \omega_4^*) \qquad (2.26)\\
M_g &= p(I^r_{xx} - I^r_{zz})(-\omega_1^* + \omega_2^* - \omega_3^* + \omega_4^*) \qquad (2.27)\\
N_g &= I^r_{zz}(-\dot{\bar{\omega}}_1 + \dot{\bar{\omega}}_2 - \dot{\bar{\omega}}_3 + \dot{\bar{\omega}_4}) \qquad (2.28)
\end{aligned}
$$

2.5 Quadcopter dynamics

Using Euler's equation of rotation and Newtons second law, a set of four nonlinear equations of motion of the quadcopter can be derived which are shown in Eq. 2.29 to Eq. 2.32. Here $L_m(\boldsymbol{\sigma}, \boldsymbol{v})$, $M_m(\boldsymbol{\sigma}, \boldsymbol{v})$, $N_m(\boldsymbol{\sigma}, \boldsymbol{v})$ and $F_m(\boldsymbol{\sigma}, \boldsymbol{v})$ are the aerodynamic moments and forces that are generated by the rotors as a direct result of the motion of the quadcopter.

For example, a roll rate changes the translational speed of all rotors, causing them to generate different forces and moments. The moments $L_g(q)$ and $M_g(p)$ are the gyroscopic moments described in section 2.4. The yaw reaction torque N_g is implemented using a separate model block, as is shown in Figure 2.2. Furthermore, L, M, N and F capture the moments and forces due to changing rotor speeds $\boldsymbol{\omega}$ and any form of external moments and forces. Finally, g is the gravity acceleration.

$$I_{xx}\dot{p} + rq(I_{zz} - I_{yy}) = L_m(\boldsymbol{\sigma}, \boldsymbol{v}) + L_g(q) + L \tag{2.29}$$
$$I_{yy}\dot{q} + pr(I_{xx} - I_{zz}) = M_m(\boldsymbol{\sigma}, \boldsymbol{v}) + M_g(p) + M \tag{2.30}$$
$$I_{zz}\dot{r} + pq(I_{yy} - I_{xx}) = N_m(\boldsymbol{\sigma}, \boldsymbol{v}) + N \tag{2.31}$$
$$m\dot{V} = F_m(\boldsymbol{\sigma}, \boldsymbol{v}) + F + gm \tag{2.32}$$

Here $\boldsymbol{\sigma} = [\sigma_1 \quad \sigma_2 \quad \sigma_3 \quad \sigma_4]^T$ are the rotational speeds of the rotor with respect to the air. This is the sum of the rotational speed with respect to the quadcopter and yaw rate or the quadcopter itself. In other words, $\boldsymbol{\sigma} = \boldsymbol{\omega} + [r \quad -r \quad r \quad -r]^T$ with $\boldsymbol{\omega} = [\omega_1 \quad \omega_2 \quad \omega_3 \quad \omega_4]^T$. Furthermore, $\boldsymbol{v} = [v_1 \quad v_2 \quad v_3 \quad v_4]^T$ are the speeds seen by each individual rotor parallel to their rotation axis. This speed is dependent on the overall speed of the quadcopter V, the roll rate p and pitch rate q. A change in this local speed $\overline{\boldsymbol{v}} = [\overline{v}_1 \quad \overline{v}_2 \quad \overline{v}_3 \quad \overline{v}_4]^T$ can then be written as shown in Eq. 2.33 to Eq. 2.36.

$$\overline{v}_1 = \overline{V} - l_y p - l_x q \tag{2.33}$$
$$\overline{v}_2 = \overline{V} - l_y p + l_x q \tag{2.34}$$
$$\overline{v}_3 = \overline{V} + l_y p + l_x q \tag{2.35}$$
$$\overline{v}_4 = \overline{V} + l_y p - l_x q \tag{2.36}$$

The left side of Eq. 2.29 to Eq. 2.31 can be linearized as is shown in Eq. 2.37 to Eq. 2.39.

$$I_{xx}\dot{p} + rq(I_{zz} - I_{yy}) \approx I_{xx}\dot{p} \tag{2.37}$$
$$I_{yy}\dot{q} + pr(I_{xx} - I_{zz}) \approx I_{yy}\dot{q} \tag{2.38}$$
$$I_{zz}\dot{r} + pq(I_{yy} - I_{xx}) \approx I_{zz}\dot{r} \tag{2.39}$$

The moments L to M and force F can be linearized as shown in Eq. 2.40 to Eq. 2.43.

$$L(t) = L^* + \overline{L}(t) \tag{2.40}$$
$$M(t) = M^* + \overline{M}(t) \tag{2.41}$$
$$N(t) = N^* + \overline{N}(t) \tag{2.42}$$
$$F(t) = F^* + \overline{F}(t) \tag{2.43}$$

Then, $L_m(\boldsymbol{\sigma}, \boldsymbol{v})$, $M_m(\boldsymbol{\sigma}, \boldsymbol{v})$, $N_m(\boldsymbol{\sigma}, \boldsymbol{v})$ and $F_m(\boldsymbol{\sigma}, \boldsymbol{v})$ are functions of the thrust $f_i(\sigma_i, v_i)$ and torque $n_i(\sigma_i, v_i)$ of the i'th rotor, as is shown in Eq. 2.44 to Eq. 2.47. Here l_x and l_y were defined in Figure 15.1.

$$L_m(\boldsymbol{\sigma}, \boldsymbol{k}) = l_y[f_1(\sigma_1, v_1) + f_2(\sigma_2, v_2) - f_3(\sigma_3, v_3) - f_4(\sigma_4, v_4)] \tag{2.44}$$
$$M_m(\boldsymbol{\sigma}, \boldsymbol{k}) = l_x[f_1(\sigma_1, v_1) - f_2(\sigma_2, v_2) - f_3(\sigma_3, v_3) + f_4(\sigma_4, v_4)] \tag{2.45}$$
$$N_m(\boldsymbol{\sigma}, \boldsymbol{k}) = -n_1(\sigma_1, v_1) + n_2(\sigma_2, v_2) - n_3(\sigma_3, v_3) + n_4(\sigma_4, v_4) \tag{2.46}$$
$$F_m(\boldsymbol{\sigma}, \boldsymbol{k}) = -f_1(\sigma_1, v_1) - f_2(\sigma_2, v_2) - f_3(\sigma_3, v_3) - f_4(\sigma_4, v_4) \tag{2.47}$$

Each thrust $f_i(\sigma_i, v_i)$ and torque $n_i(\sigma_i, v_i)$ can be linearized as is shown in Eq. 2.48 and Eq. 2.49. Here f_{σ_i}, f_{v_i}, n_{σ_i} and n_{v_i} are defined in Eq. 2.50.

$$\begin{aligned} .f_i(\sigma_i, v_i) &\approx f_i^* + f_{\sigma_i}\overline{\sigma}_i + f_{v_i}\overline{v}_i \\ &= f_i^* - f_{\sigma_i}(-1)^i r + f_{v_i}\overline{v}_i \end{aligned} \tag{2.48}$$

$$\begin{aligned} n_i(\sigma_i, v_i) &\approx n_i^* + n_{\sigma_i}\overline{\sigma}_i + n_{v_i}\overline{v}_i \\ &= n_i^* - n_{\sigma_i}(-1)^i r + n_{v_i}\overline{v}_i \end{aligned} \tag{2.49}$$

$$f_{\sigma_i} = \left.\frac{\partial f_i}{\partial \sigma_i}\right|_{\omega_i^*, V^*} \qquad f_{v_i} = \left.\frac{\partial f_i}{\partial v_i}\right|_{\omega_i^*, V^*} \qquad n_{\sigma_i} = \left.\frac{\partial n_i}{\partial \sigma_i}\right|_{\omega_i^*, V^*} \qquad n_{v_i} = \left.\frac{\partial n_i}{\partial v_i}\right|_{\omega_i^*, V^*} \tag{2.50}$$

The linearized rotor thrust force expressed in Eq. 2.48 can be substituted into Eq. 2.44, resulting in an expression for the change in $L_m(\boldsymbol{\sigma}, \boldsymbol{v})$, denoted as $\overline{L}_m(\boldsymbol{\sigma}, \boldsymbol{v})$, as is shown in Eq. 2.52.

$$\begin{aligned} L_m(\boldsymbol{\sigma}, \boldsymbol{v})/l_y =& f_1^* + f_2^* - f_3^* - f_4^* \\ &+ f_{\sigma_1} r - f_{\sigma_2} r - f_{\sigma_3} r + f_{\sigma_4} r \\ &+ f_{v_1}(\overline{V} - l_y p - l_x q) + f_{v_2}(\overline{V} - l_y p + l_x q) \\ &- f_{v_3}(\overline{V} + l_y p + l_x q) - f_{v_4}(\overline{V} + l_y p - l_x q) \end{aligned} \tag{2.51}$$

$$\begin{aligned} \overline{L}_m(\boldsymbol{\sigma}, \boldsymbol{v})/l_y =& r(f_{\sigma_1} - f_{\sigma_2} - f_{\sigma_3} + f_{\sigma_4}) \\ &+ \overline{V}(f_{v_1} + f_{v_2} - f_{v_3} - f_{v_4}) \\ &- l_y p(f_{v_1} + f_{v_2} + f_{v_3} + f_{v_4}) \\ &+ l_x q(-f_{v_1} + f_{v_2} - f_{v_3} + f_{v_4}) \end{aligned} \tag{2.52}$$

Doing the same for the pitch moment $M_m(\boldsymbol{\sigma}, \boldsymbol{v})$ results in Eq. 2.54

$$\begin{aligned} M_m(\boldsymbol{\sigma}, \boldsymbol{v})/l_x =& f_1^* - f_2^* - f_3^* + f_4^* \\ &+ f_{\sigma_1} r + f_{\sigma_2} r - f_{\sigma_3} r - f_{\sigma_4} r \\ &+ f_{v_1}(\overline{V} - l_y p - l_x q) - f_{v_2}(\overline{V} - l_y p + l_x q) \\ &- f_{v_3}(\overline{V} + l_y p + l_x q) + f_{v_4}(\overline{V} + l_y p - l_x q) \end{aligned} \tag{2.53}$$

$$\begin{aligned} \overline{M}_m(\boldsymbol{\sigma}, \boldsymbol{v})/l_x =& r(f_{\sigma_1} + f_{\sigma_2} - f_{\sigma_3} - f_{\sigma_4}) \\ &+ \overline{V}(f_{v_1} - f_{v_2} - f_{v_3} + f_{v_4}) \\ &+ l_y p(-f_{v_1} + f_{v_2} - f_{v_3} + f_{v_4}) \\ &- l_x q(f_{v_1} + f_{v_2} + f_{v_3} + f_{v_4}) \end{aligned} \tag{2.54}$$

For the yaw axis, Eq. 2.49 is substituted into Eq. 2.46, resulting in Eq. 2.56.

$$\begin{aligned} N_m(\boldsymbol{\sigma}, \boldsymbol{v}) =& - n_1^* + n_2^* - n_3^* + n_4^* \\ &- n_{\sigma_1} r - n_{\sigma_2} r - n_{\sigma_3} r - n_{\sigma_4} r \\ &- n_{v_1}(\overline{V} - l_y p - l_x q) + n_{v_2}(\overline{V} - l_y p + l_x q) \\ &- n_{v_3}(\overline{V} + l_y p + l_x q) + n_{v_4}(\overline{V} + l_y p - l_x q) \end{aligned} \tag{2.55}$$

$$\begin{aligned} \overline{N}_m(\boldsymbol{\sigma}, \boldsymbol{v}) =& - r(n_{\sigma_1} + n_{\sigma_2} + n_{\sigma_3} + n_{\sigma_4}) \\ &+ \overline{V}(-n_{v_1} + n_{v_2} - n_{v_3} + n_{v_4}) \\ &+ l_y p(n_{v_1} - n_{v_2} - n_{v_3} + n_{v_4}) \\ &+ l_x q(n_{v_1} + n_{v_2} - n_{v_3} - n_{v_4}) \end{aligned} \tag{2.56}$$

Finally, the value for $\overline{F}_m(\boldsymbol{\sigma}, \boldsymbol{v})$ can be calculated according to Eq. 2.58.

$$\begin{aligned} F_m(\boldsymbol{\sigma}, \boldsymbol{v}) = &-(f_1^* + f_2^* + f_3^* + f_4^*) \\ &- f_{\sigma_1} r + f_{\sigma_2} r - f_{\sigma_3} r + f_{\sigma_4} \\ &- f_{v_1}(\overline{V} - l_y p - l_x q) - f_{v_2}(\overline{V} - l_y p + l_x q) \\ &- f_{v_3}(\overline{V} + l_y p + l_x q) - f_{v_4}(\overline{V} + l_y p - l_x q) \end{aligned} \tag{2.57}$$

$$\begin{aligned} \overline{F}_m(\boldsymbol{\sigma}, \boldsymbol{v}) = &+ r(-f_{\sigma_1} + f_{\sigma_2} - f_{\sigma_3} + f_{\sigma_4}) \\ &- \overline{V}(f_{v_1} + f_{v_2} + f_{v_3} + f_{v_4}) \\ &+ l_x q(f_{v_1} - f_{v_2} - f_{v_3} + f_{v_4}) \\ &+ l_y p(f_{v_1} + f_{v_2} - f_{v_3} - f_{v_4}) \end{aligned} \tag{2.58}$$

Substituting Eq. 2.52, Eq. 2.54, Eq. 2.56 and Eq. 2.58 into Eq. 2.29 to Eq. 2.32, while taking into account the linearization results of Eq. 2.37 to Eq. 2.39 and Eq. 2.40 to Eq. 2.43, results in a set of first order differential equations as is shown in Eq. 2.59.

$$\begin{bmatrix} I_{xx}\dot{p} \\ I_{yy}\dot{q} \\ I_{zz}\dot{r} \\ m\dot{\overline{V}} \end{bmatrix} = \begin{bmatrix} L_p & L_q & L_r & L_{\overline{V}} \\ M_p & M_q & M_r & M_{\overline{V}} \\ N_p & N_q & N_r & N_{\overline{V}} \\ F_p & F_q & F_r & F_{\overline{V}} \end{bmatrix} \begin{bmatrix} p \\ q \\ r \\ \overline{V} \end{bmatrix} + \begin{bmatrix} \overline{L} \\ \overline{M} \\ \overline{N} \\ \overline{F} \end{bmatrix} \tag{2.59}$$

Note that the equalities in Eq. 2.60 to Eq. 2.63 are assumed to be true.

$$-f_1^* - f_2^* + f_3^* + f_4^* = L^* \tag{2.60}$$
$$-f_1^* + f_2^* + f_3^* - f_4^* = M^* \tag{2.61}$$
$$n_1^* - n_2^* + n_3^* - n_4^* = N^* \tag{2.62}$$
$$f_1^* + f_2^* + f_3^* + f_4^* = F^* + gm \tag{2.63}$$

Moving I_{xx}, I_{yy}, I_{zz} and m in Eq. 2.59 to the right hand side results in the state equation of the state space system used for the quadcopter dynamics block in Figure 2.2. The entries of the matrix in Eq. 2.59 are written out below. Note the added gyroscopic effect terms derived in section 2.4 for the L_q and M_p entries.

$$\begin{aligned} L_p &= l_y^2(-f_{v_1} - f_{v_2} - f_{v_3} - f_{v_4}) \\ L_q &= l_x l_y(-f_{v_1} + f_{v_2} - f_{v_3} + f_{v_4}) + (I_{zz}^r - I_{yy}^r)(-\omega_1^* + \omega_2^* - \omega_3^* + \omega_4^*) \\ L_r &= l_y(f_{\sigma_1} - f_{\sigma_2} - f_{\sigma_3} + f_{\sigma_4}) \\ L_{\overline{V}} &= l_y(f_{v_1} + f_{v_2} - f_{v_3} - f_{v_4}) \end{aligned}$$

$$\begin{aligned} M_p &= l_y l_x(-f_{v_1} + f_{v_2} - f_{v_3} + f_{v_4}) + (I_{xx}^r - I_{zz}^r)(-\omega_1^* + \omega_2^* - \omega_3^* + \omega_4^*) \\ M_q &= l_x^2(-f_{v_1} - f_{v_2} - f_{v_3} - f_{v_4}) \\ M_r &= l_x(f_{\sigma_1} + f_{\sigma_2} - f_{\sigma_3} - f_{\sigma_4}) \\ M_{\overline{V}} &= l_x(f_{v_1} - f_{v_2} - f_{v_3} + f_{v_4}) \end{aligned}$$

$$\begin{aligned} N_p &= l_y(n_{v_1} - n_{v_2} - n_{v_3} + n_{v_4}) & F_p &= l_y(f_{v_1} + f_{v_2} - f_{v_3} + f_{v_4}) \\ N_q &= l_x(n_{v_1} + n_{v_2} - n_{v_3} - n_{v_4}) & F_q &= l_x(f_{v_1} - f_{v_2} - f_{v_3} + f_{v_4}) \\ N_r &= (-n_{\sigma_1} - n_{\sigma_2} - n_{\sigma_3} - n_{\sigma_4}) & F_r &= (-f_{\sigma_1} + f_{\sigma_2} - f_{\sigma_3} + f_{\sigma_4}) \\ N_{\overline{V}} &= (-n_{v_1} + n_{v_2} - n_{v_3} + n_{v_4}) & F_{\overline{V}} &= (-f_{v_1} - f_{v_2} - f_{v_3} - f_{v_4}) \end{aligned}$$

2.6 Input and outputs in the frequency domain

The disturbance moments and forces L_d, M_d, N_d and F_d serve as the inputs to the system model, as is shown in Figure 2.2. The output accuracy of the model is arguably as dependent on the accuracy of the input signals as on the quality of the system model. The combination of the input signals and the system model can therefore be seen as the 'total model'.

As briefly mentioned in section 2.1, it is assumed that L_d, M_d, N_d and F_d are exclusively generated by the fluctuations of thrust and torque of each rotor at a given rotational speed and descent speed. At each rotor rotational speed and descent speed the thrust and torque can be plotted in the frequency domain. This could show that the fluctuation in thrust and torque happens more at certain frequencies than at other frequencies. For example, it would not be a stretch to imagine that the periodic vortex shedding in the VRS could cause a dominant thrust fluctuation at the vortex shedding frequency.

Due to the fact that the thrust and torque could only be measured with a maximum frequency of around 5 Hz, it is assumed here that the thrust and torque f_i and n_i are flat functions in the frequency domain. In this case their stochastic nature can be fully captured by their standard deviations σ_{f_i} and σ_{n_i}. The standard deviations of L_d, M_d, N_d and F_d are direct functions σ_{f_i} and σ_{n_i}, as is shown for the roll axis in Eq. 2.65. In Eq. 2.64 the assumption is made that f_1, f_2, f_3 and f_4 are uncorrelated.

$$\begin{aligned} L_d &= l_y(f_1 + f_2 - f_3 - f_4) \\ \mathrm{Var}(L_d) &= \mathrm{Var}(l_y(f_1 + f_2 - f_3 - f_4)) \\ &= l_y^2(\mathrm{Var}(f_1) + \mathrm{Var}(f_2) + \mathrm{Var}(-f_3) + \mathrm{Var}(-f_4)) \qquad (2.64) \\ \sigma_{L_d}^2 &= l_y^2(\sigma_{f_1}^2 + \sigma_{f_2}^2 + \sigma_{f_3}^2 + \sigma_{f_4}^2) \qquad (2.65) \end{aligned}$$

The variance $\sigma_{L_d}^2$ and the PSD of the L_d signal, W_{L_d}, can be related as is shown in Eq. 2.66. Here ω_s is the angular frequency at which samples are taken from the random thrust and torque signal and ω_{nq} is the corresponding Nyquist angular frequency.

$$\sigma_{L_d}^2 = \frac{1}{\pi}\int_0^{\omega_{nq}} W_{L_d}\, d\omega = \frac{\omega_{nq} W_{L_d}}{\pi} = \frac{\omega_s W_{L_d}}{2\pi} \qquad (2.66)$$

Combining Eq. 2.65 and Eq. 2.66 results in Eq. 2.67.

$$\begin{aligned} \frac{\omega_s W_{L_d}}{2\pi} &= l_y^2(\sigma_{f_1}^2 + \sigma_{f_2}^2 + \sigma_{f_3}^2 + \sigma_{f_4}^2) \\ W_{L_d} &= \frac{2\pi}{\omega_s} l_y^2(\sigma_{f_1}^2 + \sigma_{f_2}^2 + \sigma_{f_3}^2 + \sigma_{f_4}^2) \qquad (2.67) \end{aligned}$$

The rotor thrust and torque standard deviations, σ_{f_i} and σ_{n_i}, are a function of the local rotor speed v_i and rotor rotational rate ω_i. It is here assumed however that the change in local speed v_i does not result in large changes of standard deviations σ_{f_i} and σ_{n_i}. For the input signals it is therefore assumed that $v_i \approx V^*$. Taking this into account and repeating the derivations for M_d, N_d and F_d results in the four expressions for PSD of

the input signals as is shown in Eq. 2.68 to Eq. 2.71.

$$W_{L_d} = \frac{2\pi}{\omega_s} l_y^2 \sum_{i=1}^{4} \sigma_{f_i}^2(\omega_i, \overline{V}) \tag{2.68}$$

$$W_{M_d} = \frac{2\pi}{\omega_s} l_x^2 \sum_{i=1}^{4} \sigma_{f_i}^2(\omega_i, \overline{V}) \tag{2.69}$$

$$W_{N_d} = \frac{2\pi}{\omega_s} \sum_{i=1}^{4} \sigma_{n_i}^2(\omega_i, \overline{V}) \tag{2.70}$$

$$W_{F_d} = \frac{2\pi}{\omega_s} \sum_{i=1}^{4} \sigma_{f_i}^2(\omega_i, \overline{V}) \tag{2.71}$$

The system model shown in Figure 2.2 can be written as a state space system or a matrix of transfer functions. Since the transient response is not of much interest for steady flight conditions where the propwash occurs, the transfer functions can be replaced by frequency response functions. The PSDs of the output signals p, q, r and $\overline{V}$, denoted by $S_{pp}(\omega)$, $S_{qq}(\omega)$, $S_{rr}(\omega)$ and $S_{\overline{V}\overline{V}}(\omega)$, respectively, can then be expressed as shown in Eq. 2.72. The matrix in this equation contains the frequency response functions where the subscripts indicate the output and input signals that each frequency response function relates.

$$\begin{bmatrix} S_{pp}(\omega) \\ S_{qq}(\omega) \\ S_{rr}(\omega) \\ S_{\overline{V}\overline{V}}(\omega) \end{bmatrix} = \begin{bmatrix} |H_{pL}(\omega)|^2 & |H_{pM}(\omega)|^2 & |H_{pN}(\omega)|^2 & |H_{pF}(\omega)|^2 \\ |H_{qL}(\omega)|^2 & |H_{qM}(\omega)|^2 & |H_{qN}(\omega)|^2 & |H_{qF}(\omega)|^2 \\ |H_{rL}(\omega)|^2 & |H_{rM}(\omega)|^2 & |H_{rN}(\omega)|^2 & |H_{rF}(\omega)|^2 \\ |H_{\overline{V}L}(\omega)|^2 & |H_{\overline{V}M}(\omega)|^2 & |H_{\overline{V}N}(\omega)|^2 & |H_{\overline{V}F}(\omega)|^2 \end{bmatrix} \begin{bmatrix} W_{L_d} \\ W_{M_d} \\ W_{N_d} \\ W_{F_d} \end{bmatrix} \tag{2.72}$$

Chapter 3

Experimental Setup

For this project a variety of physical experiments were performed. Most of these experiments served to gather data in order to model the separate model blocks shown in Figure 2.2 as accurately as possible. Other experiments were performed with the quadcopter in its entirety to gather data to validate the performance of the model.

In section 3.1 some specifications of the quadcopter are presented that were used for the duration of this project for both modelling and performing experiments. In section 3.2 the setup of the wind tunnel tests is explained that focused on modelling an isolated rotor in an air flow. In section 3.3 measurements of the actuators transient responses are discussed. In section 3.4 it is explained how the controller gains of the Betaflight firmware were found since these are not equal to the gains shown in the Betaflight configurator. How the various masses and MMOIs were found that are used in the model is treated in section 3.5. In section 3.6 the wind tunnel test is discussed where the quadcopter was placed in a gimbal while the flight controller was disabled. In section 3.8 a similar test with an active flight controller is discussed. It was necessary to confirm that no airframe eigenfrequencies were low enough in order to pollute the propwash oscillation measurements. This is done in section 3.7. Finally, in section 3.9, the flight tests are discussed during which the propwash effect is provoked on purpose. This data is ultimately used to validate the model performance.

3.1 Quadcopter specifications

A custom build 5 inch freestyle quadcopter was used as the basis for all experiments described in this chapter. This quadcopter was build using a carbon fibre TBS Source One V4 frame and four Emax Eco II series 2207 motors, which were rated at 2400 kV and had 14 poles. A Kakute f7 v1.5 flight controller was used in conjunction with an MPU6000 V1.2 IMU unit. Betaflight V4.2.9 was installed as flight controller firmware. In Table 3.1 the most important Betaflight settings are listed. In Table 3.2 the controller gains as shown in the Betaflight configurator are presented that were used for experiments with active flight controller. Unfortunately the software did not allow for completely disabling the feedforward control gains, which is why they were set at the almost negligible value of 1. For the quadcopter an Aikon AK32 V3 55A 4in1 6S ESC unit was used running BLHeli32 firmware, where some of the relevant settings are shown in Table 3.3. Electronics were powered by a Tattu Funfly 1300MAH 100C 6S lithium polymer battery. Furthermore, two different rotor sets were used, including the HQProp 5x5x3 rotor and HQProp

5x4.5x3 rotor. The motor idle setting of 2.5 % corresponded roughly to 2700 rpm, and at maximum throttle setting a rotational speed of roughly 33 000 rpm could be reached in hover conditions. To control the quadcopter a RadioMaster Zorro transmitter was used with a TBS crossfire module. Finally, a Skyzone Cobra X was used in combination with two standard 5.8Ghz dipole antennas. In Figure 3.2 some pictures are shown of the quadcopter, with and without ballast.

Table 3.1: Betaflight settings.

Name	**Setting**	**Name**	**Setting**
Feed forward transition	Off	Anti gravity	Off
Anti gravity	Off	I term rotation	Off
Dynamic damping	Off	Throttle boost	Off
Motor output limit	Off	Dynamic idle	Off
Vbat PID compensation	Off	Integrated yaw	Off
Absolute conrol	0	TPA	1
Bi-directional D-shot	On	ESC_SENSOR	On
Bi-dir. D-shot version	DSHOT600	Motor idle	2.5 %

Table 3.2: Betaflight configurator controller gains.

Axis	**P gain**	**I gain**	**D gain**	**Feedf.**
Roll	42	85	30	1
Pitch	46	90	32	1
Yaw	45	90	0	1

Table 3.3: BLHeli32 ESC settings.

Name	**Setting**	**Name**	**Setting**
Ramp up power	40 %	Temperature protection	140 °C
Low RPM Power Protect	On	Low Voltage Protection	Off
Sine Modulation Mode	Off	Stall Protection	Normal
Demag Compensation	Low	Motor Timing	16°
Maximum Acceleration	Maximum	Auto Telemetry	Off
SBUS Channel	Off	Minimum Throttle	1040
Maximum Throttle	2000	Center Throttle	1500
Brake On Stop	80 %	Non Damped Mode	Off
PWM Frequency Low	48 kHz	PWM Frequency High	48 kHz

3.2 Isolated rotor in wind tunnel

The purpose of this experiment was to aid in designing the 'rotor aerodynamics' block in Figure 2.2. For this experiment a rotor was placed inside a wind tunnel as is shown in Figure 3.1a. The wind tunnel that was used is the Open Jet Facility which is run by Delft

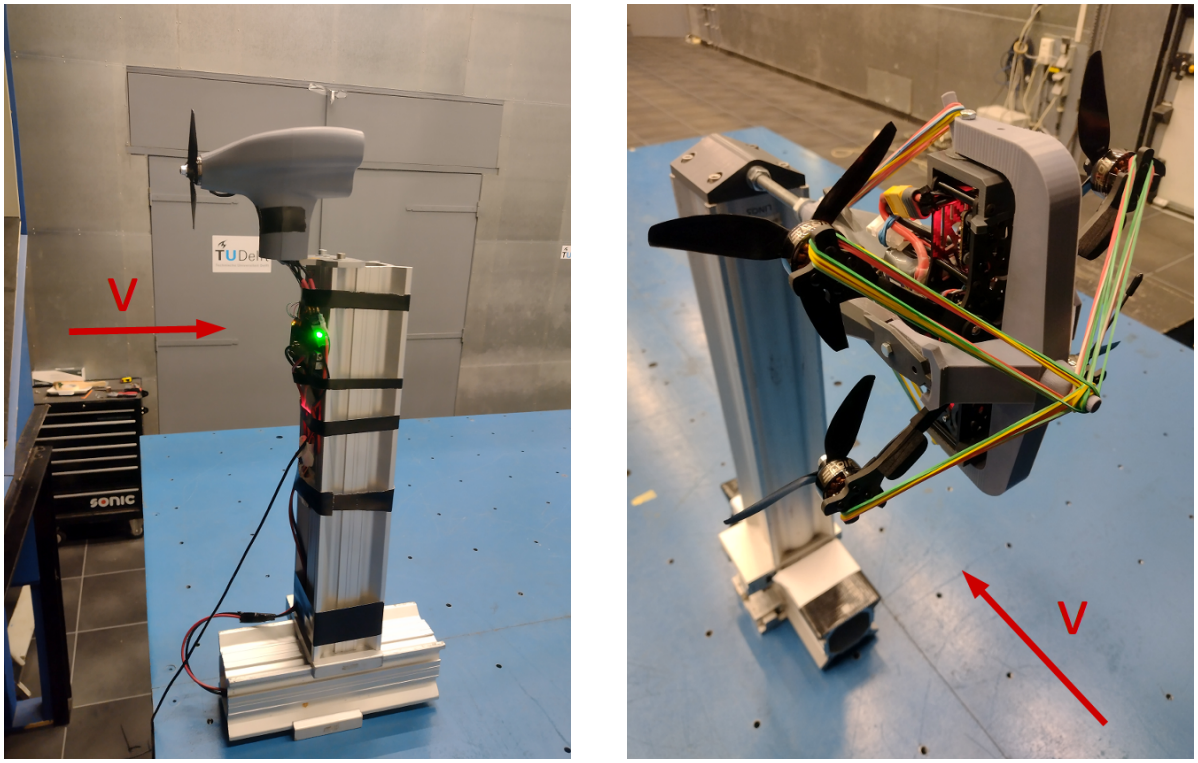

(a) Test setup for measuring isolated rotor thrust and torque.

(b) Test setup for measuring quadcopter movements while suspended in a gimbal.

Figure 3.1: Test setup of wind tunnel tests.

University of Technology. The tunnel was operated with a temperature and air density of 19 °C and 1.20 kg m^{-3}, respectively.

The thrust, torque and rotational speed of the rotor was measured at a frequency of 5 Hz using 'series 1585 thrust stand' from Tyto Robotics. The motor was powered using the same 6S lithium polymer battery as mentioned in section 3.1. An aerodynamic fairing was made around the thrust stand to reduce aerodynamic forces working on the stand itself which inherently added to the thrust measurements, and to reduce any interaction effects between the rotor and the stand. Aerodynamic forces working on the fairing did not influence the measured thrust and torque. The fairing was designed using Catia V6 and 3D-printed using a stock Creality 3D Ender 3 V2.

Thrust and torque was measured over a period of 20 s for the 5x4.5x3 and a 5x5x3 three bladed 5 inch rotors. Wind speeds were set at -25 m s^{-1} to 25 m s^{-1} in steps of roughly 3 m s^{-1}, including 0 m s^{-1}, and rotor rotational speeds were set at 3000 rpm to 20.000 rpm with steps of 1000 rpm. Testing two different rotors at 17 wind speeds and 18 rotor speeds for 20 s equals 3 h24 min of data recording time. For negative speeds the rotor was flipped and the motor speed was reversed. An ESC was used with the same settings as listed in Table 3.3.

3.3 Actuator transient response

The purpose of this experiment was to aid in designing the 'LPF' blocks in Figure 2.2. The test setup was equal to the one depicted in Figure 3.1a, except the experiment was not conducted inside a wind tunnel. The transient response of the motor and rotor combination was recorded by switching the ESC input rapidly between a high and low value. Input values to the ESC ranged from 8 % to 55 %, which roughly corresponded to rotational speeds of 3000 rpm and 21 000 rpm, respectively. For this test the 5x4.5x3 rotors were used.

The low and high ESC input values have a respective difference and an average value. Multiple test series were performed that were each characterized by a distinct difference and average value. Difference values of 5 %, 10 % and 15 % were used, as well as 10 different linearly spaced average values in the range of 8 % to 55 %. For each test series the input was changed 40 times between low and high with a frequency of 5 Hz. The input signal was generated automatically using the scripting tool in the RCBenchmark software suite from Tyto Robotics.

3.4 PID gain measurements

The purpose of this experiment was to aid in designing the 'PID' blocks in Figure 2.2. Unfortunately, the PID control gains that can be set in the Betaflight configurator are not equal to the gains needed for Eq. 2.1. Reliable information on how the actual gains are calculated within Betaflight could not be found. These gains were therefore measured experimentally.

For this experiment the quadcopter was suspended in the gimbal like construction shown in Figure 3.1b for safety considerations. Absence of the rubber bands allowed the quadcopter to move freely. In the Betaflight configurator all gains were set at zero, except for the P gain of the roll axis. The quadcopter was then given a sinusoidal type of roll rate by grabbing and moving the quadcopter manually side to side at frequencies between 1 Hz and 2 Hz. This process was then repeated at several different throttle settings, and for all the different individual gains in Betaflight. An exception to this were the feedforward gains which are not modelled and were always set at their minimum value. For this test the 5x4.5x3 rotors were used.

The rotor rotational speeds and the attitude rates were written to an onboard SD card with a frequency of almost 1000 Hz. Looking at Figure 2.2, and knowing which gain was nonzero during the experiment, the actual gain can be calculated that is used by Betaflight.

3.5 Mass and MMOI measurement

The mass of the quadcopter, batteries and rotors were each measured using a scale. The MMOI of the quadcopter with battery, but without rotors was measured experimentally using the pendulum method. For this the quadcopter was suspended on two parallel wires with a length of slightly more than 1 m and a separation distance of roughly 90 mm. Three

sets of 100 oscillations were then timed and averaged. This was repeated for the roll, pitch and yaw axis.

The MMOI of an individual rotor was obtained by modeling the rotor in Catia V6 and giving the 3D model a material density such that the weight of the model corresponded to the measured weight of the real rotor. MMOIs were then calculated in Catia V6.

3.6 Gimbal tests with elastic bands

As mentioned in section 3.2, the thrust stand in Figure 3.1a had a maximum measurement rate of 5 Hz. It therefore only allowed for measuring the variance of the thrust, torque and rotor rotational speed, but not whether these quantities had certain dominant frequency components. As an alternative, the quadcopter was mounted in a gimbal as is shown in Figure 3.1b. This gimbal was designed in Catia V6 and produced using a stock Creality 3D Ender 3 V2. Ball bearings with an outer diameter of 12 mm were used to reduce friction around all axes. For this test the yaw axis was fixed, only allowing roll and pitch movement over a range of motion of 18°. The PID control gains in Betaflight were set to zero, practically turning off the flight controller. The rotational speeds of the rotors could collectively be set using the transmitters throttle channel. Rubber bands were used to keep the quadcopter centered in the gimbal while still allowing movement of the quadcopter. Pitch and roll rate were recorded on the onboard SD card at a frequency of almost 1000 Hz. For this test the 5x5x3 rotors were used

With the wind tunnel turned off, the quadcopter was pulled manually to an extreme orientation in the gimbal and released in order to let the elastic bands move the quadcopter back to its neutral orientation. The pitch and roll rates that were measured during the resulting oscillation could later be used to model the complete system as a damped mass spring system. After this system identification test, measurements were performed with rotor speed ranging from 3000 rpm to 20 000 rpm in steps of 1000 rpm and four wind tunnel speeds, namely $10\,\mathrm{m\,s^{-1}}$, $15\,\mathrm{m\,s^{-1}}$, $20\,\mathrm{m\,s^{-1}}$ and $25\,\mathrm{m\,s^{-1}}$.

The procedure above allowed for reconstructing the forces and moments that work on the combination of all rotors based on the measured pitch and roll rates, without the rotors changing speed. Since the data was recorded at 1000 Hz, possible dominant thrust or torque oscillations could be identified with a frequency of up to 500 Hz.

3.7 Structural vibration tests

The quadcopter itself has a structure that will oscillate at its eigenfrequencies if excited properly. These oscillations are picked up by the IMU of the quadcopter. To make sure these oscillations did not interfere with any measured gyroscope data, a structural vibration test was performed. The quadcopter was suspended by a wire by attaching it close to the center of gravity of the quadcopter. A small hammer was then used to delicately hit the air frame at a variety of places. IMU data was recorded on the onboard SD card at a rate of almost 1000 Hz.

(a) Standard flight configuration.

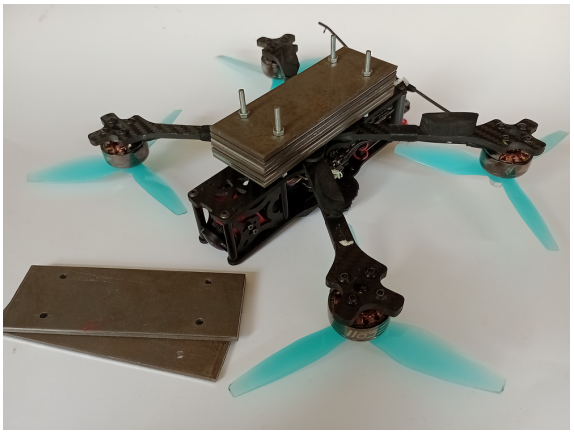

(b) Underside mounted ballast weights.

Figure 3.2: Quadcopter with 5x4.5x3 rotors, battery and ballast weights.

3.8 Gimbal tests with controller

This experiment served to produce data to validate the model shown in Figure 2.2. For this test the quadcopter was placed in the gimbal as is shown in Figure 3.1b, but with no locked axes and without the rubber bands. The flight controller was turned on to allow the quadcopter to stabilize itself in the air stream. Four different wind tunnel speeds were used, namely $0\,\mathrm{m\,s^{-1}}$, $10\,\mathrm{m\,s^{-1}}$, $15\,\mathrm{m\,s^{-1}}$ and $20\,\mathrm{m\,s^{-1}}$. For each wind speed the average rotor speeds were set ranging from 3000 rpm to 20 000 rpm in steps of 1000 rpm. As is explained section 5.3, some throttle settings caused excessive deviation in rotation speed between rotors, making it difficult to accurately set the average rotor speed. For this test the 5x4.5x3 rotors were used.

3.9 Flight tests with ballast

For verification purposes, actual flight tests were performed that adhere to the assumptions made for the model. That means, a series of vertical descents were performed from an altitude of around 250 m. These test were performed in a meadow near Zunderdorp located to the north of Amsterdam, which is just outside of the controlled traffic zone of Schiphol airport. Due to practical reasons, test were performed during winter time, but only on days with no precipitation and wind speeds below $10\,\mathrm{m\,s^{-1}}$.

To control the descent speed, throttle levels were varied where lower throttle setting corresponded to higher descent speeds. Of course, this meant only certain combinations of descent speed and rotor speeds could be achieved. To get around this, several steel plates were cut to size as ballast that could be mounted to the underside of the quadcopter. This made it possible to add ballast up to around 1 kg to the quadcopter in steps of roughly 40 g. The quadcopter without ballast can be seen in Figure 3.2a. In Figure 3.2b the steel ballast plates mounted to the underside of the quadcopter are shown. The plates were attached to the frame by replacing four of the M3 frame bolts with four M3 threaded rods. For each rod, one nut was used to secure the frame fulfilling the function of the original frame bolt, and one nut to secure the plates onto the rods.

During these descents the quadcopter was kept at a level altitude by using the trim buttons on the controller. No stick inputs were given during the descents. It was possible to show the roll and pitch angle in the Betaflight OSD while flying. However, these angles are calculated from fusing the data from the accelerometer and the gyroscope. This means in practice that these estimated angles can drift away quite a bit from their true value. To get around this, the roll and pitch angles were estimated visually. For this the quadcopter was set on level ground, and a set of markers were turned on in the Betaflight OSD that coincided with the horizon. During flight the quadcopter could now be kept level by comparing the positions of the markers with the position and orientation of the horizon.

In the end almost 100 descents were performed with ballasts of 614 g and 944 g, and a variety of thrust settings. A proper set of thrust values was determined beforehand, but were later determined on the fly since the remaining battery capacity was found to have a large effect on the resulting descent speed. This is because the descent speed appeared to be very sensitive to the set rotor speeds, and the rotor speeds are a function of throttle setting and battery voltage.

Chapter 4

Data Processing and Experimental Results

This chapter covers the direct results of the experiments discussed in chapter 3. As will be evident, quite some conclusions can be drawn about the possible underlying causes of the propwash effect from these individual experiments. This holds especially for the performed wind tunnel test, both with the isolated rotors and the quadcopter in its entirety.

In section 4.1 the results of the isolated rotor tests will be discussed. It will be demonstrated how force and torque can be modelled as function of rotor rotational speed and descent speed using multivariate simplex B-splines. In section 4.2 the results from the actuator transient response tests from section 3.3 will be discussed. The PID gain measurements from section 3.4 and MMOI measurements from section 3.5 will be presented in section 4.3 and section 4.4, respectively. In section 4.5 the results of the gimbal test with elastic bands will be treated. The setup of this experiment was discussed in section 3.6. Finally, in section 4.6, the results of the structural vibration tests from section 3.7 will be presented.

4.1 Isolated rotor wind tunnel data

This section covers the results of the wind tunnel tests described in section 3.2. A parameter that is convenient in the analyses of rotor aerodynamics is the advance ratio μ. In this report this parameter is calculated according to Eq. 4.1, where ω is the rotor rotation speed in $\mathrm{rad\,s^{-1}}$ and D is the diameter of the rotor.

$$\mu = \frac{2v}{\omega D} \tag{4.1}$$

The data recorded during isolated rotor wind tunnel tests captures a large amount of interesting behaviour of the used rotors. In subsection 4.1.1 the measured trust and torque at various rotor speeds and winds speeds are discussed. In subsection 4.1.2 it is shown how much the thrust and torque vary when the wind speed and rotor speed are kept constant. In subsection 4.1.3 the derivatives of thrust and torque with respect to wind speed and rotor rotational speed are discussed. Finally, in subsection 4.1.4 the difference between the two considered rotors are highlighted.

The figures used in this section are great for general interpretations but not so much for extracting more precise information from the measured data. Because of this, a set of much more detailed plots is included in Appendix A.

4.1.1 Average thrust and torque

The recorded wind tunnel data consists of a set of thrust and torque measurements at various wind and rotor rotational speeds. It is necessary to obtain mathematical functions $f(\omega, v)$ and $n(\omega, v)$, that minimize the error between the measurements and the estimation function in some way.

A method that is often used for this is least squares regression using multivariate polynomials as basis functions. Unfortunately, in practice, regression with global polynomials has a rather low maximum on the amount of basis functions that can be used due to limited accuracy of how computers represent numbers. This type of regression was experimented with, but the limit on on the amount of basis functions appeared to be far to low for the fidelity that is required to accurately represent the measured data.

Due to the shortcomings of global basis functions, the transition was made to multivariate simplex B-splines [20, 21]. This type of estimation uses a set of local polynomial basis functions which estimate the data only in a small domain of the independent variable space. This allows for keeping the order of the polynomials low, removing issue found with global polynomial basis functions described above.

An important aspect of multivariate simplex B-splines is the triangulation of the independent variable domain. For this application the interval of the rotor speed ω was divided into j equal intervals and the wind speed v into k equal intervals. A Delaunay triangulation was then applied to the resulting grid, which resulted in $2jk$ triangles with equal size. The simplex B-spline estimation is further characterised by the order of the polynomials that estimate the data, and the smoothness parameter l. A smoothness value of $l = 0$ means the zero'th derivative at the border of each neighboring simplex is made equal. A value of $l = 1$ means the zero'th and first derivative these borders is made equal, and so on.

Constructing the simplex B-spline estimation thus revolves around choosing the parameters k, j, the polynomial order and the smoothness parameter l. There is not necessarily a trivial way to find these parameters. Generally it can be said that if these parameters are chosen too low, the simplex function is too course and has not enough precision. On the other hand, parameter values that are too high cause overfitting of the data. To deal with this, around 20 % of the data was used as validation data. This validation data was not used to fit the model and was sampled randomly from the complete data set. Minimizing the residue of the found model and this validation data set was then used as an objective while tuning the mentioned parameters.

The approach used here to find all parameter values involved first setting the smoothness parameter l. Since the spline did not need to be differentiated, a value of $l = 0$ would technically be acceptable. Unfortunately, but logically, this gave rise to visible edges in the spline model at places where two splines met and little data was present. Assuming

the discontinuity of these lower derivatives was unlikely to be representative for the real world phenomenon, a higher value of $l = 2$ was chosen. A polynomial order equal to 5 was then chosen which was found high enough to introduce enough degrees of freedom of the spline considering the smoothness parameter of $l = 2$, and low enough to stay clear of the computer calculation errors described above. The parameters j and k were then increased incrementally while trying to minimize the residue of the model and the validation data. Due to the gridded structure of the recorded data however, it was found that as residue got close to being minimized, the spline had the tendency to become quite unstable and very oscillatory. Because of this, j and k were kept low enough to stay out of this instability zone, and set at a value of $j = 4$ and $k = 5$.

In Figure 4.1 the simplex B-spline is visualized that represents the thrust generated by the 5x4.5x3 rotor at different speeds v and rotor speeds ω. This thrust is the average thrust measured over the 20 s interval at which the wind speed and rotor speed are kept constant. In Figure 4.1b the spline is plotted in three dimensions. In Figure 4.1a a heat map of the same simplex B-spline is shown, which can be regarded as a top view of Figure 4.1b. In this heat map the lines of constant advance ratios μ are also indicated. Furthermore, the boundaries between the different operating states of the rotor are indicated with the dashed lines. The upper dashed line connects points that satisfy Eq. 2.14. The area above this line thus covers the TWS. The lower dashed line follows Eq. 2.16, meaning that the area between this line and the line $\mu = 0$ represents the pre-VRS.

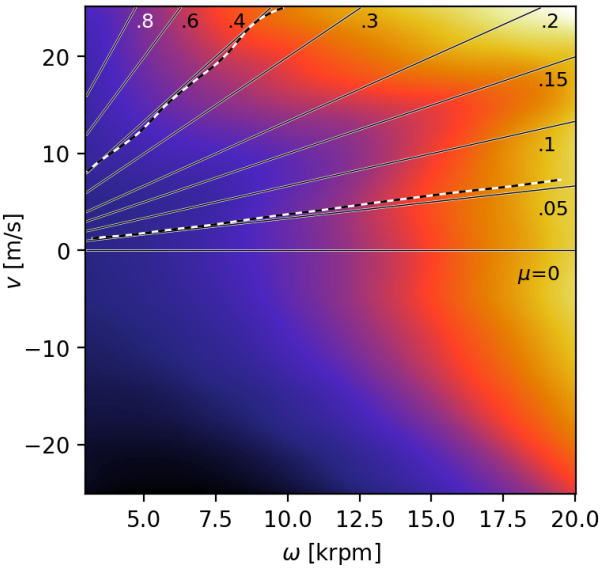

(a) Heat map of thrust as function of descent speed and rotor rotational speed. Upper and lower dashed lines indicate f_{t1} and f_{t2}, respectively.

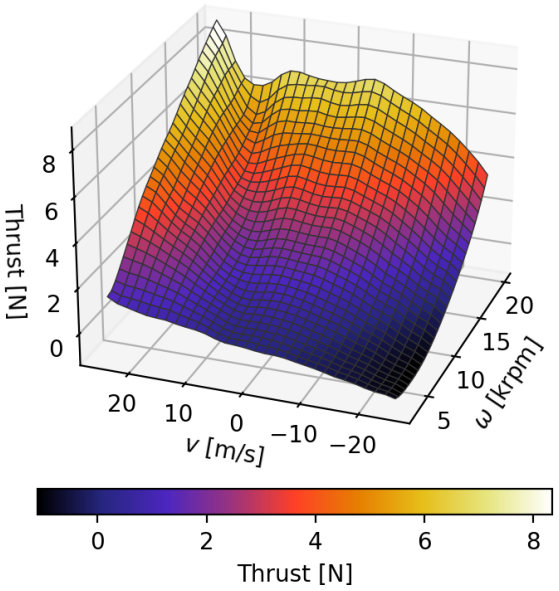

(b) 3D view of the simplex B-spline capturing thrust as function of descent speed and rotor rotational speed.

Figure 4.1: Estimated thrust data for the 5x4.5 isolated rotor. Positive speeds refer to the rotor in axial descent.

Several interesting aspects can be noticed from Figure 4.1. First of all, it seems that the boundaries between the theoretical rotor operating states lay on constant advance

ratio lines. Secondly, there seems to be a drop in thrust at an advance ratio of roughly $\mu = .14$. This is characteristic behaviour of a rotor in the VRS, since the power required to generate the large vortices reduce the power that is left to generate thrust. This drop in thrust also seems to happen at a very constant advance ratio.

In Figure 4.2 the simplex B-spline is shown for the measured average torque that is experienced by the rotor. It can be noticed that in the VRS the required moment is clearly lower than for other rotor operating states. This is again expected because the vortices reduce the angle of attack of the blades and therefore a reduction of drag can be seen.

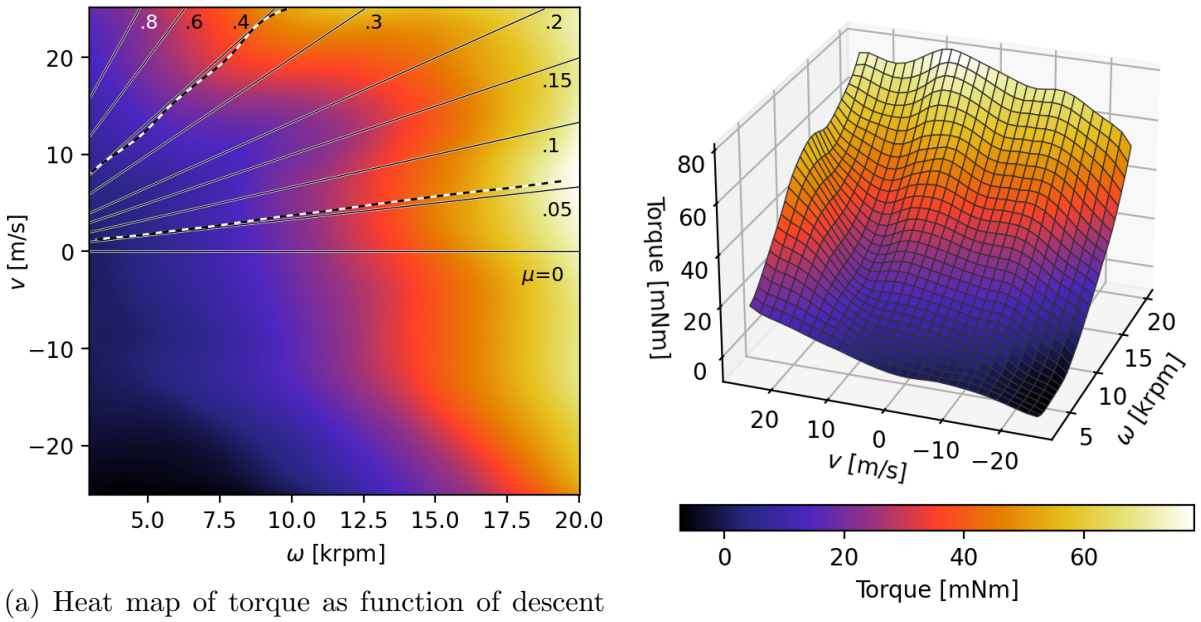

(a) Heat map of torque as function of descent speed and rotor rotational speed. Upper and lower dashed lines indicate f_{t1} and f_{t2}, respectively.

(b) 3D view of the simplex B-spline capturing torque as function of descent speed and rotor rotational speed.

Figure 4.2: Estimated torque data for the 5x4.5 isolated rotor. Positive speeds refer to the rotor in axial descent.

4.1.2 Variation in thrust and torque

The measured STDs of thrust σ_f and torque σ_n are used as an input to the system model from Figure 2.2, as was explained in section 2.6. As with the average measured thrust and torque, σ_f and σ_n can also be modelled using simplex B-splines. To do this, first each measurement period of 20 s where the wind speed and rotor speeds are held constant is used to calculate a single value for σ_f and σ_n. Each STD is thus calculated using roughly $20\,\text{s} \cdot 5\,\text{Hz} = 100$ measurements samples. Doing this for each wind speed and rotor speed combination results in a data set which can be used to construct a simplex B-spline. Note that this data set is roughly 100 times smaller than the amount of measurements.

The simplex B-splines minimizes the sum of the residues squared. That means that when the absolute value of σ_f and σ_n is very small, then the magnitude of the estimation error with respect to the actual value becomes very large. This is problematic since the

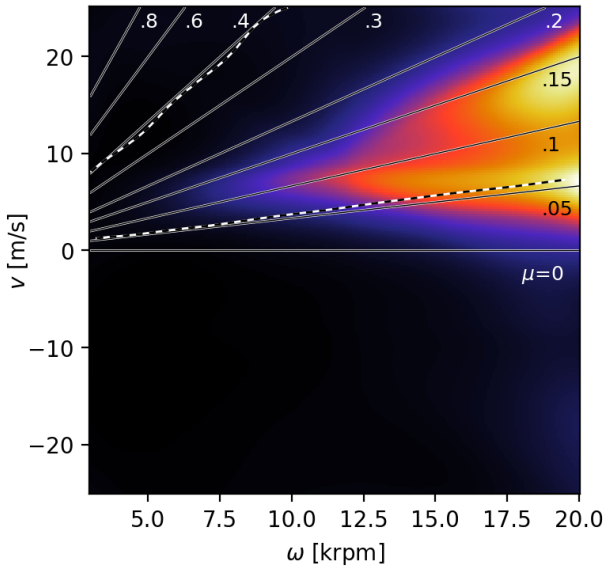

(a) Heat map of thrust standard deviation σ_f as function of descent speed and rotor rotational speed. Upper and lower dashed lines indicate f_{t1} and f_{t2}, respectively.

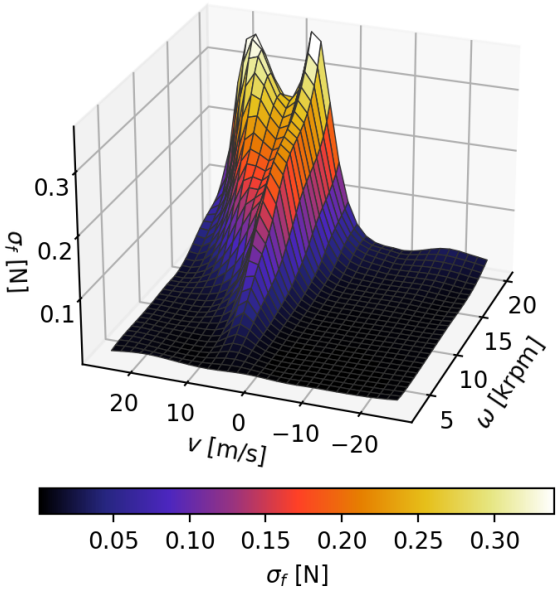

(b) 3D view of the simplex B-spline capturing thrust standard deviation as function of descent speed and rotor rotational speed.

Figure 4.3: Estimated thrust standard deviation for the 5x4.5 isolated rotor. Positive speeds refer to the rotor in axial descent.

values of σ_f and σ_n are multiplied with transfer functions to calculate the output of the model. That is, if the values of σ_f and σ_n are directly estimated using simplex B-splines, the output of the model will have very large relative errors when the input values are small. To get around this problem, the values of σ_f and σ_n are first transformed to a log-space, so $\hat{\sigma}_f = \log_{10}(\sigma_f)$ and $\hat{\sigma}_n = \log_{10}(\sigma_n)$. Simplex B-splines are then estimated for $\hat{\sigma}_f$ and $\hat{\sigma}_n$. The estimated values of σ_f and σ_n can be retrieved by using them as exponent. That is, $\sigma_f = 10^{\hat{\sigma}_f}$ and $\sigma_n = 10^{\hat{\sigma}_n}$. This also prevents the estimated values of σ_f and σ_n to become negative.

In Figure 4.3 the spline is shown that approximates $\sigma_f(\omega, v)$. For this spline similar parameters were used as described in subsection 4.1.1. In accordance with general literature, it can be observed that the most excessive fluctuations occur in the region that is assumed to be the VRS. However, it seems that these fluctuations also occur at very low advance ratios. It can thus be stated that the rotor behaves relatively normal in the pre-VRS state when it come to average thrust generation, but excessive thrust fluctuations already start as soon as the airspeed deviates from zero. Furthermore it can be noticed that for $\mu > .2$, which is thought to correspond to the transition of the VRS to the TWS, the thrust fluctuations are small and of similar magnitude as found for the rotor operating under negative speeds v.

In Figure 4.4 the STD of torque is shown. Although subtle differences can be seen when comparing these plots with the thrust STD from Figure 4.3, the locations of excessive fluctuations are very similar.

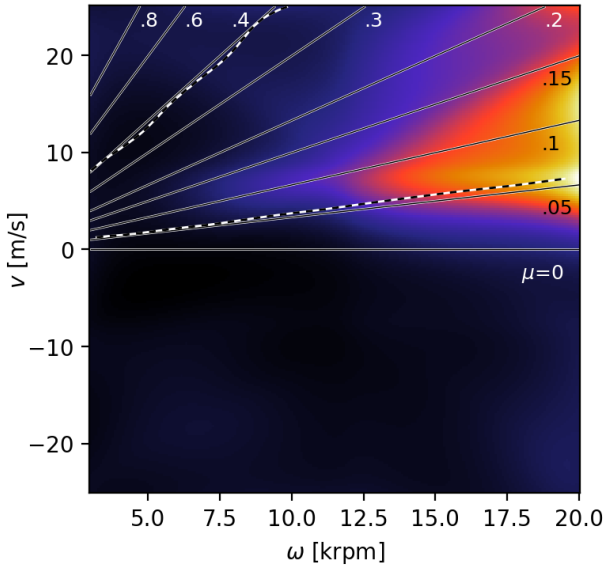

(a) Heat map of torque standard deviation σ_n as function of descent speed and rotor rotational speed. Upper and lower dashed lines indicate f_{t1} and f_{t2}, respectively.

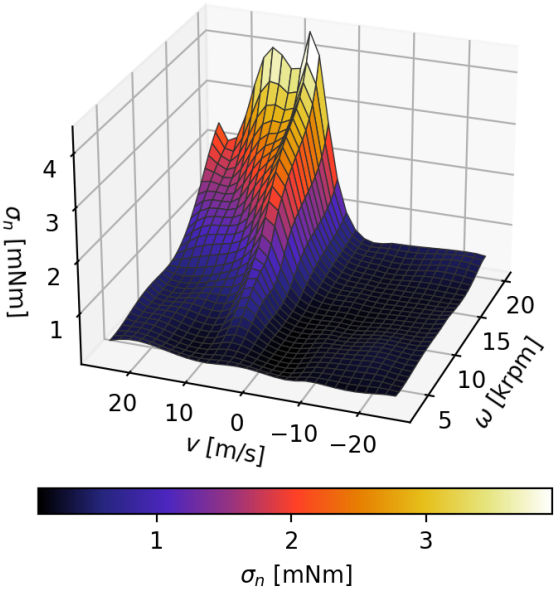

(b) 3D view of the simplex B-spline capturing torque standard deviation as function of descent speed and rotor rotational speed.

Figure 4.4: Estimated torque standard deviation for the 5x4.5 isolated rotor. Positive speeds refer to the rotor in axial descent.

4.1.3 Derivatives with respect to wind speed and rotation speed

The system model does not require the values of the absolute thrust and torque. In fact, it needs the partial derivatives of thrust and torque with respect to the wind speed and rotor speed. A straight forward way of obtaining these would be to take the partial differentials of the $f(\omega, v)$ and $n(\omega, v)$ splines as were shown in subsection 4.1.1. Unfortunately this did not give satisfactory results. The reason for this is that when looking at the data, there seem to be points where the thrust and torque curves make very sharp bends. This can be appreciated better by looking at the plots in Appendix A. Although this can not be noticed when looking at the spline, these sharp bends make the splines rather oscillatory in nature. When the partial derivative is taken this oscillatory properties get amplified a lot. Since the absolute values of the partial derivatives are rather small, this oscillatory property becomes too dominant.

It should be noted that taking the derivative of the spline in general is a proper solution. In this particular case however it was reasoned that there are simply to little combinations of v and ω at which data is recorded. This limits the amount of parameters that can be used to construct the spline and forces the spline to follow the sharp bends with a surface featuring relatively limited resolution. This in turn introduces a ripple through the complete spline, which is comparable to how a Fourier series has trouble approximating a square wave.

To get around this problem, the derivatives were found numerically at each combination of v and ω using a first order finite difference scheme. The partial derivatives are

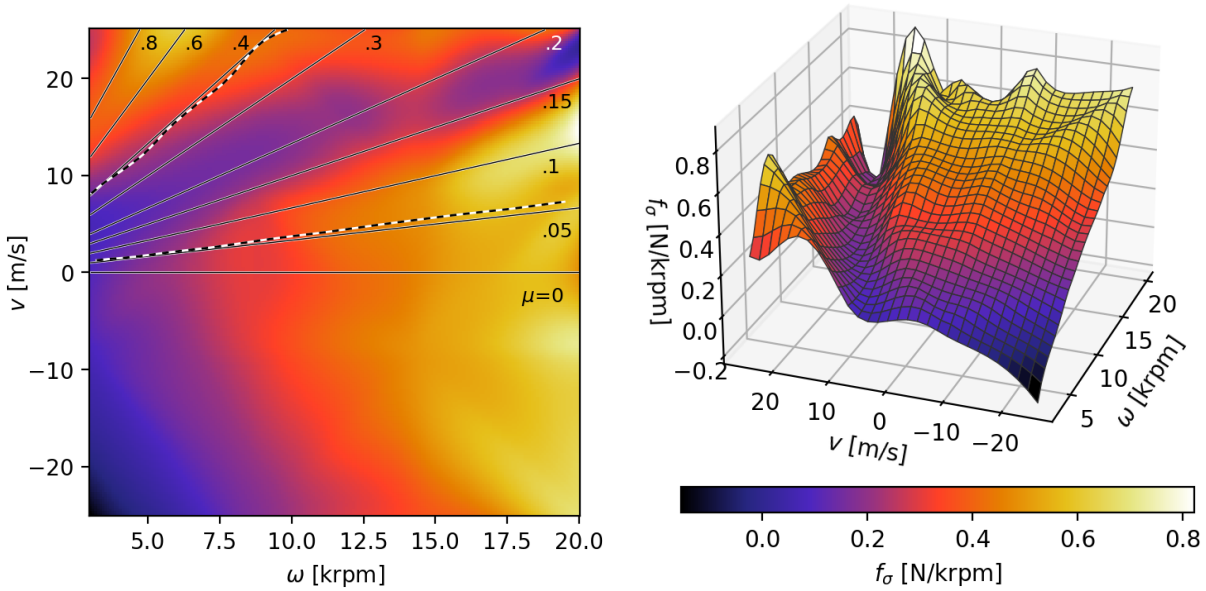

(a) Heat map of the change in thrust w.r.t rotor rotational speed as function of descent speed and rotor rotational speed. Upper and lower dashed lines indicate f_{t1} and f_{t2}, respectively.

(b) 3D view of the simplex B-spline capturing the change in thrust w.r.t rotor rotational speed as function of descent speed and rotor rotational speed.

Figure 4.5: Change in thrust w.r.t rotor rotational speed for the 5x4.5 isolated rotor. Positive speeds refer to the rotor in axial descent.

thus directly calculated using the data. This results in values for the partial derivatives at each combination of v and ω where force and torque were recorded for 20 s.

In Figure 4.5 the estimated partial derivative f_σ is depicted. This derivative is arguably the most influential since it determines how effective the actuators are in terms of control. A high value of f_σ means the overall gain in the control loop is high. As expected, f_σ generally increases when the rotor speed is increased. However, for advance ratios of $.15 < \mu < .2$ and high rotor speeds, the derivative is almost as low as when the rotor is idling. This is likely due to the characteristics of the VRS, where an increase in rotor speed partly starts increasing the power delivered to the vortices, rather than increasing thrust. This derivative only becomes negative at very low negative speeds and low rotor speeds. This is interesting since theoretically this would mean the control gain flips sign and that the quadcopter becomes unstable. Since this happens in the normal operating state of the rotor, this finding is outside the scope of this report.

In Figure 4.6 the estimated partial derivative f_v is shown. This variable is influential to how much natural stability the quadcopter has. In other words, when this derivative is high, the quadcopter tends to generate a moment to oppose the current attitude rate. Of course this stability effect is in practice rather small. Interesting to note is the sudden transition from a low to high value at an advance ratio of $\mu = .15$.

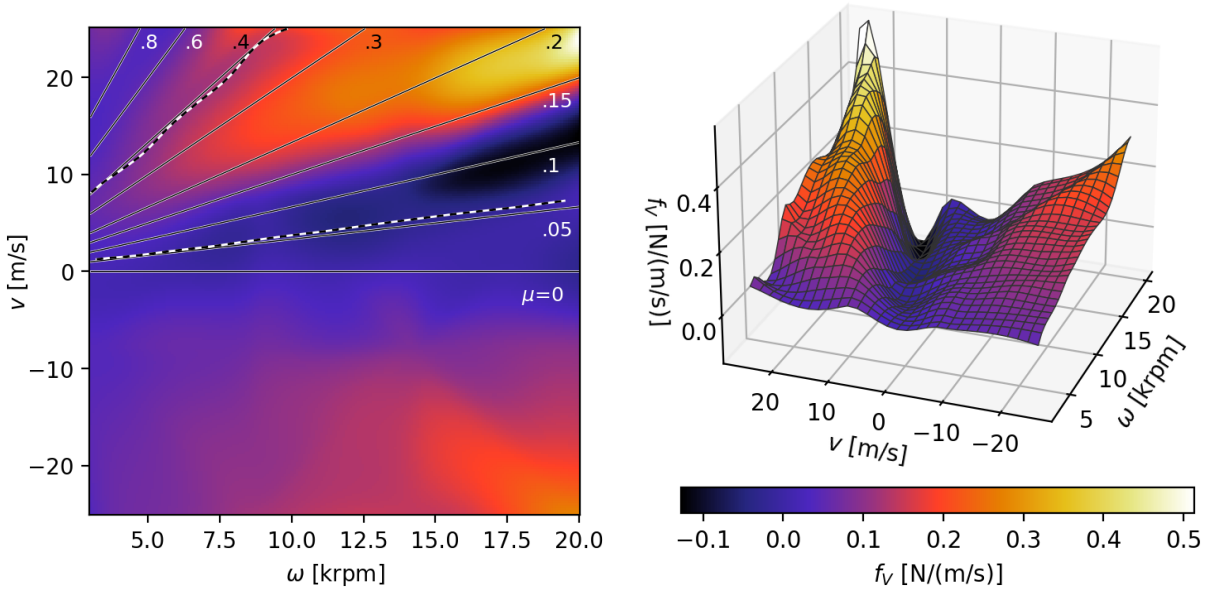

(a) Heat map of the change in thrust w.r.t descent speed as function of descent speed and rotor rotational speed. Upper and lower dashed lines indicate f_{t1} and f_{t2}, respectively.

(b) 3D view of the simplex B-spline capturing the change in thrust w.r.t descent speed as function of descent speed and rotor rotational speed.

Figure 4.6: Change in thrust w.r.t descent speed for the 5x4.5 isolated rotor. Positive speeds refer to the rotor in axial descent.

In Figure 4.7 the estimated partial derivative n_σ is shown. Where the value of f_σ is low between advance ratios of $.15 < \mu < .2$, the value for n_σ is low for advance ratios of $.2 < \mu < .35$. This goes to show that the TWS can have a comparable effect on the control effectiveness of the rotors from an aerodynamic standpoint.

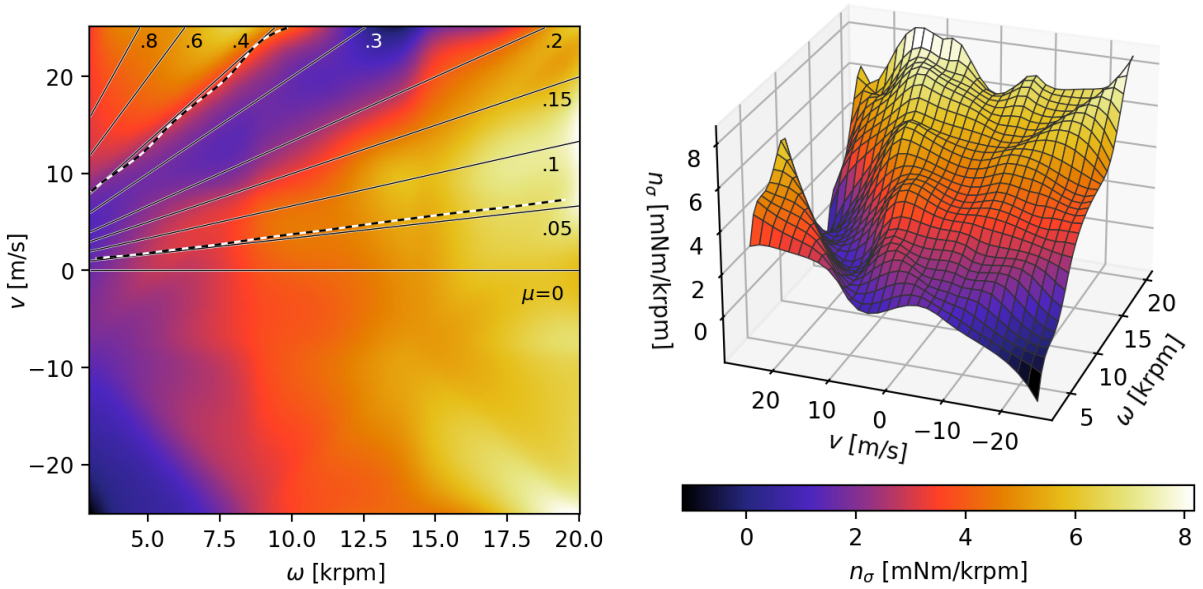

(a) Heat map of the change in torque w.r.t rotor rotational speed as function of descent speed and rotor rotational speed. Upper and lower dashed lines indicate f_{t1} and f_{t2}, respectively.

(b) 3D view of the simplex B-spline capturing the change in torque w.r.t rotor rotational speed as function of descent speed and rotor rotational speed.

Figure 4.7: Change in torque w.r.t rotor rotational speed for the 5x4.5 isolated rotor. Positive speeds refer to the rotor in axial descent.

Finally, in Figure 4.8 the derivative of torque with respect to descent speed, n_v, is shown. It can be noted that derivative is highest in the TWS at high rotor rotational speeds, and lowest in the VRS at high rotor rotational speeds.

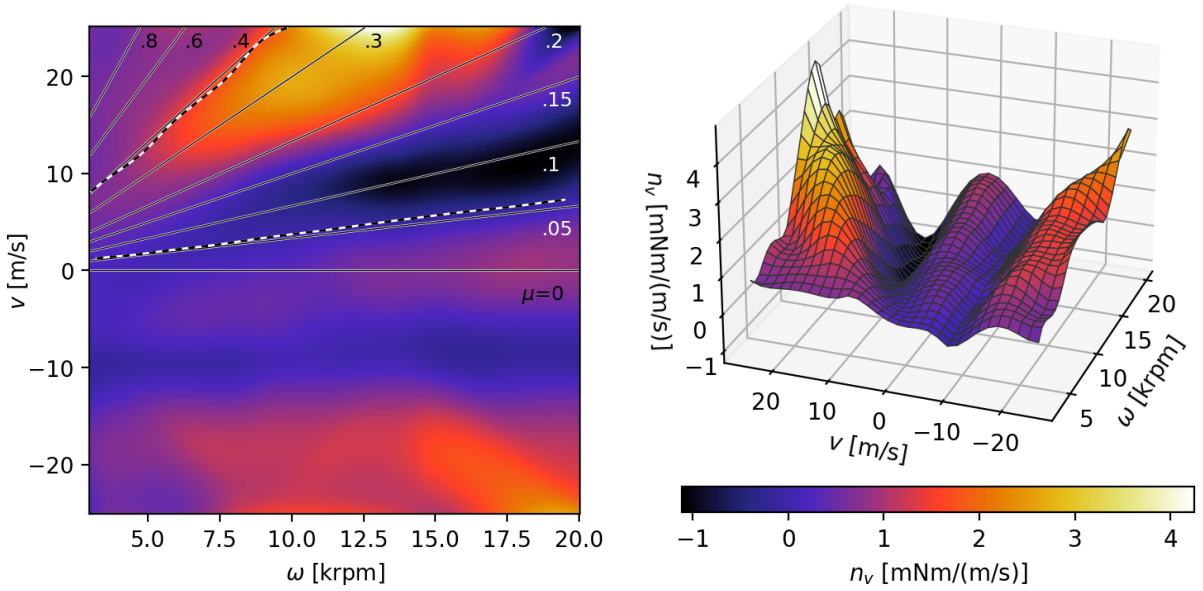

(a) Heat map of the change in torque w.r.t descent speed as function of descent speed and rotor rotational speed. Upper and lower dashed lines indicate f_{t1} and f_{t2}, respectively.

(b) 3D view of the simplex B-spline capturing the change in torque w.r.t descent speed as function of descent speed and rotor rotational speed.

Figure 4.8: Change in torque w.r.t descent speed for the 5x4.5 isolated rotor. Positive speeds refer to the rotor in axial descent.

4.1.4 Difference between rotors

In the wind tunnel two rotors were tested with different pitch angles of the blades. These rotors are the 5x5x3 rotor and the 5x4.5x3 rotor, where the former has a higher pitch than the latter. The rotors generate different thrust, thrust fluctuations, torque and torque fluctuations at given combinations of wind speed and rotor speed. The difference in values of these variables between these rotors, Δf, Δn, $\Delta\sigma_f$ and $\Delta\sigma_n$, respectively, is defined in Eq. 4.2 to Eq. 4.5.

$$\Delta f = f^{5\times5} - f^{5\times4.5} \tag{4.2}$$
$$\Delta n = n^{5\times5} - n^{5\times4.5} \tag{4.3}$$
$$\Delta\sigma_f = \sigma_f^{5\times5} - \sigma_f^{5\times4.5} \tag{4.4}$$
$$\Delta\sigma_n = \sigma_n^{5\times5} - \sigma_n^{5\times4.5} \tag{4.5}$$

In Figure 4.9 the difference in thrust between the rotors is visualized. Apparently, between $0\,\mathrm{m\,s^{-1}}$ and $10\,\mathrm{m\,s^{-1}}$ and for higher the rotor speeds, the thrust of the 5x5x3 rotor is up to 1 N higher than the 5x4.5x3 rotor.

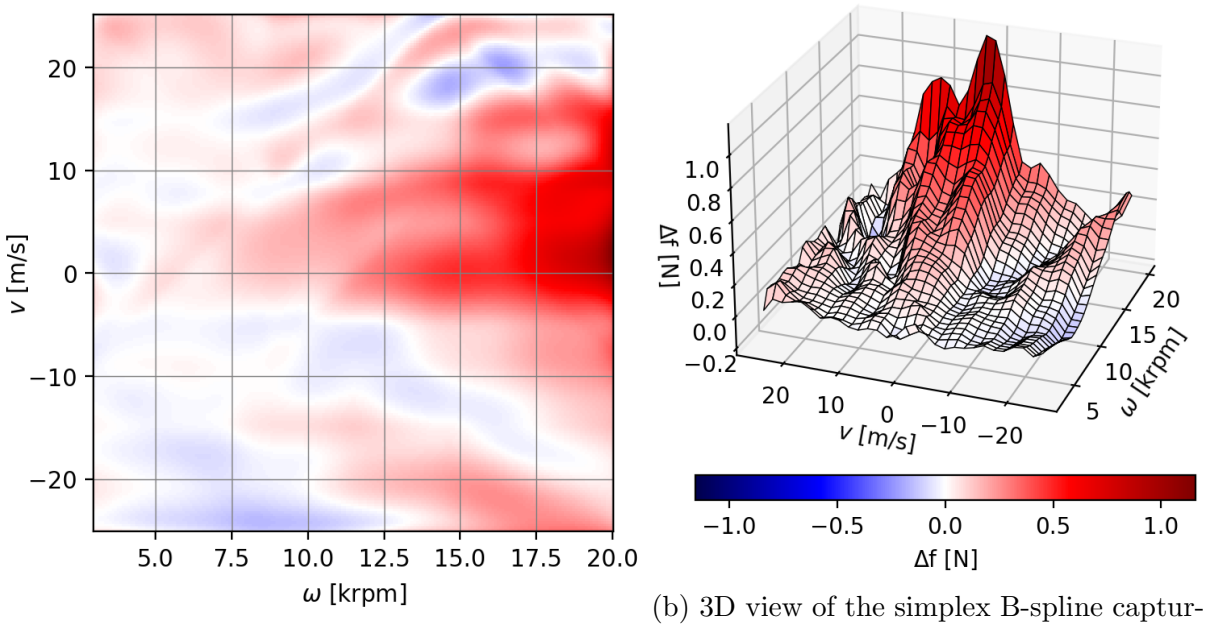

(a) Heat map of increase in thrust as function of descent speed and rotor rotational speed.

(b) 3D view of the simplex B-spline capturing the increase in thrust as function of descent speed and rotor rotational speed.

Figure 4.9: Increase in thrust of the 5x5x3 rotor w.r.t the 5x4.5x3 rotor. Positive speeds refer to the rotor in axial descent.

In Figure 4.10 the difference in torque between the rotors is visualized. As expected, for negative speeds v the torque is higher due to the increased angle of attack. Interestingly enough, the opposite appears to be the case for positive speeds.

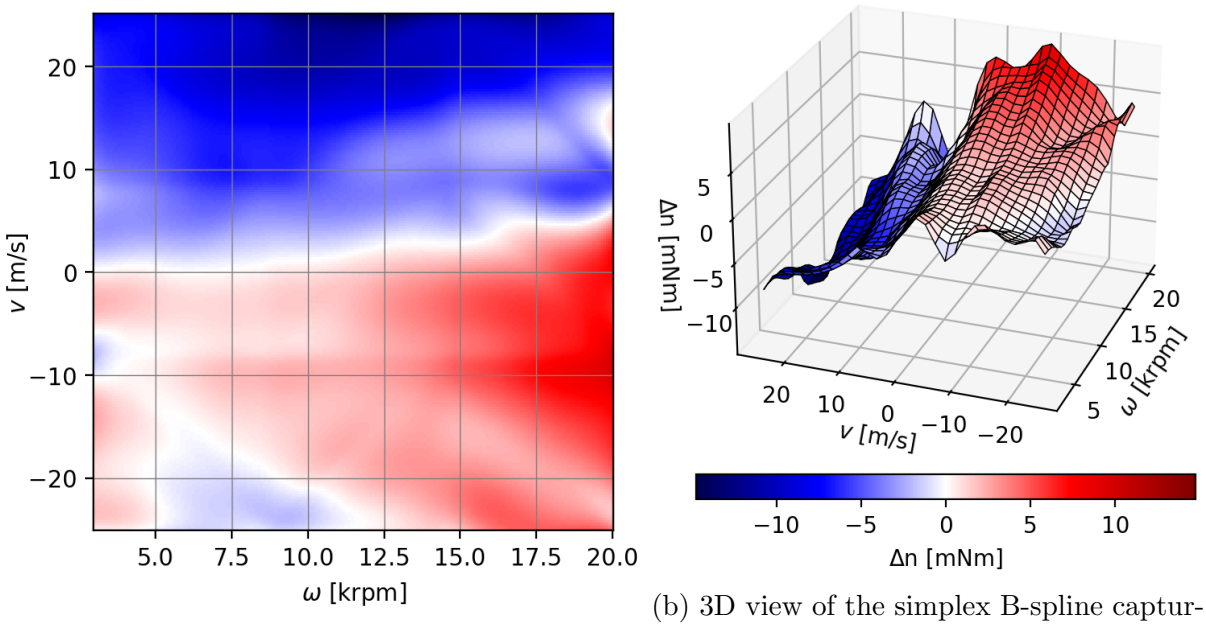

(a) Heat map of increase in torque as function of descent speed and rotor rotational speed.

(b) 3D view of the simplex B-spline capturing the increase in torque as function of descent speed and rotor rotational speed.

Figure 4.10: Increase in torque of the 5x5x3 rotor w.r.t the 5x4.5x3 rotor. Positive speeds refer to the rotor in axial descent.

In Figure 4.11 the difference in force fluctuation between the rotors is shown. In general in can be said that the 5x5x3 rotor generates higher thrust fluctuations. It should be noted that the absolute thrust generated is also higher. However, there seem to be areas where the 5x4.5x3 rotor actually generates more thrust fluctuation.

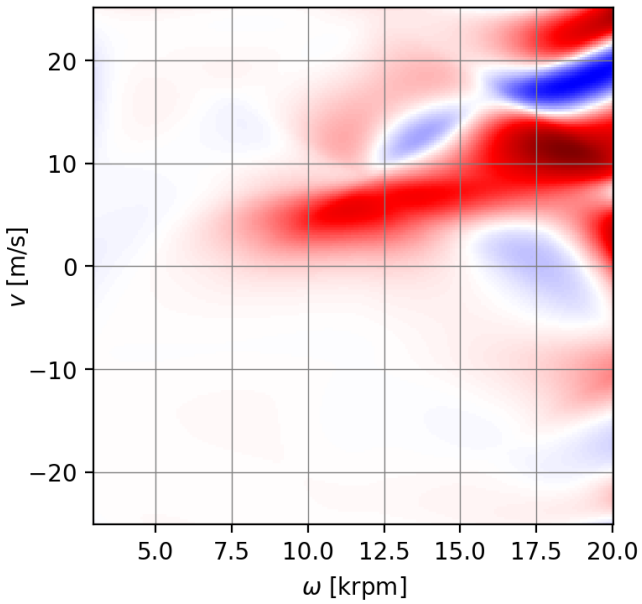

(a) Heat map of increase in σ_f as function of descent speed and rotor rotational speed.

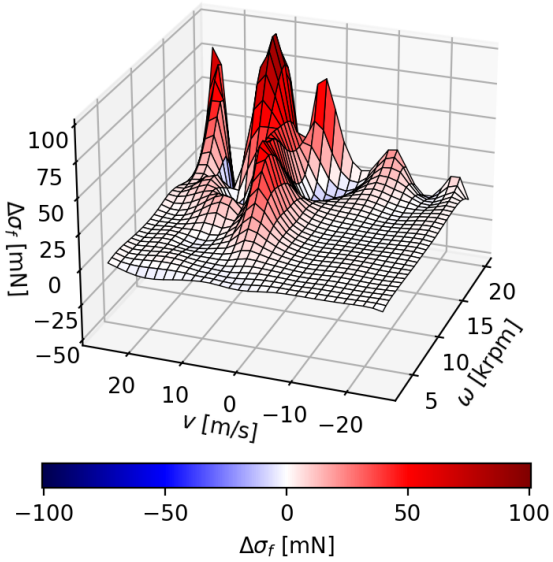

(b) 3D view of the simplex B-spline capturing the increase in σ_f as function of descent speed and rotor rotational speed.

Figure 4.11: Increase in σ_f of the 5x5x3 rotor w.r.t the 5x4.5x3 rotor. Positive speeds refer to the rotor in axial descent.

In Figure 4.12 the difference in torque fluctuation between the rotors is presented. As can be seen it is not possible to say something about the increase in σ_n in general.

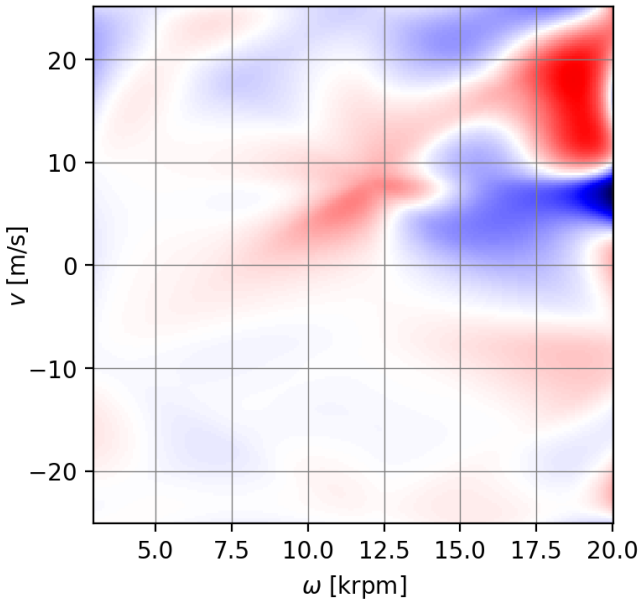

(a) Heat map of increase in σ_n as function of descent speed and rotor rotational speed.

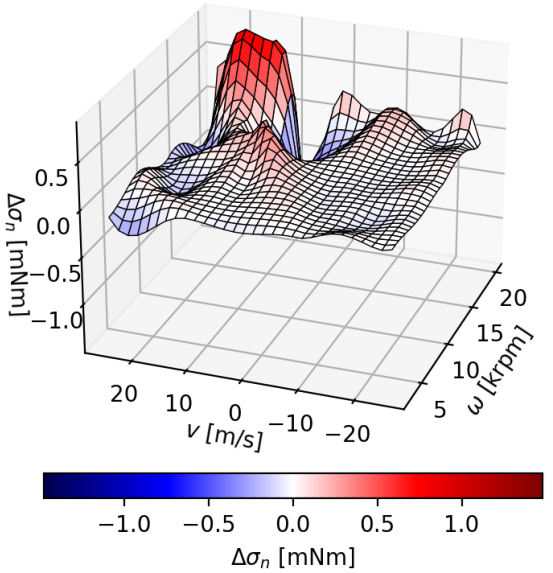

(b) 3D view of the simplex B-spline capturing the increase in σ_n as function of descent speed and rotor rotational speed.

Figure 4.12: Increase in σ_n of the 5x5x3 rotor w.r.t the 5x4.5x3 rotor. Positive speeds refer to the rotor in axial descent.

4.2 Actuator transient response

In Figure 4.13 a small part of the recorded data is shown, which was obtained as was described in section 3.3. The data shown consists of intervals where ω increases and decreases. Some of these parts appeared to have clear outliers and were not included for the estimation. These parts are indicated in orange in Figure 4.13. Furthermore, it can be noted that most of the data points that coincide with the initial rise or fall in ω are also not included. This was a practical necessity due to the recorded ω signal having a variable delay with respect to the recorded ESC input signal. This is unfortunate since these points contain the most information on how fast ω changes as a result of an ESC input.

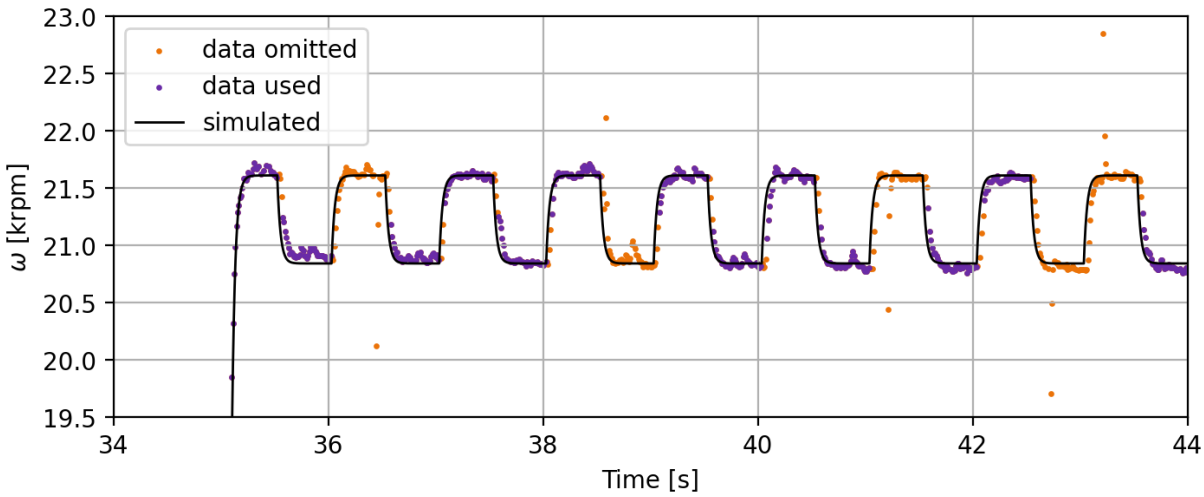

Figure 4.13: A part of the measured rotor speed samples used to estimate a_0.

In the sequence shown in Figure 4.13, ω fluctuates around approximately 21.2 krpm and deviates with approximately 0.8 krpm. Referring to the concepts explained in section 2.3, for this sequence $\omega^* = 21.2\,\text{krpm}$ and $\overline{\omega}_{max} = 0.4\,\text{krpm}$. Many series were performed with different values for ω^* and $\overline{\omega}_{max}$.

Once a certain ESC input is given, the resulting rotor speed ω does not only depend on the actuator properties, but also on the voltage applied to the motor. Since a battery was used for the test, this voltage tended to drop as the test progressed. Therefore a new signal, s_{esc}, was used that is equal to the actual ESC input multiplied by the normalized voltage. The latter is defined as the instant battery voltage divided by the initial battery voltage. Of course, during the rapid switching of the ESC input, the voltage also fluctuates due to the changing load. This rapid change in voltage is also present during flight and was therefore not used to calculate the normalized voltage. As a result, the normalized voltage was calculated with a filtered instantaneous voltage, where the filter consisted of both a forward and backward first order LPF with a cut of frequency of 1 Hz. This way the voltage drop due to a depleting battery is taken into account, but not the voltage ripple due to changing actuator loads.

For the estimation process, the coefficients α_0, α_1 and α_2 in Eq. 4.6 were estimated using OLS. This equation is directly taken from section 2.3, with the exception that u_{in} is replaced with s_{esc}. Again, this does not change anything when looking at the transient

response. To set up the estimation matrices for the estimation, the derivative $\dot{\bar{\omega}}$ is required to be known for each data point. The value for this derivative was estimated using a first order difference scheme that was applied directly to the data.

$$\dot{\bar{\omega}} = -\alpha_0 \bar{\omega} + \alpha_1 s_{esc} + \alpha_2 \tag{4.6}$$

The value of α_0 is relevant for implementing the LPF block from Figure 2.2. In Figure 4.14 the estimated values of α_0 are shown for different values of ω^*. These values are visualised using error bars, where the total length of the error bar is equal to two times the estimated STD of the estimated parameter. Long error bars thus indicate that the measured data for a particular series is less certain about what the value of α_0 should be. Interestingly enough, the estimated value for α_0 varies much more between measurement series that what the STD of each individual series would suggest. Its unclear what the cause of this is.

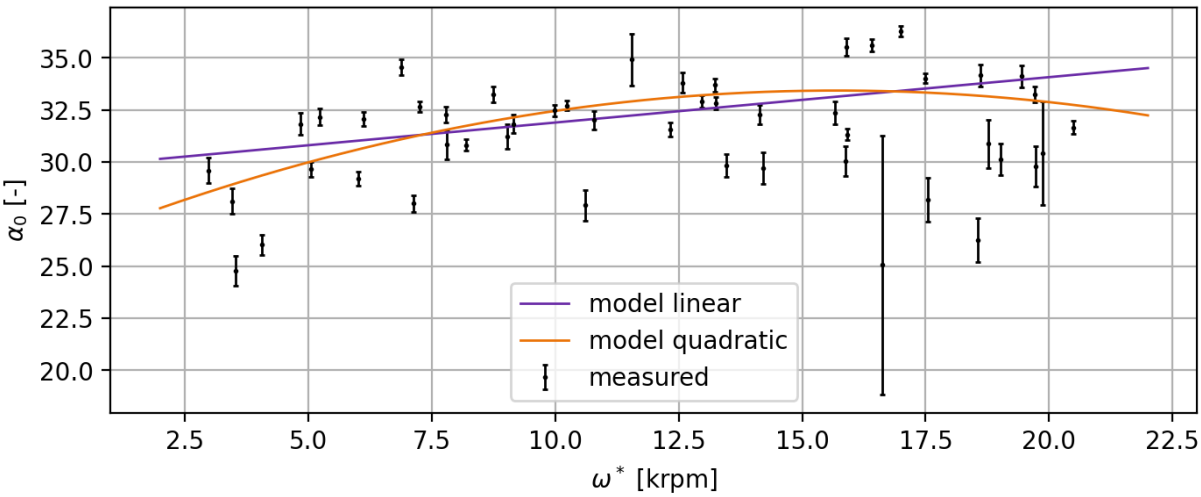

Figure 4.14: Linear and quadratic models of the dependency of α_0 on the rotor speed.

To model the LPF block it is necessary to know how α_0 varies as function of ω^*. According to the derivation in section 2.3, this should be a linear function with two parameters. Again, these parameters could be estimated using OLS where its data points are the mean estimated values of α_0 as shown in Figure 4.14. However, it makes sense to give more weight to estimates of α_0 that have very low estimated STD. Therefore, WLS was used with a diagonal weight matrix, with on the diagonal the reciprocals of the variances. Estimating the parameters this way results in the linear model as shown in Figure 4.14. As can be seen, also a quadratic model is included that has an additional parameter. Although inconsistent with the derivation in section 2.3, this model seems to fit the data much better. Since there is not an immediate necessity to comply with any theoretical model, it was decided to use this latter model for the implementation of the LPF block from section 2.3. The estimated equations for the linear and quadratic model from Figure 4.14 are shown in Eq. 4.7 and Eq. 4.8, respectively, where the unit of ω^* is krpm.

$$\alpha_0(\omega^*) \approx 29.71 + .2182\omega^* \tag{4.7}$$

$$\alpha_0(\omega^*) \approx 26.01 + .9458\omega^* - .0301{\omega^*}^2 \tag{4.8}$$

4.3 PID gain measurement

From the P, I, and D gains, the P terms is the most straight forward to calculate, since it is simply the ratio of the change in rotor speed and attitude rate. Referring to the experiments described in section 3.4, for each measurement this G_P was calculated, except for measurements where the attitude rate was smaller than $1\,\mathrm{rad\,s^{-1}}$. For the roll axis this calculation is shown in Eq. 4.9, where T is the total measurement time, p is the roll rate and G_P^p is the P term gain for the roll controller. The mean of the calculated values for the P gains was then taken as the final estimation G_P, as is shown in Table 4.1, where the superscript p refers to the roll axis. This table also shows the STD of the measured values of the gain, which are rather large. However, visually inspecting the data revealed that this was primarily due to some sort of delay between the attitude signal and the rotor speed signals. Unfortunately this delay could not entirely be removed by manually shifting the signals as it appeared that this delay varied somewhat in time. The noise on the measurements, especially the rotor speed, of course also contributes to this STD.

$$G_P^p \approx \frac{1}{T} \int_T \left[\frac{\omega_1(t) - \omega_2(t) - \omega_3(t) + \omega_4(t)}{4p(t)} \right] dt \tag{4.9}$$

Table 4.1: Controller gains estimations.

Name	**Value**	**STD**
G_P^p	660.0	48.82
G_I^p	7268	1768
G_D^p	20.64	5.122
G_P^r	330.1	53.68
G_I^r	6159	352.2

The I gain requires the integrated signal of the attitude rate, as is shown for the roll axis in Eq. 4.10. Here ξ is simply a different symbol to indicate time. Unfortunately, simply integrating the attitude rate makes errors accumulate causing the integrated attitude rate to wander off from this integrated signal as calculated by the flight computer. To get around this, both a backward and forward second order Butterworth HPF was applied to the integrated signal to keep it from wandering. The filter had a cut off frequency of 0.1 Hz. This cut off frequency was low enough so that the individual oscillations that excited the controller were barely influenced. Furthermore, only data points were included for the gain calculation where the integrated attitude rate was larger than 0.1 rad. The results for both pitch and yaw are shown in Table 4.1, where the superscript r refers to the yaw axis.

$$G_I^p \approx \frac{1}{T} \int_T \left[\frac{\omega_1(t) - \omega_2(t) - \omega_3(t) + \omega_4(t)}{4 \int_0^t p(\xi)\, d\xi} \right] dt \tag{4.10}$$

Finally, the D gain can be calculated when the derivative signal of the attitude rate is known, as is shown in Eq. 4.11. In this case this derivative was calculated using a first order difference scheme. For the calculation of the average gain, only data points were included where the derivative signal was larger than $50\,\mathrm{rad\,s^{-2}}$. The results are shown in

Table 4.1. Note that the yaw controller does not use a D term.

$$G_D^p \approx \frac{1}{T} \int_T \left[\frac{\omega_1(t) - \omega_2(t) - \omega_3(t) + \omega_4(t)}{4 \left. \frac{dp(\xi)}{d\xi} \right|_{\xi=t}} \right] dt \tag{4.11}$$

As is obvious, Table 4.1 only presents the roll and yaw gains. This is because it is assumed that the gains for pitch and roll are the same. Some quick experimenting showed that these gains are indeed very similar. In other words, $G_P^q = G_P^p$, $G_I^q = G_I^p$ and $G_D^q = G_D^p$, where the superscript q refers to the pitch axis.

4.4 Mass and MMOI measurement

The measured and calculated masses and MMOIs of both the quadcopter and its rotors are shown in Table 4.2. In this table the subscript and superscript d refers to the quadcopter (drone) including the battery, but excluding the rotors and ballast. These properties follow directly from the pendulum experiment as described in section 3.5. The subscript and superscript r refers to the properties of a single rotor and motor bell. These properties were derived from the rotor Catia model. The subscript and superscript f refers to the standard flight configuration as was shown in Figure 3.2a, which consist of the flight ready quadcopter without ballast plates. The mass m_f can simply by found by adding m_d and four times the rotor mass m_r. The standard flight MMOIs, I^f, can be found by adding the effect of the offset of mass of the four rotors to I^d using the parallel axis theorem. Note that the effect of I^r should not be included here since this contribution is already taken care of by the modelling of gyroscopic effects as was discussed in section 2.4.

Table 4.2: Masses and MMOIs.

Name	Value	Unit
m_d	583	g
I_{xx}^d	1.753	$\mathrm{g\,m^{-2}}$
I_{yy}^d	1.635	$\mathrm{g\,m^{-2}}$
I_{zz}^d	2.698	$\mathrm{g\,m^{-2}}$
m_r	4.8	g
I_{xx}^r	1.889×10^{-3}	$\mathrm{g\,m^{-2}}$
I_{yy}^r	1.889×10^{-3}	$\mathrm{g\,m^{-2}}$
I_{zz}^r	3.767×10^{-3}	$\mathrm{g\,m^{-2}}$
m_f	0.602	g
I_{xx}^f	1.907	$\mathrm{g\,m^{-2}}$
I_{yy}^f	1.725	$\mathrm{g\,m^{-2}}$
I_{zz}^f	2.942	$\mathrm{g\,m^{-2}}$

In section 3.9 the use of ballast weights was described. Of course the addition of the ballast does not only change the weight of the quadcopter but also its MMOI. To reduce this increase in MMOI as much as possible, a ballast material was chosen with a high density and the ballast was placed as close to the CG of the quadcopter as possible. Unfortunately, the influence of the ballast on the MMOI could not be nullified. To include

the effect of the ballast weights, the ballast plates were weighed and measured. A mathematical expression was then found for the position of every attached ballast plate as a function of the ballast plate stack height. The resulting influence of the ballast plates on the MMOIs in Table 4.2 could then be calculated for any amount of added ballast plates.

The MMOIs that are used for the model in chapter 2, namely I_{xx}, I_{yy} and I_{zz}, are the total MMOIs of the quadcopter during flight. Without ballast plates these MMOIs are equal to the standard flight configuration MMOIs I^f_{xx}, I^f_{yy} and I^f_{zz}. If ballast plates are carried by the quadcopter, their influence is added to I^f resulting in the final values for I_{xx}, I_{yy} and I_{zz} used in the model.

4.5 Gimbal tests with elastic bands

As mentioned in section 3.6, for this experiment the intention was to record the quadcopters attitude rates at rotor speeds ranging from around 3000 rpm to 20 000 rpm. Unfortunately, for higher rotor rotational speeds the quadcopter started to rotate too violently causing the gimbal to hit its rotation end stops. Measuring at rotor rotational speeds close to 20 000 rpm would have caused inaccurate data, which led to the decision to measure only up to the point at which excessive rotation started to occur.

With the wind tunnel and rotors of the quadcopter turned off, the system identification test was performed to estimate the damped natural frequency ω_{gim} and damping ratio ζ_{gim} of the gimbal system with elastic bands. The differential equation of the rotational damped mass spring system around the roll axis can be written as is shown in Eq. 4.12, where k_x, d_x and I^g_{xx} are the effective stiffness, the effective damping and the effective mass moment of inertia of the gimbal system. The functions $L_d(t)$ and $\phi(t)$ are the externally applied roll moment and the roll angle, respectively. A similar equation holds for the pitch axis.

$$L_d(t) = I^g_{xx}\ddot{\phi}(t) + k_x\dot{\phi}(t) + d_x\phi(t) \tag{4.12}$$

The roll angle $\phi(t)$ is obviously related to the roll rate $p(t)$ as shown in Eq. 4.13. Because the gyroscope samples the roll rate $p(t)$, discrete methods have to be used to approximate $\ddot{\phi}(t)$ and $\phi(t)$. The former is approximated by applying a first order forward difference scheme to the roll rate measurements, and the latter is approximated by using trapezoidal integration. To keep the integral from wandering due to an accumulation of measurement errors, the integrated signal is post processed using a forward and a backward running high pass filter with a cut off frequency of 0.02 Hz.

$$\ddot{\phi}(t) = \dot{p}(t) \qquad \dot{\phi}(t) = p(t) \qquad \phi(t) = \int_0^t p(\xi)d\xi \tag{4.13}$$

Once the gimbal is pulled back manually and released to induce an oscillation, the roll moment is zero, so $L_d(t) = 0$. The measured roll rate $p(t)$ can then be used to estimate the values of the ratios k_x/I^g_{xx} and d_x/I^g_{xx} using least squares and Eq. 4.12. To find the values of the individual parameters k_x, d_x and I^g_{xx}, the mass moment of inertia of the quadcopter itself was used for I^g_{xx}. This value was found experimentally by hanging the quadcopter by two wires and measuring oscillation times. The actual value of I^g_{xx} should be slightly higher due to gimbal parts. This is especially true for the pitch axis, because the gimbal assembly that rotates around this axis weighs around 60 g. This difference

causes conservative estimates for $L_d(t)$ later on.

Once the parameters k_x, d_x and I^g_{xx} are known, the gimbal oscillation can be simulated and compared to the actual measured oscillation. Visually this reveals that there is definitely some residual behaviour that is not captured by the estimated model of the gimbal system, especially for the pitch axis. An example of a comparison between measured and simulated pitch and roll rate can be seen in Figure 4.15.

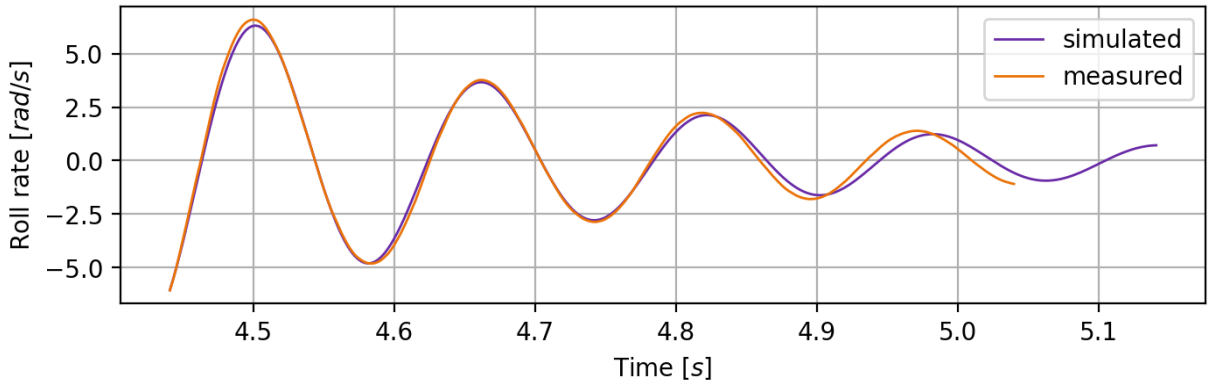

(a) Measured and simulated roll rate as function of time.

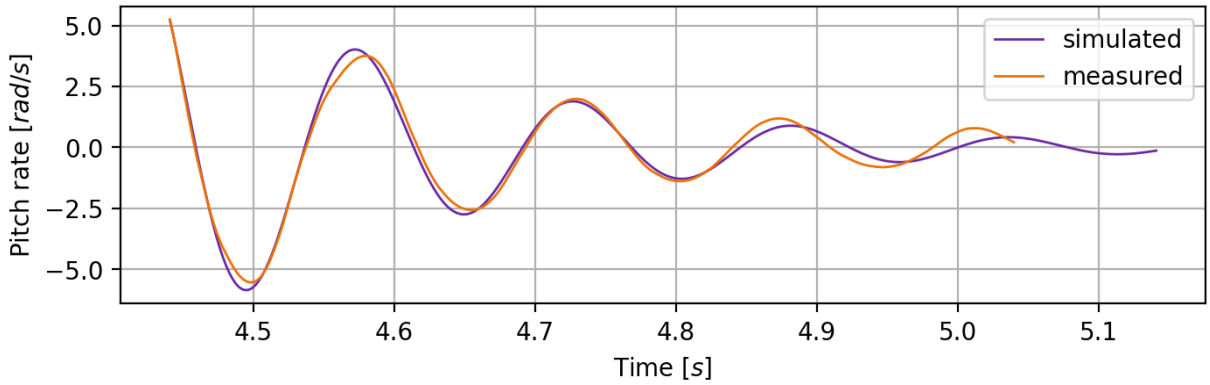

(b) Measured and simulated pitch rate as function of time.

Figure 4.15: Example comparison between measurements and simulation of the gimbal oscillation.

The gimbal model can now be used to reconstruct roll and pitch moments from the measured roll and pitch rates. Taking the roll axis as example again, the roll moment $L_d(t)$ is related to the four rotor thrust forces $f_1(t)$, $f_2(t)$, $f_3(t)$ and $f_4(t)$ as is shown in Eq. 4.14. Assuming that thrust fluctuations of different rotors are not correlated results in Eq. 2.65, which was already derived in section 2.6. Because interaction effects are ignored, the rotors operate under identical conditions. The thrust STD is therefore the same for all rotors, so $\sigma_{f_1} = \sigma_{f_2} = \sigma_{f_3} = \sigma_{f_4} = \sigma_f$. This finally relates σ_f to σ_L, as is shown in Eq. 4.15. Of course this also be applies to the pitch axis, where L_d is replaced

with M_d, l_y with l_x and $p(t)$ with $q(t)$.

$$L_d = l_y(f_1 + f_2 - f_3 - f_4) \tag{4.14}$$

$$\begin{aligned} \mathrm{Var}(L_d) &= \mathrm{Var}(l_y(f_1 + f_2 - f_3 - f_4)) \\ \sigma_L^2 &= l_y^2(\sigma_{f_1}^2 + \sigma_{f_2}^2 + \sigma_{f_3}^2 + \sigma_{f_4}^2) \end{aligned} \tag{2.65}$$

$$\sigma_L^2 = 4l_y^2\sigma_f \tag{4.15}$$

Knowing the values of the parameters k_x, d_x and I_{xx}^g from Eq. 4.12 allows for reconstructing $L_d(t)$ at each point in time. The PSD (power spectral density) of the roll moment $P_L(f)$ and the PSD of the rotor thrust force $P_f(f)$ are related in the same way as the variances of the respective time domain signals, as is shown in Eq. 4.16. Again, the same holds for the pitch axis, as is shown in Eq. 4.17.

$$P_L(f) = 4l_y^2\, P_f(f) \tag{4.16}$$

$$P_M(f) = 4l_x^2\, P_f(f) \tag{4.17}$$

According to the above procedure, the PSD of the thrust of a single rotor, $P_f(f)$, can be estimated from the measured roll rate $p(t)$, and also from the measured pitch rate $q(t)$. In Figure 4.16 the estimated $P_f(f)$ functions are shown for descent speeds of $10\,\mathrm{m\,s^{-1}}$, $15\,\mathrm{m\,s^{-1}}$,$20\,\mathrm{m\,s^{-1}}$ and $25\,\mathrm{m\,s^{-1}}$, and for four different rotor rotational speeds. Each PSD shown is the average of the PSD according to the roll rate and PSD according to pitch rate. Note that both of these roll and pitch PSDs are very similar and pretty much overlap for all speed and rotor rotational speed combinations.

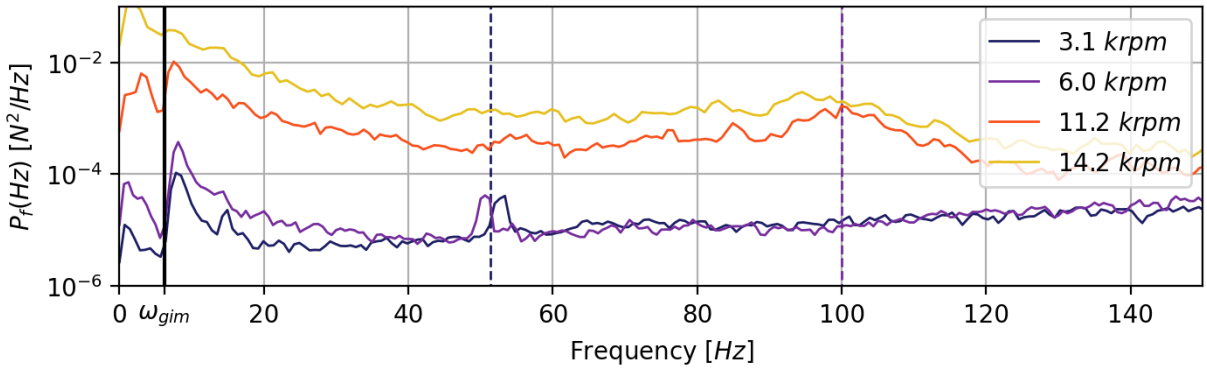

(a) V = 10 m s^{-1}

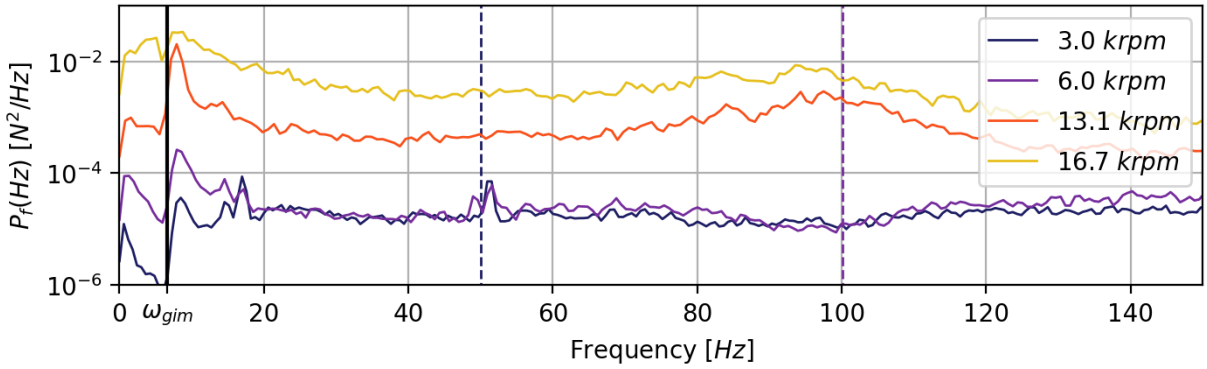

(b) V = 15 m s^{-1}

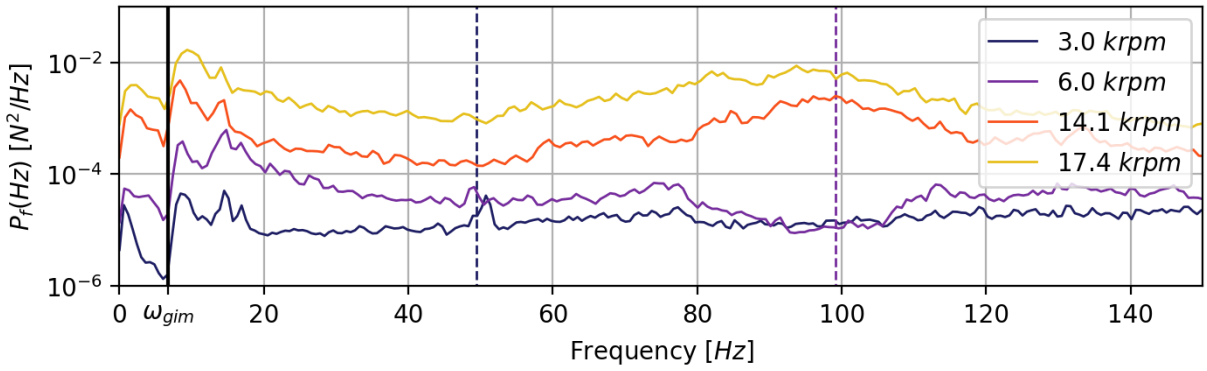

(c) V = 20 m s^{-1}

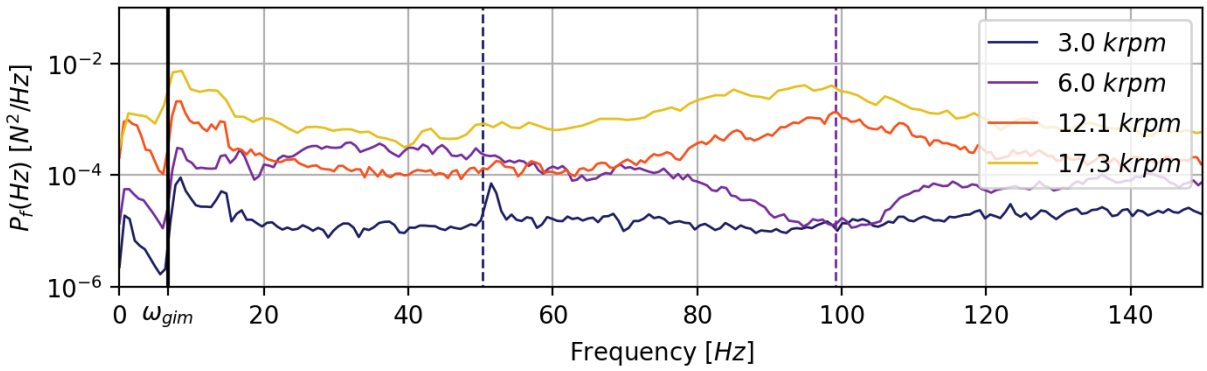

(d) V = 25 m s^{-1}

Figure 4.16: PSDs of single rotor thrust $f(t)$ based on the reconstructed roll moment $L_d(t)$ and pitch moment $M_d(t)$. The damped natural frequency of the gimbal is indicated with ω_{gim}. Dashed lines indicate the rotational speed of the rotors in Hz, and match in color with their respective PSD.

Firstly, in Figure 4.16 the vertical black line marked with ω_{gim} on the frequency axis indicates the estimated damped frequency of the gimbal system. As can be seen, the PSDs either increase or decrease notably close to this line. It is very plausible that this is due to unmodeled gimbal dynamics that are not captured by the damped mass spring approximation that was used to reconstruct the $L_d(t)$ and $M_d(t)$ signal. Of course this can not be said with certainty. Secondly, it can be seen that for frequencies up to 80 Hz the PSDs are fairly flat. Lastly, the dashed lines in Figure 4.16 indicate the frequency at which the rotors are rotating, and match in color with their respective PSD. The small peak at around 50 Hz is likely not due to the rotating rotors, as it shows up in PSDs corresponding to much higher rotor rotational speeds (not shown in the figure) as well.

The total variance of rotor thrust, σ_f^2, is proportional to the area under the PSDs in Figure 4.16. However, it was found experimentally that there are several airframe eigenfrequencies above 90 Hz, as will be discussed in section 4.6. This makes it unclear how much of the signal power above, say, 80 Hz is due to thrust fluctuation and how much is due to frame resonance. To get around this, the area under the PSD is only taken up to 80 Hz to find the variance σ_f^2. Consequently, fluctuations above 80 Hz that are actually due to thrust fluctuation are discarded. This makes the estimation of σ_f^2 conservative.

In Figure 4.17 the estimated STD σ_f that is calculated using the reconstructed $L_d(t)$ and $M_d(t)$ signals is compared to the σ_f values for a rotor in isolation as were found in subsection 4.1.2. Standard deviations estimated using $L_d(t)$ and $M_d(t)$ signals are indicated with 'from p(t)' and 'from q(t)', respectively, and the isolated rotor thrust STD is indicated with the black line. It is relevant to know how much of the estimated σ_f from $p(t)$ and $q(t)$ is due to gyroscope sensor noise. It was found experimentally that the gyroscope primarily produces quantization noise. The gyroscope has a resolution of $0.0174\,\mathrm{rad\,s^{-1}}$, which is small compared rotational speeds measured during the experiment as can be seen in Figure 4.15. In this case a common assumption is that quantization errors can be modelled as additive white noise [22]. The STD of this noise is then approximately $\sqrt{1/12} \cdot .0174$. Its possible to reconstruct $L_d(t)$ and $M_d(t)$, and thus σ_f, as a result of only this noise signal. These σ_f values due to noise only are indicated by the dashed lines in Figure 4.17. Of course in reality these rotor forces do not exist. The STDs reconstructed from $p(t)$ and $q(t)$ indicated by triangles in Figure 4.15 are already corrected for this noise.

As can be seen in Figure 4.17, σ_f is generally significantly larger for rotors mounted to the quadcopter compared to the rotors in isolation. This strongly suggest that rotor-rotor interaction, or maybe even rotor-frame interaction, causes a significant increase in the fluctuation of thrust.

Furthermore, it can be observed that the estimated value of σ_f is on average slightly higher when it is estimated using the pitch rate $q(t)$. A possible reason for this is that the system identification of the gimbal system performed notably worse (roughly 10 % to 30 % in terms of residue STD) for the pitch axis compared to the roll axis. This could mean that the reconstructed $M_d(t)$ signal contains more power that is actually due to the uncaptured system dynamics of the gimbal, rather than the power due to fluctuation in thrust. This would cause the estimated value of σ_f to be higher for the pitch axis.

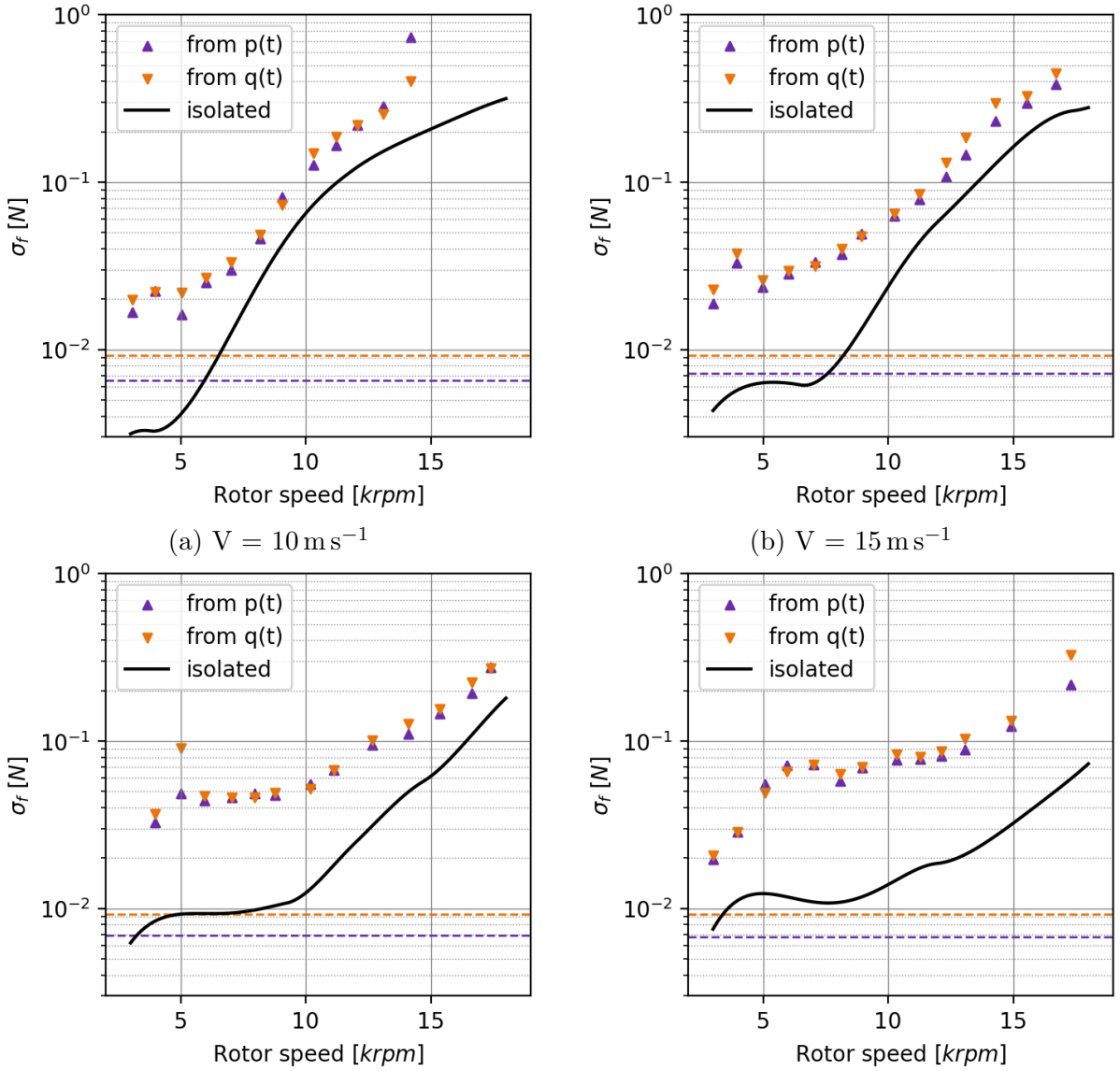

(a) V = 10 m s^{-1}

(b) V = 15 m s^{-1}

(c) V = 20 m s^{-1}

(d) V = 25 m s^{-1}

Figure 4.17: Rotor thrust standard deviation. The black line represents isolated rotor thrust data. Purple and orange triangles represent thrust standard deviations reconstructed from the measured roll rate and measured pitch rate, respectively, which are corrected for gyroscope noise. The purple and orange dashed lines correspond to gyroscope noise only along the roll and pitch axis, respectively.

Another potential cause might be the incorrect assumption that the rotor forces are uncorrelated, which was made in Eq. 2.65. If these correlations would in fact be non-zero, they can be divided into the sum of thrust correlations between the left and right rotors, and the sum of thrust correlations between front and rear rotors. It is not hard to show that if these 'left to right' and 'font to rear' correlations are different, then the thrust variance σ_f^2 reconstructed from the roll rate would be different from the value for σ_f^2 reconstructed from the pitch rate. This might indeed be the case, since the rotors are separated more along the body frame y-axis compared to the body frame x-axis due to the presence of the quadcopters 'fuselage'. Not taking into account the higher thrust correlation between the front and rear rotors would result in different estimations for σ_f^2.

Of course values shown in Figure 4.17 are estimations of the actual values. It should be noted that the STDs reconstructed from the quadcopters movement are estimated conservatively due to the low assumed values for I_{xx}^g and I_{yy}^g, the exclusion of frequencies above 80 Hz and the subtraction of gyroscope noise. Estimations of the isolated rotor thrust STDs on the other hand are are likely to be too high since sensor noise and test stand vibrations are not subtracted.

4.6 Structural vibration tests

In Figure 4.18 the some PSD are shown of the attitude rates p, q and r, that were recorded during the structural vibration test. During the experiment, the quadcopter could move around fairly unrestricted because it was only attached with a single wire close to the CG. This caused the quadcopter to slowly oscillate after each hammer impact, which of course has noting to do with the structural eigenmodes. This dominant oscillation of around 2 Hz to 3 Hz can clearly be observed in both subplots of Figure 4.18 for both roll and pitch.

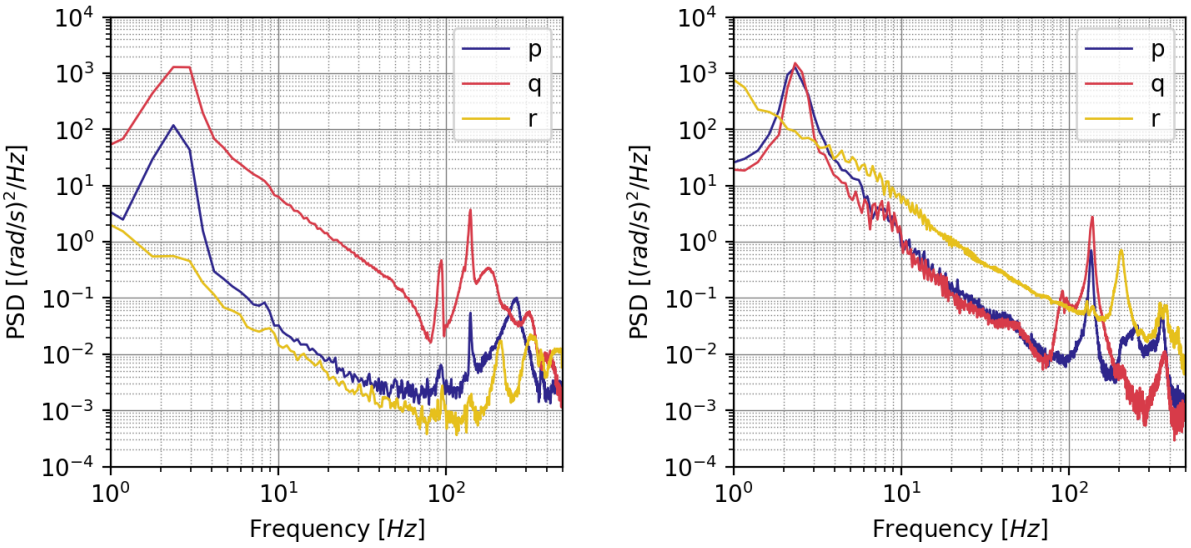

(a) Camera impact

(b) Yaw impact

Figure 4.18: PSD of attitude rates as a result of an impact test.

In Figure 4.18a the PSD's are shown for the case where the quadcopter is hit on the main frame close to the FPV camera. Because the impact force has a large moment arm

with respect to the attachment point of the wire, eigenmodes around the pitch axis are much more excited compared to the roll and yaw axis. However, it can be seen that for all rotation axes, the first notable resonance peaks occur at frequencies of 90 Hz and 150 Hz. These peaks even seem to be visible in the yaw rate PSD.

In Figure 4.18a the PSD's are shown for the case where the quadcopter is hit on the arm close to the place where the motor is attached. The arm is hit in a way that the quadcopter starts spinning in yaw direction shortly after impact. This is the reason the yaw PSD is now much larger. The first pure yaw oscillation seems to occur at around 200 Hz. The resonant peaks of the roll and pitch rate seem again to occur at frequencies of around 90 Hz and 150 Hz.

For the derivation of the model in chapter 2 the assumption was made that there are no structural eigenmodes around frequencies that the model will be evaluated. This experiment shows that the model is only really valid for frequencies lower than 80 Hz. This frequency is based on the first resonance peak at 90 Hz and a margin of 10 Hz. Of course the limit of 80 Hz was already enforced by the decision to exclude the effect attitude filters in Betaflight.

Chapter 5

Evaluation of the Complete Model

Previous chapter covered all experimental results which can be used to quantify all the parameters of the model blocks presented in Figure 2.2. At this point the model is therefore fully defined. As discussed earlier, the model takes a couple of arguments which are the descent speed, rotor rotational speeds and the amount of ballast. Matching the values of these arguments with values determined during flight testing and wind tunnel tests allows for evaluating how the model matches with real world data. This chapter revolves around this evaluation process and various other found characteristics of both the model and measured flight dynamics.

In section 5.1 the resulting model is analysed by looking at how its poles and zeros change as a result of various flight conditions. In section 5.2 the model is compared with the flight data from section 3.9 and the wind tunnel tests from section 3.8. Finally, in section 5.3, a very interesting effect is discussed which was found during the execution of both the flight tests and wind tunnel tests. This effect is the quite drastic divergence of rotational speeds of one diagonal rotor pair compared to the other diagonal pair.

5.1 Analyses of model characteristics

In this section the model characteristics are analysed by looking at its poles and zeros. As was explained in previous chapters, the model from chapter 2 is linearized around an operating point. This operating point is defined by the linearization descent speed V^* and the four linearization rotor rotational speeds ω_1^* to ω_4^*. Assigning a number to these variables results in a specific realisation of the linear model with its particular characteristics. To avoid having to analyse too many different operating points, in this section the model characteristics are mainly analysed as a function of descent speed V^* and a single rotor rotational speed which is the same for all rotors, i.e $\omega_i^* = \omega^*$. The plots in this section represent the model using the 5x4.5 rotor.

An appropriate way to analyse these characteristics is to look at the placement of the poles and zeros of input to output transfer functions of the model. Since the model has four inputs and four outputs, it can technically be described by a set of 16 transfer functions. The the total thrust input F_d and the descent speed output $\overline{V}$ signals of the model are not analysed in detail since their respective transfer functions are rather trivial and fluctuations in speed were found to contribute little to the oscillatory properties of the propwash effect. As a result, the main focus lies on how a roll moment L_d, pitch

moment M_d and yaw moment N_d affect the attitude rates.

It can be seen from Figure 2.2 that if the four rotor rotational speeds are the same, then the system is uncoupled and movements around each attitude axis do not influence each other. In Figure 5.1a, Figure 5.1b and Figure 5.1c a pole-zero map is shown for the uncoupled roll, pitch and yaw axis for a common rotor rotational speed of $\omega_i^* = 9000\,\text{krpm}$ and a descent speed of $v^* = 0\,\text{m}\,\text{s}^{-1}$. Each of these maps indicate that for each axis there are two complex poles which exist mainly due to the interaction of the P and D terms of the controller with the quadcopter dynamics, and a pole on the real axis mainly caused by the I term of controller. Note that for this model the roll and pitch model have an additional pole and zero on the real axis at a very high value due to the pseudo derivative used, as was shown in Eq. 2.1. As intended, these do not impact the model at relevant frequencies for the propwash effect.

In Figure 5.1d the poles and zeros are shown for the roll rate as a function of roll moment in the case that the rotor rotational speeds are not the same, or more to be more specific, $\omega_1 = 5\,\text{krpm}$, $\omega_2 = 8\,\text{krpm}$, $\omega_3 = 12\,\text{krpm}$ and $\omega_4 = 15\,\text{krpm}$. As can be seen, yaw dynamics now impact the roll behaviour, but little since the poles are pretty much cancelled by zeros. The imaginary poles of the pitch dynamics however are canceled to a lesser degree compared to the yaw dynamics. In fact, in general it can be noted that the larger the difference between the rotor rotational speeds, the more the roll and pitch rate dynamics are coupled. This is not only due to the gyroscopic effect of the rotors, but also because the rotors operate at different points in the thrust-rpm curve. A control input for the roll axis will therefore excite the pitch axis and vice verse.

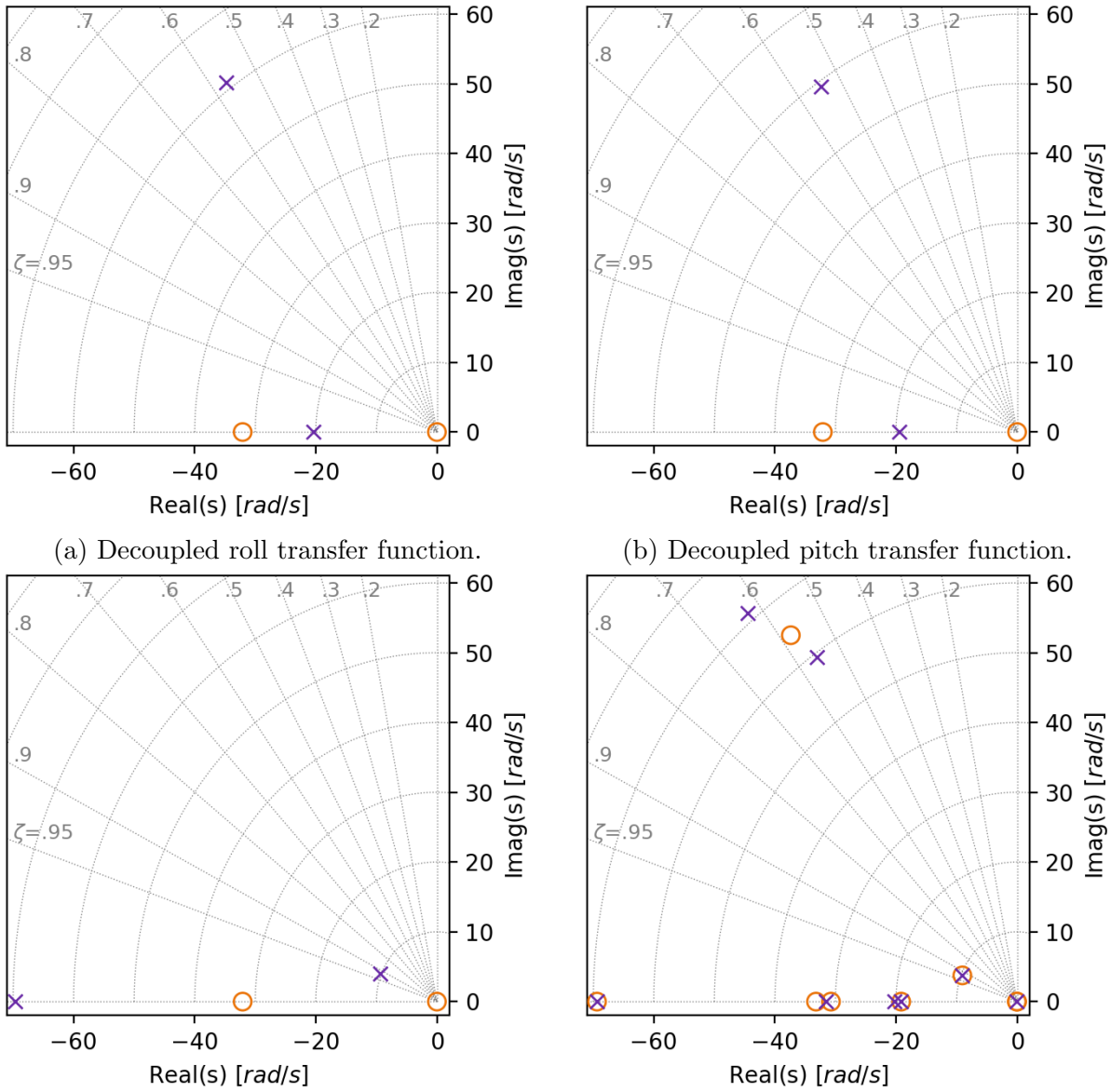

(a) Decoupled roll transfer function.

(b) Decoupled pitch transfer function.

(c) Decoupled yaw transfer function.

(d) Coupled roll transfer function.

Figure 5.1: Poles and zeros of each attitude axis and of the full model.

Another interesting fact is the additional pole in Figure 5.1d on the real axis with a value of $31\,\mathrm{rad\,s^{-1}}$. This pole is likely caused by the difference in transient response between the rotors. Forcing equal transient responses while leaving the rest of the model the same removes the pole at this position. Lastly, the pole at the origin is caused by the transfer function of the descent speed caused by the total thrust. For all attitude axes, there is a zero cancelling this pole, indicating that vertical movement of the quadcopter has a negligible impact on the propwash effect.

To gain insight into the actual causes of the propwash effect, it is interesting to look at how the position of the system poles and zeros change as a function of descent speed and rotor rotational speeds. Here only cases are considered where the rotor rotational speeds are the same. In Figure 5.2 the movement of poles are shown as a function of common rotor rotational speed, and at different descent speeds V^*.

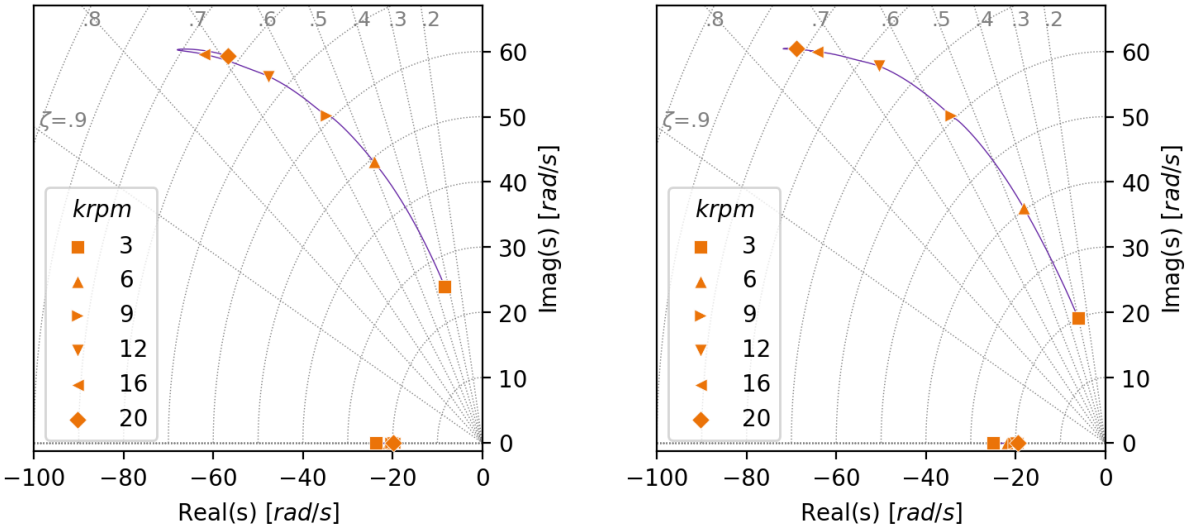

(a) V = 0 m s^{-1} (b) V = 5 m s^{-1}

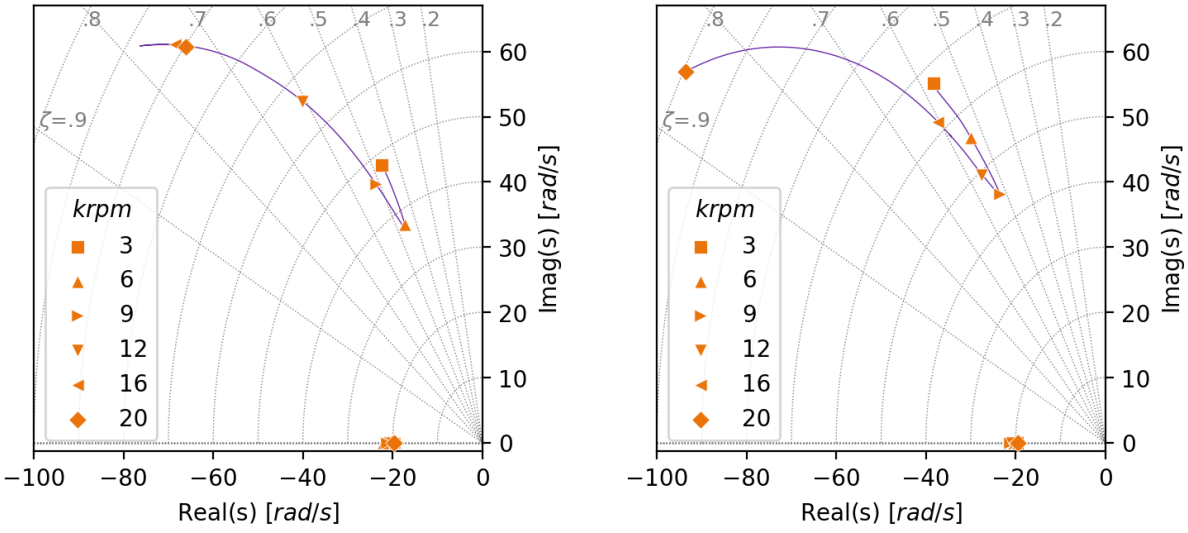

(c) V = 10 m s^{-1} (d) V = 15 m s^{-1}

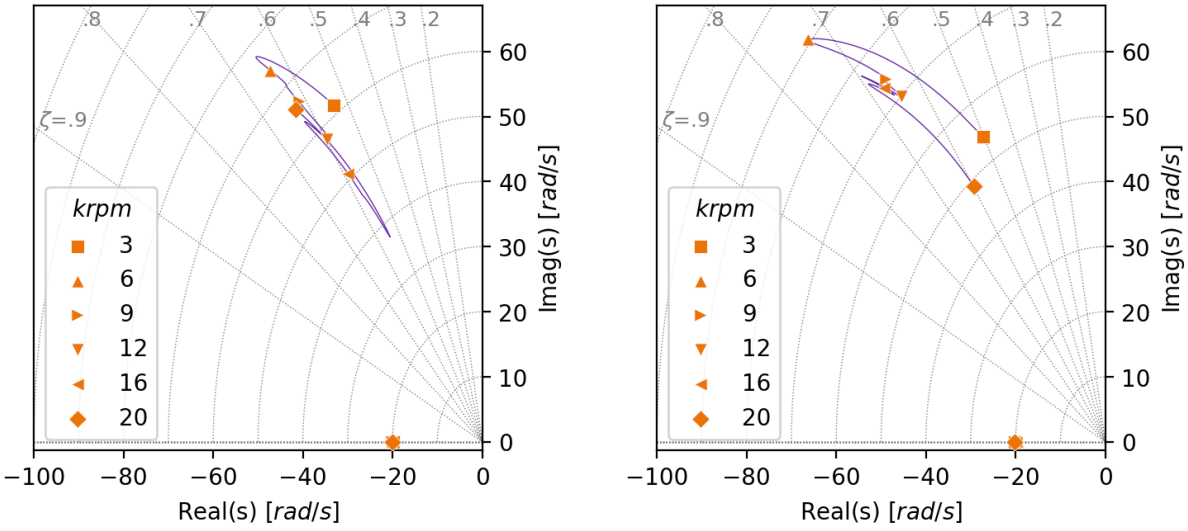

(e) V = 20 m s^{-1} (f) V = 25 m s^{-1}

Figure 5.2: Change of roll model poles as a function of rotor speed.

First of all it can be noted that especially the complex poles move around quite a bit, in contrast to the real pole. This suggest that the propwash effect could potentially be improved by changing the P and D gains, but not the I gain. This idea is reinforced by the fact that setting the I gain at zero does relatively little to the position of the complex poles.

Secondly, the complex poles primarily move along a similar arc. Diving deeper into the model reveals that this is actually due to changing value of the derivative of rotor thrust w.r.t rotor rotational speed, or f_σ. For example, according to Figure 5.2a, the lowest value of this derivative is found at low rotor rotational speeds, resulting in slower dynamics with a lower damping ratio ζ. At higher speeds, the poles start to deviate slightly from this common arc, which is caused by other effects such as the derivative of rotor thrust w.r.t local rotor descent speed v. Intuitively, higher values of this derivative increases the effective damping ratio, which moves the poles more towards the real axis.

Lastly, it can be seen that for no speed the poles move into the right half plane. Only for low rotor rotational speeds and low descent speeds, the damping ratio gets rather low. In no case however does the roll axis become unstable. Very similar behaviour of the poles shown in Figure 5.2 can be seen for the pitch axis.

In Figure 5.3 the same set of plots is shown, but this time for the yaw axis. Note that the real axis pole falls outside of the plotting frame. These figures show that the yaw dynamics differ from the roll and pitch dynamics in a few distinct ways. First of all, the complex poles represent slower dynamics and generally a higher damping ratio. Secondly, the poles occasionally move out of the complex plane. This means the yaw dynamics are not oscillatory in nature at these points. Lastly, at speeds close to $25\,\mathrm{m\,s^{-1}}$, the poles move into the right hand plane at a common rotor rotational speed of around 14 krpm, which can be seen in Figure 5.3f.

The cause of the right half plane poles is revealed by Figure 4.7, which shows that the derivative n_σ becomes negative at this point of operation. This can more clearly be seen in Figure A.9e. This means an increase in rotor rotational speed actually slightly decreases the amount of torque, which makes the relevant control law destabilizing rather that stabilizing. Furthermore, the quadcopter becomes unstable in yaw because a sudden yaw rate results in a yaw moment that actually increases the yaw moment even more. However, this latter effect is a lot smaller that the control inversion effect.

Overall it can be concluded that the model system dynamics definitely change at different descent speeds compared to the hover scenario. However, the pitch and roll attitude dynamics never get close to being unstable. The model only suggests the yaw dynamics can become unstable at high descent speeds and at a narrow range of rotor rotational speeds. For all attitude axes it can be observed that the damped system frequencies can vary quite a bit.

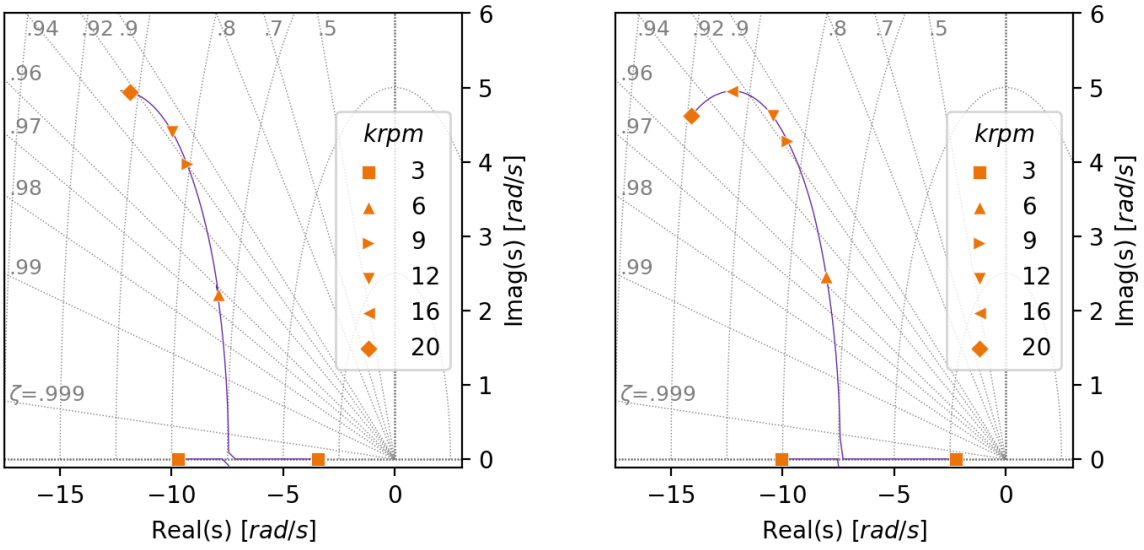

(a) $V = 0\,m\,s^{-1}$

(b) $V = 5\,m\,s^{-1}$

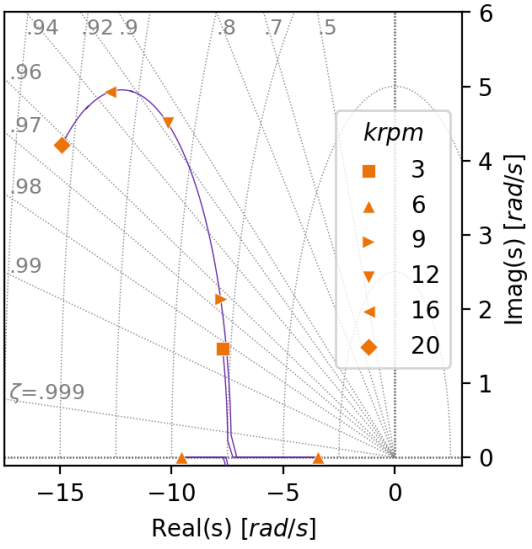

(c) $V = 10\,m\,s^{-1}$

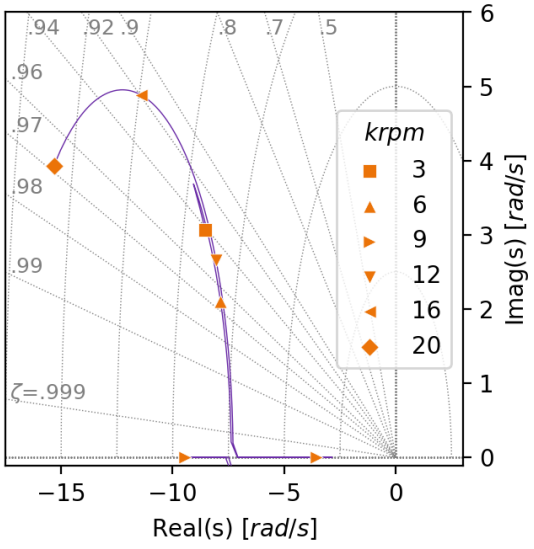

(d) $V = 15\,m\,s^{-1}$

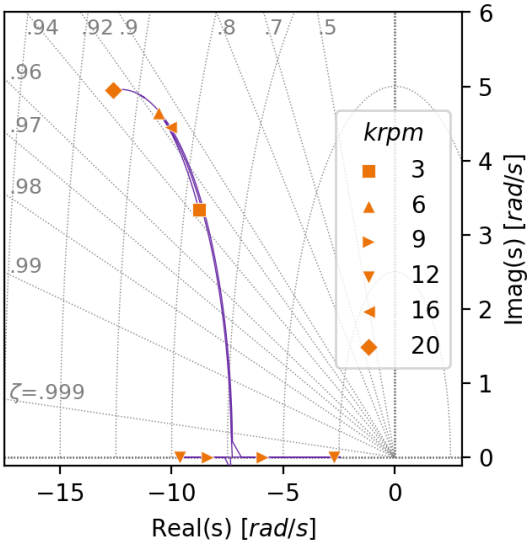

(e) $V = 20\,m\,s^{-1}$

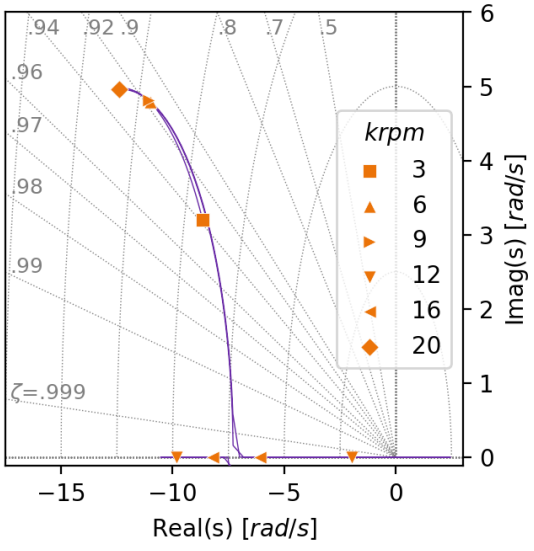

(f) $V = 25\,m\,s^{-1}$

Figure 5.3: Change of yaw model poles as a function of rotor speed.

5.2 Comparison of model output with flight data

The model characteristics presented in section 5.1 are perhaps interesting in itself, but rather meaningless when not compared to actual flight data. Therefore this will be covered in the present section. The comparison will aid in the understanding what the causes of the propwash effect are.

To be more complete, the model will not only be compared to flight data, which corresponding experiment was discussed in section 3.9, but also to recorded data where the quadcopter is mounted inside a gimbal with active controller, as was described in section 3.8. Both experiments have their own advantages and disadvantages. To name some, the flight test experiment is a test where nothing is touching the quadcopter externally. This means it is certain that all movement of the quadcopter is caused by aerodynamic forces and inertia of masses. Unfortunately, to reach all speeds required, ballast weights need to be added to the quadcopter, which changes mass properties, inertia properties and theoretically aerodynamics. Besides this it can not be guarantied that the quadcopter descents along a perfect vertical path due to wind gusts and a lack of proper position tracking. This is one of the advantages of mounting the quadcopter inside the wind tunnel, where the speed and quadcopter orientation can be precisely controlled. The downside of the wind tunnel setup is not only that the gimbal might apply some small moments to the quadcopter, but also that the gimbal always changes the aerodynamics so some degree due to its presence in the airflow.

For the flight tests the descent speed has to be determined with some decent accuracy at multiple times per second. The initial idea was to simply take the derivative of the barometer to calculate the descent speed. However, it became clear that this is rather inaccurate because the barometer measures air pressure, and can therefore also pick up dynamic pressures. That is, if there is a lot of turbulent airflow inside the frame, this introduces measurement errors in the barometer readings. To get around this, the altitude was estimated by combining the barometer readings with the accelerometer readings using a linear Kalman filter. The filter equations are shown in Eq. 5.1 and Eq. 5.2, which are the used state and measurement equation, respectively. Here h is the estimated altitude, h_m is the altitude measured by the barometer, n_h is the noise of the barometer altitude measurements, a_z is the acceleration along the z-axis of the body frame measured by the accelerometer, n_a is the noise of the the acceleration measured by the accelerometer and λ_a is the estimated bias of the accelerometer measurements.

$$\begin{bmatrix} \dot{h} \\ \dot{V} \\ \dot{\lambda}_a \end{bmatrix} = \begin{bmatrix} 0 & -1 & 0 \\ 0 & 0 & -1 \\ 0 & 0 & 0 \end{bmatrix} \begin{bmatrix} h \\ V \\ \lambda_a \end{bmatrix} + \begin{bmatrix} 0 \\ 1 \\ 0 \end{bmatrix} a_m + \begin{bmatrix} 0 \\ 1 \\ 0 \end{bmatrix} n_a \tag{5.1}$$

$$h_m = h + n_h \tag{5.2}$$

To make the Kalman filter function properly, the STDs of the barometer noise n_h and accelerometer noise n_a had to be known. The latter was determined by placing the quadcopter on a table without the rotors rotating and recording the accelerometer measurement $a_m(t)$ for a time span of 30 s. The recorded measurements showed a close to linearly changing bias λ_a of around $0.05\,\mathrm{m\,s^{-2}}$ over the period of 30 s. Therefore first a linear function was fitted to the measurement signal using OLS. This function was then subtracted from the signal, which resulted in a fairly accurate estimation of the noise

signal n_a. The STD was then found to be equal to $10.7\,\mathrm{mm\,s^{-2}}$.

The noise STD of the barometer measurements was initially set at a guessed value of 1 m. The Kalman filter using the STDs of $10.7\,\mathrm{mm\,s^{-2}}$ and 1 m for n_h and n_a, respectively, was then used to estimate the altitude h of some recorded descent flights. This estimated altitude h could then be subtracted from the recorded barometer altitude h_m, which resulted in an estimation of the barometer measurement noise n_h. This noise signal could be used to set a new value for the STD of the barometer noise in the Kalman filter. This process was repeated a couple of times resulting in a quickly converging estimate of the barometer noise STD. The final estimated value used for the Kalman filter was 2.0 m. Comparing the barometer measurements with the final Kalman filtered altitude estimate revealed that the barometer noise was quite far from being Gaussian noise as the barometer measurements are dependent on quadcopter speed and quadcopter orientation due to aerodynamic effects. However, the Kalman filter is still believed to produce more accurate estimates of the velocity V compared to the case where only the barometer is used as sensor.

It should be noted that for the Kalman filter derivation the assumption is made that quadcopters attitude angles are small. Between descents this assumption did not hold since the quadcopter had to be flown back to the starting point, which required large pitch angles at the least. The Kalman filter was therefore initialized every time the quadcopter started to ascent in a vertical manner to the targeted initial descent height.

It appeared harder than expected to give the quadcopter a constant descent speed. First of all, once the descent was initiated, it took some time for the quadcopter to reach its terminal velocity. This transient response time easily took more than 5 s, after which the quadcopter had already lost a large part of its initial altitude. Besides this, the velocity did not remain perfectly constant once a 'steady' descent state had been reached. Therefore multiple smaller intervals of data with a length ranging from 2 s to around 15 s were extracted where the estimated descent speed V and rotor rotational speeds ω_i did not deviate more than $2\,\mathrm{m\,s^{-1}}$ and 1000 rpm, respectively. Descents where the rotor rotational speeds came close to 3000 rpm were not used since this is an indication that the mixer described in section 2.2 does not behave linearly anymore.

Each descent can be characterised by the descent speed V and a throttle setting. This throttle setting is usually quantified by a percentage or number between 0 and 1. Since the relation between the throttle setting and rotor rotational speed is not necessarily known, it is difficult to give any interpretation to how and why certain throttle settings influence the flight test results. Therefore the new variable ω_h is defined, which is an alternative way to quantify the throttle setting. Here ω_h is equal to the average rotor rotational speed of the four rotors with zero flight speed (hence the subscript h for 'hover') and a disabled flight controller. In this ideal case the four rotor rotational speeds would be equal. Each throttle setting can thus be referred to by stating the value of ω_h that this throttle setting would cause. The relation between throttle setting δ and ω_h is shown in Eq. 5.3, and was estimated using data recorded for finding the P term of the flight controller, which was described in section 3.4.

$$\omega_h = 2828 + 37800 \cdot \delta \tag{5.3}$$

All descents can now be characterised by the the combination of V and ω_h. In Figure 5.4a all the descents that were used for analyses are plotted, where each dot refers to a descent with the earlier stated requirements for speed and rotor rotational speed deviations. As can be seen, no results are available for lower values of speed and ω_h. One reason for this is the fact that its not possible to make the quadcopter lighter after removing all the ballast plates. Another reason is that for many low to intermediate values of speed and ω_h the diverging rotor speed effect occurs, which is described in section 5.3. While this effect occurs, often times the slower rotating rotors hit the lower limit of 3000 rpm, resulting in the mixer becoming nonlinear and therefore the exclusion of the data set. On the other hand, descents with very high values of V and ω_h are also not present due to the fact that there is a limit on the amount of ballast that can be added to the quadcopter. In Figure 5.4b a similar plot is shown, but this time for the performed wind tunnel tests. As can be seen, the distribution of V and ω_h can be done in a more systematic way.

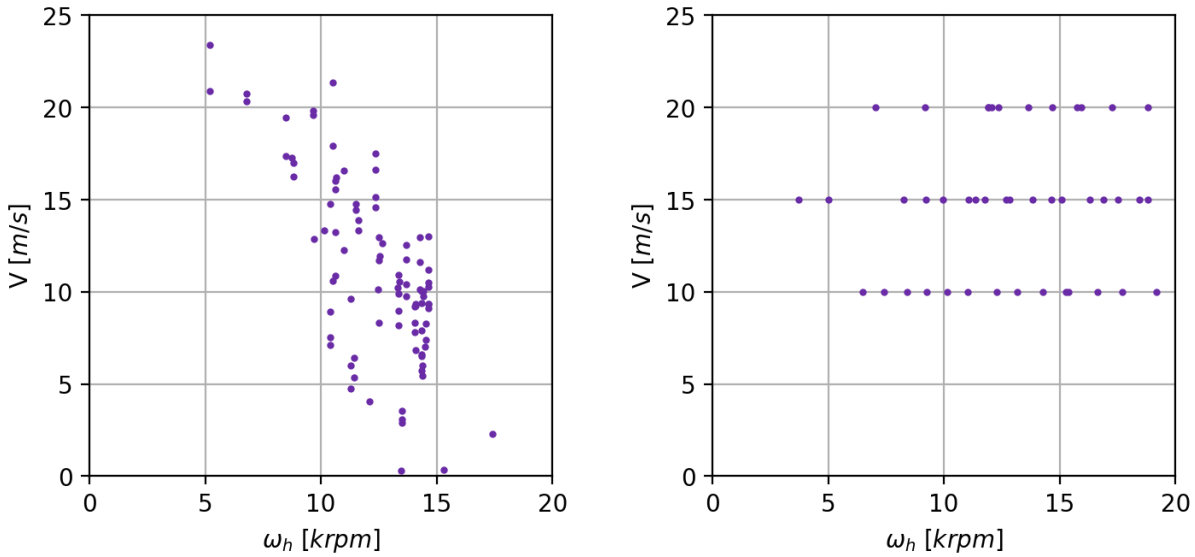

(a) Flight tests.

(b) Wind tunnel tests

Figure 5.4: Flight speed and ω_h combinations corresponding to used experiment data.

Since the motions experienced during the propwash effect are stochastic in nature, it makes sense to compare the model behaviour and recorded flight behaviour in the frequency domain. In Figure 5.5, an example is given of the PSDs for pitch, roll and yaw, according to the model and to the flight data. For this descent the speed is equal to 20.4 $\mathrm{m\,s^{-1}}$ and the average rotor rotational speed is 5.7 krpm. Although the PSD's of each descent can vary significantly, the shown PSD's are rather representative in the fact that the model PSD is much lower in magnitude but captures the frequencies at which maximum power occurs rather well, or at least for the roll rate and pitch rate. Note that the PSD's considered are only analysed in the range of 1 Hz to 80 Hz. How well the data and model PSD's match in this range is an indicator for how accurate the model describes the real world effect. The lines labelled with 'prop' indicate the frequencies at which the rotors are rotating. As can be seen in the figure, there are two rotors rotating at a speed under 80 Hz. The impact that rotating rotors have on the resulting PSD's can especially be noted for the yaw rate. This makes sense form a physical standpoint if the rotors are ever so slightly out of balance, which in practice they usually are.

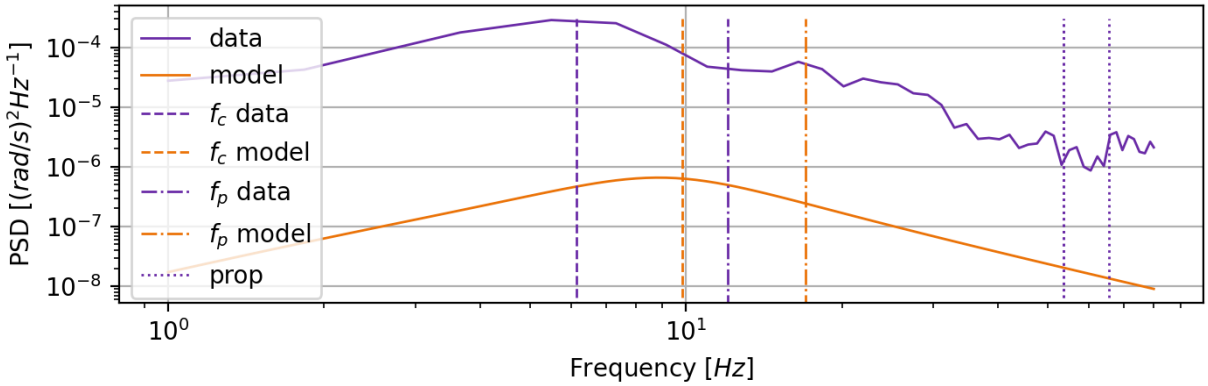

(a) Roll rate

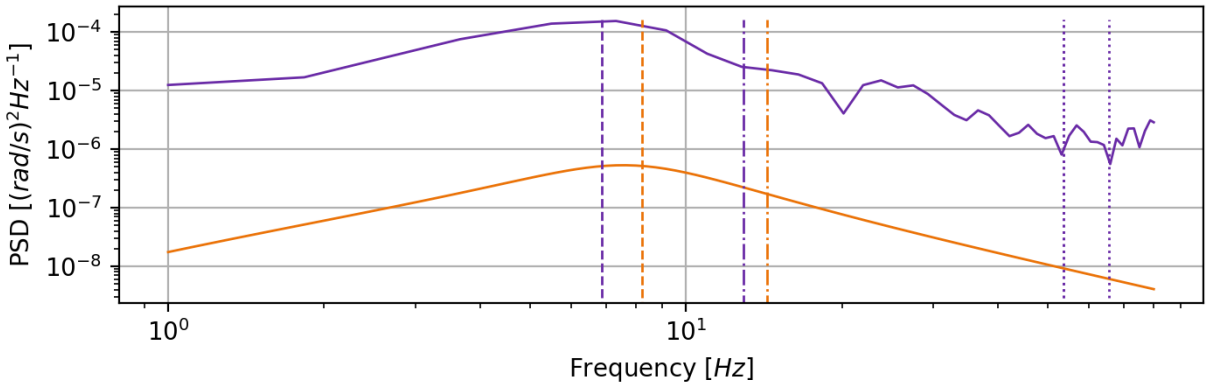

(b) Pitch rate

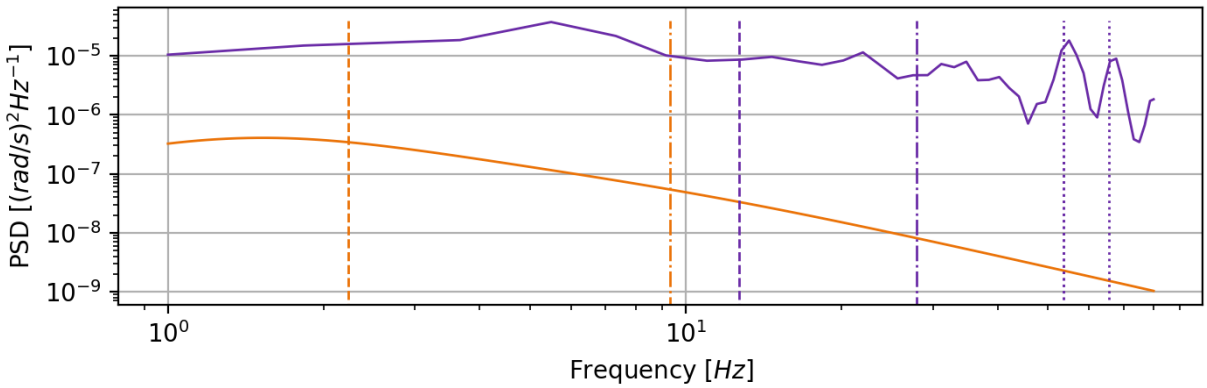

(c) Yaw rate

Figure 5.5: PSD's according to the model and flight data with $V = 20.4\,\mathrm{m\,s^{-1}}$ and a mean rotor speed of 5.7 krpm.

To compare all PSD's of all performed descents, some metrics are defined. The first one is the 'center frequency' f_c. This frequency is defined by the fact that the power from 1 Hz to the center frequency is equal to the power present between the center frequency and 80 Hz. This metric is effective in indicating around which frequency the bulk of the power in the signal can be found. However, since most PSD's in this case are rather distributed rather than having clear spikes of increased power, this metric is not really effective in locating the frequency at which most power is present, or so called 'peak frequencies'. To get around this, the second metric used is the 'peak frequency' f_p. To find this frequency the PSD is first cubed in order to give more priority to frequencies with a

high PSD value. The center frequency is then found for this resulting graph, as was done earlier with the original PSD. The last metric is the area under the PSD's from 1 Hz to 80 Hz, which is a measure for the total around of power in the signal in this frequency range.

The metrics f_c and f_p are indicated as dashed and dash dotted lines, respectively, in Figure 5.5 for both the data and model. These frequencies can be found for each performed descent, resulting in a series of values for f_c and f_p. In Table 5.1 the mean values and STD of the series of values is presented corresponding to the data only. As can be seen, the peak frequencies are generally lower compared to the center frequencies. Furthermore, the oscillation frequencies are highest for the pitch axis and lowest for the yaw axis. This is likely due to the different MMOIs around these axes. Also, the rather high values of STDs indicate that the oscillation frequencies vary quite a lot. Unfortunately, no significant correlation of the center and peak frequencies was found with descent speed, rotor rotational speed or amount of ballast.

Table 5.1: Flight test center and peak frequencies.

Frequency	**Axis**	**Data mean**	**Data STD**	**Error mean**	**Error STD**
Center	roll	14.7 Hz	3.8 Hz	−18.0 %	103.4 %
	pitch	12.7 Hz	4.1 Hz	−21.7 %	94.8 %
	yaw	23.6 Hz	5.9 Hz	71.3 %	16.5 %
Peak	roll	9.3 Hz	4.3 Hz	−9.3 %	29.2 %
	pitch	7.1 Hz	3.4 Hz	−7.7 %	41.4 %
	yaw	11.2 Hz	10.0 Hz	60.1 %	11.0 %

In the last two columns of Table 5.1, the model frequencies, denoted for now with f^{model}, are compared to the frequencies corresponding to the data, denoted for now with f^{data}. The 'error mean' column values are found by calculating the error for every descent as shown in Eq. 5.4 and then taking the mean values of these errors. The 'error std' column captures the STD of these found errors. It can be seen from these columns that for the roll and pitch axis the mean estimated model frequencies are rather close to the data frequencies. For the yaw axis however the model seems to consistently estimate the oscillation frequencies to low. This could partly have to do with the fact that rotor resonance increases the value of the PSD at higher frequencies which increases the center and peak frequencies of the data PSD. Of course these rotor imbalances are not taken into account for the model. It can also be noted that the error STDs are rather high, especially for the center frequencies. It is important to note that this is likely only partly due to the inaccuracy of the model. Factors such as for how long data is recorded influence this value as well. The longer a descent is recorded, the less variance there should be in terms of estimated data center and peak frequencies. Since some descents used are only two seconds long, and the PSD's go as low as 1 Hz, some found values for center and peak frequencies are likely subject to a high amount of variance.

$$\text{Error} = \frac{f^{data} - f^{model}}{f^{data}} \cdot 100\,\% \tag{5.4}$$

In Figure 5.6 the PSD of an example wind tunnel data set is compared with the PSD that the model generate at the same speed and rotor rotational speeds. These plots

represent the other wind tunnel data sets fairly well in the sense that the flight tunnel data seem to have more power concentrated at higher frequencies. Although speculative, it is suspected that this has to do with eigenfrequencies of the test stand to which the quadcopter is mounted. Similarly to the flight test data, Table 5.2 shows the center and peak frequencies of the wind tunnel data and how this compares the the frequencies estimated by the model. By purely looking at the mean errors for roll and pitch it can be stated that the model performs worse matching with the wind tunnel data compared to the flight test data. On the other hand it can be noted that the error STDs are generally lower, with the exception for the peak frequency of the yaw rate. This reinforces the idea that longer measurement times decrease the error STD.

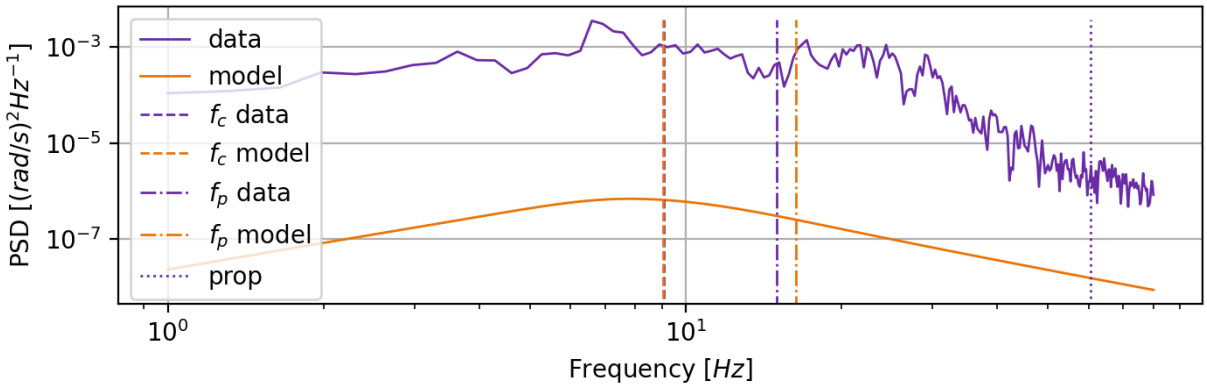

(a) Roll rate

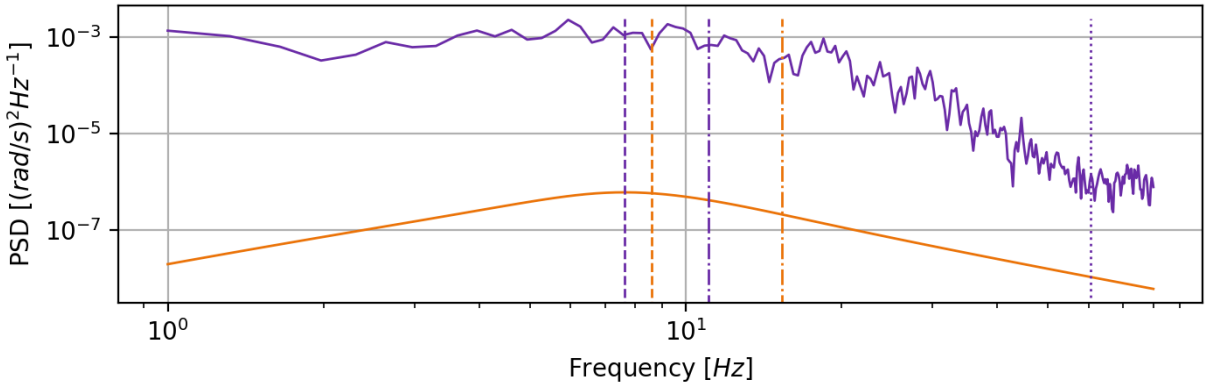

(b) Pitch rate

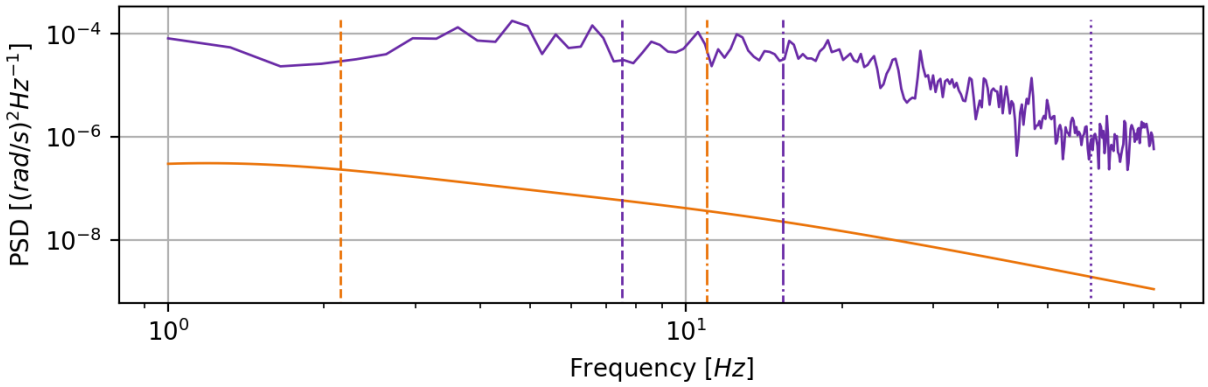

(c) Yaw rate

Figure 5.6: PSD's according to the model and wind tunnel data with $V = 15\,\mathrm{m\,s^{-1}}$ and a mean rotor speed of 5.7 krpm.

Table 5.2: Wind tunnel center and peak frequencies.

Frequency	Axis	Data mean	Data STD	Error mean	Error STD
Center	Roll	22.1 Hz	5.8 Hz	33.9 %	32.2 %
	Pitch	15.4 Hz	3.0 Hz	−25.6 %	68.6 %
	Yaw	18.9 Hz	8.2 Hz	56.2 %	32.8 %
Peak	Roll	18.8 Hz	9.6 Hz	13.9 %	26.2 %
	Pitch	9.2 Hz	3.1 Hz	−14.3 %	31.9 %
	Yaw	11.5 Hz	9.8 Hz	16.1 %	52.8 %

The above shows that the estimated center and peak frequencies are in general definitely approaching the real life center and peak frequencies. Unfortunately the opposite is true for the total estimated power and total actual power. In Figure 5.7 flight test total power is plotted against the ratio of model total power and flight test total power. As can be seen, the total power estimated by the model is orders of magnitude lower than the flight data suggest. In Figure 5.8 the comparison between total estimated power and total actual power for the wind tunnel data is shown. Here the difference is even larger. It can be safely concluded that the model is not capable of estimating how intensely the propwash effect will manifest itself during flight.

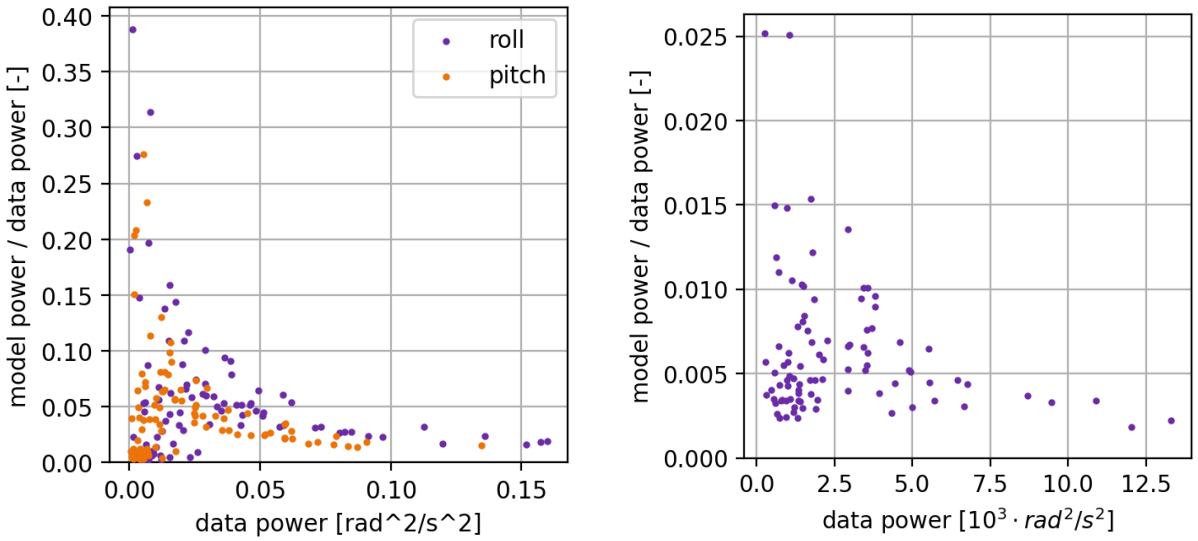

(a) Roll and pitch.

(b) Yaw.

Figure 5.7: The ratio of the total estimated model power over flight test total power.

5.3 The diverging rotor speed effect

The model introduced in chapter 2 is assumed to be valid when the quadcopter descents in vertical straight line and the velocity vector remains close to parallel with the z-axis of the quadcopter. Although the quadcopter oscillates around its attitude axes during the descent, from an aerodynamic perspective this flight condition is really symmetric. From this symmetry property it feels intuitive that all four rotor rotational speeds should remain very similar. However, during the wind tunnel experiments with the complete

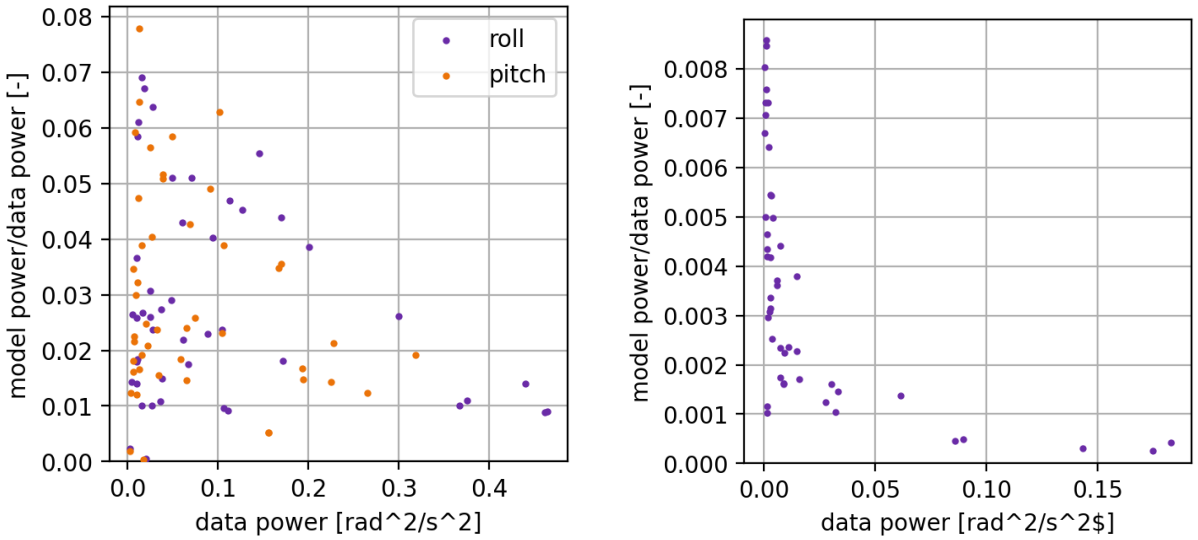

(a) Roll and pitch.

(b) Yaw.

Figure 5.8: The ratio of the total estimated model power over wind tunnel total power.

quadcopter in the gimbal, discussed in section 3.8, and the flight tests, it could be observed that the rotor rotational speeds can in fact differ enormously.

In Figure 5.9, data from a selected test run from the gimbal experiment is shown. For this test run the wind tunnel speed was set at $15\,\mathrm{m\,s^{-1}}$. The quadcopter is stabilized around its yaw axis by the flight controller, but besides this it is not restricted in yaw in any way. The third subplot shows that the controller performs quite well as the yaw rate r is kept close to zero. The first subplot shows the low pass filtered rotor rotational speeds. As can be seen from 0 s to around 90 s, the rotational speeds of rotor 2 and 4 start to deviate with roughly 10 000 rpm from rotors 1 and 3. Looking at the rotor rotational speed directions in Figure 15.1, this suggest the quadcopter is generating a yaw moment. After performing several wind tunnel tests and flight tests, the effect seems to be closely correlated to the external air speed and the throttle setting. This throttle setting, expressed as ω_h, can be seen in the second subplot of Figure 5.9.

This particular divergence in rotor rotatinoal speeds could happen because of multiple reasons. The first possibility is that the quadcopter is fighting a positive disturbance yaw moment. In this case the rotor rotational speeds would start to deviate as is shown to generate an opposing negative yaw moment. The only thing that could generate this moment is the gimbal. However, even after thorough inspection of the gimbal it seems impossible that this could have been the case. Also, the effect is seen during flight where nothing is touching the quadcopter. The second option is that the quadcopter is decreasing its yaw rate. The third subplot in Figure 5.9 shows the yaw rate stays pretty much equal to zero, negating this option as well. Another possible option is the fact that the rotors are in fact not experiencing a clear airflow. This seems more plausible since the rotors are blowing against the airflow which makes it possible for the rotors to operate in their own and each others wake.

After establishing the existence of this 'diverging rotor speed' effect, it is convenient to define a variable to quantify how much this effect is occurring at a given moment.

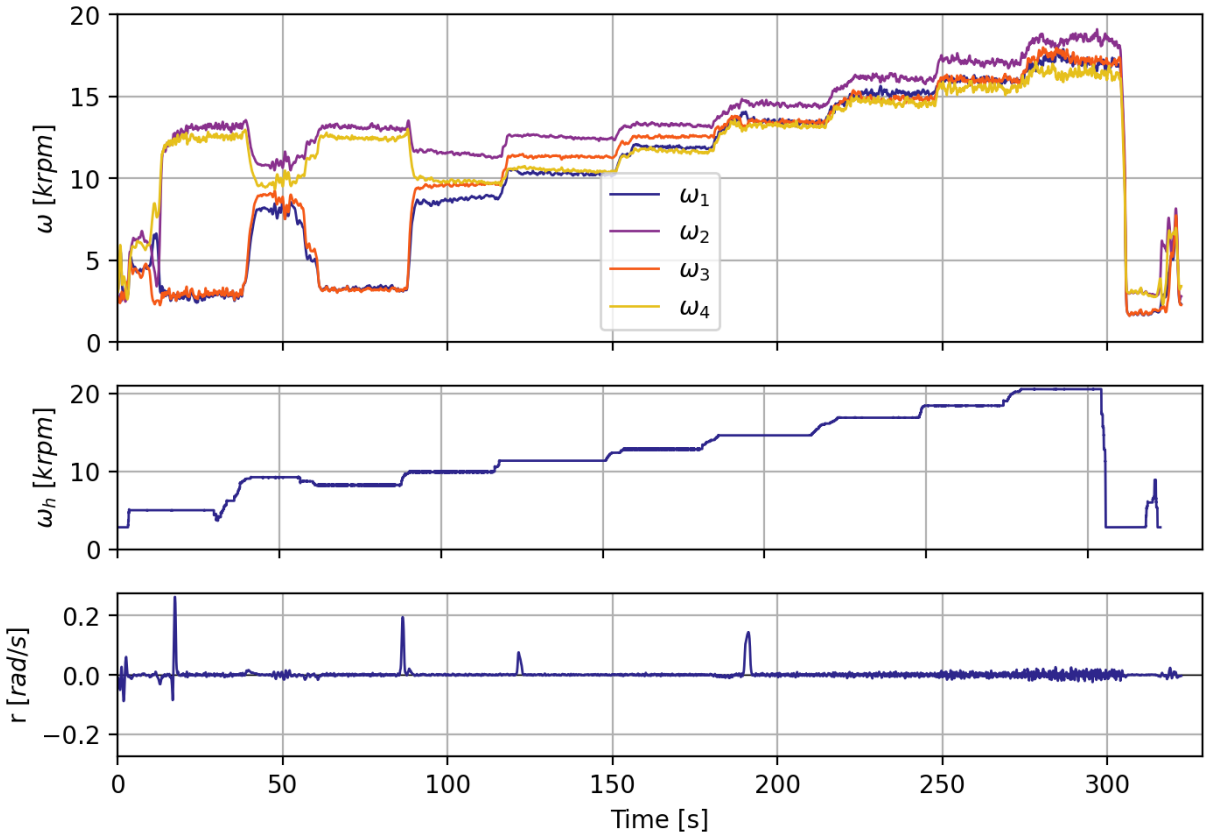

Figure 5.9: Test run 3 as example revealing the diverging rotor speed effect.

Here this is variable is taken to be $\Delta\omega_N$, which is calculated using Eq. 5.5.

$$\Delta\omega_N = -\omega_1 + \omega_2 - \omega_3 + \omega_4 \tag{5.5}$$

In Figure 5.10 the value of $\Delta\omega_N$ is plotted for various throttle settings, and for each of the six wind tunnel tests that were performed with fully functioning flight controller. Each data point represents the average value of $\Delta\omega_N$ and average value of the throttle setting over a time interval of 0.4 s. The data points in Figure 5.10 thus represent all the data recorded during the six wind tunnel tests. Looking at Figure 5.10a and Figure 5.10b, at a wind speed of $10\,\mathrm{m\,s^{-1}}$ and throttle settings below 7 krpm, the rotor rotational speeds seem to deviate for a large part of time. As the speed is increased to $15\,\mathrm{m\,s^{-1}}$ and $20\,\mathrm{m\,s^{-1}}$ in Figure 5.10c to Figure 5.10f, this critical throttle setting clearly increases. This also hints strongly at the fact that this effect is related to advance ratio and thus the operating state of the rotors. Interestingly enough, in Figure 5.10d and Figure 5.10f it can be noted that the rotor rotational speed divergence can happen in both directions.

Initially the reason for this effect was thought to be a faulty setup of one of the experiments. Some validation tests however revealed that this is most certainly not the case. During the validation process some thought was given to what might be causing the effect. The most plausible explanation was determined to be the following. It is assumed the rotors receive enough power to blow the air back into the external airflow. As soon as the diagonally opposed rotor pair that rotates CW starts rotating faster than the other pair, there could be an overall CW rotation in the flow below the quadcopter. This overall flow rotation could push the rotor wake of the faster CW rotating rotors towards the slower CCW rotating rotors, where the latter then encounters this wake. This

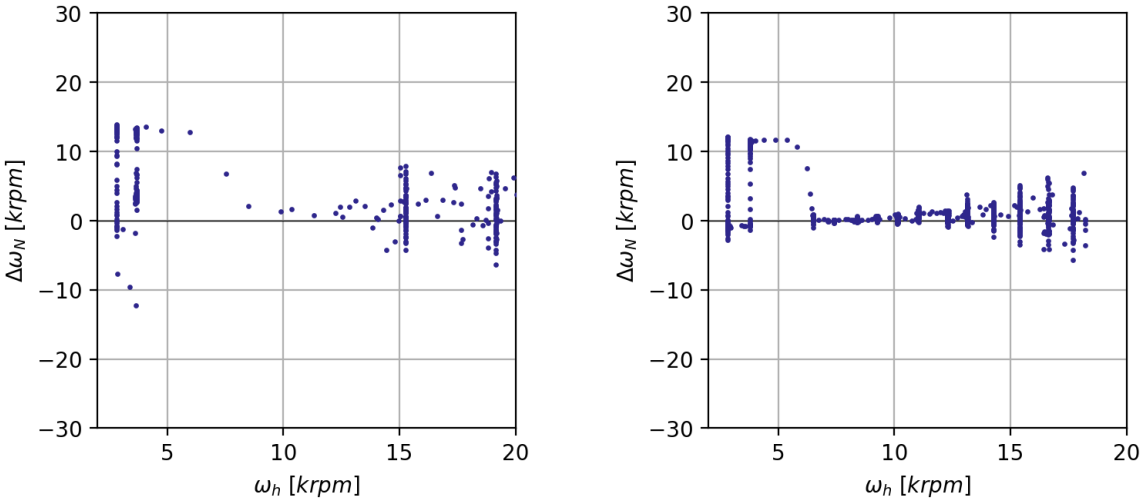

(a) Test run 1, V = 10 m s^{-1}

(b) Test run 2, V = 10 m s^{-1}

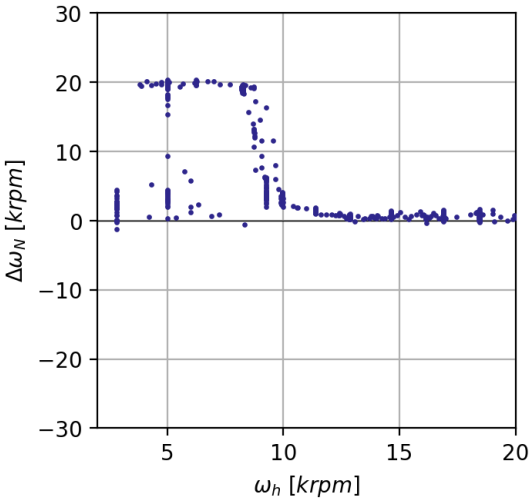

(c) Test run 3, V = 15 m s^{-1}

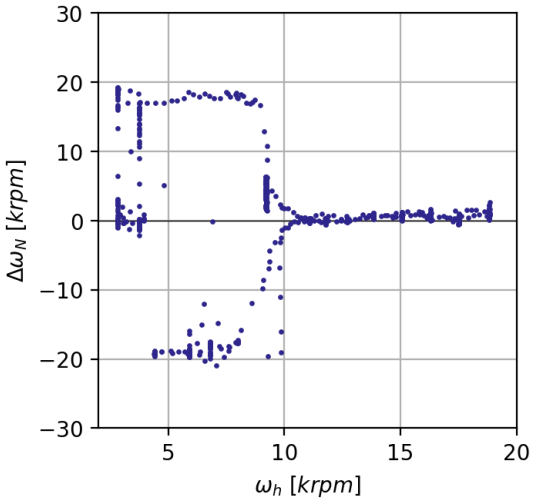

(d) Test run 4, V = 15 m s^{-1}

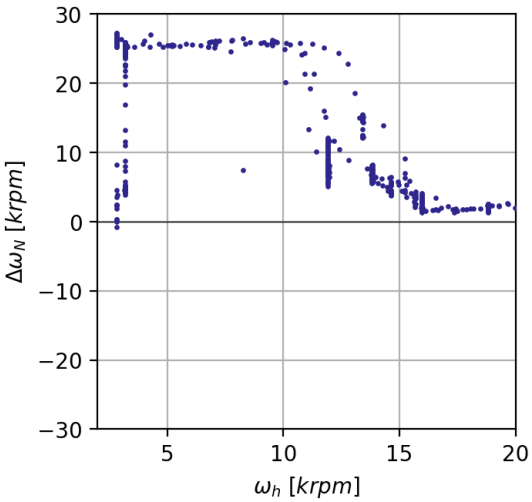

(e) Test run 5, V = 20 m s^{-1}

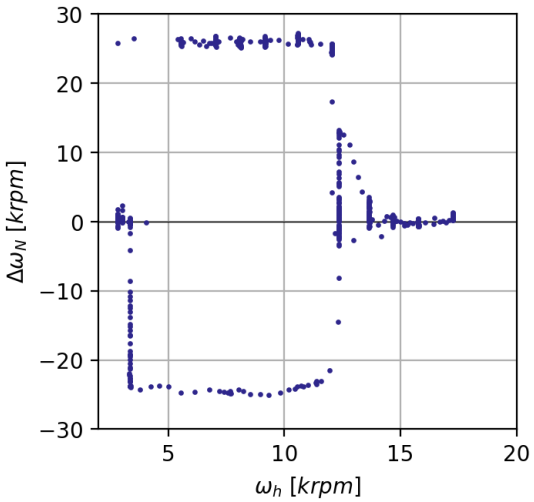

(f) Test run 6, V = 20 m s^{-1}

Figure 5.10: Measured rotor speed divergence as function of throttle setting.

means the slowly rotating CCW rotors start to see rotating flow in opposite direction to their own rotation, and as a result they will produce more drag and thus a positive yaw moment on the quadcopter. To counter this external yaw moment, the quadcopter increases the rotational speed of the CW rotating rotors even more. This completes the positive feedback loop making the rotor rotational speeds of the two rotor pairs diverge.

Of course the above explanation is entirely speculative and can not be confirmed with the data gathered for this project. It would however explain the large amount of divergence and the fact that this can happen in both directions. The fact that the effect is so extreme makes this an interesting topic for future research.

Chapter 6

Conclusion

While the complex aerodynamics of the VRS for helicopters has seen quite some scientific attention in the past decades, the in a sense comparable propwash effect found in small scale quadcopter flight has not. The experiments and theory described in this report were initially suspected to support an more scientific explanation for the causes for and mechanics behind the propwash effect. Unfortunately, this is hardly the case. However, the model that was proposed and the experiments that were performed definitely give some major insight into what is likely to contribute to any oscillations, what is likely not to contribute, and why isolated rotor aerodynamics might contribute a lot less to the propwash effect than initially thought.

Arguably, the backbone of the proposed model is the isolated rotor wind tunnel data. This data reveals that the mathematically defined borders between the pre-VRS and VRS, and between the TWS and the WMS are located at constant advance ratio lines. This suggests that modeling rotor aerodynamics in the propwash effect might be more convenient as function of advance ratio and total blade velocity, rather than descent speed and rotor rotational speed. From the data it can be seen that there is indeed a notable drop in thrust and drag toque in the VRS region. This drop also follows the structure of the constant advance ratio lines.

The VRS also seems to be area of highest intensity of thrust fluctuation. In the VRS it seems to be the case that an increase in rotor rotational speed drastically increases the thrust fluctuations. Contrary to the absolute thrust values, the thrust fluctuations also occur in the pre-VRS. That is, as soon as the descent speed becomes positive, thrust fluctuations can be observed. Interestingly enough, outside the VRS and inside the assumed TWS and WMS, the fluctuation is similar as found for the rotor in its normal operating state, which is very small. Similar conclusions can be drawn for the measured drag torque.

For the proposed model the derivatives of thrust and torque with respect to rotor rotational speed and descent speed are relevant. The value for f_σ generally increases as rotor rotational speed is increased. There is however a region of low values for f_σ at the boundary of the VRS and TWS. This effectively decreases the overall flight controller gain in this region for roll and pitch rate. On the other hand, the value does not become negative. Explanations of the propwash effect that are based on the sudden loss of lift due to blade stall are therefore unlikely to be correct. A positive value of f_v causes the quadcopter to theoretically be a stable system, since this opposes any roll or pitch rota-

tion. This derivative appears to be low in the VRS, but high when approaching TWS. The impact of this derivative on model behaviour is generally overshadowed by the authority of the flight controller. Finally, n_σ is similar in hover compared to the VRS, but drops notably in the TWS. This indicates the relevance of the TWS besides the more commonly known VRS.

After modeling the different components of the quadcopter, a model can be constructed which has 11 states. When the rotational speeds of all rotors are equal, the model suggests that all attitude rates are uncoupled, which means the dynamics in roll, pitch and yaw can be modeled independently. However, when the rotor rotational speeds are not equal, the roll and pitch axis can show quite some coupled behavior. This is not only due to gyroscopic effects and different motor transient responses, but also to the fact that each rotor operates at points with different thrust and torque derivatives.

The poles of the model definitely move around as the descent speed is changed or the rotor rotational speeds are varied. For the roll and pitch axis, the poles mainly indicate a damped natural frequency that is quite variable. For hover conditions it can be stated that higher rotor rotational speeds are related to higher natural frequencies. For descent speeds that are non-zero this relation does not hold anymore. The damping ratios are also not constant, but these are not as variable as the natural frequency. The model indicates that there are no conditions where either the roll or pitch axis becomes unstable. The yaw axis behaves relatively similarly with the exception that the natural frequency is lower and the damping ratio is on average a lot higher. Furthermore, for the yaw axis there seems indeed to be a point where the model becomes unstable. This happens at speeds of around $25\,\mathrm{m\,s^{-1}}$ and rotor rotational speeds of roughly $14\,000\,\mathrm{rpm}$. Since this is quite on the edge of the flight envelope, this instability could not be confirmed during flight tests or wind tunnel tests.

Tweaking the control gains of the flight controller reveals that the placement of the characteristic poles is primarily dependent on the P and D gains. The model suggests that for hover, increasing either parameter increases the damping ratios of roll and pitch. Of course this comes at the price of increased control effort. Again, for non-zero descent speeds such a relation does not hold anymore. Changing the I gain on the other hand did not influence the position of the characteristic poles nearly as much as changing P and D gains.

To evaluate the performance of the model, simulations of the model were compared to flight data. Unfortunately only experiments could be done for a part of the flight envelope due to practical limitations. Comparison between the model and the flight data reveals that center and peak frequencies for the roll and pitch axis are on average estimated reasonably accurately by the model. This indicates that the dynamics of the quadcopter as incorporated by the model are likely to be very determinative for which frequencies are dominant during the propwash effect. Unfortunately, the error between the estimated frequencies and measured frequencies shows quite some variance. It is hard to say with certainty how much of this variance is due to inaccuracies in the model or limitations of the experimental data, such as the relatively short measurement times of the descents during flight testing. The frequencies estimated for the yaw axis are rather inaccurate. This could partly be caused by the high sensitivity of the yaw rate to rotor imbalances.

This means the PSDs of the yaw rate get polluted by vibrations that are caused by the rotor vibrations, rather than dynamics that are captured by the model.

Model simulations were also compared to wind tunnel test where the quadcopter was mounted in a gimbal. Interestingly enough, the errors between the model estimated frequencies and the frequencies according to the data were larger when compared to the errors found for the flight tests. It is suspected that this has to do with the dynamics of the gimbal mount itself since the higher frequencies of the power spectral density of the wind tunnel data consistently contained more power than when compared to flight test data.

Both the flight tests and wind tunnel tests reveal however that the overall intensity of the oscillations around all axes is drastically underestimated by the model. The estimated power of the roll, pitch and yaw rate signals are often orders of magnitude smaller what the data suggests. The model uses the thrust and torque fluctuations measured for the isolated rotor wind tunnel tests as input. This strongly suggests that the thrust and torque fluctuations experienced by a rotor in isolation contribute in fact only fractionally to the attitude oscillations experienced during the propwash effect. This is somewhat confirmed by the test where the drone is placed inside a gimbal with disabled controller. Comparing the data of this experiment with isolated rotor data also shows that the oscillations in attitude are much larger than what can theoretically be caused by fluctuations in thrust and torque for an isolated rotor.

In chapter 1 a set of research questions was formulated. Below the questions are repeated and accompanied by their respective answers, which are based on the knowledge gained during this study.

1. *What selection of the rotor forces and moments are worth measuring, considering practical limitations of the test stand?*

   In general, the interesting forces that work on the rotor are the thrust force and hub forces, and the interesting moments are the roll moment, pitch moment and torque. To reduce the scope of the project, it was decided to only consider perfect axial decent. Due to symmetry reasons, it makes sense in this case to only measure the thrust force and torque. This decision was reinforced by the fact that the already available Tyto test stand could be used, which significantly decreased the time and resources needed to construct the test setup.

2. *What variables need to be measured during isolated rotor experiments that are not forces or moments?*

   For the isolated rotor experiments, it appeared crucial to measure the rotor rotational speed, as well as the wind speed, since these primarily affect the rotor thrust and torque. Furthermore, it appeared important to measure the ESC input signal to verify that the ESC maps it input signal to a rotor rotational speed in a close to linear way. Battery voltage was also recorded in order to account for battery sag and depletion. For experiments with the quadcopter in its entirety, it turned out that measuring gyroscope attitude rates and rotor rotational speed were sufficient for most experiments. For troubleshooting, it appeared convenient to record the controllers P, I and D term outputs as well. For actual flight tests, it appeared

necessary to record barometer altitude and accelerometer data in order to estimate the descent speed.

3. *Given the available resources, what test stand is appropriate to measure the selected variables?*

   Since it was decided to only measure thrust and torque, the Tyto test stand was used as measuring device for experiments with the rotor in isolation. This decision was reinforced by the fact that this stand was already available. Besides this there was already quite some experience with this device within the faculty, allowing for quick trouble shooting and repairs.

4. *Given the available resources, what wind tunnel test setup would allow for measuring the stochastic nature of the rotor forces and moments to an extent that is relevant for quadcopter control?*

   The only downside of the Tyto stand appeared to be the low thrust and torque measurement rate of roughly 5 Hz. Some thought was initially put into the concept recording these variables at a much higher rate. This equipment, allowing precise measurements at a high frequency for a rotor this small was not directly available. Making a custom stand was quickly deemed to difficult with the given time constraints. This had to do with the fact that the stand dynamics itself become relevant when looking at the individual frequency components at such a high frequency range. Making a stand that is stiff enough, has little interference with the rotor aerodynamics and still works with simple bar load cells is a difficult problem in itself and was therefore not pursued.

5. *What independent variables need to be varied during the isolated rotor experiment and over what range?*

   To reduce the scope of the project it was decided to only consider pure axial descent, so no varying angle of attack. For the isolated rotor tests, this left only the speed and rotor rotational speed as dependent variables. Some test flights revealed that during the performance of some common aerobatic manoeuvres the rotor rotational speeds only rarely exceeded 20 000 rpm, which is why this speed was chosen as upper limit for rotor rotational speed. The lower limit of 3000 rpm was largely determined by the Tyto test stand, which had trouble recording measuring rotor rotational speed under 3000 rpm. Furthermore this speed matched well with common idle speeds used in Betaflight. The largest wind speed of $25\,\mathrm{m\,s^{-1}}$ was primarily determined by the maximum speed of the OJF. The amount of steps that were used for the wind speed and rotor rotational speed was picked based on the available amount of time in the wind tunnel. The aim was to have roughly the same amount of steps along the wind speed axis as the rotor rotational speed axis.

6. *What model structure is best suited to implement in simulation of the rotor dynamics?*

   It appeared quickly that the data could not be estimated accurately enough by a single multivariate polynomial due to computational errors that become to large when taking a polynomial order that is to high. Therefore Simplex B-splines were used which do not have this constraint. Furthermore, the latter is very effective in dealing with scattered data and allows for the possibility of using a courser

triangulation grid in areas where less fidelity is needed, such as when the rotor is in its normal operating state. This last advantage is not exploited in this report.

7. *Could a the controller use the rotor model as a static mapping from required force to required rotor rotational speed?*

   It has become clear that the so called thrust and torque curves definitely undergo a lot of change when the rotor operates in axial descent. However, it has also be shown that generally these curve differences should not change the quadcopters stability to a high degree. Only for very specific speed and rotor rotational speed combinations, calculations show that the quadcopter might be unstable. However, it has also been shown that other effects are at play which make the dynamics of the quadcopter deviate significantly form what would expected based on isolated rotor characteristics. Although a static mapping could be used to correct for the deviation of thrust and torque curves, it remains unclear at this point how the local wind speeds vary at each rotor, and whether this can even be captured by a single number. It is therefore difficult to say at any time on what thrust or torque curve each rotor is operating, making the inclusion of these curves in the controller difficult.

8. *What sensor data would be needed by the controller to function properly?*

   If it is assumed that the rotors operate in isolation, the wind speed and rotor rotational speed need to be known. This report has only focused on pure axial descent. In reality the quadcopter as a certain angle of attack, which could greatly influence the results presented in this document. This angle of attack then also needs to be known. However, it has been discussed how rotor-rotor interaction is likely to dominant to ignore in this flight condition. The mechanics of this interaction are still poorly understood, making it difficult to say what variables need to be measured by the controller to get an estimation of the 'state' of this interaction at any point in time.

9. *How can knowledge of the estimated model potentially be used in the design of quadcopter controllers?*

   The only concepts that could directly be applied to the flight controller design at this point is probably the change thrust and torque curves, and the knowledge of at what speeds and rotor rotational speeds the most fluctuation occurs of thrust and torque. Assuming the quadcopter is in pure axial descent, and the descent speed is known, then the thrust and torque curves could be used to correct the controller gains. Furthermore, at conditions were thrust and torque fluctuations occur, controller gains can be adjusted. For example, D-gains can be reduced in this fluctuation region to avoid motor overheating, allowing a higher D-gain at other flight conditions.

It can then be concluded that isolated rotor aerodynamics, variable motor transient responses, gyroscopic effects, reaction torque effects and airspeed of rotors due to attitude rates, at most cause the frequencies of the propwash effect to be more dominant around a specific range of frequencies. On the other hand, either one of these concepts or a combination of them are most certainly not the main cause for oscillations during the propwash effect. Modeling these concepts based on actual measurement data shows that the resulting oscillations are up to orders of magnitude smaller than the oscillations

found in real life.

Chapter 7

Recommendations

The question then remains what the excessive vibrations during the propwash effect are caused by. The most logical next step would be to consider the rotor to rotor interaction. It is not hard to imagine that the turbulent wake of one rotor is ingested by another rotor, which could greatly amplify the thrust and torque fluctuation generated by the latter rotor enormously. Of course, the interaction between four rotors rotating at different speeds is quite a challenge to understand, let alone model. In chapter 1 some studies were mentioned that performed aerodynamic analyses of two small scale rotors operating close to each other. Unfortunately these studies only considered cases with the rotors rotating equally fast. It would be very interesting to perform the same experiments, but with different rotor rotational speeds. This would already give great insight in the possible operation of four rotors in close proximity. Based on the findings in this report, it is recommended to first gain a thorough understanding of the interaction effects in a simple and controlled environment before attempting to comprehend the propwash effect of a quadcopter as a whole.

An unexpected founding of this study is the diverging rotor speed effect discussed in section 5.3. This effect also hints at the fact that the propwash effect might in fact be far more complex than the sum of four individual rotor characteristics. To shed more light on this topic, a potential approach would be to start looking at the interaction between two rotors at different rotor rotational speeds, and see if similar effects occur. Something that would also shed much more light on this topic is placing four rotors in a wind tunnel and analysing the flow when two diagonally opposed rotor pairs are given more rotational speed than the other pair. If possible, measuring the yaw moment on the combination of the four rotors while performing this experiment would give additional valuable information. Luckily the effect seems to be easy to reproduce since it happens in a wide range of rotor rotational speeds and is straightforward to measure.

Part II

Scientific Paper: Assessing the Contribution of Isolated Rotor Aerodynamics to Quadcopter Attitude Oscillations in Axial Descent

Abstract

This study aims to quantify the aerodynamic behaviour of fixed pitch rotors with a diameter of 12.7 cm in axial descent, and its contribution to the attitude oscillations found for quadcopters under similar flight conditions. Wind tunnel tests are performed with an isolated rotor, as well as a complete quadcopter mounted inside a gimbal that allows for roll and pitch motions. Isolated rotor wind tunnel tests show that thrust and torque fluctuations manifest in the pre-vortex ring state, but peak in the vortex ring state. The derivatives of thrust and torque with respect to airspeed remain positive in ranges from $0\,\mathrm{m\,s^{-1}}$ to $25\,\mathrm{m\,s^{-1}}$ and 3000 rpm to 20 000 rpm. Comparison of these results with measured quadcopter motions reveal that isolated rotor characteristics only partly explain the attitude oscillations found for quadcopters in axial descent.

Chapter 8

Introduction

In the past decade the popularity of small scale quadcopters as UAVs has drastically increased. These quadcopters distinguish themselves from other UAVs by their ability of vertical take off and landing, their ability to hover efficiently [2] and above all their potential for incredible maneuverability. Their parts are cheap, making them in their entirety cheap to manufacture and service [3, 4]. Also, their inherent flexibility, robustness and accessibility allows these rotorcraft to be effective tools in surveying, transportation, research, disaster risk management, humanitarian work [5] and many more.

This surge in popularity has continuously been mirrored by the amount of research that has been done on the topic of improving flight characteristics of quadcopters. The majority of studies rely on models assuming small airspeeds [23, 1, 24, 25], which allows for modelling thrust curves as static quadratic functions [23, 26]. Many quadcopters use a simple PID controller that is optimized for the hover condition, which is characterised by small aerodynamic interaction between the rotors [6]. However, when speeds increase, a variety of complex aerodynamic effects become more dominant [7, 8]. This causes a linear controller with fixed gains to be an inadequate solution to retain the stability and maneuverability that the quadcopter can theoretically have at these speeds [9]. One area of research is therefore the design of more advanced control of quadcopters. Consequently, this raises the need for a better understanding of system dynamics at these speeds.

This study revolves around the flight condition where the velocity vector points points towards the underside of quadcopter. In this flight condition the rotor is set up in a way to blow against the direction of the external airflow. The behavior of an isolated rotor in this flight condition has been extensively researched for helicopter flight [10, 11], as it is usually characterized by excessive vibration and thrust fluctuations. Standard procedure for most larger rotorcraft has therefore been to keep the rotors out of this state where possible [12, 13].

Unsurprisingly, these severe oscillations during downward velocities are also commonly found for quadcopter flight, especially during the performance of more aggressive flight manoeuvres. Analogous to the strategy for helicopters, multiple studies have focused on motion planning algorithms to avoid this part of flight envelope [12, 13]. These algorithms use models predicting in which flight states the VRS (vortex ring state) can occur [14]. For example, instead of descending in a straight vertical line, the quadcopter can descent while following a spiral trajectory [15]. The interesting option of giving the

quadcopter a high yaw rate during a vertical descent has also been shown to be effective in avoiding the VRS [14], because this way all rotors have an edgewise velocity component.

Other studies have focused on the interaction effects of two small scale rotors in axial descent while operating in each others vicinity. Here attention is given to the behaviour of the flow [16], and its impact on thrust forces [17, 18]. In these studies the two rotor rotational speeds are kept equal and constant. Quadcopter flight is likely much more complicated than this as there are four rotors which rotational speeds are continuously varied by the controller. Since rotor interaction affects quadcopter attitude, the controller and aerodynamics are coupled in a complex feedback loop.

The oscillations experienced by small scale quadcopters are often attributed to the characteristics of a rotor in the VRS. As of writing, no research could be found that investigates the relation between the characteristics of an isolated rotor that operates in the VRS and the severity of the oscillations found during actual quadcopter flight. The study presented in this paper aims to shed more light on this topic. This is done by placing both an isolated rotor as well as a complete quadcopter inside a wind tunnel. Analysing the data produced by the former experiment already gives great insight in possible causes for oscillations found for quadcopters in axial descent. Measuring the roll and pitch oscillations of the complete quadcopter in the wind tunnel allows for reconstructing the thrust that works on each of the four rotors. This can then be compared to the isolated rotor wind tunnel test results to asses how much of the attitude oscillations are actually due to these isolated rotor characteristics.

Chapter 9

General definitions and rotor operational states

To quantify vectors, the body frame is used as a frame of reference, which is shown in Figure 9.1. This frame rotates as if attached to the quadcopters airframe. The x-axis of this frame points towards the front of the quadcopter, the y-axis to its right side and the z-axis towards its bottom. Rotational speed around the x-axis is referred to as roll rate, rotational speed around the y-axis as pitch rate, and rotational speed around the z-axis as yaw rate.

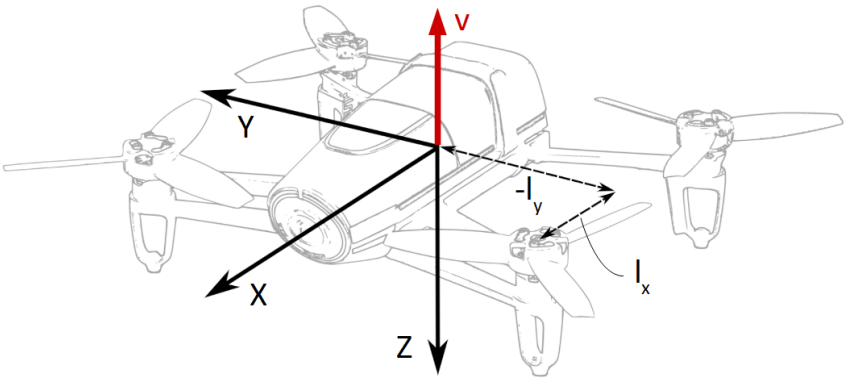

Figure 9.1: Body frame drawn on a Parrot Bebop quadcopter. (from [1], modified)

In Figure 9.1 a vector is also indicated in dark red which refers to the speed of the air with respect to the quadcopter. It is assumed that this vector remains close to parallel with the z-axis. The z-axis component of this vector is equal to $-v$. This means that a positive value for v refers to the situation where the rotors are blowing against the direction of the external airflow, which corresponds to a quadcopter in axial descent. Furthermore, the values l_x and l_y are used to indicate the positions of the rotor rotation axes. The (x, y) position of rotors one, two, three and four in the xy-plane of the body frame are $(l_x, -l_y)$, $(-l_x, -l_y)$, $(-l_x, l_y)$ and (l_x, l_y), respectively.

According to literature a rotor can operate in a couple of different states that each have different aerodynamic characteristics. When the speed v is negative, the rotor is in its normal operating state. As one would increase this speed starting at a speed of $0\,\mathrm{m\,s^{-1}}$, one would encounter the pre-VRS, the VRS, the TWS (turbulent wake state)

and the WMS (windmilling state), and in that order. The normal operating state, VRS, TWS and WMS are presented schematically in Figure 9.2a, Figure 9.2b, Figure 9.2c and Figure 9.2d, respectively. In these figures, i is the induced velocity of the rotor, w is the decrease of air speed in the far wake, A is the rotor disk area and f is the thrust force that works on the rotor.

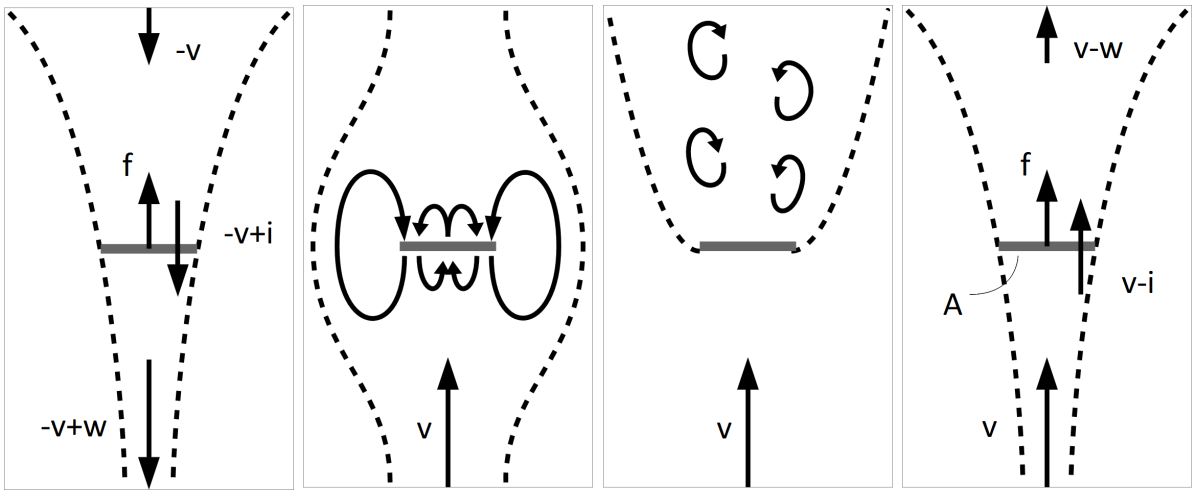

(a) Normal state (b) VRS (c) TWS (d) WMS

Figure 9.2: Operating states of a rotor.

The names of the mentioned rotor operational states are based on the characteristic behavior of the air around the rotor in that particular state. However, momentum theory can be used to define more theoretical border between the pre-VRS and VRS, and between the TWS and WMS, which is convenient for the interpretation of wind tunnel measurements in subsequent sections.

Taking Figure 9.2d as a reference, the mass flow during windmilling, $\dot{m}_{wm}$, through the rotor can be expressed as shown in Eq. 9.1, where ρ is the density of the air. Furthermore, comparing the flow properties way below the rotor with the flow way above the rotor by applying the laws of conservation of momentum and energy results in Eq. 9.2 and Eq. 9.3, respectively.

$$\dot{m}_{wm} = \rho A(v - i) \tag{9.1}$$

$$f = \dot{m}v - \dot{m}(v - w) = \dot{m}w \tag{9.2}$$

$$f(v - i) = \frac{1}{2}\dot{m}v^2 - \frac{1}{2}\dot{m}(v - w)^2 \tag{9.3}$$

Combining Eq. 9.2 and Eq. 9.3 gives $w = 2i$. Its not difficult to see that the higher the thrust f, the more the air is slowed down and thus the higher w. However, its not possible for w to become larger then v, since then the air speed in the far wake would reverse and the flow model no longer holds. At the thrust f where $v = w$, the rotor is assumed to transition from the WMS to the TWS. At this point $f = f_{t1}$. Filling in $v = w$

into Eq. 9.2 results in Eq. 9.4.

$$\begin{aligned} f &= \dot{m}_{wm} w \\ &= \rho A (v - \frac{1}{2} w) w \\ f_{t1} &= \rho A (v - \frac{1}{2} v) v \\ &= \frac{1}{2} \rho A v^2 \end{aligned} \tag{9.4}$$

For the normal operating state, Eq. 9.2 and Eq. 9.3 are exactly the same if the sign conventions shown in Figure 9.2a are used. However, the mass flow is now positive in the opposite direction. That is $\dot{m}_{no} = -\dot{m}_{wm}$, where $\dot{m}_{no}$ is the mass flow for the normal operating state.

As mentioned, the transition between the normal state to the pre-VRS happens when the airflow v becomes positive. In this pre-VRS state the flow model of Figure 9.2a is technically incorrect, but in practice the model equations hold up quite well when $v < i_{v=0}/2$ [11], where $i_{v=0}$ is the induced velocity the rotor would generate at the same thrust level but with zero external airspeed $v = 0$. The thrust at $v = 0$, $f_{v=0}$, can be related to $i_{v=0}$ using Eq. 9.2, as is shown in Eq. 9.5.

$$\begin{aligned} f &= \dot{m}_{no} w \\ &= 2\rho A (i - v) i \\ f_{v=0} &= 2\rho A i_{v=0}^2 \\ i_{v=0} &= \sqrt{\frac{f_{v=0}}{2\rho A}} \end{aligned} \tag{9.5}$$

The rotor is assumed to transition from the pre-VRS to the VRS once f reaches a value as is shown in Eq. 9.6, where the result of Eq. 9.5 is substituted into $v = i_{v=0}/2$. At this point $f = f_{t2}$.

$$\begin{aligned} v &= i_{v=0}/2 \\ v &= \frac{1}{2} \sqrt{\frac{f}{2\rho A}} \\ f_{t2} &= 8\rho A v^2 \end{aligned} \tag{9.6}$$

Momentum theory does not say anything about what happens to the thrust and induced velocity in the VRS and the TWS. Assuming a constant air speed v, its therefore only possible to state the following.

- Starting in the WMS and increasing rotor rotational speed, a mathematically defined TWS is reached when the thrust increases to a value of $f_{t1} = \rho A v^2/2$.
- Starting in the pre-VRS and decreasing rotor rotational speed, a mathematically defined VRS is reached when the thrust decreases to a value of $f_{t2} = 8\rho A v^2$.

Chapter 10

Experimental Setup

For this study two types of wind tunnel experiments were performed. For the first experiment a separate rotor mounted to a BLDC motor was placed inside a wind tunnel under axial descent conditions. For the second experiment the quadcopter was placed inside a gimbal like structure and placed in a wind tunnel in a similar way. Here the quadcopter was stabilized by elastic bands allowing the flight controller to be turned off.

10.1 Quadcopter specifications

A custom build quadcopter was used as the basis for all experiments. This quadcopter was build using a carbon fibre TBS Source One V4 frame and four Emax Eco II series 2207 motors, which were rated at 2400 kV and had 14 poles. The motors were equipped with three bladed HQProp 5x5x3 rotors which had a diameter of 12.7 cm (5 inch). A Kakute f7 v1.5 flight controller was used in conjunction with an MPU6000 V1.2 IMU unit. Betaflight V4.2.9 was installed as flight controller firmware. To read rotor rotational speed, bidirectional DShot600 was used. For the quadcopter an Aikon AK32 V3 55A 4in1 6S ESC (electronic speed control) unit was used running BLHeli32 firmware, where some of the relevant settings are shown in Table 10.1. Electronics were powered by a Tattu Funfly 1300MAH 100C 6S lithium polymer battery. The motor idle setting of 2.5 % corresponded roughly to 2700 rpm, and at maximum throttle setting a rotational speed of roughly 33 000 rpm could be reached in hover conditions. Finally, to control the quadcopter a RadioMaster Zorro transmitter was used with a TBS crossfire module.

Table 10.1: BLHeli32 ESC settings.

Name	**Setting**	**Name**	**Setting**
Ramp up power	40 %	Temperature protection	140 °C
Low RPM Power Protect	On	Low Voltage Protection	Off
Sine Modulation Mode	Off	Stall Protection	Normal
Demag Compensation	Low	Motor Timing	16°
Maximum Acceleration	Maximum	Auto Telemetry	Off
SBUS Channel	Off	Minimum Throttle	1040
Maximum Throttle	2000	Center Throttle	1500
Brake On Stop	80 %	Non Damped Mode	Off
PWM Frequency Low	48 kHz	PWM Frequency High	48 kHz

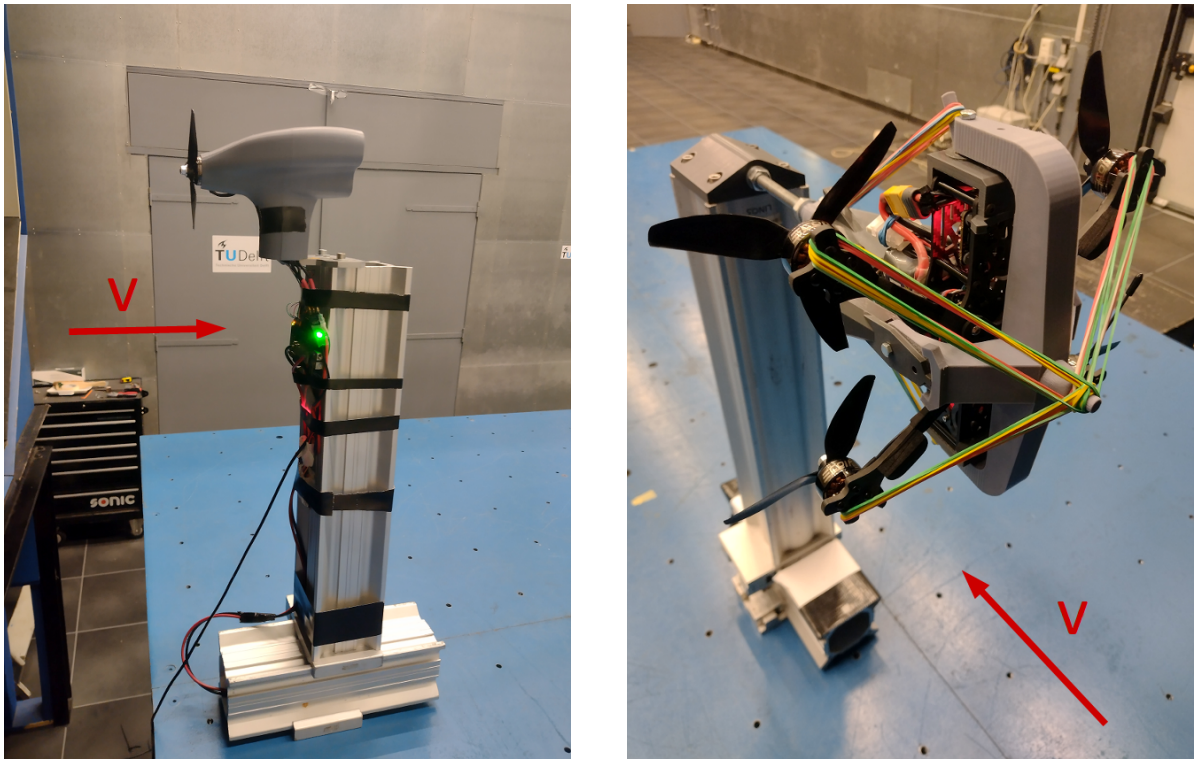

(a) Test setup for measuring isolated rotor thrust and torque.

(b) Test setup for measuring quadcopter movements while suspended in a gimbal.

Figure 10.1: Test setup of wind tunnel tests.

10.2 Isolated rotor in wind tunnel

For this experiment a rotor was placed inside a wind tunnel as is shown in Figure 10.1a. The wind tunnel that was used is the Open Jet Facility which is run by Delft University of Technology. The tunnel was operated with a temperature and air density of 19 °C and 1.20 kg m^{-3}, respectively.

The thrust, torque and rotational speed of the rotor was measured at a frequency of 5 Hz using 'series 1585 thrust stand' from Tyto Robotics. The motor was powered using the same 6S lithium polymer battery as mentioned in section 10.1. An aerodynamic fairing was made around the thrust stand to reduce aerodynamic forces working on the stand itself which inherently added to the thrust measurements, and to reduce any interaction effects between the rotor and the stand. Aerodynamic forces working on the fairing did not influence the measured thrust and torque. The fairing was designed using Catia V6 and 3D-printed using a stock Creality 3D Ender 3 V2.

Thrust and torque was measured over a period of 20 s. Wind speeds were set at -25 m s^{-1} to 25 m s^{-1} in steps of roughly 3 m s^{-1}, including 0 m s^{-1}, and rotor rotational speeds were set at 3000 rpm to 20.000 rpm with steps of 1000 rpm. Testing at 17 wind speeds and 18 rotor rotational speeds for 20 s equals 1 h42 min of data recording time. For negative speeds the rotor was flipped and the motor speed was reversed. An ESC was used with the same settings as listed in Table 10.1.

10.3 Gimbal tests with elastic bands

For this experiment the quadcopter was mounted in a gimbal as is shown in Figure 10.1b. This gimbal was designed in Catia V6 and produced using a stock Creality 3D Ender 3 V2. Ball bearings with an outer diameter of 12 mm were used to reduce friction around all axes. For this test the yaw axis was fixed, only allowing roll and pitch movement over a range of motion of 18°. The PID control gains in Betaflight were set to zero, practically turning off the flight controller. The rotational speeds of the rotors could collectively be set using the transmitters throttle channel. Multiple wind tunnel experiments were performed with differing rotational speeds of the four rotors. During each experiment the rotational speed was kept constant. Between experiments this rotational speed was increased. Note that all four rotors rotated at the same speed at any time. Rubber bands were used to keep the quadcopter centered in the gimbal while still allowing movement of the quadcopter. Pitch and roll rate were recorded on the onboard SD card at a frequency of almost 1000 Hz.

With the wind tunnel turned off, the quadcopter was pulled manually to an extreme orientation in the gimbal and released in order to let the elastic bands move the quadcopter back to its neutral orientation. The pitch and roll rates that were measured during the resulting oscillation could later be used to model the complete system as a damped mass spring system. After this system identification test, measurements were performed with rotor rotational speeds ranging from 3000 rpm to 20 000 rpm in steps of 1000 rpm and four wind tunnel speeds, namely $10\,\mathrm{m\,s^{-1}}$, $15\,\mathrm{m\,s^{-1}}$, $20\,\mathrm{m\,s^{-1}}$ and $25\,\mathrm{m\,s^{-1}}$.

The procedure above allowed for reconstructing the forces and moments that work on the combination of all rotors based on the measured pitch and roll rates, without the rotors changing speed. Since the data was recorded at 1000 Hz, possible dominant thrust or torque oscillations could be identified with a frequency of up to 500 Hz.

Chapter 11

Data Processing and Experimental Results

This section covers the direct results of the experiments discussed in chapter 10, as well as some techniques used to process and interpret the data.

11.1 Isolated rotor average thrust and torque

The recorded wind tunnel data consists of a set of thrust and torque measurements at various wind and rotor rotational speeds. To aid in visualization and interpretation of this obtained data, multivariate simplex B-splines [20, 21] were used to approximate the obtained data. This type of estimation uses a set of local polynomial basis functions which estimate the data only in a small domain of the independent variable space. This allows for keeping the order of the polynomials low, removing common issues found with global polynomial basis functions.

An important aspect of multivariate simplex B-splines is the triangulation of the independent variable domain. For this application the interval of the rotor rotational speed ω was divided into four equal intervals and the wind speed v into five equal intervals. A Delaunay triangulation was then applied to the resulting grid, which resulted in 40 triangles with equal size. The simplex B-spline estimation is further characterised a polynomial order of five and the smoothness parameter of $l = 2$. A smoothness value of $l = 0$ means the zero'th derivative at the border of each neighboring simplex is made equal. A value of $l = 1$ means the zero'th and first derivative these borders is made equal, and so on.

In Figure 11.1 the simplex B-spline that represents the thrust generated by the rotor at different speeds v and rotor rotational speeds ω is visualized. This thrust is the average thrust measured over the 20 s interval at which the wind speed and rotor rotational speed are kept constant. In Figure 11.1b the spline is plotted in three dimensions. In Figure 11.1a a heat map of the same simplex B-spline is shown, which can be regarded as a top view of Figure 11.1b. In this heat map the lines of constant advance ratios μ are also indicated. Here μ is defined as shown in Eq. 11.1, where R is the rotor radius in meter and ω the rotor rotational speed in $\mathrm{rad\,s^{-1}}$. Furthermore, the boundaries between the different operating states of the rotor are indicated with the dashed lines. The upper dashed line, which corresponds to f_{t1}, indicates the transition between the TWS and WMS. The area above this line covers the TWS. The lower dashed line corresponds to

f_{t2}, meaning that the area between this line and the line $\mu = 0$ represents the pre-VRS.

$$\mu = \frac{v}{\omega R} \tag{11.1}$$

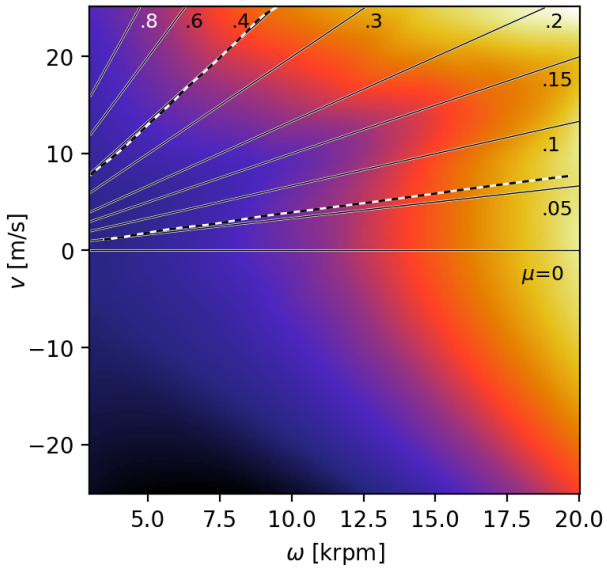

(a) Heat map of thrust as function of descent speed and rotor rotational speed. Upper and lower dashed lines indicate f_{t1} and f_{t2}, respectively.

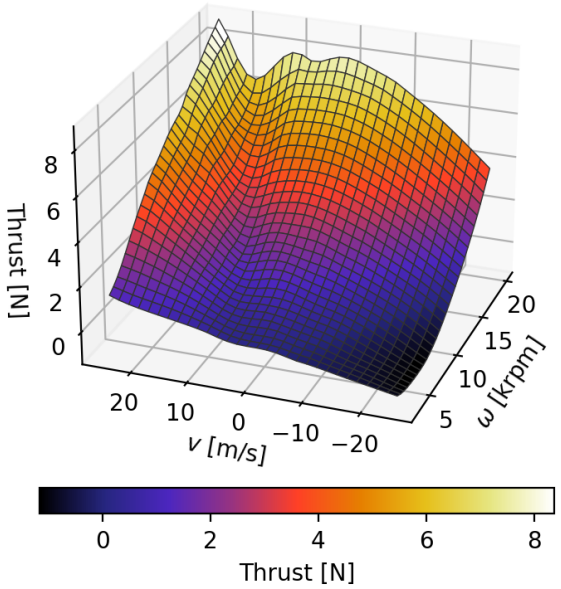

(b) 3D view of the simplex B-spline capturing thrust as function of descent speed and rotor rotational speed.

Figure 11.1: Estimated thrust data for the isolated rotor. Positive speeds refer to the rotor in axial descent.

Several interesting aspects can be noticed from Figure 11.1. First of all, the boundaries between the theoretical rotor operating states lay on constant advance ratio lines. Secondly, there is a drop in thrust at an advance ratio of roughly $\mu = .14$. This is characteristic behaviour of a rotor in the VRS, since the power required to generate the large vortices reduce the power that is left to generate thrust. This drop in thrust also seems to happen at a very constant advance ratio.

In Figure 11.2 the simplex B-spline is shown for the measured average torque that is experienced by the rotor. It can be noticed that in the VRS the required torque is clearly lower than for other rotor operating states. This is again expected because the vortices reduce the angle of attack of the blades and therefore a reduction of drag can be seen.

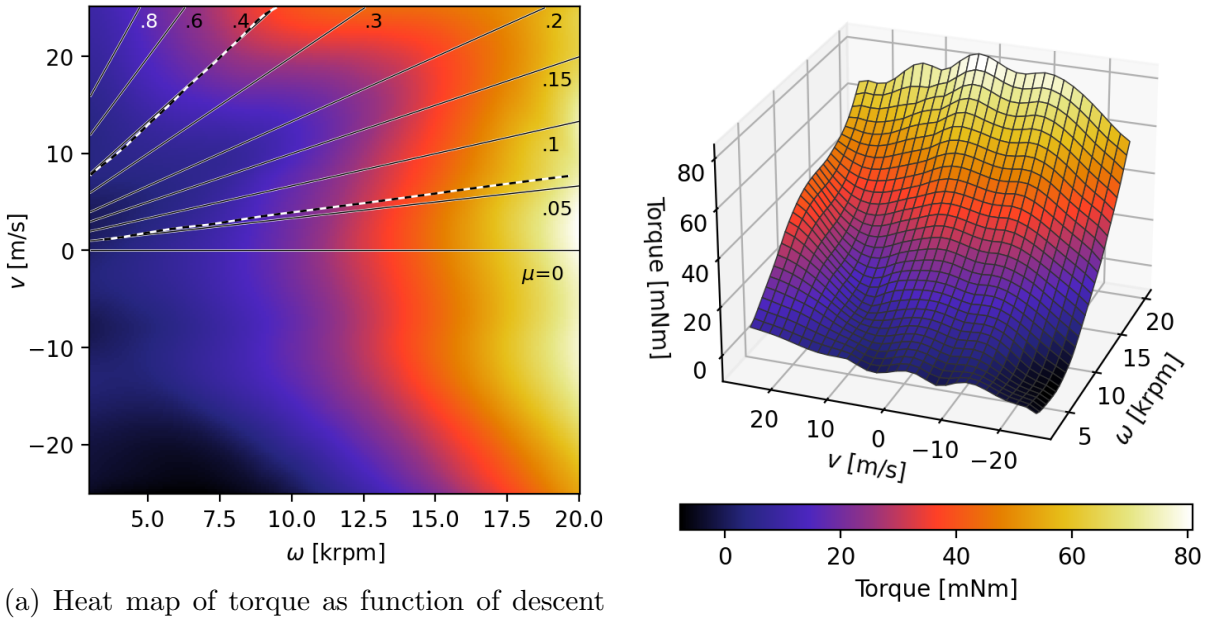

(a) Heat map of torque as function of descent speed and rotor rotational speed. Upper and lower dashed lines indicate f_{t1} and f_{t2}, respectively.

(b) 3D view of the simplex B-spline capturing torque as function of descent speed and rotor rotational speed.

Figure 11.2: Estimated torque data for the isolated rotor. Positive speeds refer to the rotor in axial descent.

11.2 Isolated rotor variation in thrust and torque

As with the average measured thrust and torque, the measured standard deviations of thrust σ_f and torque σ_n can also be modelled using simplex B-splines. To do this, first each measurement period of 20 s where the wind speed and rotor rotational speeds are held constant is used to calculate a single value for σ_f and σ_n. Each standard deviation is thus calculated using roughly $20\,\mathrm{s} \cdot 5\,\mathrm{Hz} = 100$ measurements samples. Doing this for each wind speed and rotor rotational speed combination results in a data set which can be used to construct a simplex B-spline. Note that this data set is roughly 100 times smaller than the amount of measurements.

Simplex B-splines use a form of constrained least squares to minimize the model residues globally. However, for estimation of standard deviations it is convenient if the residues are made smaller in regions where the measured standard deviations are also small. This is first of all to avoid the spline to accidentally become negative at locations with small values of standard deviation. Secondly, the standard deviations are later visualized in a plot with a logarithmic scale. It is therefore more appropriate to minimize a cost function related to the ratio of model residue to absolute data point value, rather than just the residue value. To do this, the measured values of σ_f and σ_n are first transformed to a log-space, so $\hat{\sigma}_f = \log_{10}(\sigma_f)$ and $\hat{\sigma}_n = \log_{10}(\sigma_n)$. Simplex B-splines are then estimated for $\hat{\sigma}_f$ and $\hat{\sigma}_n$. The estimated values of σ_f and σ_n can be retrieved by using $\hat{\sigma}_f$ and $\hat{\sigma}_n$ as exponent. That is, $\sigma_f = 10^{\hat{\sigma}_f}$ and $\sigma_n = 10^{\hat{\sigma}_n}$, where $\hat{\sigma}_f$ and $\hat{\sigma}_n$ are estimated by the spline.

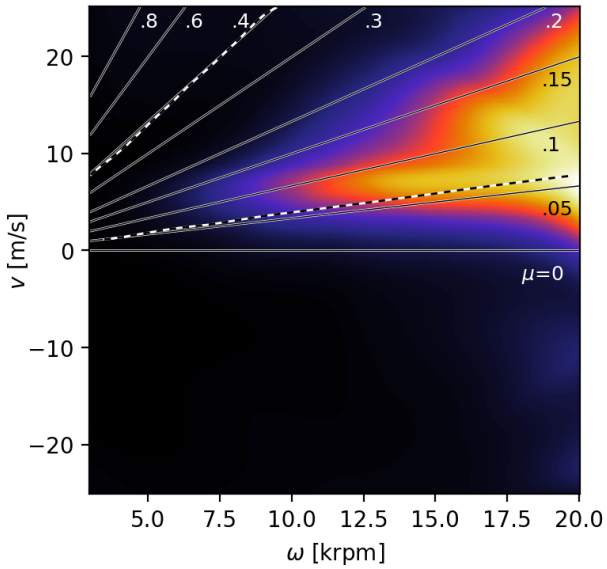

(a) Heat map of thrust standard deviation σ_f as function of descent speed and rotor rotational speed. Upper and lower dashed lines indicate f_{t1} and f_{t2}, respectively.

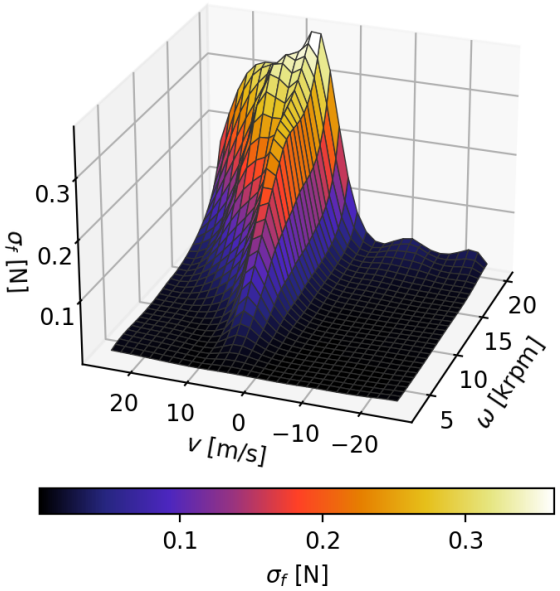

(b) 3D view of the simplex B-spline capturing thrust standard deviation as function of descent speed and rotor rotational speed.

Figure 11.3: Estimated thrust standard deviation for the isolated rotor. Positive speeds refer to the rotor in axial descent.

In Figure 11.3 the spline is shown that approximates $\sigma_f(\omega, v)$. For this spline similar parameters were used as described in section 11.1. In accordance with general literature, it can be observed that the most excessive fluctuations occur in the region that is assumed to be the VRS. However, it seems that these fluctuations also occur at very low advance ratios (μ). It can thus be stated that the rotor behaves relatively normally in the pre-VRS state when it comes to average thrust generation, but excessive thrust fluctuations already start as soon as the airspeed deviates from zero. For $\mu > .2$, which is thought to roughly correspond to the transition of the VRS to the TWS, the thrust fluctuations are small and of similar magnitude as found for the rotor operating under negative speeds v.

In Figure 11.4 the standard deviation of torque is shown. Although subtle differences can be seen when comparing these plots with the thrust standard deviation from Figure 11.3, the locations of excessive fluctuations are very similar.

11.3 Derivatives with respect to wind speed and rotation speed

The partial derivatives of $f(\omega, v)$ and $n(\omega, v)$ are arguably even more interesting to analyse then the absolute values of these functions. If there would be no rotor to rotor and rotor to airframe interaction, the following statements should hold. Firstly, the derivative of thrust with respect to rotor rotational speed, f_ω, is a measure of control effectiveness of the actuators. A low value for this derivative means the overall gain in the control loop of the quadcopter is low. Secondly, the derivative of thrust with respect to descent

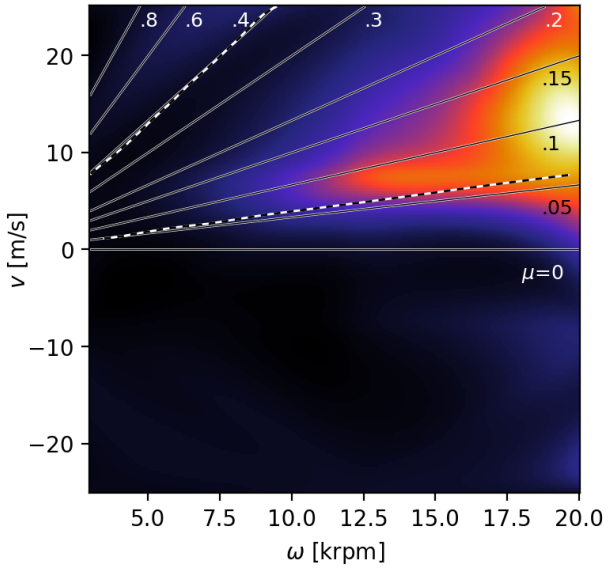

(a) Heat map of torque standard deviation σ_n as function of descent speed and rotor rotational speed. Upper and lower dashed lines indicate f_{t1} and f_{t2}, respectively.

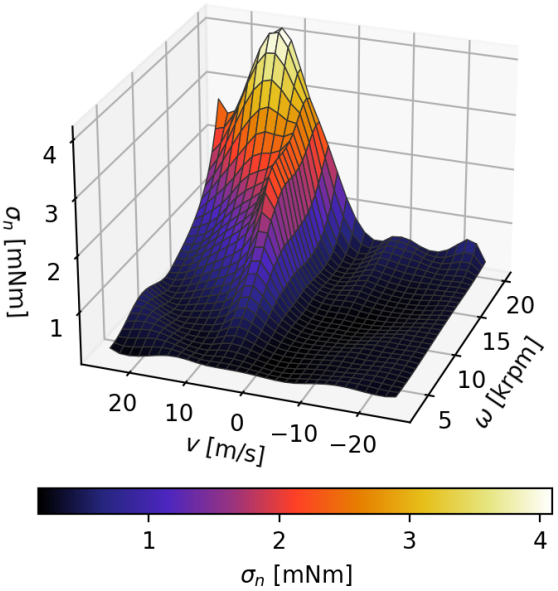

(b) 3D view of the simplex B-spline capturing torque standard deviation as function of descent speed and rotor rotational speed.

Figure 11.4: Estimated torque standard deviation for the isolated rotor. Positive speeds refer to the rotor in axial descent.

speed, f_v, is a measure of the natural stability of the quadcopter. A positive value for this derivative would theoretically cause the quadcopter to oppose any pitch or roll rate by generating a counter moment [27], although in practice this effect is very small. Note that this stability is inherent to the quadcopter and has nothing to do with the controller. Thirdly, a high value for the derivative of torque with respect to rotor rotational speed, n_ω, is related to stability around the yaw axis, as well as a high amount of control effectiveness around this axis. Finally, the derivative of torque with respect to descent speed, n_v, is an indication of coupling between the roll, pitch and yaw axis. Again, this latter effect is in practice rather small.

In Figure 11.5 the estimated partial derivative f_ω is depicted. This derivative is arguably the most influential since it determines how effective the actuators are in terms of control. As expected, f_ω generally increases when the rotor rotational speed is increased. However, for advance ratios of $.15 < \mu < .2$ and high rotor rotational speeds, the derivative is almost as low as when the rotor is idling. This is likely due to the characteristics of the VRS, where an increase in rotor rotational speed partly starts increasing the power delivered to the vortices, rather than increasing thrust. This derivative only becomes negative at speeds close to $-25\,\mathrm{m\,s^{-1}}$ and low rotor rotational speeds. This is interesting since theoretically this would mean the control gain flips sign and that the quadcopter becomes unstable. Since this happens in the normal operating state of the rotor, this finding is outside the scope of this work.

In Figure 11.6 the estimated partial derivative f_v is shown. Interesting to note is the sudden transition from a low to high value at an advance ratio of $\mu = .15$.

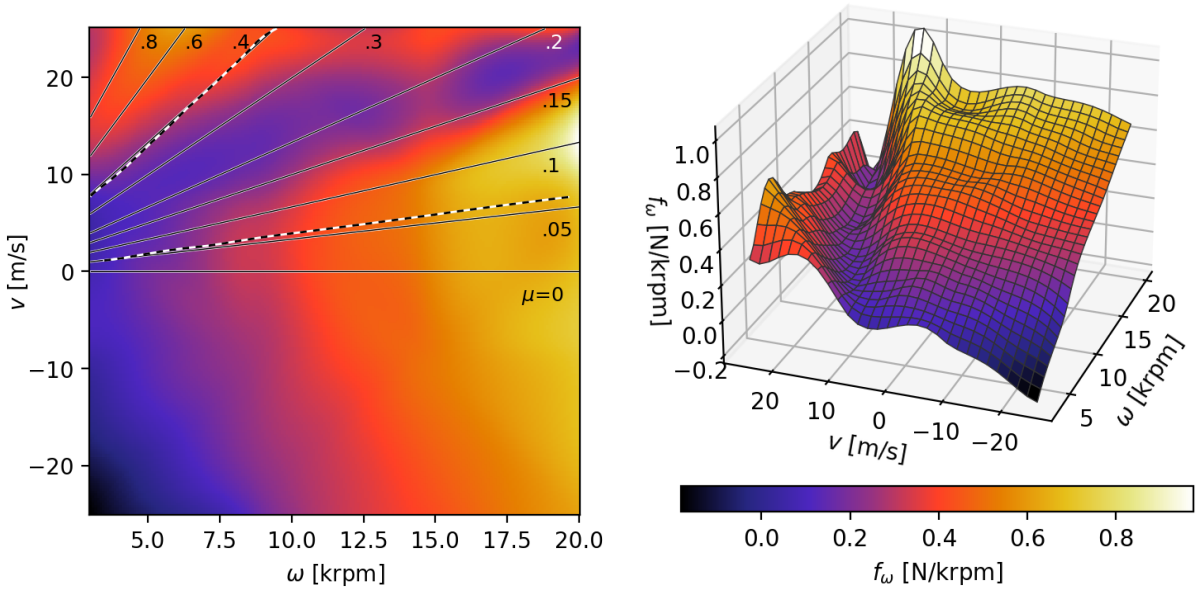

(a) Heat map of the change in thrust w.r.t rotor rotational speed as function of descent speed and rotor rotational speed. Upper and lower dashed lines indicate f_{t1} and f_{t2}, respectively.

(b) 3D view of the simplex B-spline capturing the change in thrust w.r.t rotor rotational speed as function of descent speed and rotor rotational speed.

Figure 11.5: Change in thrust w.r.t rotor rotational speed. Positive speeds refer to the rotor in axial descent.

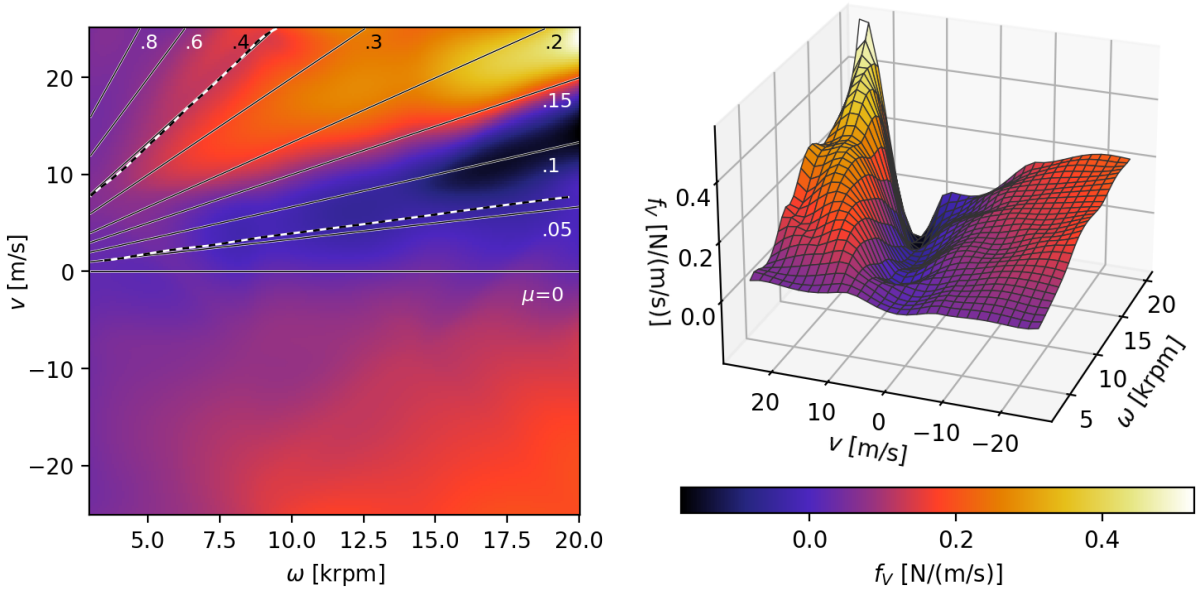

(a) Heat map of the change in thrust w.r.t descent speed as function of descent speed and rotor rotational speed. Upper and lower dashed lines indicate f_{t1} and f_{t2}, respectively.

(b) 3D view of the simplex B-spline capturing the change in thrust w.r.t descent speed as function of descent speed and rotor rotational speed.

Figure 11.6: Change in thrust w.r.t descent speed. Positive speeds refer to the rotor in axial descent.

In Figure 11.7 the estimated partial derivative n_ω is shown. Where the value of f_ω is low for advance ratios of $.15 < \mu < .2$, the value for n_ω is low for advance ratios of $.2 < \mu < .35$. This goes to show that the TWS can have a comparable effect on the control effectiveness of the rotors from an aerodynamic standpoint.

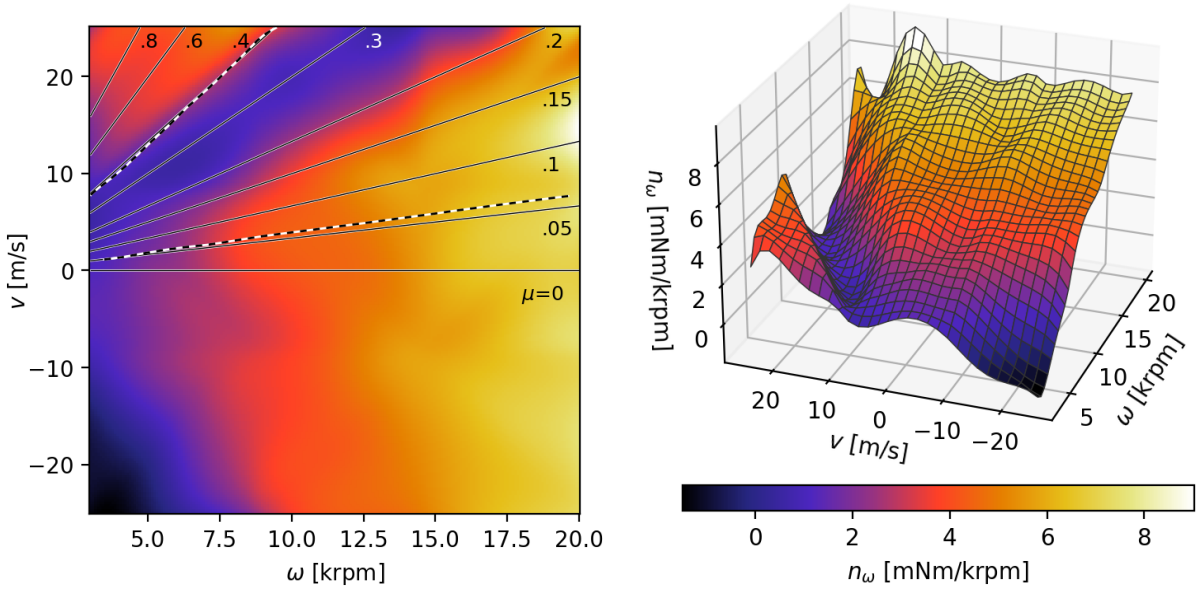

(a) Heat map of the change in torque w.r.t rotor rotational speed as function of descent speed and rotor rotational speed. Upper and lower dashed lines indicate f_{t1} and f_{t2}, respectively.

(b) 3D view of the simplex B-spline capturing the change in torque w.r.t rotor rotational speed as function of descent speed and rotor rotational speed.

Figure 11.7: Change in torque w.r.t rotor rotational speed. Positive speeds refer to the rotor in axial descent.

Finally, in Figure 11.8 the derivative of torque with respect to descent speed is shown. It can be noted that the derivative is highest in the TWS at high rotor rotational speeds, and lowest in the VRS at high rotor rotational speeds.

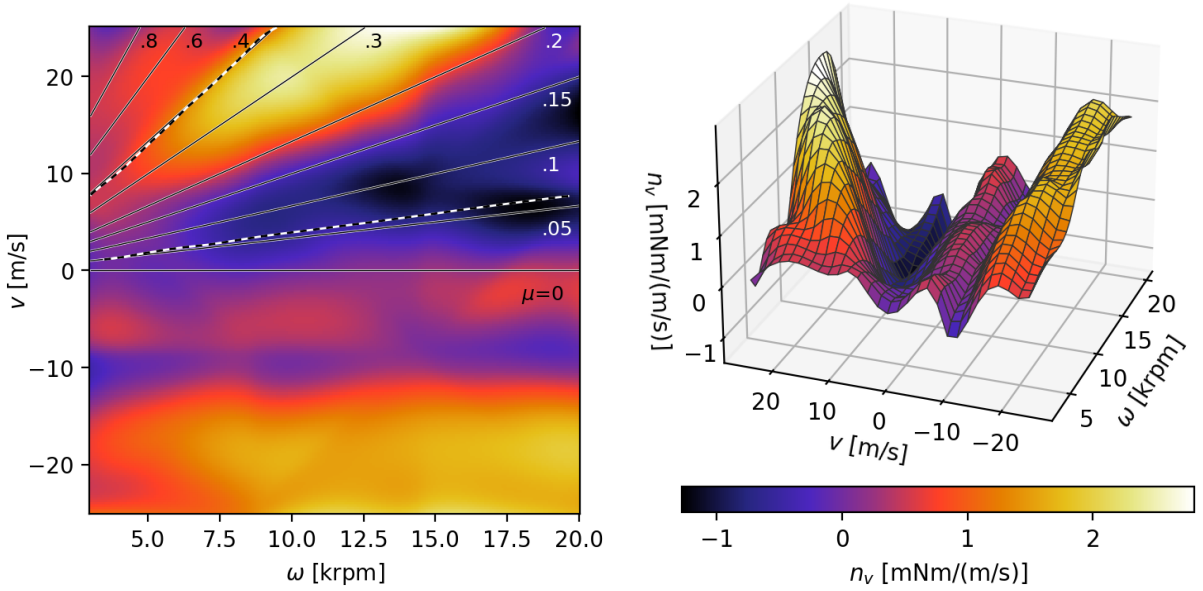

(a) Heat map of the change in torque w.r.t descent speed as function of descent speed and rotor rotational speed. Upper and lower dashed lines indicate f_{t1} and f_{t2}, respectively.

(b) 3D view of the simplex B-spline capturing the change in torque w.r.t descent speed as function of descent speed and rotor rotational speed.

Figure 11.8: Change in torque w.r.t descent speed. Positive speeds refer to the rotor in axial descent.

11.4 Gimbal tests with elastic bands

For this experiment the intention was to record the quadcopters attitude rates at rotor rotational speeds ranging from around 3000 rpm to 20 000 rpm. Unfortunately, for higher rotor rotational speeds the quadcopter started to rotate too violently causing the gimbal to hit its rotation end stops. Measuring at rotor rotational speeds close to 20 000 rpm would have caused inaccurate data, which led to the decision to measure only up to the point at which excessive rotation started to occur.

With the wind tunnel and rotors of the quadcopter turned off, the system identification test was performed to estimate the damped natural frequency ω_{gim} and damping ratio ζ_{gim} of the gimbal system with elastic bands. The differential equation of the rotational damped mass spring system around the roll axis can be written as is shown in Eq. 11.2, where k_x, d_x and I^g_{xx} are the effective stiffness, the effective damping and the effective mass moment of inertia of the gimbal system. The functions $L(t)$ and $\phi(t)$ are the externally applied roll moment and the roll angle, respectively. A similar equation holds for the pitch axis.

$$L(t) = I^g_{xx}\ddot{\phi}(t) + k_x\dot{\phi}(t) + d_x\phi(t) \tag{11.2}$$

The roll angle $\phi(t)$ is obviously related to the roll rate $p(t)$ as shown in Eq. 11.3. Because the gyroscope samples the roll rate $p(t)$, discrete methods have to be used to approximate $\ddot{\phi}(t)$ and $\phi(t)$. The former is approximated by applying a first order forward difference scheme to the roll rate measurements, and the latter is approximated by using

trapezoidal integration. To keep the integral from wandering due to an accumulation of measurement errors, the integrated signal is post processed using a forward and a backward running high pass filter with a cut off frequency of 0.02 Hz.

$$\ddot{\phi}(t) = \dot{p}(t) \qquad \dot{\phi}(t) = p(t) \qquad \phi(t) = \int_0^t p(\xi) d\xi \tag{11.3}$$

Once the gimbal is pulled back manually and released to induce an oscillation, the roll moment is zero, so $L(t) = 0$. The measured roll rate $p(t)$ can then be used to estimate the values of the ratios k_x/I^g_{xx} and d_x/I^g_{xx} using least squares and Eq. 11.2. To find the values of the individual parameters k_x, d_x and I^g_{xx}, the mass moment of inertia of the quadcopter itself was used for I^g_{xx}. This value was found experimentally by hanging the quadcopter by two wires and measuring oscillation times. The actual value of I^g_{xx} should be slightly higher due to gimbal parts. This is especially true for the pitch axis, because the gimbal assembly that rotates around this axis weighs around 60 g. This difference causes conservative estimates for $L(t)$ later on.

Once the parameters k_x, d_x and I^g_{xx} are known, the gimbal oscillation can be simulated and compared to the actual measured oscillation. Visually this reveals that there is definitely some residual behaviour that is not captured by the estimated model of the gimbal system, especially for the pitch axis. An example of a comparison between measured and simulated pitch and roll rate can be seen in Figure 11.9.

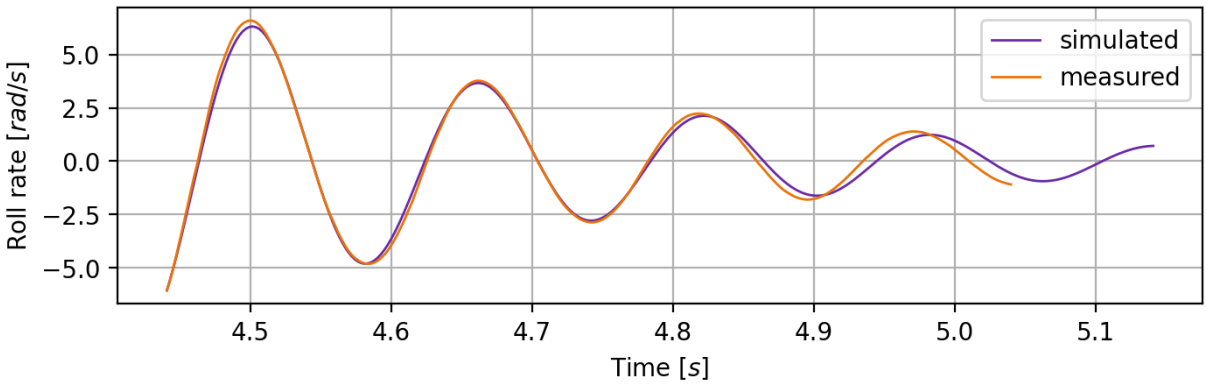

(a) Measured and simulated roll rate as function of time.

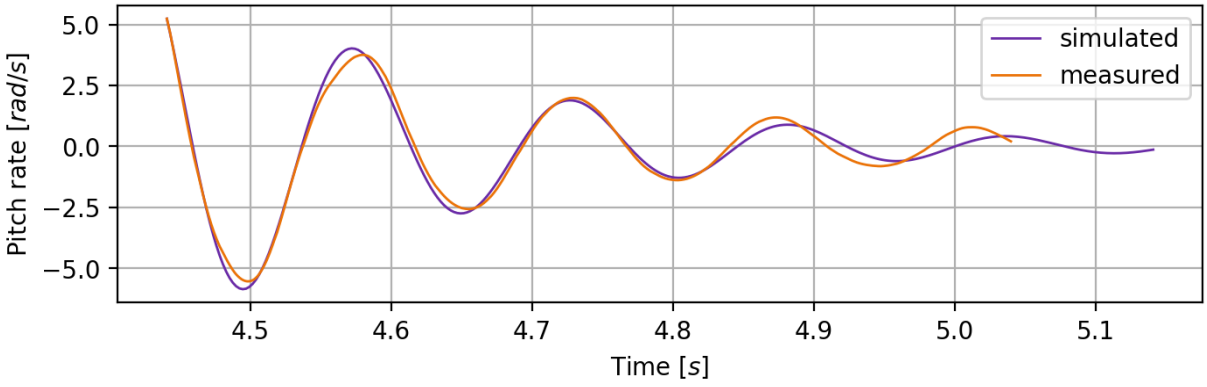

(b) Measured and simulated pitch rate as function of time.

Figure 11.9: Example comparison between measurements and simulation of the gimbal oscillation.

The gimbal model can now be used to reconstruct roll and pitch moments from the measured roll and pitch rates. Taking the roll axis as example again, the roll moment $L(t)$ is related to the four rotor thrust forces $f_1(t)$, $f_2(t)$, $f_3(t)$ and $f_4(t)$ as is shown in Eq. 11.4. Assuming that thrust fluctuations of different rotors are not correlated results in Eq. 11.5. Because interaction effects are ignored, the rotors operate under identical conditions. The thrust standard deviation is therefore the same for all rotors, so $\sigma_{f_1} = \sigma_{f_2} = \sigma_{f_3} = \sigma_{f_4} = \sigma_f$. This finally relates σ_f to σ_L, as is shown in Eq. 11.6. Of course this also be applies to the pitch axis, where L is replaced with M, l_y with l_x and $p(t)$ with $q(t)$.

$$L = l_y(f_1 + f_2 - f_3 - f_4) \tag{11.4}$$

$$\begin{aligned} \mathrm{Var}(L) &= \mathrm{Var}(l_y(f_1 + f_2 - f_3 - f_4)) \\ \sigma_L^2 &= l_y^2(\sigma_{f_1}^2 + \sigma_{f_2}^2 + \sigma_{f_3}^2 + \sigma_{f_4}^2) \end{aligned} \tag{11.5}$$

$$\sigma_L^2 = 4l_y^2\sigma_f \tag{11.6}$$

Knowing the values of the parameters k_x, d_x and I_{xx}^g from Eq. 11.2 allows for reconstructing $L(t)$ at each point in time. The PSD (power spectral density) of the roll moment $P_L(f)$ and the PSD of the rotor thrust force $P_f(f)$ are related in the same way as the variances of the respective time domain signals, as is shown in Eq. 11.7. Again, the same holds for the pitch axis, as is shown in Eq. 11.8.

$$P_L(f) = 4l_y^2\, P_f(f) \tag{11.7}$$

$$P_M(f) = 4l_x^2\, P_f(f) \tag{11.8}$$

According to the above procedure, the PSD of the thrust of a single rotor, $P_f(f)$, can be estimated from the measured roll rate $p(t)$, and also from the measured pitch rate $q(t)$. In Figure 11.10 the estimated $P_f(f)$ functions are shown for descent speeds of $10\,\mathrm{m\,s^{-1}}$, $15\,\mathrm{m\,s^{-1}}$,$20\,\mathrm{m\,s^{-1}}$ and $25\,\mathrm{m\,s^{-1}}$, and for four different rotor rotational speeds. Each PSD shown is the average of the PSD according to the roll rate and PSD according to pitch rate. Note that both of these roll and pitch PSDs are very similar and pretty much overlap for all speed and rotor rotational speed combinations.

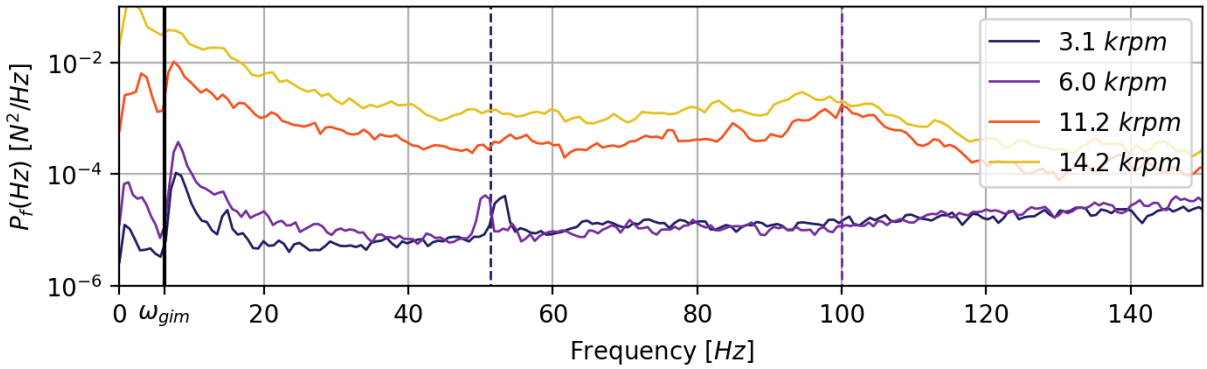

(a) $\mathrm{V} = 10\,\mathrm{m\,s^{-1}}$

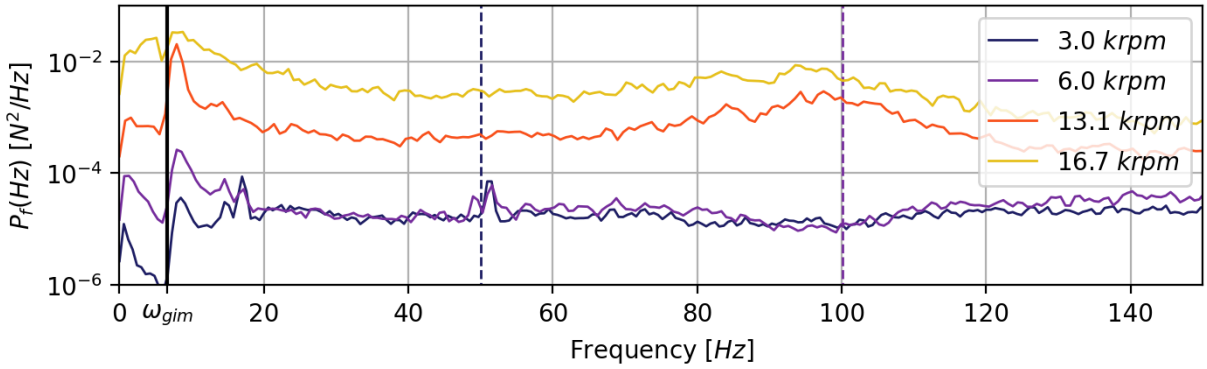

(b) $\mathrm{V} = 15\,\mathrm{m\,s^{-1}}$

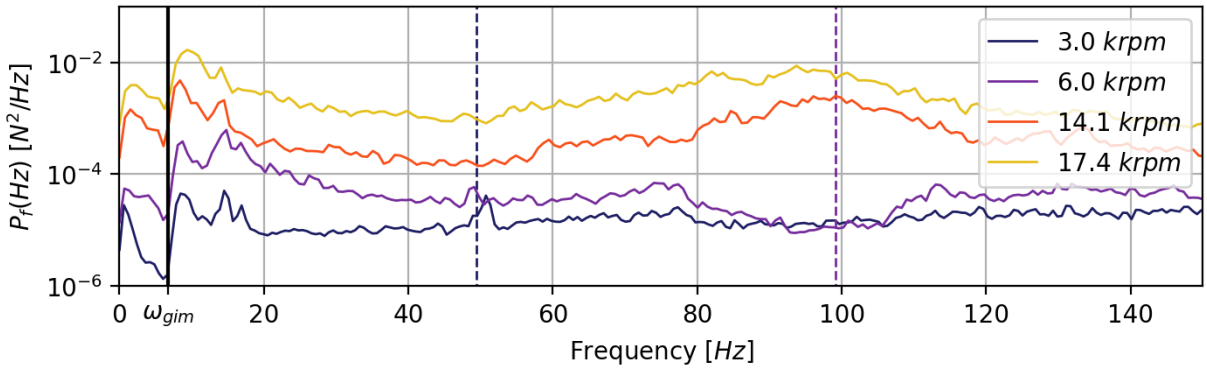

(c) $\mathrm{V} = 20\,\mathrm{m\,s^{-1}}$

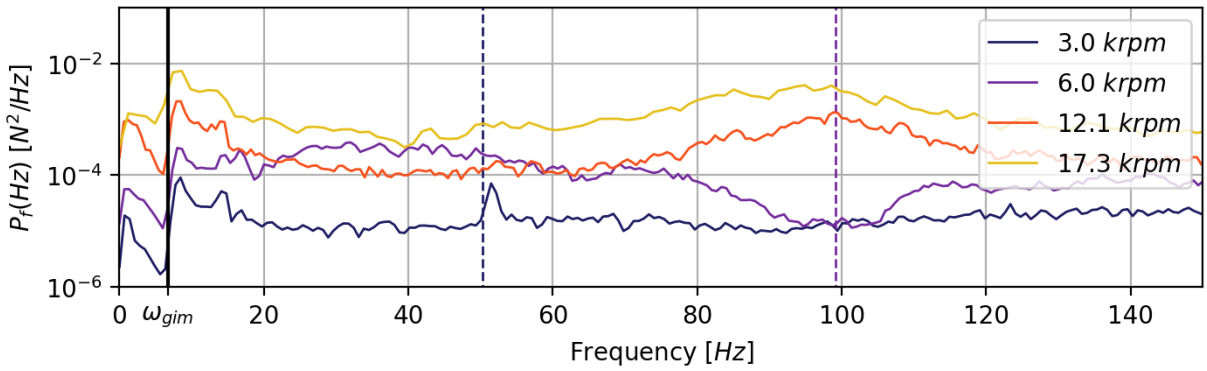

(d) $\mathrm{V} = 25\,\mathrm{m\,s^{-1}}$

Figure 11.10: PSDs of single rotor thrust $f(t)$ based on the reconstructed roll moment $L(t)$ and pitch moment $M(t)$. The damped natural frequency of the gimbal is indicated with ω_{gim}. Dashed lines indicate the rotational speed of the rotors in Hz, and match in color with their respective PSD.

Firstly, in Figure 11.10 the vertical black line marked with ω_{gim} on the frequency axis indicates the estimated damped frequency of the gimbal system. As can be seen, the PSDs either increase or decrease notably close to this line. It is very plausible that this is due to unmodeled gimbal dynamics that are not captured by the damped mass spring approximation that was used to reconstruct the $L(t)$ and $M(t)$ signal. Of course this can not be said with certainty. Secondly, it can be seen that for frequencies up to 80 Hz the PSDs are fairly flat. Lastly, the dashed lines in Figure 11.10 indicate the frequency at which the rotors are rotating, and match in color with their respective PSD. The small peak at around 50 Hz is likely not due to the rotating rotors, as it shows up in PSDs corresponding to much higher rotor rotational speeds (not shown in the figure) as well.

The total variance of rotor thrust, σ_f^2, is proportional to the area under the PSDs in Figure 11.10. However, it was found experimentally that there are several airframe eigenfrequencies above 90 Hz. This makes it unclear how much of the signal power above, say, 80 Hz is due to thrust fluctuation and how much is due to frame resonance. To get around this, the area under the PSD is only taken up to 80 Hz to find the variance σ_f^2. Consequently, fluctuations above 80 Hz that are actually due to thrust fluctuation are discarded. This makes the estimation of σ_f^2 conservative.

In Figure 11.11 the estimated standard deviation σ_f that is calculated using the reconstructed $L(t)$ and $M(t)$ signals is compared to the σ_f values for a rotor in isolation as were found in section 11.2. Standard deviations estimated using $L(t)$ and $M(t)$ signals are indicated with 'from p(t)' and 'from q(t)', respectively, and the isolated rotor thrust standard deviation is indicated with the black line. It is relevant to know how much of the estimated σ_f from $p(t)$ and $q(t)$ is due to gyroscope sensor noise. It was found experimentally that the gyroscope primarily produces quantization noise. The gyroscope has a resolution of $0.0174\,\mathrm{rad\,s^{-1}}$, which is small compared rotational speeds measured during the experiment as can be seen in Figure 11.9. In this case a common assumption is that quantization errors can be modelled as additive white noise [22]. The standard deviation of this noise is then approximately $\sqrt{1/12} \cdot .0174$. Its possible to reconstruct $L(t)$ and $M(t)$, and thus σ_f, as a result of only this noise signal. These σ_f values due to noise only are indicated by the dashed lines in Figure 11.11. Of course in reality these rotor forces do not exist. The standard deviations reconstructed from $p(t)$ and $q(t)$ indicated by triangles in Figure 11.9 are already corrected for this noise.

As can be seen in Figure 11.11, σ_f is generally significantly larger for rotors mounted to the quadcopter compared to the rotors in isolation. This strongly suggest that rotor-rotor interaction, or maybe even rotor-frame interaction, causes a significant increase in the fluctuation of thrust.

Furthermore, it can be observed that the estimated value of σ_f is on average slightly higher when it is estimated using the pitch rate $q(t)$. A possible reason for this is that the system identification of the gimbal system performed notably worse (roughly 10 % to 30 % in terms of residue standard deviation) for the pitch axis compared to the roll axis. This could mean that the reconstructed $M(t)$ signal contains more power that is actually due to the uncaptured system dynamics of the gimbal, rather than the power due to fluctuation in thrust. This would cause the estimated value of σ_f to be higher for the pitch axis.

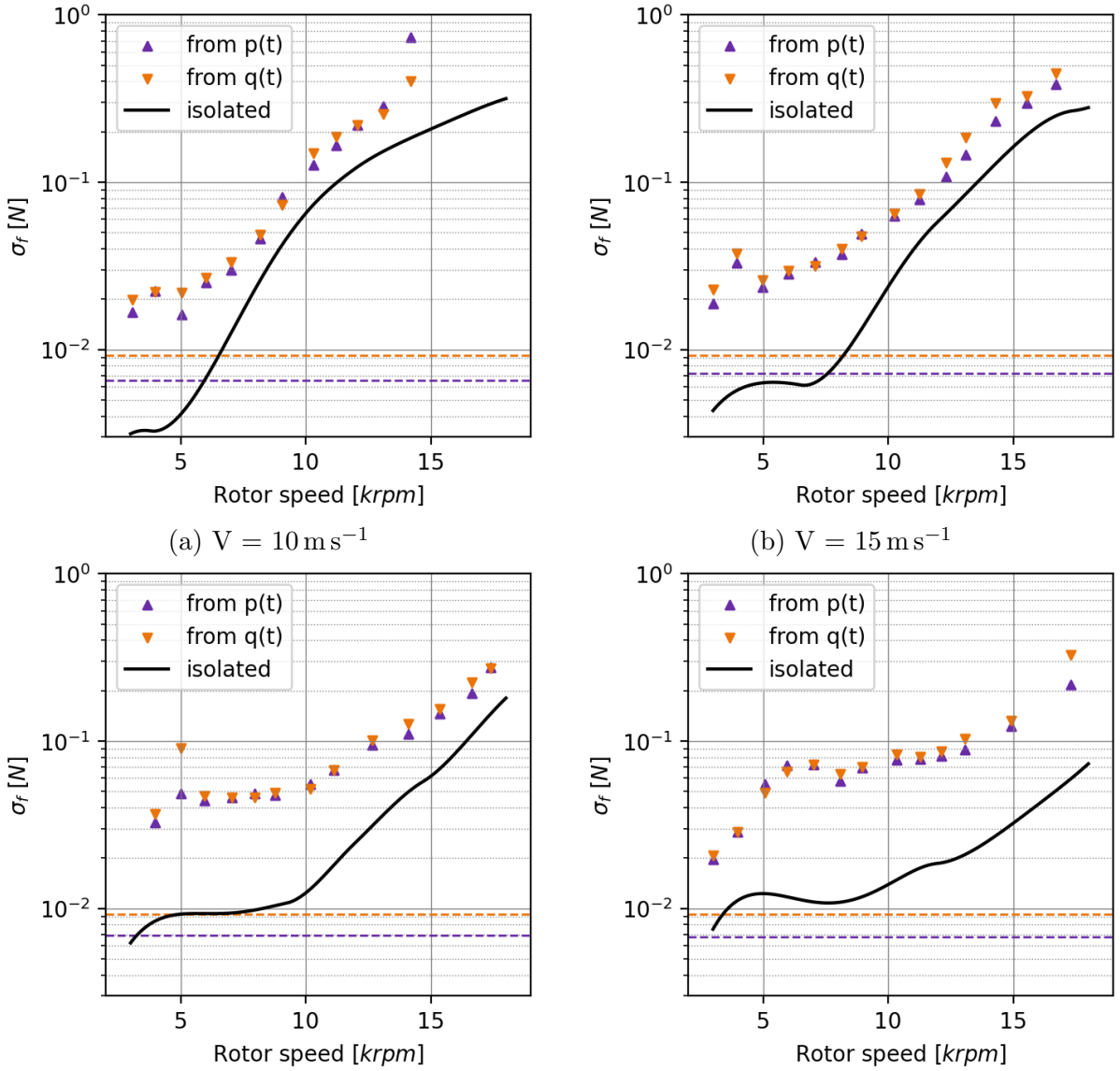

(a) V = 10 m s^{-1}

(b) V = 15 m s^{-1}

(c) V = 20 m s^{-1}

(d) V = 25 m s^{-1}

Figure 11.11: Rotor thrust standard deviation. The black line represents isolated rotor thrust data. Purple and orange triangles represent thrust standard deviations reconstructed from the measured roll rate and measured pitch rate, respectively, which are corrected for gyroscope noise. The purple and orange dashed lines correspond to gyroscope noise only along the roll and pitch axis, respectively.

Another potential cause might be the incorrect assumption that the rotor forces are uncorrelated, which was made in Eq. 11.5. If these correlations would in fact be non-zero, they can be divided into the sum of thrust correlations between the left and right rotors, and the sum of thrust correlations between front and rear rotors. It is not hard to show that if these 'left to right' and 'font to rear' correlations are different, then the thrust variance σ_f^2 reconstructed from the roll rate would be different from the value for σ_f^2 reconstructed from the pitch rate. This might indeed be the case, since the rotors are separated more along the body frame y-axis compared to the body frame x-axis due to the presence of the quadcopters 'fuselage'. Not taking into account the higher thrust correlation between the front and rear rotors would result in different estimations for σ_f^2.

Of course values shown in Figure 11.11 are estimations of the actual values. It should be noted that the standard deviations reconstructed from the quadcopters movement are estimated conservatively due to the low assumed values for I_{xx}^g and I_{yy}^g, the exclusion of frequencies above 80 Hz and the subtraction of gyroscope noise. Estimations of the isolated rotor thrust standard deviations on the other hand are are likely to be too high since sensor noise and test stand vibrations are not subtracted.

Chapter 12

Conclusion

While the complex aerodynamics of helicopters in axial descent have seen quite some scientific attention in the past decades, the comparable attitude oscillations found for small scale quadcopter flight have not. Often times these oscillations are assumed to be a direct result of the rotors operating in either the VRS or TWS. The experiments described in this paper suggest that isolated rotor aerodynamics might contribute a lot less to attitude oscillations than is commonly assumed.

The data from the isolated rotor wind tunnel tests reveal that the mathematically defined borders between the pre-VRS and VRS, and between the TWS and the WMS are located at constant advance ratio lines. This suggests that modeling rotor aerodynamics in axial descent might be more convenient as function of advance ratio and total blade velocity, rather than descent speed and rotor rotational speed. From the data it can be seen that there is indeed a notable drop in thrust and drag toque in the VRS region. This drop also follows the structure of the constant advance ratio lines.

The VRS also seems to be area of highest intensity of thrust fluctuation. In the VRS it seems to be the case that an increase in rotor rotational speed drastically increases the thrust fluctuations. Contrary to the absolute thrust values, the thrust fluctuations also occur in the pre-VRS. That is, as soon as the descent speed becomes positive, thrust fluctuations can be observed. Interestingly enough, outside the VRS and inside the assumed TWS and WMS, the fluctuation is similar as found for the rotor in normal operating state, which is very small. Similar conclusions can be drawn for the measured drag torque.

The derivatives of thrust and torque with respect to rotor rotational speed and descent speed reveal primary characteristics of the quadcopters if the rotors would operate as if they were in isolation. The value for f_ω generally increases as rotor rotational speed is increased. There is however a region of low values for f_ω at the boundary of the VRS and TWS. This effectively decreases the overall flight controller gain in this region for roll and pitch rate. A positive value of f_v causes the quadcopter to theoretically be a stable system, since this opposes any roll or pitch rotation. This derivative appears to be low in the VRS, but high when approaching TWS. The impact of this derivative on system dynamics is generally overshadowed by the authority of the flight controller. Finally, n_ω is similar in hover compared to the VRS, but drops notably in the TWS. This indicates the relevance of the TWS besides the more commonly mentioned VRS. Neither the f_ω or n_ω partial derivatives are negative in the range of $0\,\mathrm{m\,s^{-1}}$ to $25\,\mathrm{m\,s^{-1}}$ and 3 krpm to

20 krpm. Instability of quadcopters in axial descent due to actuator effectiveness inversion or sudden loss of lift due to blade stall as universal explanation is therefore unlikely.

Comparing results for wind tunnel experiments using the complete quadcopter with results from the isolated rotor experiments reveals a similar dependence of thrust fluctuations on airspeed and rotor rotational speed. However, thrust fluctuations for the rotor in isolation seem to be much smaller than found for the quadcopter in its entirety. This suggests that the isolated rotor states such as the VRS, TWS and WMS only partly explain the attitude oscillations in axial descent. The measured oscillations are larger for the pitch axis than the roll axis. Although this could be due to estimation errors, it is possible this is caused by the rotors being spaced further apart along the body frame y-axis. Since rotor operating states do not fully explain the attitude oscillations, principles like rotor to rotor interaction deserve more attention to explain quadcopter flight dynamics in axial decent.

Part III

Literature study: Nonlinear Control of High Performance Quadcopters

Chapter 13

Introduction

In recent years, UAV's (unmanned aerial vehicles) have seen a huge rise in popularity. In the military they have been used for decades as they are suited for the dull, dirty and dangerous tasks. They are cheaper to operate and reduce risks to personnel [28]. Due to the recent advances in technology since 2000, especially smartphone technology, there has been a great increase in the use of UAV's for civilian use as well. One particularly popular UAV platform is the quadcopter, which belongs to the family of multirotor UAV's.

It is found that the quadcopter as UAV and MAV (micro air vehicle) has a very wide range of application possibilities. They have been shown to be effective in tasks such as surveying, transportation, research, disaster risk management, humanitarian work [5] and many more. This is arguable due to the very specific characteristics of the quadcopter configuration. Firstly, quadcopters are mechanically very simple, making them accessible for the non-expert to build and maintain. Parts are cheap, making them in their entirety cheap to manufacture and service [3, 4]. Secondly, they have the ability of vertical take-off and landing, are very maneuverable, and are relatively efficient in hover conditions [2].

Although quadcopters are mechanically very simple, it can be argued that the complexity is largely captured in the control algorithm necessary to fly in a stable and controlled manner. Initially many control algorithms were focused on the hover condition. This allows for making a large amount of assumptions causing various linear control strategies to be very effective. However, when flight speeds, attitude angles and rotational rates increase as is the case during aggressive and high speed flight, these assumptions do not hold anymore. The dynamic equations that describe the motion of the quadcopter become highly nonlinear, giving rise to the need for more advanced control strategies. Furthermore, aerodynamic effects become significant. Both the aerodynamic forces on the fuselage, forces on the propellers and rotor to rotor interaction effects [7] need to be accurately modelled in order to achieve high control performance [9]. Besides this, the underactuated nature of quadcopters make them fail to satisfy Brockett's condition [29], which guaranties the proof of existence for a stabilising time-invariant smooth feedback controller [30]. This all makes general control of quadcopters a difficult problem, and is therefore and active field of research.

This report is the documentation of a literature study that is performed in preparation of a masters thesis project. The goal of this literature study is to gain insight into the current state of research when it comes to advanced control of quadcopters.

Here the focus lays in how quadcopter flight behaviour can be modelled and how this information is then used in algebraic control strategies such as linear parameter varying control, incremental nonlinear dynamic inversion and Lyapunov based techniques. Less developed and more exotic control techniques such as neural networks and fuzzy logic are not treated to maintain a reasonable scope of this study. In this report, a variety of research is included with the goal of sampling an apparent large field of research. For a more systematic overview of all published scientific articles in this field, several surveys have been created with this exact objective [29, 31].

This report is structured as follows. In chapter 14, a quick historic overview is given of the quadcopter. After this the basic functionality of the quadcopter is discussed, together with some of its most popular real world applications. Several aerodynamic effects are treated that give an idea of how forces and moments generated the propellers and airframe can be modelled. In chapter 16, various advanced control strategies are presented that are common in quadcopter control. Finally, in chapter 17, gaps in current quadcopter control research are identified. Based on this a research topic is proposed in the form of a research question and several subquestions.

Chapter 14

The quadcopter as MAV

This chapter serves as an introduction to the the quadcopter and its characteristic configuration, and attempts to give a high level overview of how they were developed, how they work and how they are currently used in real world scenarios. In section 14.1 a brief overview is given of the emergence and history of the quadcopter, both as full scale aircraft and MAV. In section 14.2 several common applications of the quadcopter MAV are listed, highlighting some of its inherent advantages. Finally in section 14.3 an explanation is given of some of the most important components of a quadcopter and how these can be used to achieve stable and controlled flight.

14.1 The birth and rise of the quadrotor

The modern quadcopter as its known today is generally considered to be very young technology. Only in the last 10 to 15 years a massive increase has been seen in both the amount of use cases and incorporated level of technology. However, the very distinctive design configuration of the quadcopter itself can be traced back all the way to the beginning of the 20'th century. In this section a brief overview is given of emergence of the quadcopter UAV.

As is known by most aerospace enthusiasts, the first ever powered flight was performed by the Wright brothers in the year 1903. Surprisingly enough, it was only a couple of years later that the first aircraft was made that could be referred to as quadcopter. This machine, build in 1907 by the brothers Jacques and Louis Bréguet, consisted of a place for the 'pilot' and four arms extending from this position holding a large propeller each. The aircraft was able to reach an altitude of 1.5 m purely powered by its own engine. However, the rotor craft could not be controlled by the pilot in terms of attitude, and was therefore stabilized by human ground helpers. Although this lack of control is why it can not take credit for being the fist helicopter, it is the fist system ever to raise a pilot of the ground by means of a rotating wing lift system.

Thirteen years later, in 1920, a french engineer named Étienne Oehmichen started the design and build of the first controllable quadcopter. In 1924 this aircraft broke the distance record of helicopters at the time with 360 m. He continued to improve the design by making a total of six different rotorcraft in his life. Control was achieved by warping the rotor blades and was later enhanced by additional smaller rotors able to produce lateral forces. Stability was improved using a hydrogen filled balloon on top of the aircraft,

hinting at the general lack of stability of the quadrotor configuration. After this birth of the quadcopter many improvements were added over the course of the 20th century, causing significant increase in understanding of quadrotor performance, controllability and stability. However, the quadcopter design kept living in the shadow of the classic single rotor helicopter design.

In the late 1980's the rapid advance high density power storage, integrated miniature actuators and MEMS (micro electro-mechanical systems) opened up a world of possibilities for autonomous small scale flying robots [32]. In 1989, the Keyence Gyrosaucer E170 was the first available quadrotor toy. With the technology at the time the flying qualities were mediocre and the flight time was low. Nonetheless in terms of appearance, layout and size, this toy could be considered the first small scale quadcopter as is widely used today.

While at first the potential was seen for military purposes, in 2006 the FAA issued the first commercial drone permits. This permit allowed more freedom regarding operation of quadcopter drones making them an interesting option for applications like pipeline inspection and spraying crops. Recognising the potential, Frank Wang created the well known DJI company in this year. In 2010, the French company Parrot SA, founded in 1994, introduced the Parrot AR.Drone. This would prove to be the first successful commercial drone that was sold as a ready to fly package and could be controlled from an iOS application on a smart phone.

With drones becoming more and more popular, large companies such as FedEx, UPS and Amazon started advocating the use of drones for delivery purposes in 2013. At present day this idea is still being worked on by many companies, but general purpose delivery by drones is still something hindered by the many practical limitations. However, in the last 10 years the drone market increased exponentially due to the decrease in cost of quadcopters, the increase of performance in terms of range and maneuverability, and the significant increase in ease of use. In the last couple of years, larger electric quadcopters are also being developed that are able to carry a pilot and/or passenger. Examples of these are the Ehang in 2016 and recently the Jetson One. These are blowing new life in the quadcopter as a manned vehicle, continuing the journey that started more than a 100 years ago.

14.2 Quadrotor applications

The use of quadrotor drones and drones in general is increasing at a rapid pace. There are already over 300,000 drones registered in the US alone [33]. The use of drones will most certainly grow even more in the next couple of years. Up to 2025 the global commercial drone market is expected to grow by roughly 28.5 billion dollar, indicating a compound annual growth rate of 37 %. One of the major drivers of this growth is the rise in applications of drones [34]. This high amount of applications is due to the specific qualities of drones and specifically multirotor drones. Below some of the advantages and limitations of quadcopters drones are discussed, supported by a selection of practical applications, as is shown in Figure 14.1.

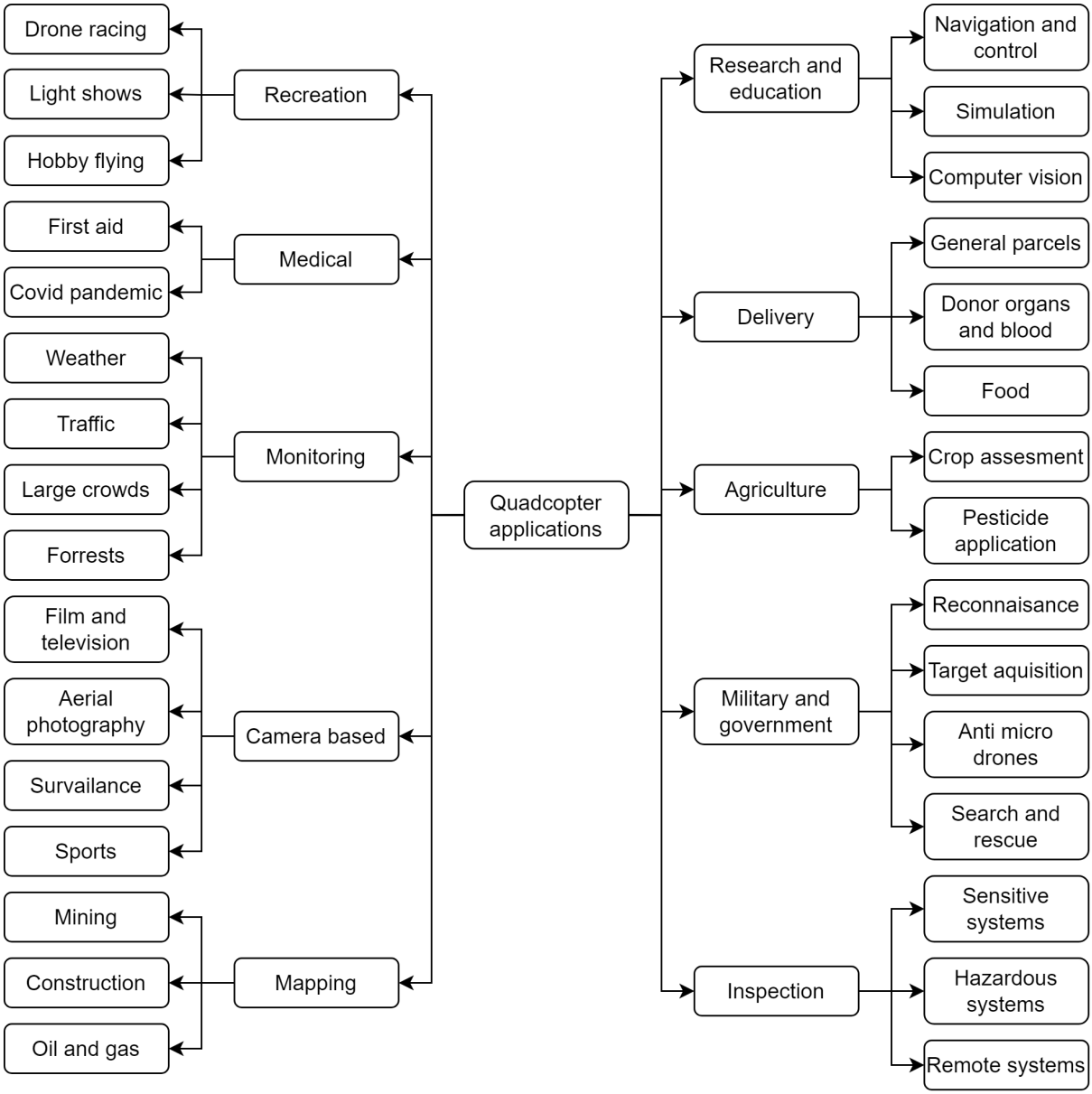

Figure 14.1: Breakdown of common applications of the quadcopter UAV.

One of the first valuable characteristics of the quadcopter is that it is relatively fast compared to other types of drones. This is mainly due to it being airborne, allowing it to travel with little drag and in straight lines. Generally only fixed wing drones are better suited for high speed applications. Because quadcopters are fast they are suited for applications where time is of the essence, such as first aid, search and rescue and delivery purposes. Furthermore quadcopters are naturally very maneuverable. This makes them suited for task like anti airborne drone operations, research on guidance and control techniques and operations in tight spaces.

Multirotors also have the advantage with respect to other airborne drones that they have the ability of vertical take off and landing, and the capability of hovering at a fixed position in space. This makes quadcopters suited for tasks where controlled, varying and slow flying speeds are needed, which are common in terrain mapping, monitoring,

surveillance and inspection. The capability of hovering and flying with low speed is also valuable when trying to reach places that are difficult to reach.

Lastly, quadcopters are mechanically very simple. This means that they are easy to build and cheap to manufacture. This makes quadcopters interesting to a wide range of users, both in military and civilian fields [35]. The mechanical simplicity also makes them robust compared to single rotor helicopter drones with a complicated rotor head. The latter is more susceptible to mechanical failure than the four fixed propellers of a quadcopter. In case of a failure, propellers and motors can be replaced easily and at little cost, making quadcopters easy to service and customize. It can be argued that most of the complexity of quadcopters is contained in the software rather that the hardware.

Unfortunately, quadcopters also have some inherent disadvantages. One of these is the fact that they use a lot of energy per unit of mass to stay in the air, compared to a fixed wing configuration. This makes them limited in terms of maximum flight time and distance. However, endurance and range performance increases as drone and battery technology advances. For example, the Mavic 3, which is one of the high end aerial photography quadcopters commercially available from DJI, has a claimed hover time of 40 min and a max flight distance of 30 km [36].

Another disadvantage is that they are fragile and suffer heavily from actuator damage. As will become more clear later on in this report, the quadcopter needs all of its four actuators to fully control its position and orientation in three dimensional space. If one actuator stops functioning due to for example a propeller strike, the quadcopter will lose control unless a special control algorithm is used. However, control during actuator failure is still a new and active field of research. The sensitivity to actuator failure is due to the inherently exposed propellers, the dependence on flight controllers for control and stability, and the lack of redundant actuators.

14.3 Basic functionality

To serve as a reference for later chapters, this section briefly lists some of the most fundamental components of the quadcopter and their functions. To be able to fly, a quadcopter carries at least a set of flight data sensors, a flight controller and four actuators. In Figure 14.2 this is presented schematically.

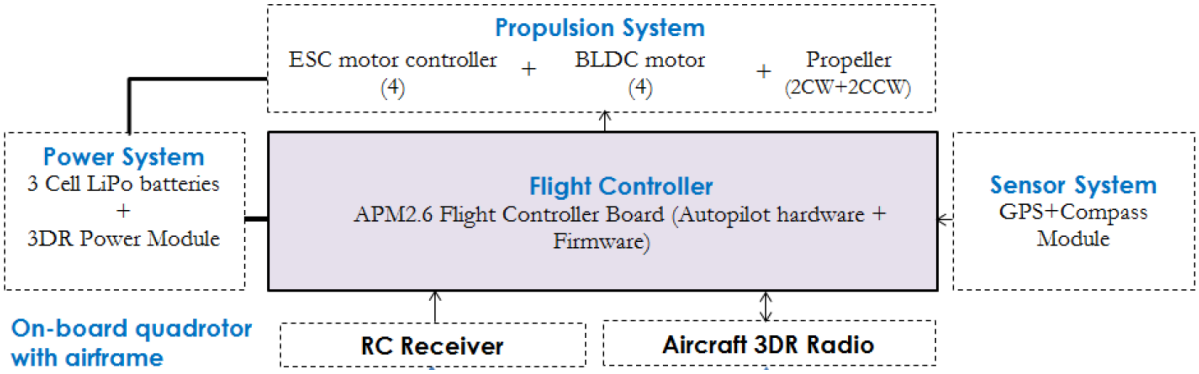

Figure 14.2: Schematic presentation of the systems aboard a standard quadcopter UAV. (from [37])

Since a quadcopter is stabilized electronically, it needs at least a basic set of sensors to determine its position and orientation is space [38]. The most critical sensors for stable flight are the gyroscope and the accelerometer, together forming the IMU. These measure the acceleration over and rotational rate around three axes. This information can be used to estimate the drones attitude. Often times the IMU is extended with a magnetometer, providing the quadcopter with information about its heading.

Many quadrotors, except for most of small size, are equipped with a barometer and GNSS (global navigation satellite system). This first sensor allows for estimating the altitude of the drone by measuring the static air pressure, resulting in altitude determination with an accuracy of a few centimeters. The GNSS allows for position determination, but in three dimensional space. For low cost GNSS modules, the measurement rate is low, and the position accuracy is often in the range of around 5 m [39]. By fusing the sensor data from the IMU, barometer and GNSS using for example a variation of the Kalman filter, the speed and position estimation can be drastically improved. For indoor applications and where precision position and speed estimation is required at a high measurement frequency, optical motion tracking systems can be used such as OptiTrack, [40, 33, 41].

Data from the sensors is sent to a flight controller responsible for at least processing the sensor data and sending inputs to the actuators. There are many options of flight controllers available in terms of both hardware and software. Below some of the most popular ones are discussed, together with their pros and cons.

In Figure 14.3 an overview is given of thee most well known flight controller software [42, 39]. These are all open source, with the exception of KISS and FlightOne Falco X. In the schematic the arrows indicate roughly which projects are derived from which. In reality this derivation tree is more complicated since features are sometimes interchanged between specific projects. The colors in the diagram indicate the main focus of the project. Boxes with dashed lines indicate that the projects are barely or not maintained anymore.

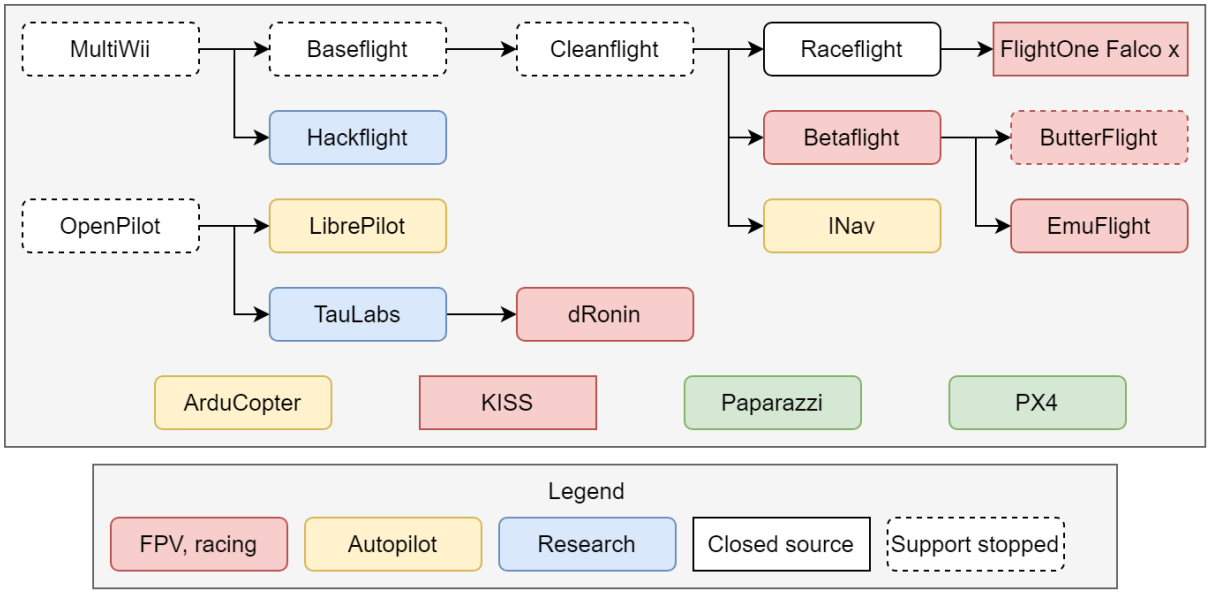

Figure 14.3: Schematic of most popular UAV flight control software.

The most popular projects are ArduPilot and PX4 [43], and are both well developed autopilot systems. Both are similar in performance, but they slightly outperform each other at specific aspects. Both are focused on reliable flight control and support a wide variety of unmanned vehicles, including quadcopters [44, 45]. PX4 supports Pixhawk hardware whereas Ardupilot is not tied to specific hardware. A major practical difference is the licence these two projects use. In contrast to Ardupilot, PX4 uses the BSD license which permits proprietary use of the software. This makes PX4 an attractive option for commercial companies [42]. When looking specifically at FPV and FPV racing, the most popular flight control software is Betaflight, which is focused on getting the most speed and performance out of the flight controller and quadcopter. It does not have its own hardware but supports many STM32 based flight controllers.

Per definition, a quadcopter has four actuators, each consisting of a motor and propeller that can be individually controlled. Due to the configuration of the actuators, the quadcopter can independently generate a moment around each axis in three dimensional space, and a force roughly normal to the average rotor plane. This last force can be referred to as the total thrust. The moments can be used to completely control the attitude of the quadcopter. Linear acceleration in three dimensions can than be controlled by specific combinations of the attitude and total thrust of the quadcopter. The control of linear acceleration allows for the control of position.

In Figure 14.4, the motors are numbered in CCW (counterclockwise) manner. The way actuators are numbered varies in literature. Here it is assumed the front of the quadcopter consists of the motors one and four, and the rear of the quadcopter consists of the motors two and three. Consider Figure 14.4a where the motors one and three rotate in CW (clockwise) direction and the other two motors CCW. A right hand roll moment can be generated by making propellers one and two spin less fast compared to the other two propellers. The increased reaction torque of faster spinning propellers cancels out, maintaining the equilibrium in yaw direction. Similarly, a pitch up moment can be generated by making propellers one and four spin faster. To generate a yaw moment to the left,

propellers two and three can be spun faster compared to the other two. This creates a total reaction torque of all propellers to the right. Because a diagonal propeller pair is has increased rotational speed, there is no pitch or roll moment. Finally, a total increase in thrust can be achieved by increasing the rotational speed of all propellers simultaneously.

To keep the control characteristics above, the following requirements can be set on the rotation direction of the four propellers. Fist of all, in hover, the moments and reaction torques should cancel each other out. That means that two propellers need to rotate CCW, and two propellers CW. Furthermore, to be able to generate a yaw moment using the reaction torques of the propellers without generating a pitch or roll moment, the diagonally opposed propellers should have the same rotation direction. Taking both these requirements into account, there is only one alternative to the rotation directions shown in Figure 14.4a, referred to as the bear hug configuration. This alternative is where all propellers rotate in the opposite direction which is referred to as the breaststroke configuration, as shown in Figure 14.4b. In terms of hover, both configurations behave very similar. At higher speeds however, some differences become apparent as is discussed in subsection 15.3.3.

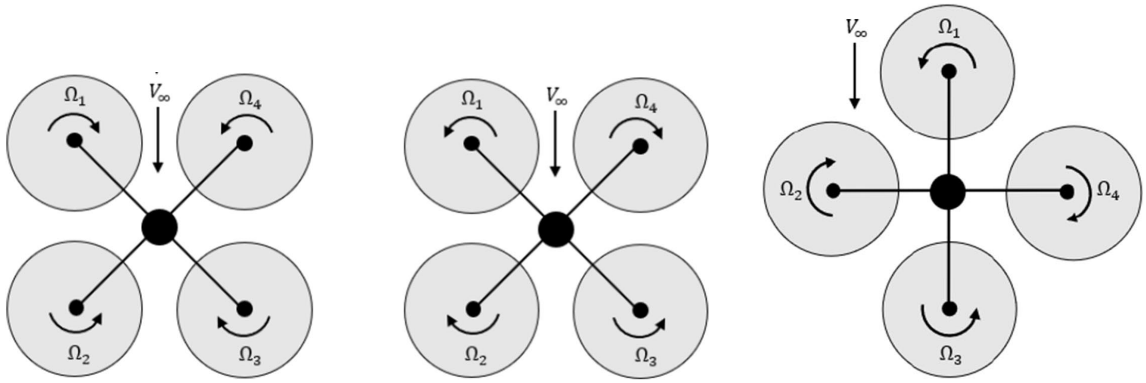

(a) Bearhug (b) Breaststroke (c) Diamond/plus

Figure 14.4: Most common quadcopter configurations. (from cite103, modified)

The configuration in Figure 14.4a and Figure 14.4b is referred to as a cross configuration, which is characterised by having two propellers in the front and two in the rear. Another less common configuration is the diamond or plus configuration, characterised by one propeller in the front and rear, and two in the middle, as shown in Figure 14.4c. In terms of control this configuration is identical to the cross configuration. However, at higher speeds, aerodynamic differences start to occur, such as less pitch moment generated as a consequence of forward speed [8]. Especially due to the asymmetry of the plus configuration, there are some asymmetrical aerodynamic effects such as a coupling of pitch and yaw control [46]. Furthermore there are derived configurations that are only symmetric around a single plane, compared to the cross and plus configurations that are symmetric around two planes. These alternative configurations are represented very little in current research, but are also less common.

Chapter 15

General quadcopter dynamics

As mentioned earlier, for the hover condition many assumptions can be made when designing a control law that allow for great simplification. In this flight condition linear control strategies are very effective, and have been applied to quadcopter control for many years. However, when the quadcopter takes on more excessive attitude angles, or when higher linear and rotational velocities are reached, many of these assumptions do no hold anymore. Under these flight conditions, designing effective control strategies becomes significantly more challenging because of this reason.

This chapter discusses how the dynamics of quadcopters can be modelled. This can partially be drawn from mathematical theory and partially from knowledge gained from experiments and CFD. In section 15.1, several reference frames are treated that are widely used in literature to express the equations of motion of quadcopters. In section 15.2 these equations of motion are derived. In section 15.3, literature is reviewed on how the forces that work on the propellers of a quadcopter can be modelled. Some of these forces are aerodynamic in nature and others are a result of gyroscopic effects. Finally, in section 15.4, the forces that work on the fuselage are discussed.

15.1 Reference frames

The first step of deriving the equations of motion of any vehicle is choosing a convenient frame of reference. If this frame is chosen properly this can greatly simplify the expressions of the equations of motion. In literature related to quadcopters, there are several reference frames that are common, and a choice between these are made depending on the application.

The inertial frame is commonly used as a frame where Newtons second law can directly be applied. This means this frame does not rotate and does not linearly accelerate. However, concepts like rotation and acceleration are relative in nature. That means, it is not necessarily trivial with respect to what the frame can not rotate and accelerate. For aviation, generally the inertial reference frame is chosen as a frame with its origin in the center of the earth, and with its axes pointing in a fixed direction in space. This way the effects of the rotation of the earth can be modelled accurately for aircraft that translate over a significant portion of earths surface. Small scale UAV's however do not move fast and far enough to really make these effects significant. Therefore, for smaller aircraft it is common to chose the inertial frame fixed to the rotating earth, so that the

frame rotates with the earth. In literature on quadcopter control, this frame is generally assumed to be the inertial frame where Newtons second law holds.

The second frame that is used extensively in literature is the body frame, as shown in Figure 15.1 This frame is commonly used to describe the equations of motion of vehicles in general, and is a frame which translates and rotates with the body of the quadcopter. Usually the x-axis is chosen to point towards the front of the quadcopter and the y-axis to the right. This choice of axis direction is common in aerospace engineering, since it causes intuitive directions of positive rotations. A positive rotation around the y-axis corresponds to nose up rotation, and a positive rotation around the z-axis causes a yaw rotation to the right, which is consistent with increasing heading angle. Furthermore, it is often preferred to let origin of the body frame coincide with the CG (center of gravity) of the quadcopter because this removes the effect of mass offset on the equations of motion. However, in practical application it is often difficult or impractical to determine the exact position of the CG. Therefore, the origin of the body frame is often chosen at some other convenient point on the quadcopter, such as the point where are the arm lengths to the motors are equal.

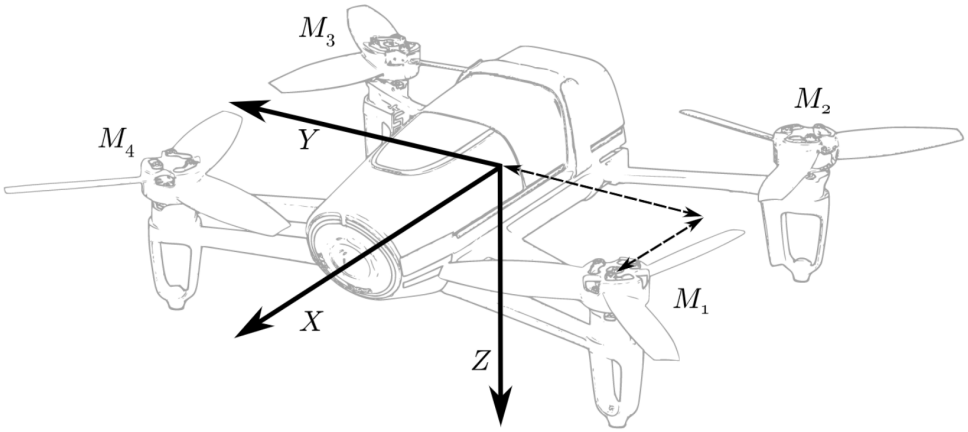

Figure 15.1: Body frame drawn on a Parrot Bebop quadcopter. (from [1], modified)

The body frame is a very common reference frame for the description of aircraft dynamics. The property that makes this frame so useful for aircraft, and a lot of other vehicles, is that the behaviour of many forces that the aircraft is subjected to are not related to the attitude of the aircraft itself. For example, the propulsion system is fixed to the airplane and generates a force in a direction that is always the same with respect to the aircraft. Expressing these thrust forces in a body frame is therefore a lot easier compared to some other reference frames. Another example are the aerodynamic forces. The magnitude and direction of these forces are generally not dependent on the attitude of the aircraft, but rather on the direction of the incoming airflow with respect to the airplane.

For a lot of models of quadcopter dynamics only the hover condition is considered. Aerodynamic forces are therefore not relevant. As will be explained in more detail later in this chapter, the only significant forces that work on the quadcopter are then the thrust forces and gravity. Because the thrust force is now the only force that rotates with the body of the quadcopter, the advantage of using a body frame becomes quite minimal

for the translational equations of motion. Therefore, in some research the translational equations of motion are expressed in the inertial frame rather than the body frame.

15.2 Translational and rotational equations of motion

The quadcopter is an under actuated dynamical system where only four motor control inputs can be used to control motion around three translation axes and three rotation axes. Because the rotational and translational dynamics are intertwined, the quadcopter still forms a controllable system. Below a mathematical description will be given of the dynamics equations which will shed more light on the way the dynamics are coupled.

Let the vector $\boldsymbol{r}$ describe the position of a reference point on the quadcopter with respect to the inertial frame. The final equations of motion will describe the motion of this specific point. This reference point can be conveniently chosen, such as the point where the moment arms of all the motors have the same magnitude. Let the vector $\boldsymbol{x}_{cg}$ describe the position of the CG of the quadcopter with respect to the reference point. This vector is assumed to be constant in the body frame, meaning there is no movement of the CG with respect to the quadcopter itself.

In scientific articles related to quadcopter control the translational equations of motion are often expressed in the inertial frame. The velocity of the CG can be expressed as function of the velocity of the reference point, $\boldsymbol{v}$, the rotation rate of the body frame, $\boldsymbol{\Omega}$, and the position of the CG, $\boldsymbol{x}_{cg}$, as is shown in Eq. 15.1.

$$\begin{aligned} \left.\frac{d(\boldsymbol{r}+\boldsymbol{x}_{cg})}{dt}\right|_I &= \left.\frac{d\boldsymbol{r}}{dt}\right|_I + \left.\frac{d\boldsymbol{r}}{dt}\right|_b + \boldsymbol{\Omega}\times\boldsymbol{x}_{cg} \\ &= \left.\frac{d\boldsymbol{r}}{dt}\right|_I + \boldsymbol{\Omega}\times\boldsymbol{x}_{cg} \\ \boldsymbol{v}_{cg} &= \boldsymbol{v} + \boldsymbol{\Omega}\times\boldsymbol{x}_{cg} \end{aligned} \tag{15.1}$$

Here $\boldsymbol{v}_{cg}$ is the velocity of the CG with respect to the inertial frame. From this expression for velocity, the acceleration can be derived as shown in Eq. 15.2.

$$\begin{aligned} \left.\frac{d\boldsymbol{v}_{cg}}{dt}\right|_I &= \left.\frac{d\boldsymbol{v}}{dt}\right|_I + \left.\frac{d\boldsymbol{\Omega}}{dt}\right|_I \times \boldsymbol{x}_{cg} + \boldsymbol{\Omega}\times\left.\frac{d\boldsymbol{x}_{cg}}{dt}\right|_I \\ &= \left.\frac{d\boldsymbol{v}}{dt}\right|_I + \dot{\boldsymbol{\Omega}}\times\boldsymbol{x}_{cg} + \boldsymbol{\Omega}\times\left(\left.\frac{d\boldsymbol{x}_{cg}}{dt}\right|_b + \boldsymbol{\Omega}\times\boldsymbol{x}_{cg}\right) \\ &= \dot{\boldsymbol{v}} + \dot{\boldsymbol{\Omega}}\times\boldsymbol{x}_{cg} + \boldsymbol{\Omega}\times(\boldsymbol{\Omega}\times\boldsymbol{x}_{cg}) \end{aligned} \tag{15.2}$$

Substituting in the second law of Newton then gives Eq. 15.3, where $\boldsymbol{F}$ denotes the summation of all external forces except for gravity, which is denoted by $\boldsymbol{g}$. The variable m is the mass of the complete quadcopter.

$$\boldsymbol{F}+\boldsymbol{g} = m(\dot{\boldsymbol{v}} + \dot{\boldsymbol{\Omega}}\times\boldsymbol{x}_{cg} + \boldsymbol{\Omega}\times(\boldsymbol{\Omega}\times\boldsymbol{x}_{cg})) \tag{15.3}$$

$$\dot{\boldsymbol{v}} = \frac{1}{m}\left[\boldsymbol{F}+\boldsymbol{g}+\boldsymbol{x}_{cg}\times\dot{\boldsymbol{\Omega}}+\boldsymbol{\Omega}\times(\boldsymbol{x}_{cg}\times\boldsymbol{\Omega})\right] \tag{15.4}$$

If the CG is chosen as reference point, $\boldsymbol{x}_{cg} = \mathbf{0}$ and Eq. 15.3 reduces to Eq. 15.5. This is often done together with the assumption that the CG is located in the center of the quadcopter.

$$\dot{\boldsymbol{v}} = \frac{1}{m}(\boldsymbol{F} + \boldsymbol{g}) \tag{15.5}$$

The rotational acceleration can be derived using the Euler equation of rotation, as shown in Eq. 15.6. Here $\boldsymbol{M}_{rp}$ is the sum of all moments around the reference point and I_v is the vehicles mass moment of inertia as shown in Eq. 15.7. It is assumed that the quadcopter is symmetric in terms of mass in the xz-plane of the body frame, equating some terms in the inertia matrix to zero.

$$\dot{\boldsymbol{\Omega}} = I_v^{-1}(\boldsymbol{M}_{rp} - \boldsymbol{x}_{cg} \times \boldsymbol{F} - \boldsymbol{\Omega} \times I_v \boldsymbol{\Omega}) \tag{15.6}$$

$$I_v = \begin{bmatrix} I_{xx} & 0 & -I_{xz} \\ 0 & I_{yy} & 0 \\ -I_{xz} & 0 & I_{zz} \end{bmatrix} \tag{15.7}$$

If the reference point on the quadcopter does not coincide with the CG, the force $\boldsymbol{F}$, which works on the reference point, also contributes to $\boldsymbol{M}_{rp}$ through the moment arm $\boldsymbol{x_{cg}}$. Hence the $\boldsymbol{x}_{cg} \times \boldsymbol{F}$ term appears in Eq. 15.6. If the reference point does coincide with the CG, $\boldsymbol{x}_{cg} = \mathbf{0}$ and Eq. 15.6 reduces to Eq. 15.8, where $\boldsymbol{M}_{cg}$ is the sum of moments around the CG.

$$\dot{\boldsymbol{\Omega}} = I_v^{-1}(\boldsymbol{M}_{cg} - \boldsymbol{\Omega} \times I_v \boldsymbol{\Omega}) \tag{15.8}$$

The translational and rotational equations of motion can be combined into one vector equation as shown in Eq. 15.9 and Eq. 15.10. The vector on the right in Eq. 15.9 contains the forces and moments seen by the quadcopter. Note that the direction of $\boldsymbol{F}$ and $\boldsymbol{M}_{rp}$ are dependent on $\boldsymbol{\eta}$, since all vectors are expressed in the inertial frame.

$$\begin{bmatrix} \dot{\boldsymbol{R}} \\ \dot{\boldsymbol{v}} \\ \dot{\boldsymbol{\eta}} \\ \dot{\boldsymbol{\Omega}} \end{bmatrix} = \begin{bmatrix} \boldsymbol{v} \\ \frac{1}{m}\left(\boldsymbol{g} + \boldsymbol{x}_{cg} \times \dot{\boldsymbol{\Omega}} + \boldsymbol{\Omega} \times (\boldsymbol{x}_{cg} \times \boldsymbol{\Omega})\right) \\ R(\boldsymbol{\eta})\boldsymbol{\Omega} \\ -I_v^{-1}(\boldsymbol{\Omega} \times I_v \boldsymbol{\Omega}) \end{bmatrix} + \begin{bmatrix} 0 \\ \frac{1}{m}\boldsymbol{F} \\ 0 \\ I_v^{-1}(\boldsymbol{M}_{rp} - \boldsymbol{x}_{cg} \times \boldsymbol{F}) \end{bmatrix} \tag{15.9}$$

$$R(\boldsymbol{\eta}) = \begin{bmatrix} 1 & \sin\phi\tan\theta & \cos\phi\tan\theta \\ 0 & \cos\phi & -\sin\phi \\ 0 & \frac{\sin\phi}{\cos\theta} & \frac{\cos\phi}{\cos\theta} \end{bmatrix} \tag{15.10}$$

Again, Eq. 15.9 simplifies quite a bit when the reference point is taken to coincide with the CG. It can be seen that the translational dynamics are dependent on the states related to rotation, but not the other way around. This is not considering the moments and forces, which could theoretically be modeled as being dependent on any combination of states. Furthermore, in practice the rotational dynamics are much faster the translational dynamics. This means that based on the principle of time scale separation [47] the rotational and translational dynamics are often treated and incorporated in a cascaded manner.

A more complex task is modeling the forces $\boldsymbol{F}$ and moments $\boldsymbol{M}_{rp}$. These can be decomposed into aerodynamic forces and moments on the fuselage, gyroscopic moments due to the rotating propellers, propulsive forces and moments generated by the propellers and finally, any additional external forces such as swing loads and interaction with solid objects. How these can by modeled will be discussed in subsequent chapters, with the exception of external forces since this is highly dependent on the application.

15.3 Forces and moments generated by the propellers

Propellers have been used to propel aircraft since the beginning of aviation. Therefore a lot of research and mathematical modeling has been performed over the years to estimate various characteristics of propeller designs. For fixed wing aircraft, preforming preliminary estimations of the propellers thrust, required power and other values is relatively straight forward. This is because normally the air flows into the rotor disk plane at an almost perpendicular angle. Furthermore the inflow velocity is positive. This allows for some significant simplifications in the mathematical models.

Due to the long lasting popularity of helicopters, somewhat more extensive models exist that allow the propeller to have a inflow component that is in plane with the rotor disk. This is sometimes referred to as propeller edgewise flight, which is a typical mode of operation for helicopters. The most well known and effective models are MT (momentum theory) and BEM (blade element theory). Combining equations of both models result in BEMT (blade element momentum theory). Since this is considered standard rotor aerodynamic theory, there exist a large amount of literature on this topic [10, 11].

Some important relations of BEMT are discussed in subsection 15.3.1. A more complicated mode of operation occurs when the rotor sees significant negative inflow. This occurs for example when a helicopter or quadcopter descents rapidly. The rotor will enter the VRS (vortex ring state), the TWS (turbulent wake state) and finally the WBS (windmill brake state). This topic is discussed in subsection 15.3.2. Finally, in subsection 15.3.3 some of the propeller interaction effects are discussed that are specific for the quadcopter configuration.

15.3.1 Isolated propeller operating in steady conditions

As mentioned before, when air is flowing perpendicular through rotor disk plane, relatively accurate analytical models exist to describe the characteristics of the propeller, such as the generated forces. Often times non dimensional parameters are used in calculations. One of these parameters is the thrust coefficient, which is the thrust generated by the propeller in non dimensional form. The expression for the thrust coefficient is shown in Eq. 15.11, where ρ is the air density, A is the area of the rotor disk, ω the rotational speed of the rotor and R the rotor radius. It can be shown using the Buckingham Pi theorem that C_T is a function of the propeller geometry, the Reynolds number, the Mach number of the blade and the advance ratio(s). The advance ratio is a value proportional to the distance travelled through the air by the propeller after a full revolution. It is therefore a measure of the total airspeed or separate airspeed components with respect

to the rotation speed of the propeller.

$$C_T = \frac{T}{\rho A(\omega R)^2} \tag{15.11}$$

Using BEMT, a set of equations can be derived that allows for calculating the total thrust T and the induced velocity v_i, as shown in Eq. 15.12 and Eq. 15.13. These equations can be derived from equations given in Johnson [11]. This is also done by Powers at al [48] although here the sign of one of the terms is switched for unclear reasons. The induced velocity is the increase in speed perpendicular to the rotor disk that is given to the air once it crosses the rotor disk. In these equations, V is the total airspeed, a the blade section two-dimensional lift curve slope, b the amount of blades of the rotor, c the blade chord, θ is the blade pitch angle which is assumed to be constant over the span of the blade, and α the angle of attack of the rotor disk. The equations have to be solved simultaneously, which is not always possible analytically.

$$T = 2\rho A v_i \sqrt{V^2 + 2V v_i \sin\alpha + v_i^2} \tag{15.12}$$

$$T = \frac{\rho a b c \omega^2 R^3}{2}\left[\frac{\theta}{3} + \frac{V^2\theta\cos^2\alpha}{2\omega^2R^2} - \frac{V\sin\alpha + v_i}{2\omega R}\right] \tag{15.13}$$

A large amount of literature on quadrotor dynamics assumes that the airspeed seen by the propellers is zero [23, 1, 24, 25]. That is, $V = 0$. Substituting into Eq. 15.12 and Eq. 15.13 results in a linear system of equations with respect to T and v_i. From this it follows that the trust T is equal to a constant K times the rotor rotation speed squared, as shown in Eq. 15.14. In a hover condition, this model has been shown to hold up well during experiments [23, 26]. With larger speeds however, assuming the speed to be nonzero can make a significant difference noticeable from speeds higher than $2\,\mathrm{m\,s^{-1}}$ [48]. The airspeed V does not necessarily have to be caused only by translation of the quadcopter, but can also be due rotation of the quadcopter itself [27].

$$T = K \cdot \omega^2 \tag{15.14}$$

The path that is followed by the rotor tips describes a circle in steady state. The plane through this circle is commonly referred to as the TPP (tip path plane). In hover or vertical flight, this TPP is parallel to the SNP (shaft normal plane), which is always perpendicular to the rotor axle. However, as soon as the rotor experiences an edge wise velocity component, the TPP will tilt with respect to the SNP. This effect is commonly referred to as blade flapping. As a result of this the thrust vector will tilt as well. This results in a drag force. This drag force is supplemented by the rotor drag force itself. The equation for this latter drag force is similar to Eq. 15.13 [11]. The combination of the thrust vector tilt and rotor drag force results in the total generated drag. The rotor side force in y-direction can be calculated in the exact same way.

The rotor drag force and side force are generally really small with respect to the generated thrust. Side forces have been found to be negligible for quadcopters during

experiments [6]. Besides this, for quadcopter configurations the side forces are largely cancelled out due to the counter rotating propeller pairs. Drag and side forces are also less relevant for quadcopters than they are for helicopters. This is because the CG of quadcopters is often very close to the rotor plane. This is not the case for helicopters, where these forces can generate significant pitch and roll moments.

Blade flapping was studied and implemented in a controller for a drone with lower CG than the rotor plane, and relatively large and flexible rotors enhancing the flapping effect [49]. A TPP angle is found of 5° at a speed of $10\,\mathrm{m\,s^{-1}}$. In the same research project a thrust model is included taking into account the thrust variation due to a change in angle of attack. A hard braking manoeuvre is performed showing significant improvements in altitude control of the quadcopter. Unfortunately, it is not further discussed how much of this improvement is due to the blade flapping model and how much due to the angle of attack model, where it has been shown that this last effect has significant influence [50]. Due to the fact that quadcopter rotor blades are directly mounted to the rotor hub without hinges or flexible structural connections, blade flapping is not often included in control models.

Besides a set of forces, there is also a moment generated by an isolated propeller. This moment can be decomposed into a pitch moment, a roll moment an yaw moment. The yaw moment can be explained as the torque required to overcome the drag and MMOI of the rotor, and is explained in more detail in subsection 15.3.4.

Pitch and roll moments are generated by the rotor due to the following effects. Firstly, in edgewise flight with higher airspeed, the thrust distribution shifts towards the part of the rotor where the blades advance into the wind, since the airspeed seen by the blades is highest here. Secondly, the propeller operates in its own down wash, making the back of the rotor generate less lift compared to the front [8]. Lastly, if the rotor head or flexibility of the rotor blades allow for a significant coning angle, the rear blades will see a lower angle of attack compared to the front, again shifting lift to the front of the rotor. It should be noted that modeling lift distribution on small scale propellers is still an active field of research [51]. When infinitely stiff blades are assumed with no flapping hinges, the lift distribution on a quadcopter rotor is estimated as shown in Figure 15.2.

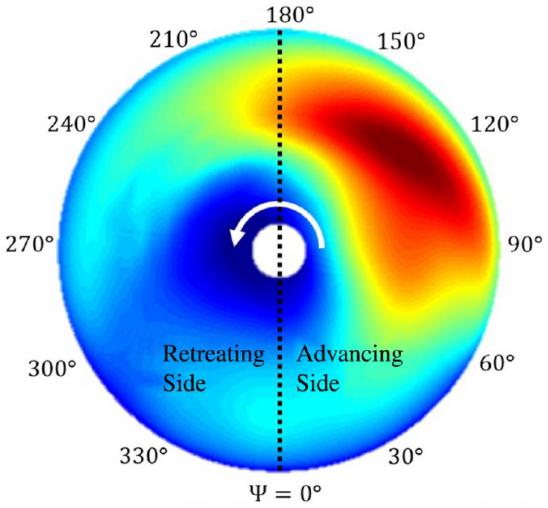

Figure 15.2: (from [8])

The combination of the gyroscopic effect and the ability of the blades to move with respect to the rotor head causes a shift of the lift distribution that was shown in Figure 15.2. For most helicopters, the blades are attached to the rotor hub using a set of hinges. In this case the shift in lift is caused by a tilt of the TPP. The downward tilt of the TPP happens 90° later than the point of highest lift. For example, if the maximum lift is located at the front of the rotor, the TPP will tilt downwards towards the left. This tilt redistributes the lift over the rotor, since TPP tilt influences the angle of attack of the blades at various stages in a rotational cycle. This redistribution of lift causes the average point of lift shift to the center of the rotor again, allowing the fuselage to experience very little moment. Together with greatly reduced stress on the blades, this is one of the main reasons fully articulated rotor heads are used in helicopters.

For quadcopters the situation is different due to the very rigid connection between the blades and the rotor hub. Instead of tilting the TPP, the original lift distribution is directly passed on the quadcopter body. In a way the rotor has very little freedom to balance its own lift distribution. Now, the advancing blades generate more lift causing a roll moment to the opposite side. Furthermore, due to the down wash effect, the extra lift in the front of the rotor causes a pitch up moment. These two moments are again reflected in Figure 15.2, and can indeed be observed in experiments [39]. Due to the general rigidity of the propellers of quadcopters there is a negligible coning angle, removing the associated pitch up moment.

15.3.2 Isolated propeller operating in the vortex ring state and beyond

When a rotorcraft descents vertically in a normal orientation, the advance ratio of the propeller becomes negative. That is, the airflow outside the rotor craft is in the opposite direction of the downwash generated by the propeller itself. As the advance ratio becomes more negative, the airflow in the center of the rotor will start to move up through the rotor, since the blades move slowest here. A vortex will emerge at the boundary of the air moving up and down in the plane of the rotor. Decreasing the advance ratio even more increases the size of this vortex, which now influences a larger part of the rotor. Also a

large tip vortex emerges. This state is referred to as the VRS, as shown in Figure 15.3. Since the airflow in the rotor is now highly turbulent and a lot of energy is lost in the additional vortex, there will be a loss of thrust and significant increase in vibration and thrust fluctuation.

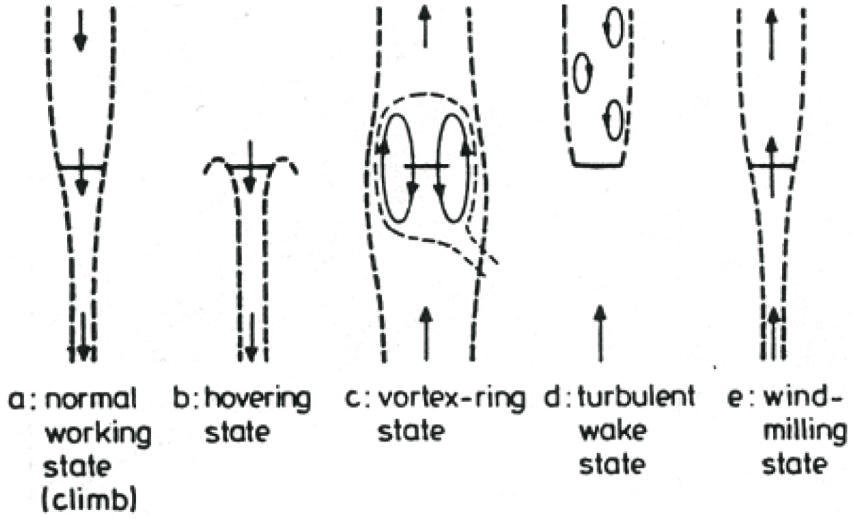

Figure 15.3: Schematic representation of ascent, hover, VRS, TWS and WBS.

Decreasing the advance ratio even more, a new state can be identified. In this state the majority of the airflow is upwards through the rotor, making the rotor behave more as a bluff body. This state is referred to as the TWS, and is the state covering the situation where the induced power is equal to the power extracted from the air stream. This situation is often tempted to be reached during helicopter autorotation which can be applied in emergency scenarios where there is a loss of power. A rotor in the TWS behaves somewhat similar to a flat disk generating a turbulent wake above it. Although the net flow through the rotor is almost zero, locally there is still quite some recirculation in the rotor disk, accompanied by turbulent airflow. However, because the vortices to not remain at the location of the rotor disk but are rather dissipated above the rotor, this state is characterised by a lot less thrust fluctuation and more control authority compared to the VRS. Furthermore, for the VRS and TWS, BEMT does not hold, making these states more difficult to model.

Finally there is the WBS. In this state there is clear upflow through the rotor, but the airflow is slowed down, generating a lifting force on the rotor. The power extracted from the air stream is more than the induced power, making the rotor function like a windmill. The boundary between the TWS and WBS is usually quite sharp, in contrast to the boundaries between the other rotor operating states.

The above mentioned rotor states originate for a majority from studies on helicopters, which typically control the pitch of the blades to control thrust. Quadcopters on the other hand make use of fixed pitch propellers and control thrust by varying rotor rpm. That means that some of these states function differently or are unreachable. For example, the autorotation can not be performed with quadcopters, and the more extreme WBS can not be reached [12]. Somewhere in the regions where the TWS and WBS occur for helicopters, other effects will likely become apparent such as blade stalling.

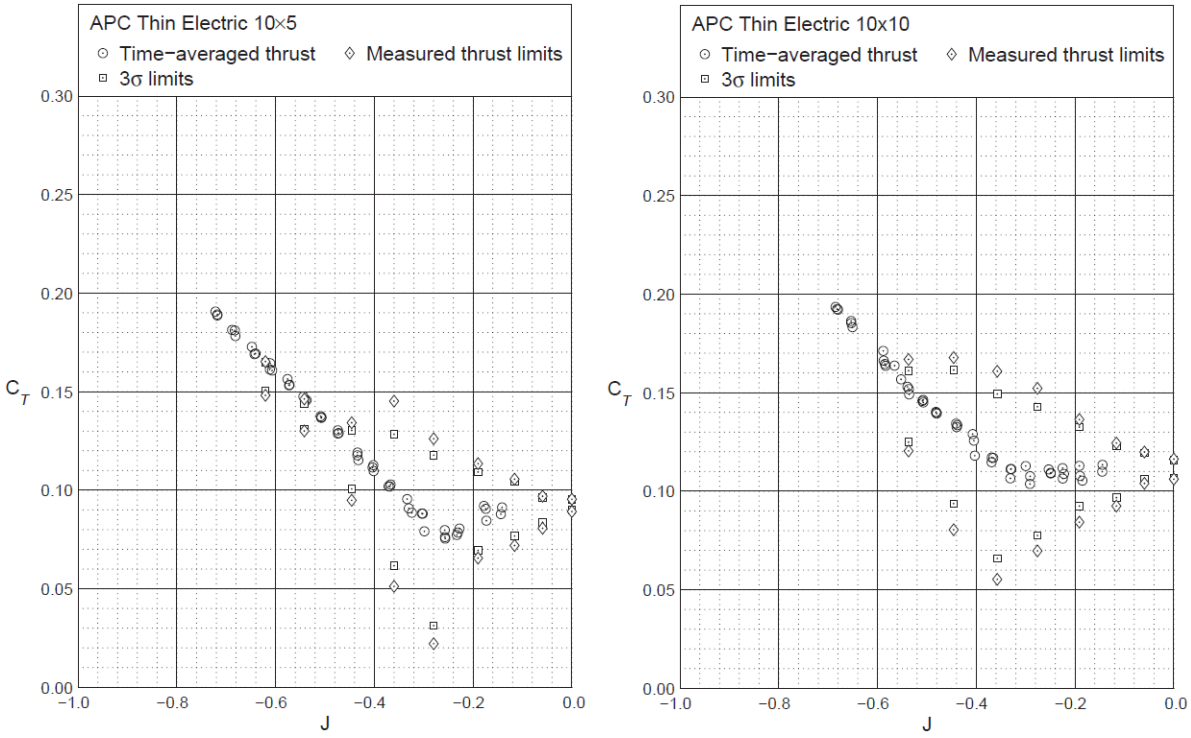

Figure 15.4: Thrust for negative advance ratios measured experiments. (from [52])

Unfortunately, small propellers with fixed pitch operating under large negative advance ratios is not extensively researched. Some experiments have been performed [52] on rotors of 25 cm in diameter with speeds up to $13\,\mathrm{m\,s^{-1}}$, of which some results are shown in Figure 15.4. It is found that for all tested propellers C_T decreases initially as the descent speed is increased. At higher speeds C_T increases again. The higher the pitch, the lower the advance ratio at which the minimum of C_T occurs, and the higher the value of the minimum C_T. Also the minimum is flatter, and thrust fluctuations are higher. Note that most racing drones have propellers that are twice as small in terms of diameter.

In helicopter flight it is common to avoid the VRS due to its unsteady and chaotic nature. For quadcopters this strategy is usually adopted, where for example drone racing manoeuvres are adjusted to avoid the VRS. Research has been performed in the past few years focusing on guidance and control algorithms that optimizes trajectories that stay out of the VRS [12, 13]. This is done by using models predicting in which flight states the VRS can occur [14].

15.3.3 Rotor Interaction

In previous sections a rotor is discussed that is isolated. In quadcopters there are four propellers operating in close vicinity to each other. Therefore it is not surprising that in general, each rotor influences the forces and moments generated by the other propellers. Modeling this interference is still an active field of research.

It has been observed that during hover, the interference between the propellers is small [6]. Significant interference starts to develop once one of the propellers operate partly in the wake of another propeller. This is the case when the quadcopter is flying

forward with a relatively low fuselage pitch angle. In this situation the rear propellers operate in the wake of the front propellers.

To understand this interaction effect better, the wake of a small scale propeller has been analysed in edgewise flight using CFD [8], as shown in Figure 15.5. It can be seen that the wake is not symmetrical, and is more pronounced at the side of the propeller with the advancing blade. This makes sense, since for a constant pitch propeller with no flapping and lead/lag hinges, the generated lift is highest for the advancing blade. On the side with the advancing blade, the roll up vortex is larger, and is deflected downwards with a higher angle compared to the retreating blade side. As a result of this, the wake in its entirety slightly deflects towards the side of the advancing blade.

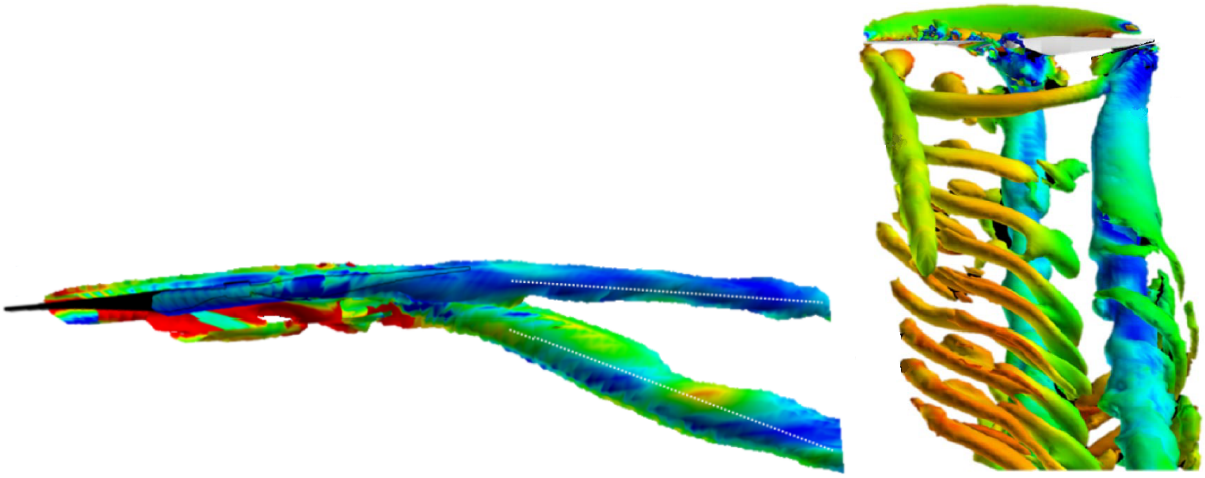

(a) Side view (b) Rear view

Figure 15.5: CFD simulation of the wake of a propeller in edgewise flight (from [8], modified).

In edgewise flight, the front propellers see a relatively clean airflow. That means that the front propellers behave relatively similar to propellers in isolation as discussed in subsection 15.3.1. This is visualised in Figure 15.6, indicating the difference in lift distribution of propellers in quadcopter configuration compared to an isolated rotor. The rear propellers on the other hand are partly exposed to the wake of the front propellers. Especially the front of the rear rotors see quite some downwash, since this area is positioned closest to the front rotor wake. More rearward, the front rotor wake has moved down enough to significantly decrease its influence on the thrust of the rear rotor. The degradation of thrust is therefore prominent in the front of the rear rotor.

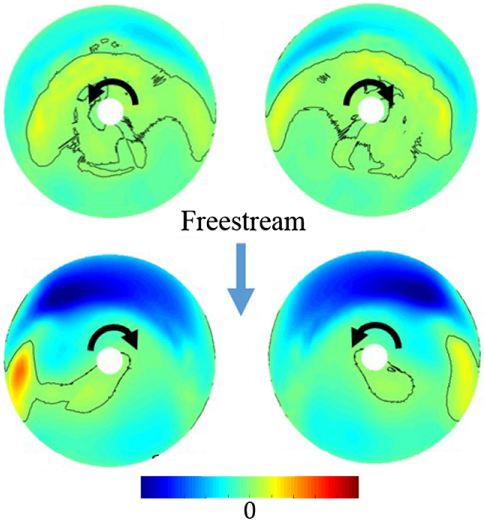

Figure 15.6: CFD calculated difference in lift distribution compared to the four rotors in isolation in forward flight, breaststroke configuration. (from [8], modified).

It was mentioned that the wake of a propeller moves slightly sideways due to difference in advancing and retreating blades. Therefore, the outside edge of the the rear propellers are positioned just outside of the wake by a small amount. In fact, this small portion of the rear rotor sees an upwash, which is typically found just outside the propeller wash. This upwash effect can be seen as the small red area on the side of the rear propellers in Figure 15.6. Now, it is not a stretch to imagine that a slight yaw angle would move one prop into more downwash, and the other rear prop into less downwash. This would result in a roll moment. Unfortunately no research was found confirming this line of thought.

The downwash seen by the rear propellers causes a reduction of thrust for the rear propeller. Research focusing on horizontal straight flight found that for airspeeds of around $10\,\mathrm{m\,s^{-1}}$ to $15\,\mathrm{m\,s^{-1}}$ the interaction effect becomes significant [6]. Note that this is partly due to the fact that a particular flight speed corresponds to a certain angle of attack to overcome the drag of the quadcopter. It could be that a quadcopter with very aerodynamic bodywork can fly at a lower angle of attack, changing the flight speed at which maximum interference happens. Thrust of the rear motors is impacted for speeds up to $11\,\mathrm{m\,s^{-1}}$ [6]. Rotor torque on the other hand does not change significantly, which means more power is required by the rear propellers. This makes sense since a propeller operating in a downwash requires more power to generate the same amount of thrust.

15.3.4 Gyroscopic rotor effects

The equations of motion from Eq. 15.9 hold for a rigid body. However, because the propellers rotate with quite a significant speed with respect to the airframe, strictly speaking, the total quadcopter can not be regarded as a rigid body. It can be shown that the rotating propellers do not change the equations of motion when it comes to translation of the quadcopter. The rotation of the propellers does however introduce an additional moment in the rotational part of the equations of motion. This is due to the gyroscopic effect and a reaction torque caused by each individual propeller.

The moments exerted by a propeller on the airframe due to rotation of the propeller itself can be derived by using the Euler equation of rotation, as shown in Eq. 15.15. Here $\boldsymbol{M}$ is the moment exerted by the airframe on the propeller expressed in the body frame, and $-\boldsymbol{M}$ is thus the moment exerted on the airframe by the propeller. The vector $\boldsymbol{\Omega}_r$ is the rotation speed of the propeller with respect to the inertial frame, expressed in the body frame. The matrix I_r is the mass moment of inertia of a propeller in the body frame as shown in Eq. 15.16. A three bladed propeller has the property that $I_{xy} = I_{yz} = I_{xz} = 0$ and $I_{xx} = I_{yy}$. Note that it is assumed that the propeller has no mass distribution in the z-direction.

$$\boldsymbol{M} = I_r \dot{\boldsymbol{\Omega}}_r + \boldsymbol{\Omega}_r \times I_r \boldsymbol{\Omega}_r \tag{15.15}$$

$$I_r = \begin{bmatrix} I_{xx} & -I_{xy} & -I_{xz} \\ -I_{xy} & I_{yy} & -I_{yz} \\ -I_{xz} & -I_{yz} & I_{zz} \end{bmatrix} = \begin{bmatrix} I_{xx} & 0 & 0 \\ 0 & I_{yy} & 0 \\ 0 & 0 & I_{zz} \end{bmatrix} \tag{15.16}$$

$$I_{xx} = \int y^2 + z^2 \, dm \qquad I_{yy} = \int x^2 + z^2 \, dm \qquad I_{zz} = \int x^2 + y^2 \, dm$$

$$I_{xy} = \int xy \, dm \qquad I_{xz} = \int xz \, dm \qquad I_{yz} = \int yz \, dm$$

The rotation of the propeller in the inertial frame is equal to the sum of the rotation of the quadcopter $\boldsymbol{\Omega}_v$, and the rotation of the propeller with respect to the quadcopter $\boldsymbol{\Omega}_{rv}$, as shown in Eq. 15.17. Substituting this sum into Eq. 15.15 results in Eq. 15.18.

$$\boldsymbol{\Omega}_r = \boldsymbol{\Omega}_v + \boldsymbol{\Omega}_{rv} \tag{15.17}$$

$$\begin{aligned}
\boldsymbol{M} &= I_r(\dot{\boldsymbol{\Omega}}_v + \dot{\boldsymbol{\Omega}}_{rv}) + (\boldsymbol{\Omega}_v + \boldsymbol{\Omega}_{rv}) \times I_r(\boldsymbol{\Omega}_v + \boldsymbol{\Omega}_{rv}) \\
&= I_r\dot{\boldsymbol{\Omega}}_v + I_r\dot{\boldsymbol{\Omega}}_{rv} + [\boldsymbol{\Omega}_v \times I_r\boldsymbol{\Omega}_v] + [\boldsymbol{\Omega}_v \times I_r\boldsymbol{\Omega}_{rv}] + [\boldsymbol{\Omega}_{rv} \times I_r\boldsymbol{\Omega}_v] + [\boldsymbol{\Omega}_{rv} \times I_r\boldsymbol{\Omega}_{rv}] \\
&= \begin{bmatrix} 0 \\ 0 \\ I_{zz}\dot{\omega} \end{bmatrix} + \begin{bmatrix} I_{xx}\dot{p} \\ I_{yy}\dot{q} \\ I_{zz}\dot{r} \end{bmatrix} + \begin{bmatrix} p \\ q \\ r \end{bmatrix} \times \begin{bmatrix} I_{xx}p \\ I_{yy}q \\ I_{zz}r \end{bmatrix} + \begin{bmatrix} p \\ q \\ r \end{bmatrix} \times \begin{bmatrix} 0 \\ 0 \\ I_{zz}\omega \end{bmatrix} + \begin{bmatrix} 0 \\ 0 \\ \omega \end{bmatrix} \times \begin{bmatrix} I_{xx}p \\ I_{yy}q \\ I_{zz}r \end{bmatrix} \\
&\quad + \begin{bmatrix} 0 \\ 0 \\ \omega \end{bmatrix} \times \begin{bmatrix} 0 \\ 0 \\ I_{zz}\omega \end{bmatrix} \\
&= \begin{bmatrix} I_{xx}\dot{p} \\ I_{yy}\dot{q} \\ I_{zz}(\dot{r} + \dot{\omega}) \end{bmatrix} + \begin{bmatrix} I_{zz}qr - I_{yy}qr \\ I_{xx}pr - I_{zz}pr \\ I_{yy}pq - I_{xx}pq \end{bmatrix} + \begin{bmatrix} qI_{zz}\omega \\ -pI_{zz}\omega \\ 0 \end{bmatrix} + \begin{bmatrix} -I_{yy}q\omega \\ I_{xx}p\omega \\ 0 \end{bmatrix} \\
&= \begin{bmatrix} I_{xx}\dot{p} \\ I_{yy}\dot{q} \\ I_{zz}(\dot{r} + \dot{\omega}) \end{bmatrix} + \begin{bmatrix} I_{zz}qr - I_{yy}qr + qI_{zz}\omega - I_{yy}q\omega \\ I_{xx}pr - I_{zz}pr - pI_{zz}\omega + I_{xx}p\omega \\ 0 \end{bmatrix} \\
&= \begin{bmatrix} I_{xx}\dot{p} \\ I_{yy}\dot{q} \\ I_{zz}(\dot{r} + \dot{\omega}) \end{bmatrix} + \begin{bmatrix} q(I_{zz} - I_{yy})(r + \omega) \\ p(I_{xx} - I_{zz})(r + \omega) \\ 0 \end{bmatrix}
\end{aligned} \tag{15.18}$$

The result of Eq. 15.18 is the specific result for three bladed propellers. The first vector in this equation accounts for the reaction torque of the propeller. Usually, only the last entry of this vector takes on significant values because generally $\dot{\omega} \gg \dot{r}$. The

second vector accounts for the gyroscopic effect. Considering a single propeller, a steady pitch rate of the airframe gives rise to a steady roll moment and vice verse. In case all propellers rotate at the same rotation rate, this gyroscopic effect is cancelled out due to their opposite rotation directions.

For two bladed propellers, $I_{xx}(t) \neq I_{yy}(t)$. Both variables vary according to a sine function where the lowest value is equal to zero. The amplitude of both is the same and equal to some positive value. Furthermore, I_{xy} is also a sine function oscillating around zero. All three values have a frequency of twice the rotation speed, but have different phases. The I_{xy} value is shifted with 45° with respect to I_{xx}, and I_{yy} with 90° with respect to I_{xx}. This oscillation behaviour of two bladed propellers at aggressive maneuvering could be one of the reasons racing drones often use three bladed propellers.

Smeur et al. [1] describes a similar derivation of the gyroscopic effects. However, the initial Euler equation that is used is different than the standard Euler equation. Unfortunately it is unclear how this variation is obtained. Its stated that the values of I_{xx}, I_{yy} and I_{xy} are not constant (and thus non zero), but disappear from the equation due to the propellers not having a rotational component in the body x-axis and y-axis. This statement is inaccurate since the Bebob drone has three bladed propellers which means the I_{xx}, I_{yy} terms are in fact constant, and $I_{xy} = 0$. Furthermore, in the gyroscopic effect terms the factors $(I_{zz} - I_{yy})$ and $(I_{xx} - I_{zz})$ are simply replaced with just I_{zz}. The validity of this is questionable since I_{xx}, I_{yy} and I_{zz} of a three bladed propeller are generally of the same order of magnitude.

15.4 Forces and moments generated by the fuselage

Compared to forces generated by the propellers, forces and moments generated by the airframe is somewhat more predictable. The actual forces and moments obviously depend on the shape of the airframe. As usual, the force can be split up into a drag force, lift force and lateral force. The moment working on the airframe can be divided by a pitch moment, roll moment and a yaw moment. The aerodynamic model of the airframe in isolation is in general difficult to derive, and can only really be obtained by measuring forces in either a wind tunnel or using CFD and varying the velocity vector.

The difficult part in estimating forces on the airframe is that the airflow around the airframe is heavily influenced by the spinning propellers. To include this interference effect, the effect of the propellers on the airflow needs to be included. It is not an option to test the complete airframe propeller combination since this would also include the forces generated by the propeller. One solution is using CFD, where it is possible to separate the forces generated by the airframe and propellers. Another theoretical option would be setting up the airframe and propellers in a wind tunnel in the normal configuration, while not physically connecting the airframe and propellers. This would allow for including the airflow as a result of the propellers, but only measuring the forces on the airframe. This would however be a tedious test setup to create.

In terms of modeling the complete quadcopter one could argue it is strictly not necessary to find the additional forces on the airframe as a result of the presence of the

propellers. It is also possible to just find the combination of the force due to the airframe and propellers, rather than trying to find their separate contributions. This essentially results in a grey box model that has shown to significantly improve the aerodynamic model of quadcopters in forward flight [53, 54]. The big downside of this method is of course that the amount of possible dependent variables has increased significantly. Now in addition to just the velocity vector, the aerodynamics are dependent on the rotational speeds of the four propellers. For experiments that make use of wind tunnel testing, this is often 'solved' by only considering horizontal straight symmetrical flight, allowing to only set the flight speed as the dependent variable.

That being said, CFD analyses shows that for a representative quadcopter in horizontal straight symmetrical flight [6], the additional drag force on the fuselage due to the propeller induced airflow is negligible. The same holds for the pitch moment. Lift on the other hand is influenced by the propellers. For most airframes it is can be assumed that a negative angle of attack causes a negative lift force. However, where the rear propellers operated in the downwash of the front propellers, the fuselage is located in the updraft of the vortices generated by the front propellers. Therefore there is an additional positive lift force on the fuselage that increases with increasing front propeller rotation speed, to the point where the lift can be positive at negative angles of attack. This study was performed on a bearhug configuration, as shown in Figure 15.7. It would be interesting to see how this last effect changes on a quadcopter with breaststroke configuration.

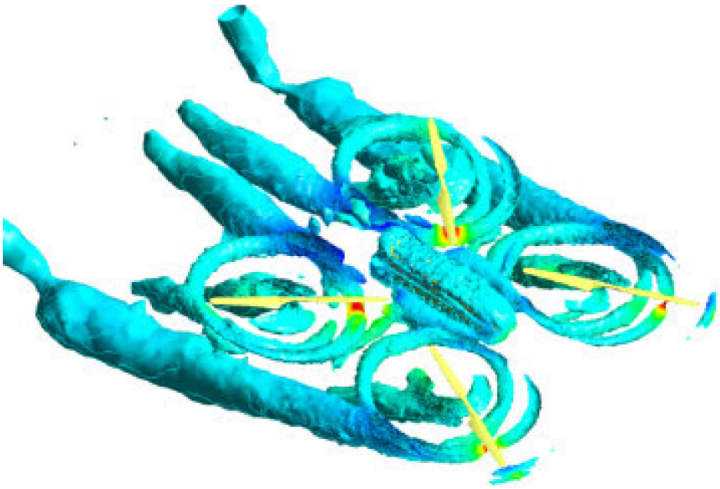

Figure 15.7: CFD analysis showing the rollup vortices prominent at the location of the advancing blades. (from [6])

Chapter 16

Advanced quadcopter control

As has become clear from chapter 15, the complete dynamic model of a quadrotor is highly nonlinear and modeling forces generated by the fuselage and propellers is still an active field of research. Around 2002 the first control algorithms were applied to quadcopters [55, 56]. Up to 2009, linear control techniques such as PID, LQR and H_∞ where found to effectively stabilise the quadcopter in conditions close to hover [29]. Between 2009 and 2013 the most amount of research has been performed on the topic of quadcopter control, including many nonlinear control strategies [31].

Due to the requirements of high speed maneuverable flight and fault tolerant behaviour, advanced control of quadcopters is still a field of research that is very much alive today. Due to the rapidly growing amount of applications of quadrotors, there is an increased need for quadcopters to safely perform high-speed trajectories in cluttered environments [57]. This often means that the assumptions that are made for linear control methods do not hold anymore, giving rise to the need for nonlinear controllers. When it comes to safety and reliability, FTC (fault tolerant control) allows for partly negating one of the big downsides of the quadcopter drone, which are its very exposed and vulnerable propellers. The FAA has recently announced new regulations describing the obligation for drones that fly over cities to be able to land with a rotor failure [58], highlighting the relevance of robust and adaptive control strategies.

The majority of the quadcopter control techniques make use of the so called time scale separation principle [59]. Here it is assumed that the attitude control is much faster than the position control allowing to cascade two controllers that control these two set of states independently. This is often referred to as the outer and inner loop, referring to the position control loop and the attitude control loop. At an even higher level there can be path planner [31], which is more in the realm of guidance rather than control. The position control can then be either implemented as an altitude hold mode, as a tracking algorithm using for example differential flatness [25] , or using a target position.

This chapter discusses some of the relevant control strategies when it comes to quadrotor control. First, in section 16.1, the important distinction will be made between adaptive and robust control philosophies. Then, in section 16.2, some of the most applied nonlinear control techniques are discussed. In section 16.3 the use of quaternions is treated both conceptually and how it can be applied directly to make an attitude controller. Finally, section 16.4 discusses the topic of FTC.

16.1 Robust and adaptive control

Many systems in the real world are nonlinear and stochastic in nature which makes linear control systems often only suitable for a specific range of system states. In subsequent sections, a selection of nonlinear controllers will be discussed. Nonlinear control is generally more complicated than linear control, but brings the great advantage of allowing optimal performance over a greater range of the nonlinear system. Unfortunately, when these controller are implemented and applied to a real world system, it is often found that the controlled system still does not perform optimal as described by its mathematics. There are many reasons why this could be the case, but there are at least two that are theoretically impossible to completely avoid in practice. These are model uncertainties and changing system dynamics.

Model uncertainties refer to the fact that it is rarely possible to describe a real life system with a hundred percent accuracy. This can be due to inability to capture the enormous complexity of real life systems, but also due to sensor noise and biases, computational errors and more. Also, in engineering applications a system is generally not modelled with the goal of achieving the highest possible accuracy due to other limitations, such as computational power necessary to simulate the model, time and effort required to obtain the model, and the general usability of the model. For control applications, where certain characteristics of the model are required, the model is kept even less complicated. That means that there is often significant mismatch in the mathematical control model and the real life system.

Besides this, the dynamics of a real life system often change as the system is being controlled. When looking at quadcopter control, there are numerous parameters that can change during flight, or in between flights. These changes can be related to drone itself, or due to its surroundings. Internal changes could be for example changes in the CG due to shifting batteries, a change in mass due to a payload being dropped, a damaged propeller and so on. External changes could be for example wind speed, air density or the ground effect. As these effects change the system dynamics, the applied controller will not perform the same compared to the original system.

The two system altering effects mentioned above can be dealt with using two very different control philosophies, namely robust control and adaptive control. Robust control focuses, as the name suggest, on designing a controller that is better able to deal with a changing system, without changing the control laws during operation. That means that when the system dynamics are different than modelled, or the dynamics change during operation, the robust controller will still be able to control the system according to certain requirements. This is contrary to adaptive control, which is based on the idea of changing the control laws during operation. The controller then adapts to the current situation.

A disadvantage of robust control is that the robustness is often based on the idea of conservatism. A robust controller can be made by tuning the controller in such a way that the system can change characteristics, but still remains stable. The issue is that generally maneuverability goes hand in hand with a low amount of stability, and vice verse. Therefore, to keep far away from an unstable system, the robust controller generally suffers in maneuverability. This illustrates that there is always the trade off

between robustness and performance. On the other hand, a big advantage is the relative simplicity of robust control, since model mismatch is not specifically dealt with in the controller. Furthermore, the speed at which the dynamics change does not impact the robustness, which makes robust control an effective solution for sudden, unpredictable and unmodelled changes to the system.

Adaptive control does not have to make the trade off between performance and robustness against model mismatch, which allows for high performance while being subjected to changes in system dynamics. Adaptive control involves monitoring output of the system and adapting the control law accordingly. Because the control system needs time to identify changing system dynamics, adaptive control is generally not suited for systems that change very rapidly. There are two control structures that fall under the name adaptive control, namely MRAC (model reference adaptive control), and the so called self tuning method [60].

The MRAC method is schematically depicted in Figure 16.1. As the name suggest, a reference model is used that describes the ideal dynamics. In the ideal case the complete system behaves the same as this model. The reference model is compared to the output of the controlled system. The error between these two signals says something about how well the controlled system matches the reference model. An adaptation law is used to tune the controller based on this error in such a way that the error is reduced as time goes on. The controller is often of a fixed structure and linear in the parameters, where the parameters can be tuned by the adaptation law. Using Lyapunov techniques it can be guarantied that the complete control system is stable and the controller converges in a way that the controlled system converges to the reference model.

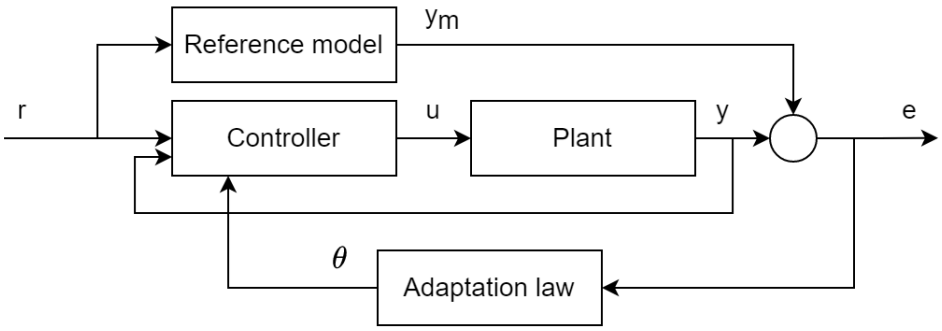

Figure 16.1: Model reference adaptive control scheme. (from [60], modified)

The self tuning method does not use a reference model, but has a separate stage where a model of the plant is estimated to a certain extend, as is shown in Figure 16.2. This can effectively be seen as online system identification. The structure of this model is often of fixed structure and linear in the parameters. These parameters are can for example be estimated in real time with least squares techniques. Any type of controller can then be designed that is not only dependent on the system states, but also on the estimated model parameters. The type of controller that can be used ranges from a simple proportional controller to a more advanced nonlinear controller including feedback linearization, as is discussed in later sections.

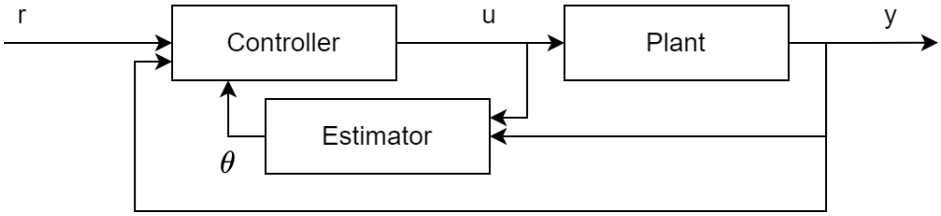

Figure 16.2: Self tuning control scheme. (from [60], modified)

It should be noted that robust control and adaptive control do not offset each other in any way. Although they can be seen as two different approaches to make a control system deal with model uncertainties better, they can in fact both be applied to the same system. For example, a self tuning control structure can be made where a controller is used that is tuned conservatively to be more robust. In a scenario where estimated system parameters can deviate significantly from their actual values, this might be valid solution.

16.2 Nonlinear quadcopter control

This chapter discusses some of the most common nonlinear control techniques that are applied to quadcopter flight. In the last decade the most research has been done in the areas of SMC (sliding mode control), backstepping and PID control [31]. The first two are discussed in subsection 16.2.5 and subsection 16.2.4, respectively. Both these methods find their roots in Lyapunov functions, which is the reason these functions are discussed in subsection 16.2.3. To draw some connections to the widely applied linear control strategies, in subsection 16.2.1 gain scheduling is discussed together with LPV (linear parameter varying) control, since these two are closely related.

16.2.1 Gain Scheduling and Linear Parameter Varying control

One of the big disadvantages of nonlinear control systems is that the control methods are complicated with respect to linear control techniques. For nonlinear systems with nonlinear controllers there is generally only a small amount of tools available for synthesising the controller in a systematic way and analysing the behaviour of resulting controlled system. The opposite is true for linear systems and linear control techniques.

Because of the versatility of linear systems and linear control techniques, linearizing the system around a specific operation point is a popular solution to the control of nonlinear systems. Depending on the amount of nonlinearity, the resulting linear controller is often only effective for a small operating range of the system, namely around the states where the system was linearized. To get around this problem, a rather intuitive solution is to linearise the system around multiple operating points, and design a linear controller with the same structure for each of the operating points. Each operating point will yield different controller gains. Scheduling the gains of the controller based on the operating points of the system then results in a controller with linear structure that is applicable to a wide range of the nonlinear model. This method is referred to as gain scheduling, which was already being developed in the 1960s [61].

Gain scheduling can be applied to systems that can be expressed as shown in Eq. 16.1, where $\boldsymbol{\theta}$ is an endogenous parameter, referring to its dependence on the system state [62]. Syntheses of the gain scheduling controller consist of taking a finite amount states as to cover the system where the controller should be effective, and finding controller gains for each of the corresponding $\boldsymbol{\theta}$ vectors. Depending on the amount of states $\boldsymbol{\theta}$ is dependent on, the amount of operating points can increase rapidly, highlighting one of the downsides of gain scheduling.

$$\begin{aligned} \dot{\boldsymbol{x}} &= A(\boldsymbol{\theta}(\boldsymbol{x}))\boldsymbol{x} + B(\boldsymbol{\theta}(\boldsymbol{x}))\boldsymbol{u} \\ \boldsymbol{y} &= C(\boldsymbol{\theta}(\boldsymbol{x}))\boldsymbol{x} + D(\boldsymbol{\theta}(\boldsymbol{x}))\boldsymbol{u} \end{aligned} \tag{16.1}$$

The result is a set of state vectors and corresponding controller gains. It is not trivial how these gains should be interpolated between points of linearization. This goes hand in hand with the fact that even when stability is guarantied for the operating points used for designing the controller gains, performance is not guarantied between these operating points.

Gain scheduling in its pure from is not extensively applied to quadrotors [31]. Sah et al. [63] used gain scheduling to account for the nonlinearities in the kinetic equations and account for values such as mass, MMOI, yaw angle and some other constants. Research on gain scheduling applied to drones for effective control at higher flight speeds in not abundant.

A special case of the system described in Eq. 16.1 is the so called linear parameter varying or LPV system. This type of system similar, with the exception that the parameter $\boldsymbol{\theta}$ is exogenous, i.e not dependent on the state, as shown in Eq. 16.2 [62]. LPV systems where first introduced as a specific kind of system in 1988 [64]. There are multiple ways to design controllers for this type of system, for example the scaled small gain approach, parameter depend Lyapunov functions and linear matrix inequalities (LMI).

$$\begin{aligned} \dot{\boldsymbol{x}} &= A(\boldsymbol{\theta}(t))\boldsymbol{x} + B(\boldsymbol{\theta}(t))\boldsymbol{u} \\ \boldsymbol{y} &= C(\boldsymbol{\theta}(t))\boldsymbol{x} + D(\boldsymbol{\theta}(t))\boldsymbol{u} \end{aligned} \tag{16.2}$$

The parameter vector $\boldsymbol{\theta}$ needs to observable, in a sense that its values can be derived from the current and past sensor values. For example, the speed, attitude angles and total thrust can be used as parameters [65], which states follow directly from the state estimation already present in the quadcopter. Note that although these parameters are technically states, they are not states that are used by the inner loop control. Since LPV control is applied to the inner loop only, the parameters are exogenous.

To give some additional examples, Pham et al. [66] uses the MMOI's, the pitch angle and yaw angle as parameters, and LMI is used to design the controller. Ameho et al. [67] assumes a linear system defined by state derivative coefficients, for example M_u being the rate at which pitch moment changes with forward speed in the inertial frame. Three of these parameters are estimated using an online system identification method based on RLS, making this classic example of adaptive control as discussed in section 16.1. The controller is designed using the H_∞ algorithm. Finally, Stephan et al. [68] focuses on a complete motor failure causing the quadcopter to spin, which is further discussed in section 16.4. Here the yaw rate is used as parameter and the controller uses state feedback where the gains are set using a method based on LMI.

16.2.2 Feedback linearization

NDI (nonlinear dynamic inversion), which is sometimes referred to as feedback linearization, is a method to linearize either the input-output, or the input-state relation of a nonlinear system [60, 69]. This is done by applying a feedback law to the system resulting in a linear system. When the system is linearized, a large amount of techniques can be applied to obtain a stable system with preferred behaviour. Note that linearization in this section refers to linearization by means of feedback and is thus very different from Jacobian linearization as treated in subsection 16.2.1.

$$\begin{aligned} \dot{\boldsymbol{x}} &= \boldsymbol{f}(\boldsymbol{x}) + \boldsymbol{g}(\boldsymbol{x})u \\ y &= h(\boldsymbol{x}) \end{aligned} \tag{16.3}$$

Although NDI can be applied to a significant subclass of systems of the form $\dot{\boldsymbol{x}} = \boldsymbol{f}(\boldsymbol{x}, \boldsymbol{u})$, consider the nonlinear system that is affine in control as shown in Eq. 16.3. Here a SISO system is presented, but a similar procedure is applicable to MIMO systems. To find a control law that linearizes the system, it is necessary to make a coordinate transformation of the states that results in a system description that is in controller form. This way the linearizing feedback control law becomes straightforward to derive. In other words, a transformation $\boldsymbol{z} = T(\boldsymbol{x})$ has to be found that puts the new system in controller form. One way to do this is to take the derivatives of the output y as the new states $\boldsymbol{z}$. For a fully observable system, that is, there are no internal dynamics, this results in a canonical form. To illustrate, the first derivative of y is shown in Eq. 16.4.

$$\begin{aligned} \dot{y} = \frac{dy}{dt} = \frac{\delta y}{\delta \boldsymbol{x}}\dot{\boldsymbol{x}} = \frac{\delta h(\boldsymbol{x})}{\delta \boldsymbol{x}}(\boldsymbol{f}(\boldsymbol{x}) + \boldsymbol{g}(\boldsymbol{x})u) = \frac{\delta h(\boldsymbol{x})}{\delta \boldsymbol{x}}\boldsymbol{f}(\boldsymbol{x}) + \frac{\delta h(\boldsymbol{x})}{\delta \boldsymbol{x}}\boldsymbol{g}(\boldsymbol{x})u \\ = L_f h(\boldsymbol{x}) + L_g h(\boldsymbol{x})\, u \end{aligned} \tag{16.4}$$

In Eq. 16.4, $L_f h(\boldsymbol{x})$ is the Lie derivative of the function $h(\boldsymbol{x})$ with respect to the function $f(\boldsymbol{x})$. Usage of the Lie derivative makes notation of the derivation of feedback more compact and clear. If the system is of order n, it can be shown that up until the $(n-1)$'th derivative of y, the term $L_g h(\boldsymbol{x}) = 0$, given that the relative degree $r = n$. That means that u only appears in the equation for the n'th derivative of y. For example, if $n = 3$ then the derivatives of y can be written as shown in Eq. 16.5, where $L_f^2 h(\boldsymbol{x}) = L_f[L_f h(\boldsymbol{x})]$.

$$\begin{aligned} \dot{y} &= L_f h(\boldsymbol{x}) \\ \ddot{y} &= L_f^2 h(\boldsymbol{x}) \\ y^{(n)} &= L_f^n h(\boldsymbol{x}) + L_g L_f^{n-1} h(\boldsymbol{x}) u \end{aligned} \tag{16.5}$$

The derivatives of y can be taken as new states, resulting in the transformation shown in Eq. 16.6, where $\boldsymbol{z}$ is the new state vector. This transformation results in a new state space system as shown in Eq. 16.7. This immediately reveals an almost linear system, except for the last row of the system containing the control input u. To linearize the system completely, a virtual control input v is introduced which is set equal to $v = L_f^n h(\boldsymbol{x}) + L_g L_f^{n-1} h(\boldsymbol{x}) u = b(\boldsymbol{x}) + a(\boldsymbol{x})u$, resulting in the system as shown in the most right hand term of Eq. 16.7. The virtual input v is thus equal to one of the states and the resulting system is linear. The control input of the actual system can thus be

written as $u = a^{-1}(\boldsymbol{x})v - b(\boldsymbol{x})$. The resulting feedback diagram is shown in Figure 16.3.

$$\boldsymbol{z} = \begin{bmatrix} z_1 \\ z_2 \\ \vdots \\ z_n \end{bmatrix} = \begin{bmatrix} y \\ \dot{y} \\ \vdots \\ y^{(n)} \end{bmatrix} = \begin{bmatrix} h(\boldsymbol{x}) \\ L_f h(\boldsymbol{x}) \\ \vdots \\ L_f^{n-1} h(\boldsymbol{x}) \end{bmatrix} = T(\boldsymbol{x}) \tag{16.6}$$

$$\rightarrow \dot{\boldsymbol{z}} = \begin{bmatrix} \dot{z}_1 \\ \dot{z}_2 \\ \vdots \\ \dot{z}_n \end{bmatrix} = \begin{bmatrix} z_2 \\ z_3 \\ \vdots \\ L_f^n h(\boldsymbol{x}) + L_g L_f^{n-1} h(\boldsymbol{x}) u \end{bmatrix} = \begin{bmatrix} z_2 \\ z_3 \\ \vdots \\ b(\boldsymbol{x}) + a(\boldsymbol{x}) u \end{bmatrix} = \begin{bmatrix} z_2 \\ z_3 \\ \vdots \\ v \end{bmatrix} \tag{16.7}$$

Unfortunately, it is not true in general that for an n'th order system that the output variable will only appear in the n'th derivative of y. It is also possible that the input already appears in a lower derivative of y. This means the relative degree r is lower than the order of the system n. When this is the case, there are so called internal dynamics that are not captured in the resulting input-output relation. These internal dynamics are problematic if they are unstable. However, when looking at how NDI is applied to control of a quadcopter with no motor failures, this is generally not the case.

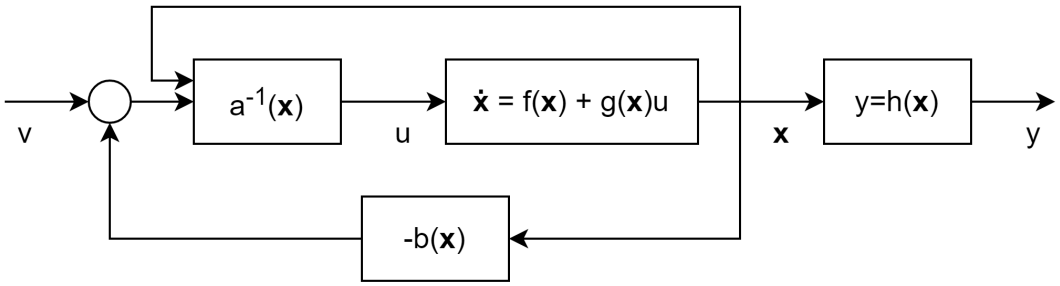

Figure 16.3: SISO NDI control schematic.

Although NDI is mathematically a very elegant solution, in practice there are some significant downsides of using this method. One of these downsides are so called singularity points, which is when the states have taken on such values that the $a(\boldsymbol{x})$ has a value of zero, or in the MIMO case when the $a(\boldsymbol{x})$ is a matrix without full rank, meaning that calculating the inverse is not possible. Another downside is the need for knowing the complete nonlinear system description of the system. If there is a mismatch between the system description as used in the NDI controller and the actual underlying system, the system will not be completely linearized. However, when it comes to quadcopter control it has been shown that, depending on the implementation, NDI still provides a certain level of robustness. For example, a variation in the parameter values of MMOI, mass, and drag coefficients of up to 30 % still does not result in critical stability loss [70].

In the late 1990s, an incremental based NDI method was proposed [71], abbreviated as INDI. The thought behind this method is that instead of calculating the current forces and accelerations on the system, the accelerations are directly measured by sensors. Consider the nonlinear system description of a nonlinear system in Eq. 16.8. This equation can be linearized around the current time point using the Taylor series expansion and neglecting

higher order terms, as shown in Eq. 16.9 and Eq. 16.10. When the sample rate is large relative to the speed of the system dynamics, according to the time scale separation principle [59], it can be assumed that the changes in the states $\Delta \boldsymbol{x}$ are much smaller than the changes in control input $\Delta \boldsymbol{u}$. This allows for removing the $F(\boldsymbol{x}_0, \boldsymbol{u}_0)$ term from the equation, resulting in Eq. 16.11. Rewriting and making the target state derivative $\dot{\boldsymbol{x}}_0$ equal to the virtual control input results in Eq. 16.12.

$$\dot{\boldsymbol{x}} = \boldsymbol{f}(\boldsymbol{x}, \boldsymbol{u}) \tag{16.8}$$

$$= \boldsymbol{f}(\boldsymbol{x}_0, \boldsymbol{u}_0) + \left.\frac{\delta \boldsymbol{f}(\boldsymbol{x}, \boldsymbol{u})}{\delta \boldsymbol{x}}\right|_{\boldsymbol{x}_0, \boldsymbol{u}_0} \cdot \Delta \boldsymbol{x} + \left.\frac{\delta \boldsymbol{f}(\boldsymbol{x}, \boldsymbol{u})}{\delta \boldsymbol{u}}\right|_{\boldsymbol{x}_0, \boldsymbol{u}_0} \cdot \Delta \boldsymbol{u} \tag{16.9}$$

$$= \dot{\boldsymbol{x}}_0 + F(\boldsymbol{x}_0, \boldsymbol{u}_0) \cdot \Delta \boldsymbol{x} + G(\boldsymbol{x}_0, \boldsymbol{u}_0) \cdot \Delta \boldsymbol{u} \tag{16.10}$$

$$\approx \dot{\boldsymbol{x}}_0 + G(\boldsymbol{x}_0, \boldsymbol{u}_0) \cdot \Delta \boldsymbol{u} \tag{16.11}$$

$$\Delta \boldsymbol{u} = G^{-1}(\boldsymbol{x}_0, \boldsymbol{u}_0)(\boldsymbol{v} - \dot{\boldsymbol{x}}_0) \tag{16.12}$$

When it comes to quadcopter control, INDI is often applied to the angular rate part of the system equations [40, 25, 72, 73, 1, 23]. One of the reasons for this is that from Eq. 16.12 it becomes clear that the amount of controlled states, which is captured by the virtual input $\boldsymbol{v}$, should in general be equal to the amount of actual control inputs denoted by $\Delta \boldsymbol{u}$ [74]. This results in a $G(\boldsymbol{x}_0, \boldsymbol{u}_0)$ matrix that is square and in general invertible. INDI thus works well when virtual control inputs are the angular rates and the total amount of thrust, and the actual control inputs are the inputs to the four propellers.

Tal et al. [25] recently showed the promising performance of INDI applied to the rate control of the quadcopter and a differential flatness based technique combined with a PD controller to perform a tracking task. Noteworthy is that there was a need for optical encoders on the four motors to get accurate information about the rotational speed of the motors. Without this the rotational speed has to be estimated based solely on the control input, which can be problematic. Luckily, a selection of flight controllers such as BetaFlight and PX4 have since recently included a protocol named bidirectional D-shot, which allows for getting real time feedback on the current motor speeds based from the ESC.

Smeur et al. has applied INDI to a Parrot Bebop and shown its performance during flight in a wind tunnel. Initially the INDI is applied to the angular rate control [1]. The characteristic issue of INDI is highlighted, which is the necessity to measure the angular acceleration. This measurement is not directly available from any sensor, and thus has to be obtained by differentiating the angular rates measured by the gyroscope. This however results in a noisy signal. To get around this a second order low pass filter is used on the signal. Unfortunately this results in a delay in the measured angular acceleration which interferes with the linearization. To get around this another low pass filter is added to the control output, negating the previously introduced time delay.

The attitude loop is initially controlled using a simple PD controller. In later research [23] the attitude is included using quaternions and a quaternion based controller [75] is used for attitude control. INDI is now also applied to the linear accelerations. Flight tests are performed outside with promising results, where a high end GPS sensor is used

to get more accurate position updates. Special attention is given to the fact that the thrust to rpm relation is linear. Since this is a rather crude approximation of the actual relation, including a more accurate relation is advised for further research.

16.2.3 Lyapunov functions

Lyapunov's second method, or direct method, was introduced by Alexandr Mikhailovich Lyapunov in 1892 in his work 'The General Problem of Motion Stability' [76]. The method is a way to say something about the stability of an autonomous nonlinear system. A fist order differential equation is called 'autonomous' if the independent variable does not appear explicitly. If the independent variable is time, this is referred to as a time invariant system. Lyapunov stability is thus applicable to systems as shown in Eq. 16.13. The power of the Lyapunov stability analysis is that it gives information about the system stability without having to find the solution of the governing differential equations.

$$\dot{\boldsymbol{x}} = F(\boldsymbol{x}) \tag{16.13}$$

To say something about the stability of a dynamic system [60], a Lyapunov function $V(\boldsymbol{x})$ has to be created that is dependent on the states of the system only. This function thus returns a specific value for each state. This function has to be continuous and have continuous partial derivatives, and it should be positive definite ($V(\mathbf{0}) = 0$, $V(\boldsymbol{x}) > 0$). If such a function is available and $dV/dt = \dot{V}$ is negative definite ($V(\mathbf{0}) = 0$, $V(\boldsymbol{x}) < 0$) on some domain D including the state origin $\boldsymbol{x} = \mathbf{0}$, then the origin is an asymptotically stable critical point. That means, any state that starts on D will end up in the origin as $t \to \infty$.

Finding a suitable Lyapunov function for a given system is not trivial, and sometimes this has to be done by trial and error. Luckily, when talking about mechanical systems, the Lyapunov function is very comparable to the principle of energy. To be more precise, usually the equation describing the total energy of the system fulfills the requirements of a Lyapunov function.

To understand why Lyapunov's second method works, lets consider a system with two states, $\boldsymbol{x} = (x_1, x_2)$. The time invariant system can then be written as shown in Eq. 16.14. The derivative of the Lyapunov function can be written as shown in Eq. 16.15.

$$\dot{\boldsymbol{x}}(t) = \begin{bmatrix} \dot{x_1} \\ \dot{x_2} \end{bmatrix} = \begin{bmatrix} f_1(x_1, x_2) \\ f_2(x_1, x_2) \end{bmatrix} \tag{16.14}$$

$$\dot{V} = \frac{dV(x_1, x_2)}{dt} = \frac{dV}{dx_1}\frac{dx_1}{dt} + \frac{dV}{dx_2}\frac{dx_2}{dt} = \nabla V(x_1, x_2) \cdot \dot{\boldsymbol{x}}(t) \tag{16.15}$$

When looking at the final product of Eq. 16.15, $\nabla V(x, y)$ is simply the gradient of the Lyapunov function, and $\dot{\boldsymbol{x}}$ is obviously the direction in which the states are changing in the state space. Thus, the derivative of the Lyapunov function is equal to the dot product of these two described vectors. In other words, if the trajectory moves in a direction of lower Lyapunov function values (for mechanical systems comparable to a lower energy

state), the system is stable around the relevant equilibrium point.

This Lyapunov function are used extensively to analyse and proof system stability for nonlinear systems such as quadcopters (e.g. [77]). Besides its many other applications, it can directly be used to synthesize a controller. For examples of this see [31]. In its most basic form a CLF (control Lyapunov function) is created including one or more parameters that can be set by the control designer. Imposing the requirement of a negative definite derivative of the Lyapunov function results in requirements on the tuning parameters. The parameters can be further tuned to achieve a specific response by back substituting the control law to find an expression for the error term as function of time.

16.2.4 Backstepping

Backstepping is a control technique that is in the top three of most researched methods for quadrotor control [31]. The backstepping control strategy was first proposed in the early 1990s [78] and it is suitable for a system that can be written in strict feedback form or lower triangular form, which is shown in Eq. 16.16. This form clearly has a recursive structure, which is exploited by the backstepping controller.

Backstepping works by synthesizing a controller for the smallest subsystem, and then recursively generating controllers for the higher order system equations. Looking at the system shown in Eq. 16.16, first a controller is made for the system equation in the first row. This may be done using any control technique. This controller calculates the desired value of z_1, lets say d_1, given a certain state error. Then a controller is made for the equation in the second row of the system, which goal is to drive the z_1 state to its desired value d_1. This is done by using the error $e_1 = z_1 - d_1$ and calculating the required value for z_2, lets say d_2 to drive the error e_1 to zero. The goal of the next controller is then to drive the value of z_2 to d_2. One can see how this process can be continued depending on the total order of the system. The controller that is generated last will be a controller for the complete system.

$$\begin{bmatrix} \dot{\boldsymbol{x}} \\ \dot{z}_1 \\ \dot{z}_2 \\ \vdots \\ \dot{z}_k \end{bmatrix} = \begin{bmatrix} f_x(\boldsymbol{x}) + g_x(\boldsymbol{x}) z_1 \\ f_1(\boldsymbol{x}, z_1) + g_1(\boldsymbol{x}, z_1) z_2 \\ f_2(\boldsymbol{x}, z_1, z_2) + g_2(\boldsymbol{x}, z_1, z_2) z_3 \\ \vdots \\ f_k(\boldsymbol{x}, z_1, \ldots, z_k) + g_k(\boldsymbol{x}, z_1, \ldots, z_k) u \end{bmatrix} \tag{16.16}$$

The controllers are designed using CLFs, as discussed in subsection 16.2.3. Therefore backstepping is often considered a Lyapunov based control approach. First, a Lyapunov function is made for the low level subsystem in the first row of Eq. 16.16 using the state errors $\boldsymbol{e}_x$, for example $V(\boldsymbol{e}_x) = \boldsymbol{e}_x^T \boldsymbol{e}_x$. Analysing this Lyapunov function should result in a control law that calculates a virtual control input d_1 as function of $\boldsymbol{e}_x$. Then, the next controller can be designed using the augmented Lyapunov function, which the same Lyapunov function as earlier, but now including the error e_1, e.g. $V(\boldsymbol{e}_x, e_1) = \boldsymbol{e}_x^T \boldsymbol{e}_x + e_1^2$. This then should reveal a effective controller for the next controller. This process is then repeated.

Backstepping can be made adaptive in the case not all parameters $\boldsymbol{\theta}$ of the model are known beforehand. Adaptive backstepping is usually implemented in a comparable way to the self tuning method discussed in section 16.1. However, the parameter estimation error $\boldsymbol{e}_\theta = \boldsymbol{\theta} - \hat{\boldsymbol{\theta}}$ where $\hat{\boldsymbol{\theta}}$ is the parameter estimation, can be included in the Lyapunov function. This allows for introducing a tuning function and update law that makes the estimate of $\boldsymbol{\theta}$ converge to its actual value, while guarantying the stability of the complete system. Robust backstepping is also possible, since the Lyapunov function allows for inspecting the relation between actual model parameter values and the selected tunable variables in the chosen controller. Controller tuning variables can therefor be set knowing the bounds on the model parameter values.

Backstepping was proposed for control on a quadcopter in 2008 [79]. Quadcopters lend themselves somewhat to backstepping due to their model structure, as becomes apparent from Eq. 15.9. In words, the position of the drone is controlled by setting a certain speed. Speed is controlled by setting a certain acceleration. Acceleration is controlled by the total amount of thrust and the orientation of the quadcopter. Then finally, the orientation is controlled by controlling the angular acceleration.

For example, Xie et al. [80] applied a adaptive backstepping controller to a quadcopter to improve tracking of a predefined path. Here the first virtual control consist of the the position of the quadcopter, the second virtual control the speed, the third the angular velocity, and finally as fourth the along path tracking error, which relates to the position along the path in time. The study deals with several issues found in backstepping applied to quadcopter, for example that they are under actuated when the translational states are included.

Bhatia et al. [81] proposed a robust adaptive backstepping controller which guaranties good tracking and fast convergence rates. An impressive amount of parameters are estimated, including MMOI, masses thrust coefficient, drag coefficient, propeller inertia, CG position and mass of payloads.

Huang et al. [82], uses a novel model identification method, after which backstepping is compared to integral-LQR and nested saturation. Here backstepping performs worst in hovering with wind disturbances.

16.2.5 Sliding mode control

As is backstepping, SMC is a control strategy that can be considered Lyapunov based. Originally described as a variable structure control strategy in 1977 [83], the basic idea is to construct a hypersurface with appropriate dimension in the state space that the system is pushed towards. Once the states reach the this surface, the system is kept on this surface, effectively making the system slide along this surface. The surface is therefore often referred to as a sliding surface. Once the system has reached and slides along the sliding surface, the system behaviour is referred to as 'sliding regime' or 'sliding mode' [60], hence the name sliding mode control. SMC is applied in two stages, namely designing the sliding surface and finding a control law keeping the states of the system on this surface.

SMC can be applied to a tracking problem, where the output of the system $y(t)$ should converge to a desired system output $y_d(t)$. The difference or error between these values, $e = y(t) - y_d(t)$, should be brought to zero. Consider the SISO nonlinear system that is affine in input in Eq. 16.3. Here $x \in R^n$ and the system has relative degree r, as touched upon in subsection 16.2.2. A sliding surface σ can now be constructed that is a function of the error e and its k derivatives, where $k = r - 1$ [84, 83]. That is, $\sigma = \sigma(e, \dot{(e)}, \ldots, e^{(k)})$. A common choice for a surface for a given value of k is given in Eq. 16.17. Here λ is a parameter that can be tuned. The sliding surface is then defined by $\sigma = 0$.

$$\sigma = \left(\frac{d}{dt} + \lambda\right)^k e \tag{16.17}$$

Now a control law has to be found that drives the value for σ to zero. A first order SMC is discontinuous, and described by Eq. 16.18, where U is a sufficiently high number. As can be seen, first order SMC can be viewed as a smart application of a bang bang controller. An advantage of this is that the controller is incredibly robust against both disturbances and model uncertainty. In fact, it is not required to know the underlying model $f(\boldsymbol{x})$ and is rather treated as a black box.

$$u = -U\text{sgn}(\sigma) = \begin{cases} -U & \sigma < 0 \\ U & \sigma > 0 \end{cases} \tag{16.18}$$

Unfortunately, these advantages come at the expense of a high control effort. As can be seen in for example linear control, the control inputs do not get smaller as the system states approach the desired state values. Do to practical limitations such as time delays and finite precision of variables, first order SMC generally suffers from the so called 'chattering phenomenon' [60]. This happens when the system has reached the sliding surface, but continuously overshoots the sliding surface due to the high control gain. This causes the system and control to fluctuate at a high frequency. This rapid switching behaviour is appropriate in many electrical system since this effectively the same as PWM. Unfortunately for many mechanical applications this oscillatory behaviour can be problematic. To get around this, a second order (2-SMC) control law can be used that is not discontinuous and thus reduces the chattering effect. This comes at the price of reduced robustness.

Backstepping was first applied to quadcopter control around 2010 [85]. Being one of the most researched control strategies applied to quadcopters [31], an extensive amount of variations and techniques related to SMC have been applied in the past. To highlight some of the more recent research, Chiew et al. [86], applied a second order SMC (2-SMC) using a logistic function to the attitude and yaw control of a quadcopter in a tracking task. This controller is then compared to a classic PD controller by evaluating overshoot, settling time and RMS tracking error. It is found that the tracking error for the sliding mode controller is reduced with around 80 %. Furthermore the chattering effect has been greatly reduced compared to a first order SMC, but has not been entirely negated.

Saad et al. [24] covered a complete pipeline allowing the user to input a target attitude and position, after which an algorithm calculates an optimized trajectory which can

be tracked using a controller. Again, the performance of a PID controller is compared to a first order SMC controller. It is found that the tracking error is roughly five times as low for SMC. Furthermore SMC shows only slightly better robustness when one of the drag force coefficients is changed. It is mentioned that both controllers suffer from the need to find an optimal set of control parameters.

Thahn et al. [87] specifically addresses the chattering phenomenon found in SMC. As is done often, the dynamics of the quadcopter are divided into an attitude part and a position part, which are controlled by separate controllers. The attitude control or inner loop is implemented using SMC, whereas position control is implemented using a variation of PID control. To improve the chattering effect, improved adaptive SMC or IASMC is proposed. This control strategy adapts the switching gain, denoted as U in Eq. 16.18, based on parameter uncertainties and external disturbances. Referring to section 16.1, this effectively moves the SMC controller more into the adaptive realm to relieve some of the required robustness. This then takes away the need for fixed and high valued U parameter. According to simulation results, a significant improvement is found in chattering reduction and tracking performance. This comes at the price of an increased amount of parameters that need to be tuned.

16.3 Quaternions

Describing the orientation of vehicles in the physical world is often done using the well known Tait–Bryan angles, which are the pitch, roll and yaw angles. These three values describe three consecutive rotations with respect to a chosen reference frame that fully describes how the object is rotated is space. However, this is not the only way to parameterize attitude. The Tait–Bryan attitude description is a specific implementation of the use of Euler angles. Euler angles are more general, and are three angles describing three consecutive rotations. The representation of attitude using Euler angles has the advantage that they are very intuitive. That is, given the three angles, the average human can easily imagine the attitude of the object without the help of a computer.

Unfortunately, the use of Euler angles also has some significant drawbacks. One of these is the so called gimbal lock singularity. When Tait–Bryan angles are used, this happens at pitch angles of $\theta = \pm\pi/2$. At these points, the yaw angle and roll angle describe the same change in orientation, making the attitude description ambiguous. Furthermore, the use of Euler angles often requires calculations with many sine and cosine functions, resulting in a relatively large computational overhead.

Luckily, there are alternative ways describe an attitude with a set of parameters. One of these are the so called Euler parameters, or unit quaternions. This attitude representation is an application of quaternions. Euler parameters do no use three consecutive rotations, but describe a transformation in four dimensional space. By writing the quaternion in a specific form, it can be seen that a quaternion effectively describes a rotation axis and and angle that the object is rotated around that axis. This is referred to as the axis-angle representation of a rotation. According to Eulers rotation theorem, any rotation can be described using this axis-angle representation. Below follows a description of how Euler angles describe attitude.

As complex numbers are a two dimensional extension to the real numbers, quaternions are a four dimensional extension to complex numbers. A quaternion can be presented as a linear combination of a real number and the imaginary numbers i, j and k, as shown in Eq. 16.19. The imaginary numbers i, j and k are defined in such a way that Eq. 16.20 holds.

$$q = a + bi + cj + dk \tag{16.19}$$

$$i^2 = j^2 = k^2 = ijk = -1 \tag{16.20}$$

Eq. 16.19 directly describes how two quaternions can be added and multiplied. It follows that quaternion multiplication is associative but not commutative. In practice, quaternions are often written in vector form, as is shown in Eq. 16.21. Usually, the first vector entry q_0 is referred to as the real part, and the second to fourth entries form the vector part of the quaternion, denoted by $\boldsymbol{q}_v$. It should be noted that the way the real part and the vector part are separated is not something that is generally agreed upon and can differ between sources. In this report the notation shown in Eq. 16.21 is used.

$$\boldsymbol{q} = \begin{bmatrix} q_0 & q_1 & q_2 & q_3 \end{bmatrix}^T = \begin{bmatrix} q_0 \\ \boldsymbol{q}_v \end{bmatrix} \tag{16.21}$$

Although convenient to write quaternions as vectors, multiplication of two quaternions should still follow the properties of i, j and k. A vector multiplication operator that follows from Eq. 16.20 is the Hamilton product, here denoted as '$\circ$'. It can for example be shown that multiplying a quaternion with its conjugate is commutative, as shown in Eq. 16.22. Here $\boldsymbol{q}^*$ denotes the complex conjugate, as shown in Eq. 16.23.

$$\boldsymbol{q} \circ \boldsymbol{q}^* = \boldsymbol{q}^* \circ \boldsymbol{q} \tag{16.22}$$

$$\boldsymbol{q}^* = \begin{bmatrix} q_0 \\ -\boldsymbol{q}_v \end{bmatrix} \tag{16.23}$$

For the purpose of describing rotations in three dimensions, unit quaternions have been proved to be really useful. A unit quaternion is a normalized quaternion, which is a quaternion with a norm equal to one, as shown in Eq. 16.24. Let $\boldsymbol{p}$ denote such a unit quaternion from now on, and let $\boldsymbol{x}$ be a regular three dimensional vector. It can than be shown that Eq. 16.25 holds, where $\boldsymbol{x}'$ is $\boldsymbol{x}$ but rotated in thee dimensional space. This rotation is defined by $\boldsymbol{p}$. In other words, the unit quaternion $\boldsymbol{p}$ can be used transform a three dimensional vector without any scaling.

$$\boldsymbol{p} = \frac{\boldsymbol{q}}{||\boldsymbol{q}||} \tag{16.24}$$

$$\begin{bmatrix} 0 \\ \boldsymbol{x}'_v \end{bmatrix} = \boldsymbol{p} \circ \begin{bmatrix} 0 \\ \boldsymbol{x}_v \end{bmatrix} \circ \boldsymbol{p}^* \tag{16.25}$$

To see what kind of rotation $\boldsymbol{p}$ causes, the unit quaternion can be written in a different format, as shown in Eq. 16.26. In this equation, $\boldsymbol{n}$ is a three dimensional unit vector describing a rotation axis, which is commonly referred as the Euler axis. The α value is the angle the object is rotated around the rotation axis.

$$\boldsymbol{p} = \begin{bmatrix} \cos(\alpha/2) \\ \sin(\alpha/2)\boldsymbol{n} \end{bmatrix} \tag{16.26}$$

One purpose of keeping track of attitude, is to convert vectors between two reference frames that do not have the same orientation. Using quaternions gives a very clean and computationally inexpensive way to do this by using Eq. 16.25. However, the entries of a unit quaternions describing rotations have very little physical meaning, and can therefore rarely by used themselves. This shows one of the advantages of Tait–Bryan angles, since these angles can be used as dependent variables for expression of forces or other physical quantities.

It can be shown that the derivative of a quaternion can be expressed as shown in Eq. 16.27. Here $\boldsymbol{\Omega}$ is the angular velocity vector. This equation can directly replace the attitude equation in the third row of Eq. 15.9, where $\boldsymbol{\Omega}$ is then the angular velocity of the quadcopter. Doing this will convert the equations of motion from a Tait–Bryan angle based system description to a quaternion based system description. As mentioned before, the direction of the forces that work on the quadcopter, such as thrust and aerodynamic forces, are dependent on the attitude of the quadcopter. Where first these forces had to be rotated using a rotation matrix based on the Tait–Bryan angles, now these have to be rotated using quaternions, which is done using Eq. 16.25.

$$\dot{\boldsymbol{q}} = -\frac{1}{2}\begin{bmatrix}0\\ \boldsymbol{\Omega}\end{bmatrix} \circ \boldsymbol{q} \tag{16.27}$$

Quaternions can thus very elegantly be used as system states describing the attitude of the quadcopter, removing all the disadvantages of using Euler angles. Another valuable addition is that its possible to make an attitude controller [75] that directly works with the values of the quaternion attitude state. That means that for the attitude controller it is not necessary to convert the attitude quaternion to attitude angles, which reduces the required computational power.

$$\boldsymbol{q}_{err} = \boldsymbol{q}_{ref} \circ \boldsymbol{q}_m^* \tag{16.28}$$

The controller works by taking the Hamilton product of the reference quaternion, representing the desired attitude, and the conjugate of the measured quaternion, representing the measured attitude, as shown in Eq. 16.28. This results in the error quaternion representing the rotation required to go from the measured attitude to the reference attitude. Looking at Eq. 16.26, the direction of the vector part of $\boldsymbol{q}_{err}$ forms the required rotation axis for corrective action of the controller. The length of the vector part of $\boldsymbol{q}_{err}$ is equal to $\sin(\alpha/2)$, and thus scales with the sine of the error angle. The vector part can thus be used in various ways to synthesise a controller calculating the required control torque. Originally the controller was implemented using two proportional gains P_q and P_Ω, as shown in Eq. 16.29. Here the required moment that has to be generated by the motors is denoted by $\boldsymbol{M}_{ref}$, and the measured angular rate as $\boldsymbol{\Omega}_m$.

$$\boldsymbol{M}_{ref} = -P_q \begin{bmatrix} q_1^{err} \\ q_2^{err} \\ q_3^{err} \end{bmatrix} - P_\Omega \boldsymbol{\Omega}_m \tag{16.29}$$

Of course an other option is to split angular rate and attitude control into an inner and outer control loop. After its original implementation [75], attitude control using quaternions has been adopted in other research [25, 23, 88].

16.4 Fault tolerant control

There are many systems on a standard quadcopter that are not present in a redundant fashion. Failure of a sensor, the flight computer and structural components are can quickly result in a crash. However, a large part of quadcopter related research is focused on fault tolerant control, where the words fault tolerant refer to the malfunction of one or multiple actuators. This is likely due to the fact that the actuators are largely of mechanical nature and are very much exposed to the quadcopters surroundings. Rotors can easily be damaged after collision with solid objects such as walls or after sucking in debris. This is especially true when flying in a cramped environment such as inside a building or forest.

This chapter briefly treats the subject of FTC for quadcopters. In subsection 16.4.1 the different ways a quadcopter actuator can fail are discussed. In subsection 16.4.2 different strategies are treated to effectively deal with these failures.

16.4.1 Types of actuator failures

Actuator failures can be categorised in multiple ways. First of all, a distinction can be made based on the degree of damage to the propeller. Actuators can become less effective or completely ineffective, commonly referred to as a partial rotor failure or complete rotor failure, respectively. Although much research treats partial rotor failure in sense of propeller damage, often the results hold for reduced effectiveness of the actuator, which is a more general failure mode. The effect of partial rotor failure is often analysed by manually reducing the effectiveness of the actuator by a certain percentage [89, 90, 91, 92, 73]. It should be noted that when in reality a part of the propeller is missing, there will be excessive vibration. Because this can interfere with sensor measurements and control algorithms, the choice can be made to completely disable the actuator once damage has been detected. The failure can now be modelled by a complete actuator failure. Other realistic cases of a complete actuator failure could be failure of the electronics related to a specific actuator, or accidental detachment of the propeller during flight. Flight testing with complete rotor failure is either performed by manually removing the propeller before flight [93, 58, 40] or disabling the actuator in the software [72].

Besides the ways the propellers can fail individually, there are several combinations of propellers possible that can fail simultaneously. The most straightforward is the single rotor failure, which is extensively researched [58, 72, 89, 94, 91, 73]. Due to directions the propellers spin as discussed in section 14.3, apparently the most effective way to keep the quadcopter flying is to enter the so called 'relaxed hover' state. In this state the opposing propeller is also relieved of its task to generate lift to keep the quadcopter balanced in roll and pitch. Due to the yaw torque imbalance, the quadcopter will start to spin quickly around its body z-axis. Control of the drone is now maintained by tilting the total thrust vector appropriately and giving up yaw angle control.

A more difficult scenario is the case of dual propeller failure, which can either refer to the failure of two diagonally opposed rotors, and two neighboring propellers. flying only on two neighbouring propellers is difficult, and it is likely that only quite exotic control strategies would be applicable, such as making the drone flip rapidly around its pitch or roll axis. Up to this date however there has not been a successful demonstration of this.

On the other hand, when two diagonally opposing rotors fail it has been shown that a similar strategy can be used as for the single rotor failure case. Here the drone is also rotated quickly around its yaw axis but now only two propellers are available for control. Since roll, pitch and the total thrust need to be controlled for stable flight, a control allocation problem has to be solved [40].

Failure of three propellers is obviously an extreme case. It has been shown however that it is possible to fly a quadcopter using a single rotor [95]. Here again the same technique is used by spinning the drone around the yaw axis. It should be noted that now the maximum thrust of the single propeller becomes critical. Not only should the propeller be able to offset the weight of the complete quadcopter, it should also have power left for attitude control.

16.4.2 Control strategies

Most FTC strategies can be classified as being either an active or passive control strategy [96, 91]. This classification is closely related to the distinction between adaptive and robust control as discussed in section 16.1.

Passive FTC is comparable to robust control. Here, the potential failure modes and their effect on the system are assumed known a priori. A controller is designed such that the overall system performance stays within specific performance specifications, even in the case of a failure. The controller does not actively recognise the failure during flight, and the structure of the controller remains the same. Passive FTC especially lends itself to partial rotor failure, since the way the quadcopter is controlled does not fundamentally change. Wang et al. [73] for example showed a passive FTC algorithm where INDI is compared to SMC. Here INDI resulted in easier implementation, reduced model dependency and improved performance and robustness.

Active FTC on the other hand is comparable to the adaptive control strategy. Once a failure occurs, the failure is actively registered and the structure of the flight controller is changed accordingly. Active FTC can be structured in multiple ways, but often consist of multiple components, such as a FDD (fault detection and diagnosis) algorithm, a URC (upset recovery control) algorithm, and a flight controller that can be reconfigured.

As soon as a failure occurs, the task of the FDD algorithm is to notice that a failure or malfunction has occurred. The failure is then quantified, for example by determining which rotor malfunctions and to what degree. For example, van Schijndel [93] used a Kalman filter that continuously estimates the effectiveness factor of every actuator using the measured propeller rpm and IMU data. From this a hypothesis test can be performed revealing the probability that a motor has failed. This process has been shown to take anywhere from 30 ms to 130 ms with high reliability. Other research [89] has shown the results of a model based observer to notice thrust losses of up to 30 %. Using this method it takes several seconds to notice an actuator failure. Furthermore FDD methods have been explored based on SMC [94] and LPV [90].

Since FDD takes some time, and there is a chance that the actuator failure occurred

due to an aggressive collision, its possible that the quadcopter has an excessive attitude and excessive rotational rates after failure diagnosis. The task of URC is to bring the quadcopter back to a more manageable attitude and rotational rate, so that the failure flight controller can effectively take over. Obviously, the higher the initial attitude and rotational rates are, the longer it takes for the drone to recover. An algorithm that focuses first on attitude recovery, and after this on yaw and vertical speed recovery, showed drop heights of up to 30 m in simulation [72].

Finally, a controller is activated that is specifically designed to deal with the relevant failure. For both single and dual rotor failure, controllers have been experimented with that make use of INDI [40, 25, 73], SMC [73, 94] and LPV [90]. Interesting to note is that there are three control inputs in the case of single rotor failure, namely pitch moment, roll moment and total thrust. Since yaw control has been given up, there are also three inner loop states to control, namely pitch, roll and vertical acceleration. In this case INDI can directly be applied due to the equal number of inputs and outputs. However, when two diagonally opposed rotors have failed, the system is under actuated and redesign of the original control outputs is necessary. This gives rise to internal dynamics, as discussed in subsection 16.2.2, of which the stability has to be guarantied [40]. This makes the problem of dual rotor failure significantly more challenging than single rotor failure.

Chapter 17

Contributing to quadcopter control research

As has become apparent from chapter 14 to chapter 16, the topic of guidance of control has received a substantial amount of attention in the scientific community. The amount of literature referred to in this report is at best a representative sample of the existing literature on this topic. The extensiveness of research on quadcopter control is likely extensive because of multiple reasons. First of all, as was discussed earlier, the quadcopter as UAV is getting more popular in a rapid pace due to the increasing amount of applications correlating with advances in technology, and due to the increased accessibility to a large part of the population. Furthermore the control of quadcopters is a relatively straight forward problem when only considering a standard hover condition. However, when incorporating higher flight speeds, accurate trajectory tracking and failing actuators, guidance and control becomes an extensive and complex problem. This complexity ask for experimenting with a wide range of solutions. Lastly, there are many facets of quadcopter control. As has been discussed in this report, problems have to be solved in the field of system identification, state estimation, trajectory generation, nonlinear control strategies, robust and adaptive flight control, FDD, URC and so on. All of the above makes advanced control of quadcopters an lively scientific field.

Based on the discussions had in the previous chapters, it is now possible to say something about the current frontier of research when it comes to quadcopter control, and where there is still significant possibility for improvement. This is touched upon in section 17.1. Based on this information, a research topic is proposed with the intention of contributing to filling some of these literature gaps. This is discussed in section 17.2.

17.1 Identifying gaps in current literature

Since advanced quadcopter control is a relatively young and complex topic, it is not hard to identify areas that lend themselves for significant improvement. What is harder is to list these gaps in a systematic way. Below a selection of areas of improvement are discussed as found by multiple sources.

Current methods that are used for state estimation work pretty well for the standard hover conditions. However, in more special cases these methods can appear to lack performance, causing deterioration of controller performance [40, 97]. These special cases

include conditions where significant drag is present, both in translation flight as well as high rotational speed flight found in fault tolerant control.

Another significant boundary found in state estimation is accurate and high frequency measurement of three dimensional position in outdoor environments. Because of this exact reason much research related quadcopter dynamics and control is performed indoors [93, 40, 72, 25, 90, 98, 99, 97, 73], allowing to use optical positioning systems like OptiTrack. Finding effective methods to get better state estimation in an outdoor environment does not only allow verification of proposed methods in the more realistic outdoor environment, but also allows for much easier research into high speed flight.

Another great amount of estimation and control strategies have only been proved in simulation [94, 91, 92, 65, 70]. Many of these strategies show very promising performance. A logical next step is to implement these methods in an actual flight controller and perfom tests on an actual quadcopter. However, as has become clear, for some strategies focused on high speed flight this is difficult due to the lack of state estimation techniques in an outdoor environment.

Control of quadcopters consist of many components. Combined with the fact that advanced control is way more dependent on the qualities of the designer, there is still a large amount of possibilities for the application of different configurations and combinations of strategies. Luckily some nonlinear techniques have been shown to work well in the area of nonlinear quadcopter control, such as INDI, LPV, backstepping and SMC. There are many more control strategies that are only experimented with more recently. An example of this are neural networks [92], which are seeing more use in many scientific fields. Another example is MPC, which generally requires a lot of computational power. Due to the ever increasing calculation power of microchips, these strategies are starting to be applied to quadcopter control more and more [33, 57].

What is remarkable is that much research focusing on high speed control makes quite radical assumptions on the model describing the relation between thrust and propeller rpm. It has become apparent that propeller dynamics are very dominant in quadcopter dynamics, and have much more effect than for example forces seen by the fuselage [6]. Some research does include models of propellers that depend on angle of attack and advance ratio [27, 48]. Furthermore, some research includes the effect of blade flapping. It is questionable how relevant this effect is for quadcopters which generally have fixed and relatively stiff rotor blades compared to helicopters, which use this effect on purpose to reduce roll moment in forward flight.

Research related to flight at significant negative propeller advance ratios is also very sparsely researched. Most research on negative advance ratio propeller behaviour is performed on larger propellers [100], and is generally focused on full scale helicopter flight. Research that is still related to quadcopters focus on the ability to automatically avoid this state of flight [12, 14], which can be seen as a way to circumvent the issue rather than solving the problem. The only research found that does actually measure quadcopter propeller forces at negative advance ratios was performed by Sun [54], where a propeller was mounted on a test stand in a wind tunnel measuring the thrust force and torque. Furthermore, although applied to slightly larger scale propellers, Shetty [52] was

not only able to measure the average thrust of propellers under negative advance ratios, but was also able to document some of the stochastic behaviour in this state of operation.

17.2 Research proposal

A proposal is made here for a research subject that has the intention to shed more light on the quadcopters behaviour where the propellers operate under negative advance ratios. Not only is this interesting from a theoretical standpoint, having a better understanding of this flight condition would potentially remove the necessity of avoiding this state altogether. From a general perspective this would significantly increase the possible flight conditions of the quadcopter which extends its performance in a very concrete way.

Interesting to know is that high negative advance ratio flight is a condition that is very familiar the the FPV racing community. When performing certain manoeuvres, such a the 'split-S', the quadcopter rotors can see large negative inflow at low rotor speeds. This can give rise to large oscillations, and is in non scientific terms often referred to as the 'prop wash effect'. Because of this the FPV racing community either tends to avoid this state during flight or increases the rotor speed at zero throttle to get rid of this effect. A more recently developed technique to increase the idle rpm is called 'dynamic idle', which basically prevents the rotor rotational speed to become to low. Again, this sounds more as a way to avoid the problem rather than a solution.

In the FPV racing community, this prop wash effect is occasionally explained by an interaction between the stalling of the blades and the controller controlling the propeller rpm. To summarise this explanation, under high negative inflows, the propeller supposedly stalls. To counteract the loss of thrust, the controller increases propeller rpm, which moves the blade out of the stall condition. Due to the significant increase in thrust the controller reduces propeller speed again. This vicious circle then continues. What this explanation essentially tries to convey is that the increase in thrust has become very sensitive to an increase in propeller rpm. If this theory is true, it would mean that different controller gains could improve the oscillations and restore performance.

The above theory is not confirmed in any scientific way, but forms an interesting hypotheses of how to deal with negative advance ratio control. However, the control problem is likely more complicated due to the stochastic behaviour of the thrust generated by the propellers, as has been shown to occur under negative inflow [52]. How much of the oscillations are due to the controller, how much due to the stochastic effects and how much due to other unknown effects remains unclear.

Based on the above, the problem is formulated which is used to derive the research objective:

> *Controllers used for quadcopters use propeller force models that are inaccurate for velocities that result in large negative propeller advance ratios. This gives rise to instability or the need for conservatively tuned controllers.*

From this identified problem the following research objective is formulated:

The objective is to improve control of the thrust and torque generated by a quadcopter propeller at large negative advance ratios by acquiring a detailed dynamic model and designing a controller for an isolated propeller in a wind tunnel that represents the negative inflow flight condition.

The research objective is considered to be completed once the following research questions have been answered.

1. What wind tunnel test setup would allow for measuring the necessary variables to extract a propeller model for negative advance ratios?
   (a) Which selection of the propeller forces and moments are worth measuring, considering practical limitations of the test stand.
   (b) What variables need to be measured during testing that are not forces or moments?
   (c) Given the available resources, what test stand is appropriate to measure the selected variables?
   (d) Given the available resources, what wind tunnel test setup would allow for measuring the stochastic nature of the forces and moments to an extent that is relevant for quadcopter control?
   (e) What independent variables need to be varied during testing and over what range?
2. What model structure is best suited to fit the measured variables from the wind tunnel test?
   (a) What model structure is best suited to implement in simulation of the propeller dynamics?
   (b) What model structure is best suited as a basis for a controller design?
3. What controller structure is most appropriate to deal with the dynamics of the propeller?
   (a) Can the controller use the propeller model as a static mapping from required force to required propeller rpm?
   (b) What sensor data is needed by the controller to function properly?
4. How well is the designed controller able to control thrust and torque compared a standard method to control thrust as applied in quadcopters?
5. How can knowledge of the estimated model and designed controller potentially be used in the design of quadcopter controllers?

Entirely removing the quadcopter itself from the research topic allows for great isolation of the problem of negative propeller inflow effects. Not only does this make it more likely that certain effects can be identified more effectively, knowledge of the propeller in isolation can also be used more effectively by future research on quadcopter control strategies.

Appendix A

Isolated Rotor Wind Tunnel Data

This appendix contains the more detailed data gathered from the isolated rotor wind tunnel tests as was described in section 3.2. The multivariate simplex B-splines from section 4.1 are based on the data in this appendix. In Table A.1 an overview is given of what x-axis and y-axis variable is used for the plots in each figure and what rotor was used to produce the data in the respective plots.

Table A.1: Isolated rotor wind tunnel data.

Rotor	**X-axis**	**Y-axis**	**Figures**
50x45	Rotor speed	Thrust	Figure A.1 to Figure A.3
50x45	Airspeed	Thrust	Figure A.4 to Figure A.6
50x45	Rotor speed	Torque	Figure A.7 to Figure A.9
50x50	Rotor speed	Thrust	Figure A.10 to Figure A.12
50x50	Airspeed	Thrust	Figure A.13 to Figure A.15
50x50	Rotor speed	Torque	Figure A.16 to Figure A.18

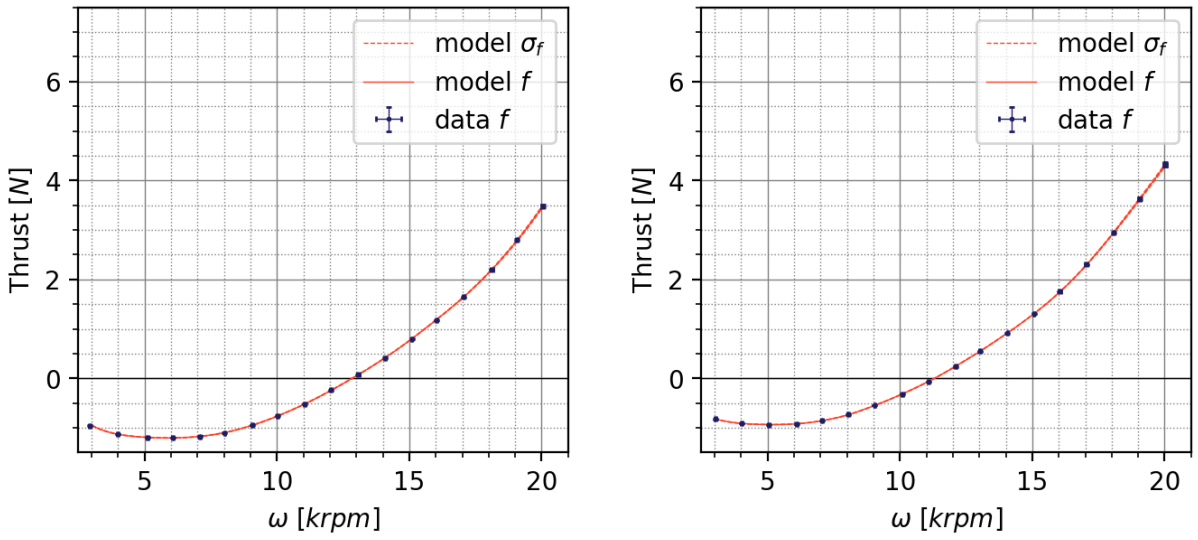

(a) V = $-25\,\mathrm{m\,s^{-1}}$

(b) V = $-22\,\mathrm{m\,s^{-1}}$

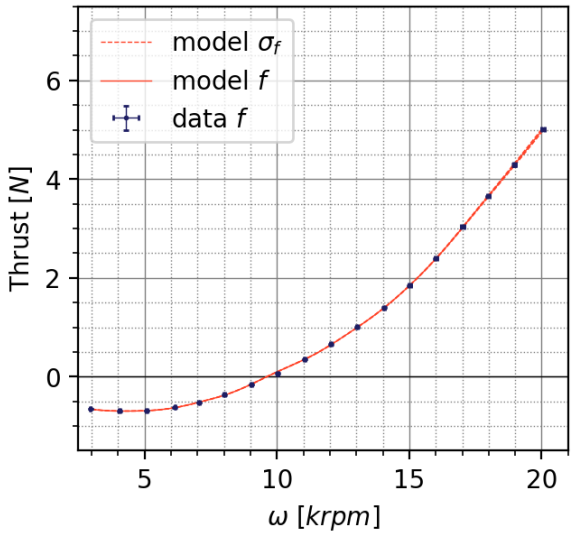

(c) V = $-19\,\mathrm{m\,s^{-1}}$

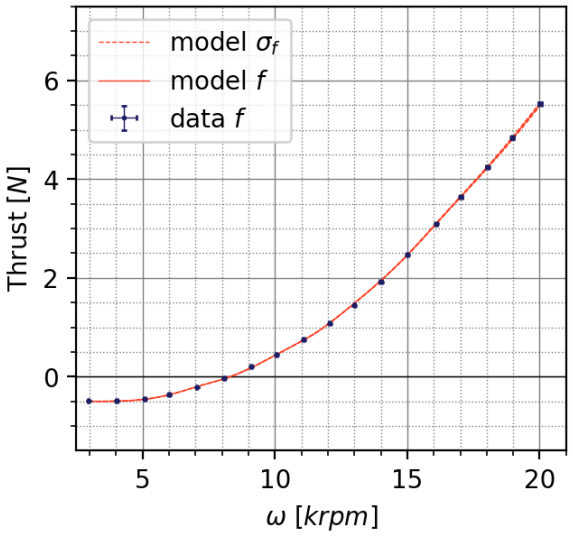

(d) V = $-16\,\mathrm{m\,s^{-1}}$

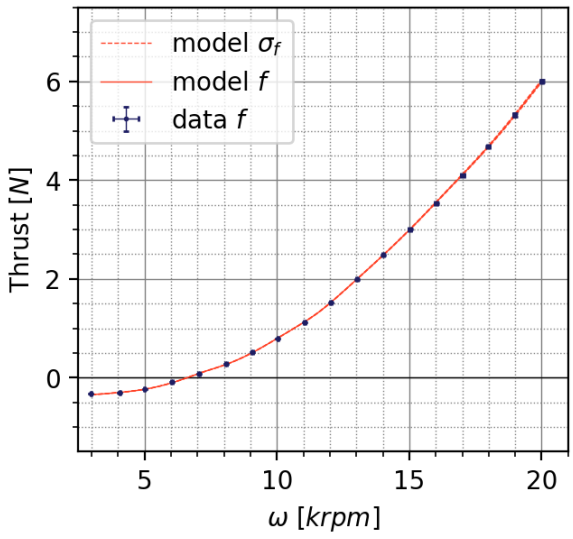

(e) V = $-13\,\mathrm{m\,s^{-1}}$

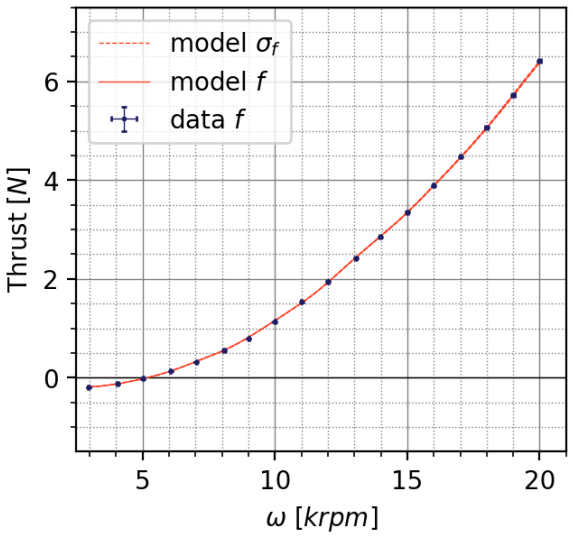

(f) V = $-10\,\mathrm{m\,s^{-1}}$

Figure A.1: Thrust-rpm curves for the 5x4.5x3 rotor ($-25\,\mathrm{m\,s^{-1}}$ to $-10\,\mathrm{m\,s^{-1}}$).

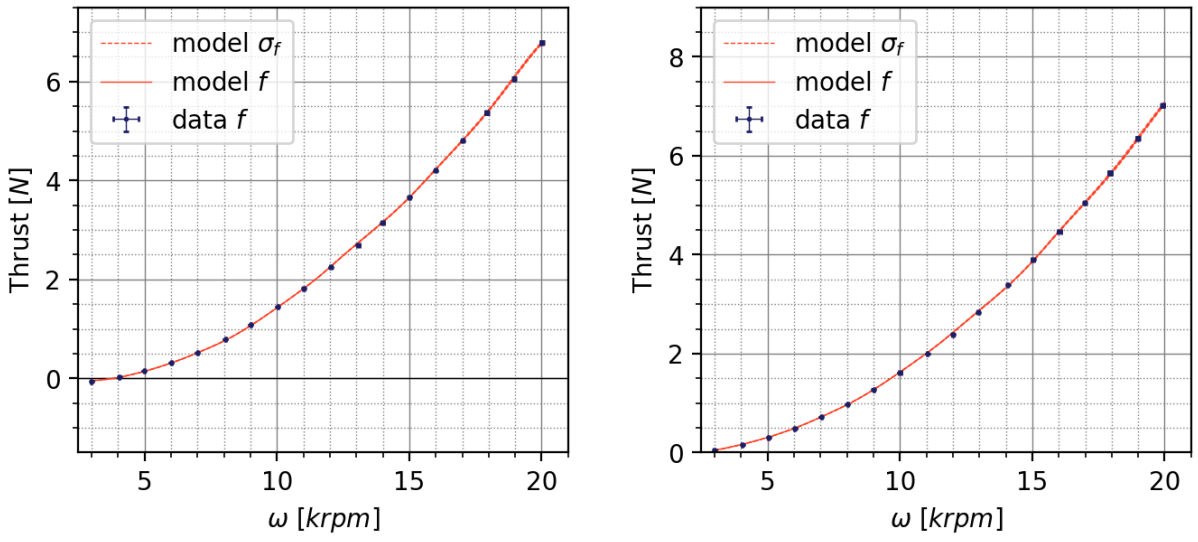

(a) V = $-7\,\mathrm{m\,s^{-1}}$

(b) V = $-4\,\mathrm{m\,s^{-1}}$

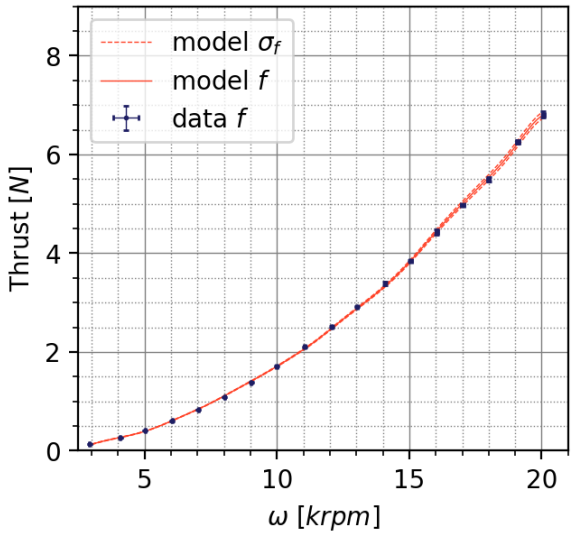

(c) V = $0\,\mathrm{m\,s^{-1}}$

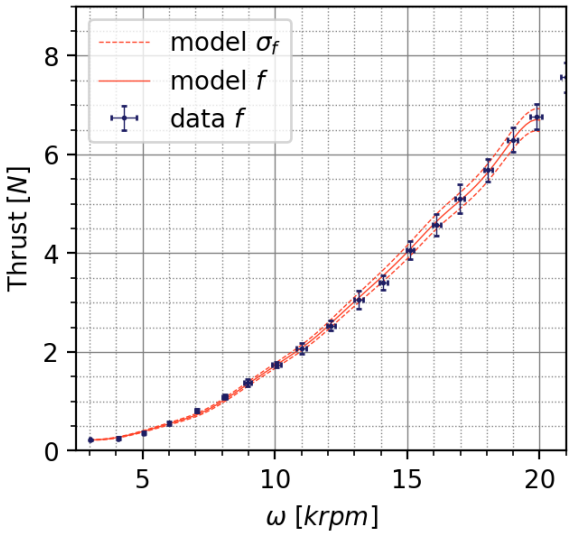

(d) V = $4\,\mathrm{m\,s^{-1}}$

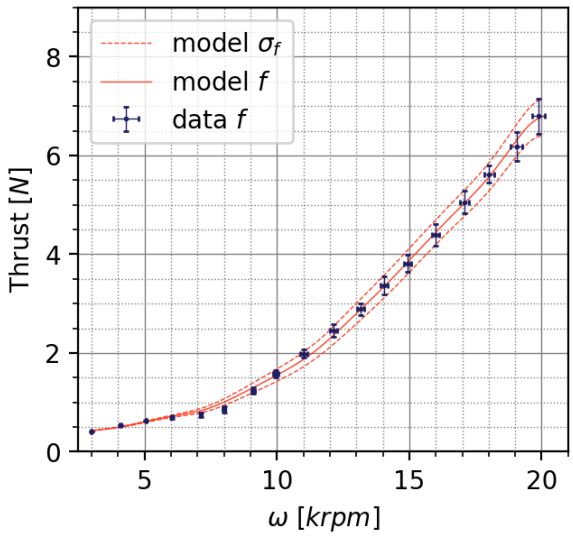

(e) V = $7\,\mathrm{m\,s^{-1}}$

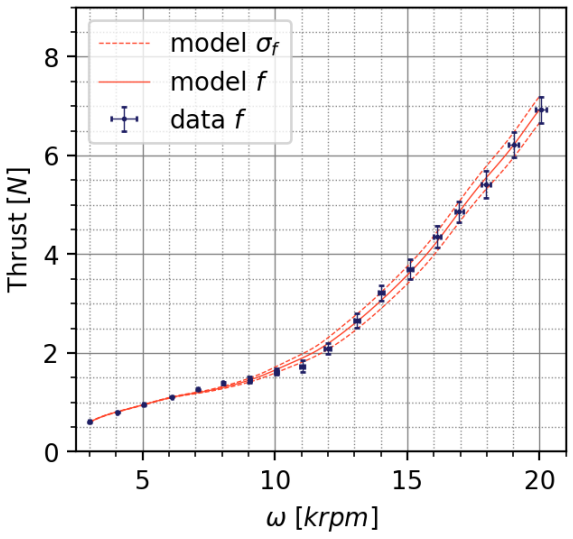

(f) V = $10\,\mathrm{m\,s^{-1}}$

Figure A.2: Thrust-rpm curves for the 5x4.5x3 rotor ($-7\,\mathrm{m\,s^{-1}}$ to $10\,\mathrm{m\,s^{-1}}$).

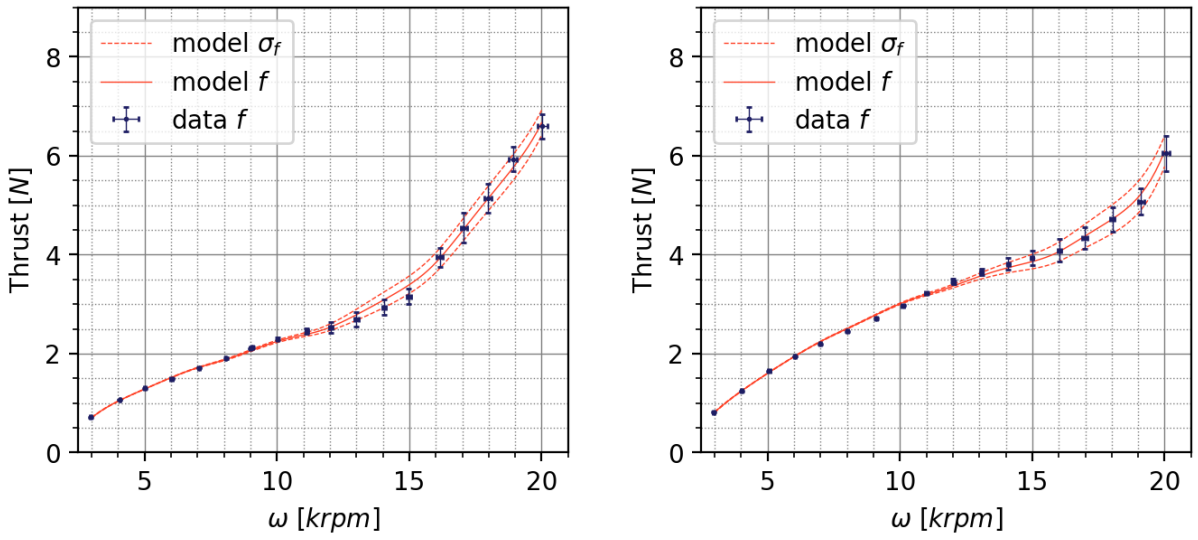

(a) V = 13 m s^{-1}

(b) V = 16 m s^{-1}

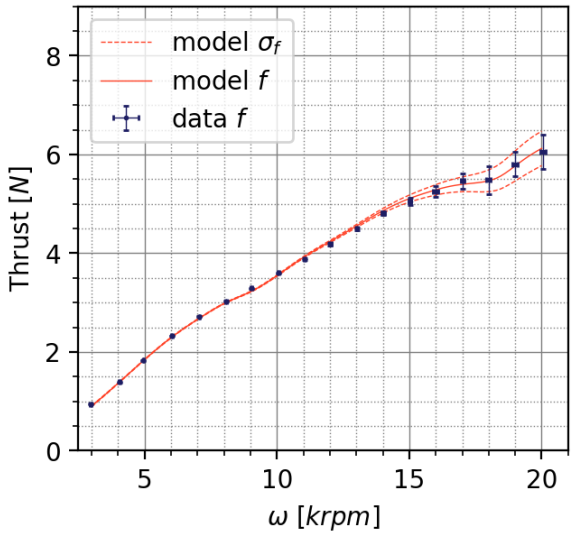

(c) V = 19 m s^{-1}

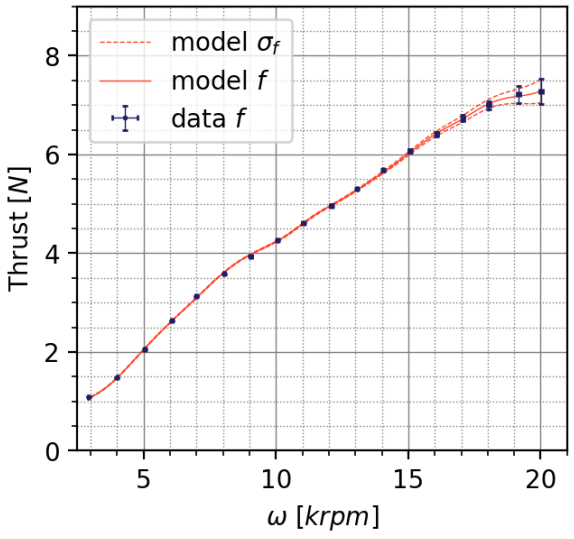

(d) V = 22 m s^{-1}

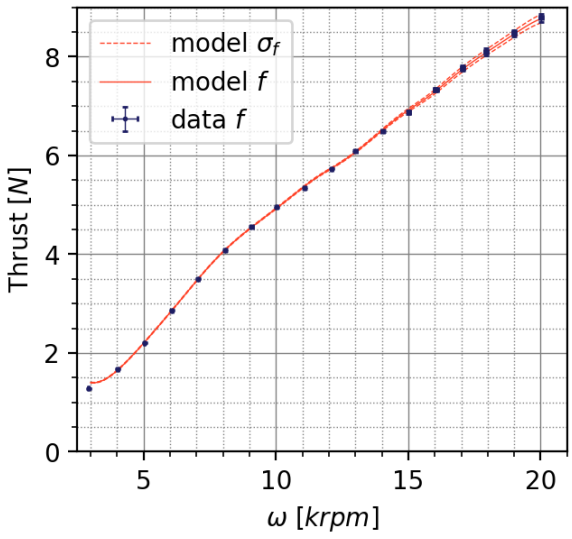

(e) V = 25 m s^{-1}

Figure A.3: Thrust-rpm curves for the 5x4.5x3 rotor (13 m s^{-1} to 25 m s^{-1}).

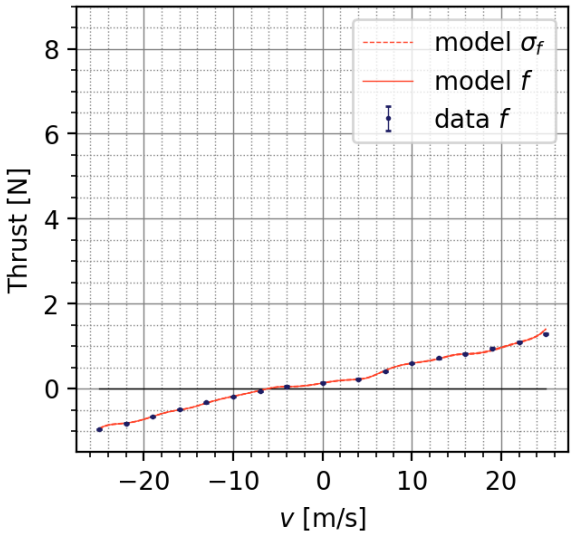

(a) $\omega = 3000\,\text{rpm}$

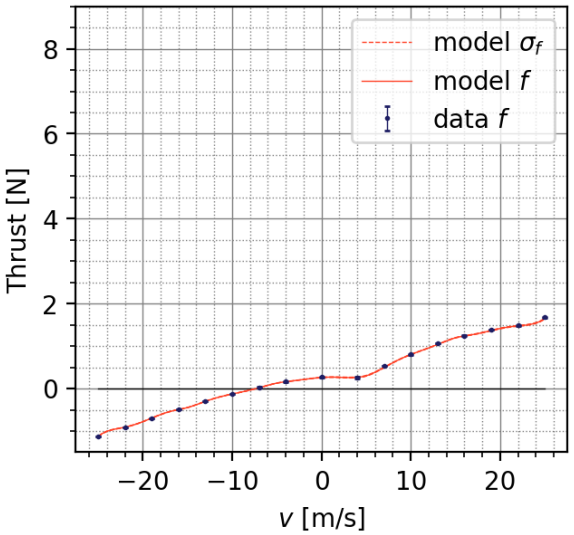

(b) $\omega = 4000\,\text{rpm}$

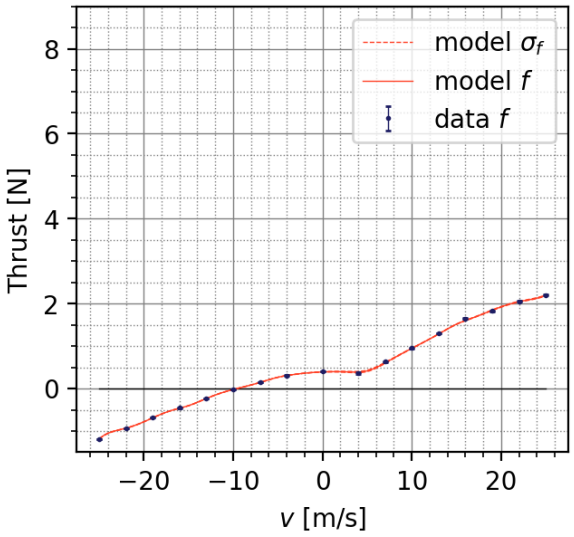

(c) $\omega = 5000\,\text{rpm}$

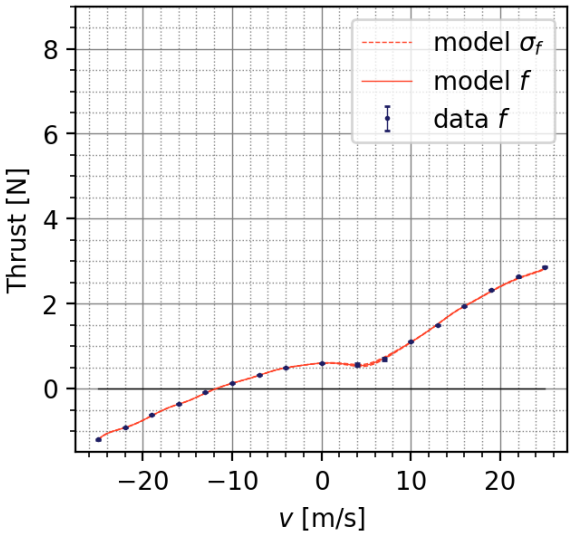

(d) $\omega = 6000\,\text{rpm}$

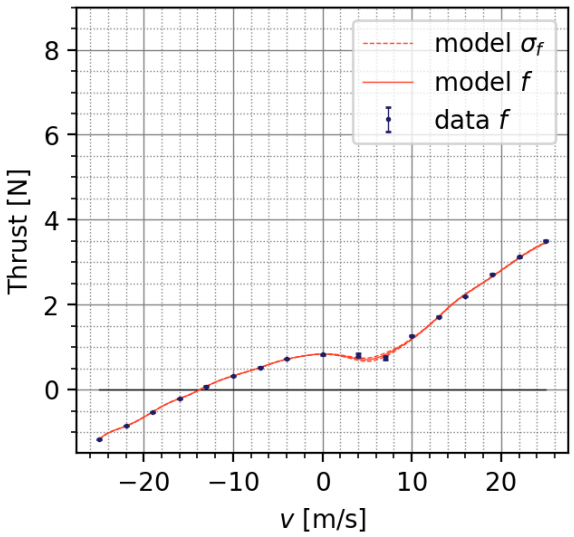

(e) $\omega = 7000\,\text{rpm}$

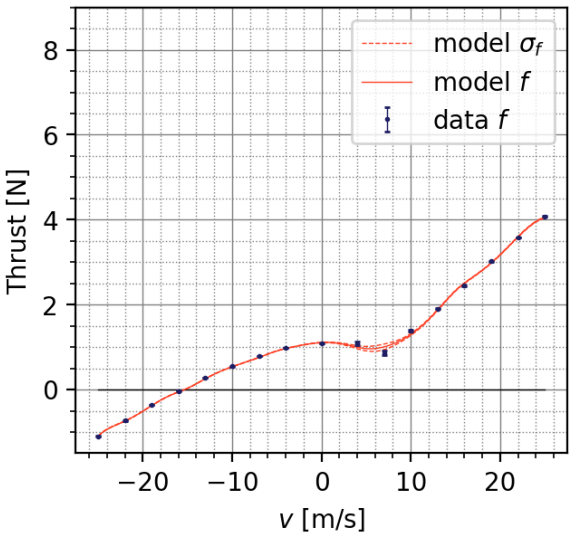

(f) $\omega = 8000\,\text{rpm}$

Figure A.4: Thrust-speed curves for the 5x4.5x3 rotor (3 krpm to 8 krpm).

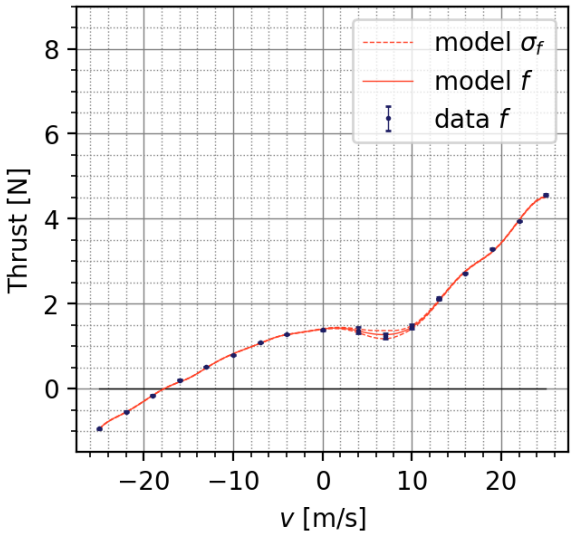

(a) $\omega = 9000\,\text{rpm}$

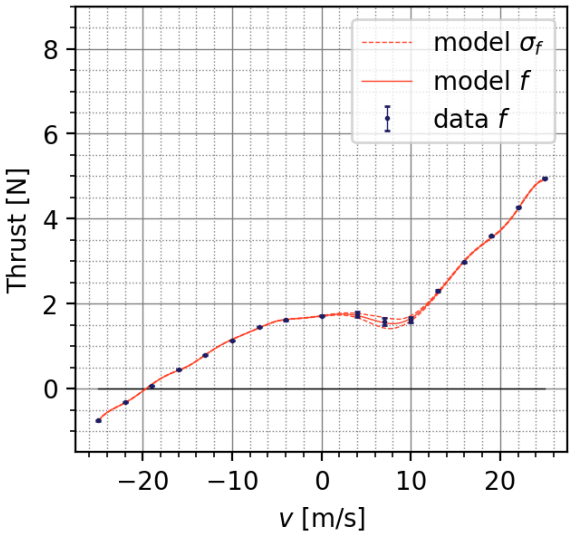

(b) $\omega = 10\,000\,\text{rpm}$

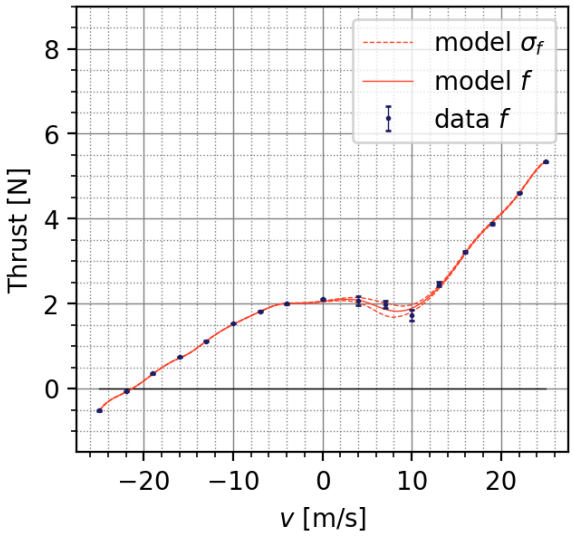

(c) $\omega = 11\,000\,\text{rpm}$

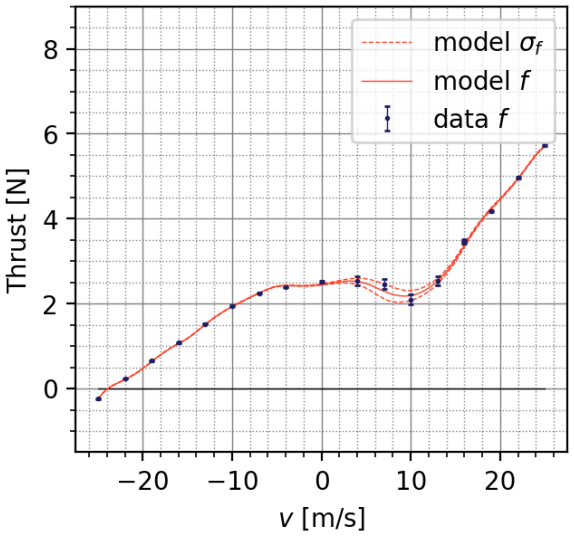

(d) $\omega = 12\,000\,\text{rpm}$

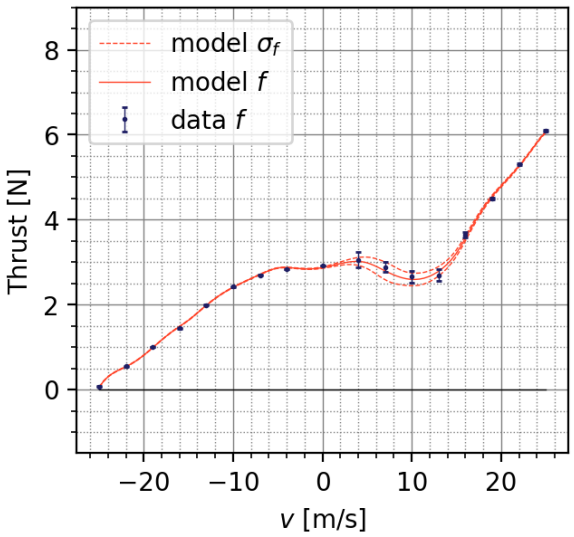

(e) $\omega = 13\,000\,\text{rpm}$

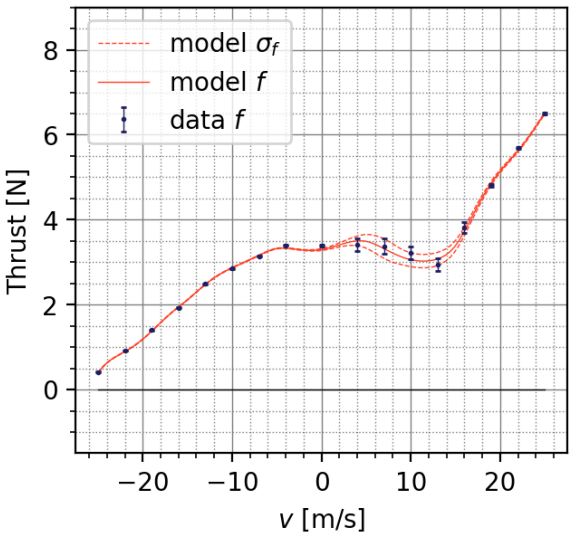

(f) $\omega = 14\,000\,\text{rpm}$

Figure A.5: Thrust-speed curves for the 5x4.5x3 rotor (9 krpm to 14 krpm).

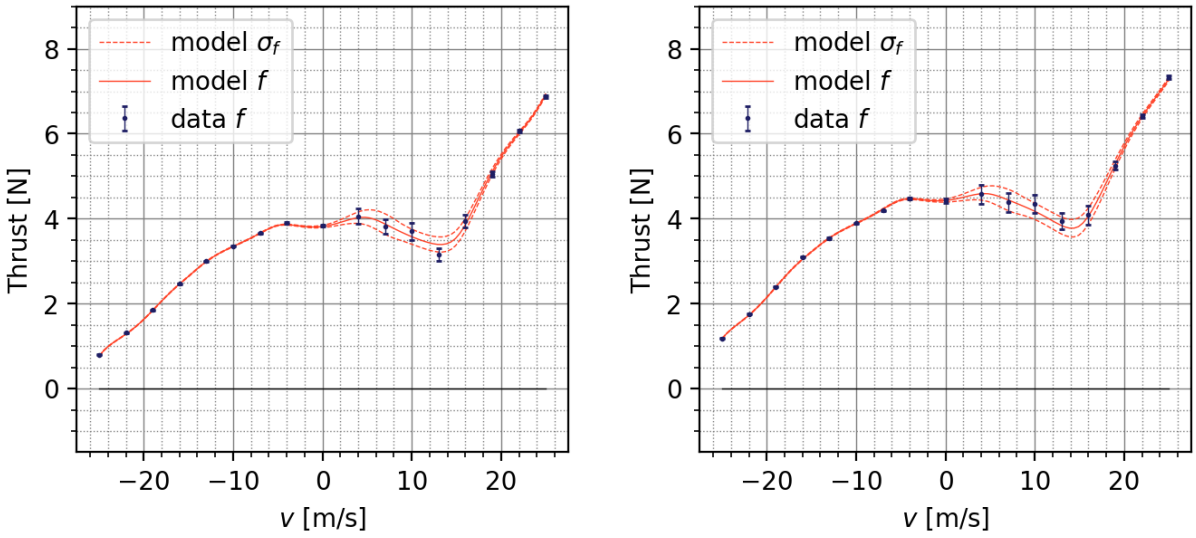

(a) $\omega = 15\,000\,\text{rpm}$

(b) $\omega = 16\,000\,\text{rpm}$

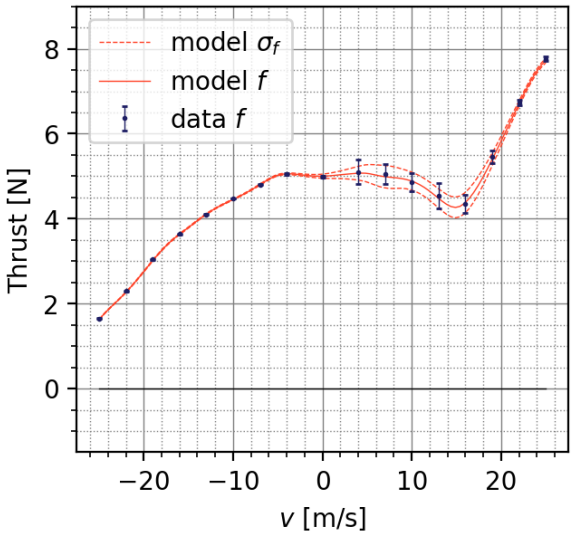

(c) $\omega = 17\,000\,\text{rpm}$

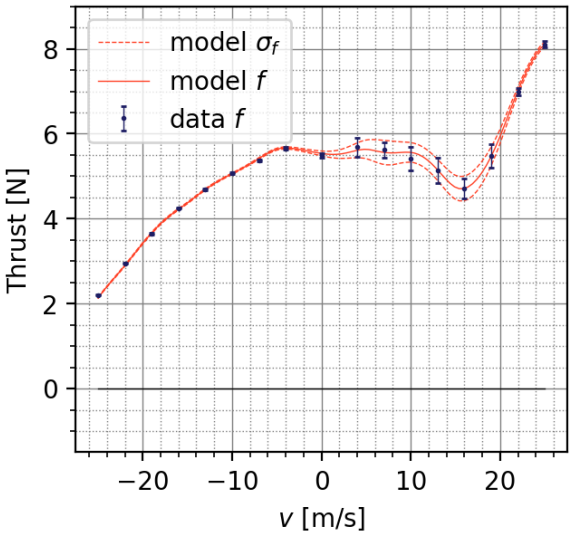

(d) $\omega = 18\,000\,\text{rpm}$

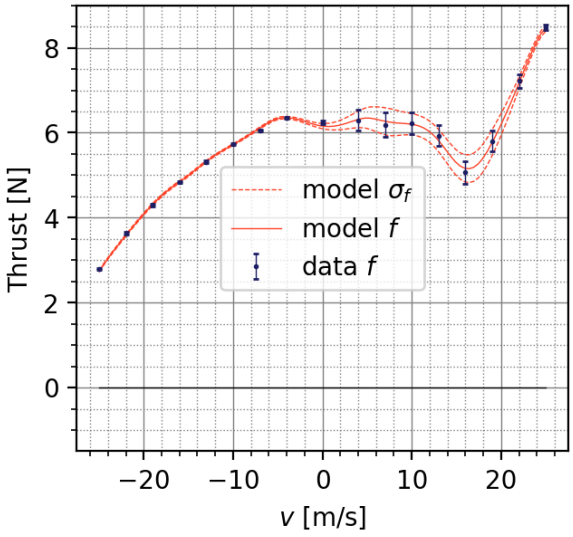

(e) $\omega = 19\,000\,\text{rpm}$

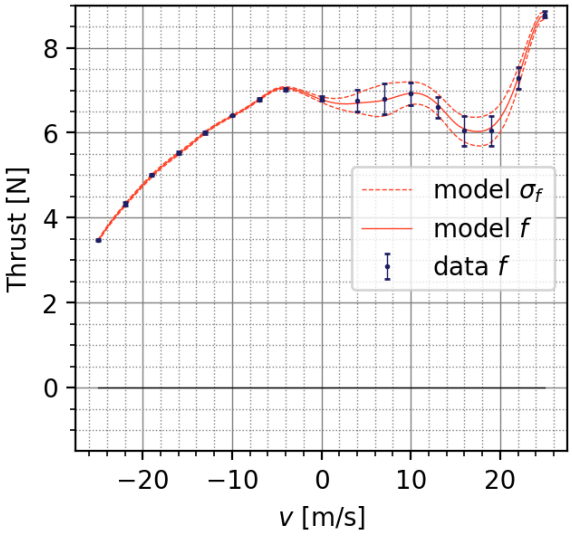

(f) $\omega = 20\,000\,\text{rpm}$

Figure A.6: Thrust-speed curves for the 5x4.5x3 rotor (15 krpm to 20 krpm).

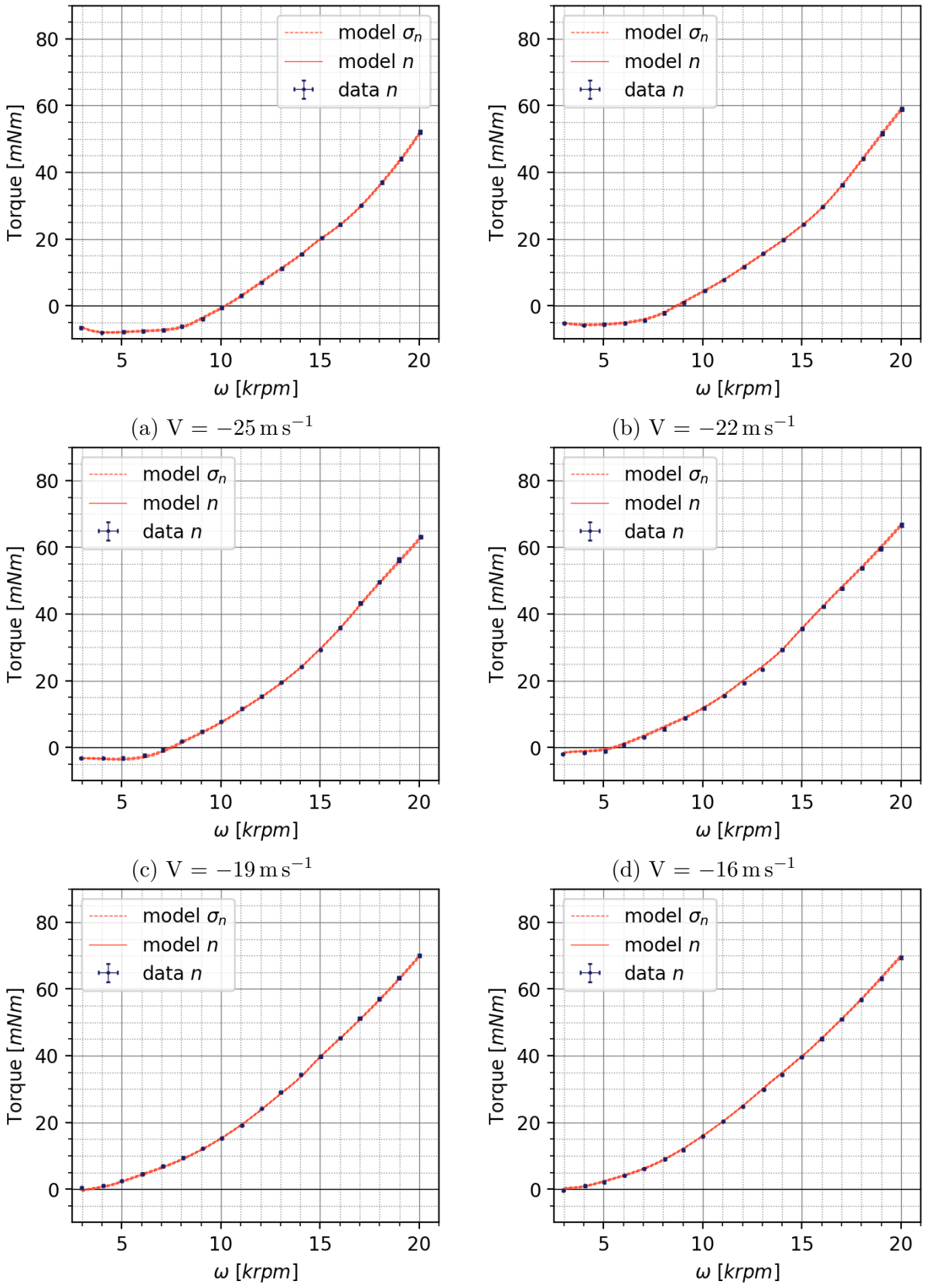

(a) V $= -25\,\mathrm{m\,s^{-1}}$

(b) V $= -22\,\mathrm{m\,s^{-1}}$

(c) V $= -19\,\mathrm{m\,s^{-1}}$

(d) V $= -16\,\mathrm{m\,s^{-1}}$

(e) V $= -13\,\mathrm{m\,s^{-1}}$

(f) V $= -10\,\mathrm{m\,s^{-1}}$

Figure A.7: Moment-rpm curves for the 5x4.5x3 rotor ($-25\,\mathrm{m\,s^{-1}}$ to $-10\,\mathrm{m\,s^{-1}}$).

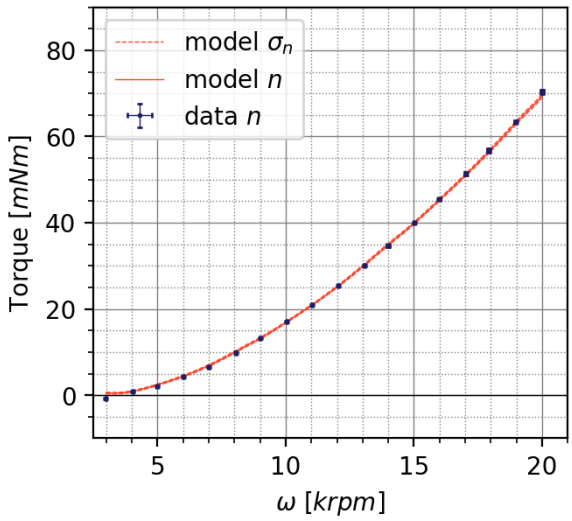

(a) V $= -7\,\mathrm{m\,s^{-1}}$

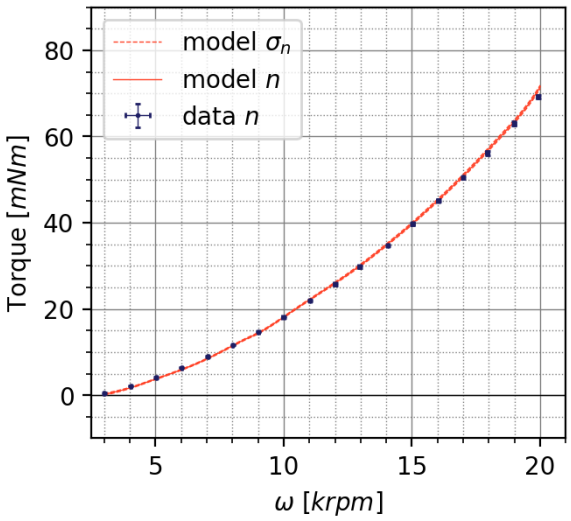

(b) V $= -4\,\mathrm{m\,s^{-1}}$

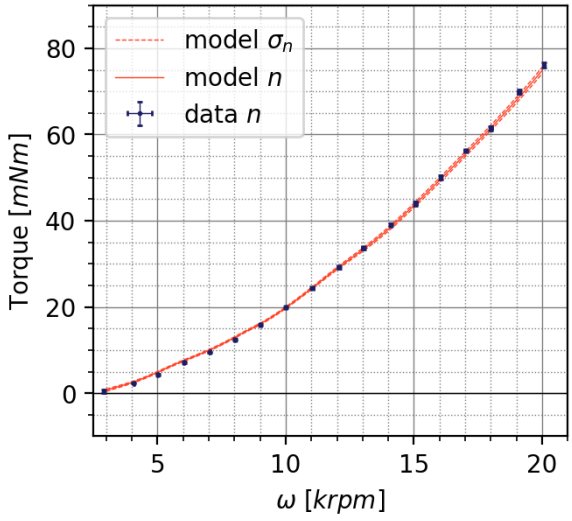

(c) V $= 0\,\mathrm{m\,s^{-1}}$

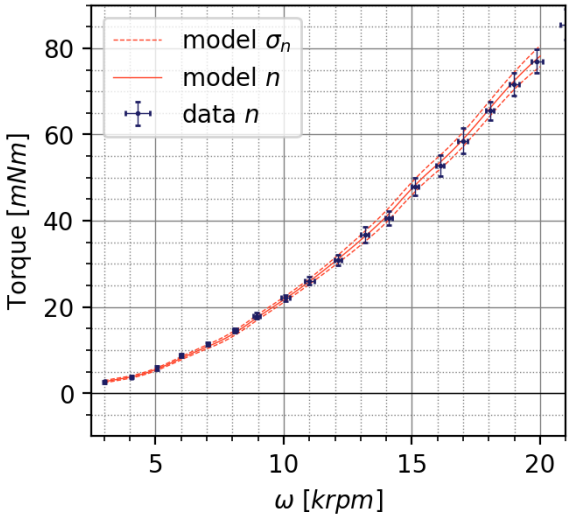

(d) V $= 4\,\mathrm{m\,s^{-1}}$

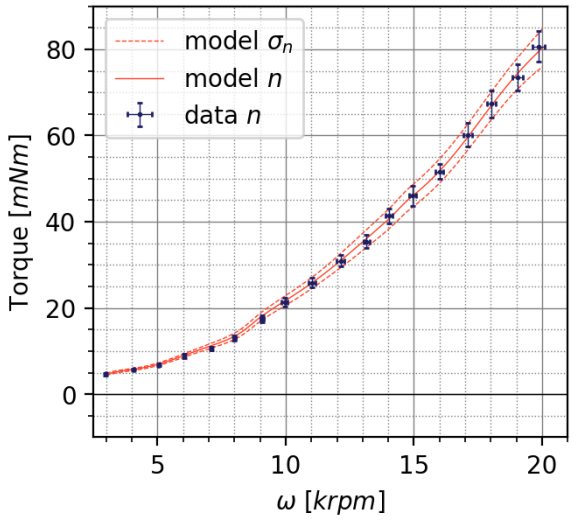

(e) V $= 7\,\mathrm{m\,s^{-1}}$

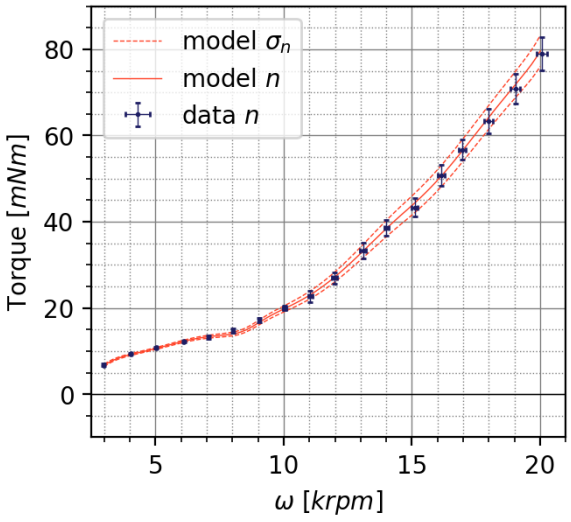

(f) V $= 10\,\mathrm{m\,s^{-1}}$

Figure A.8: Moment-rpm curves for the 5x4.5x3 rotor ($-7\,\mathrm{m\,s^{-1}}$ to $10\,\mathrm{m\,s^{-1}}$).

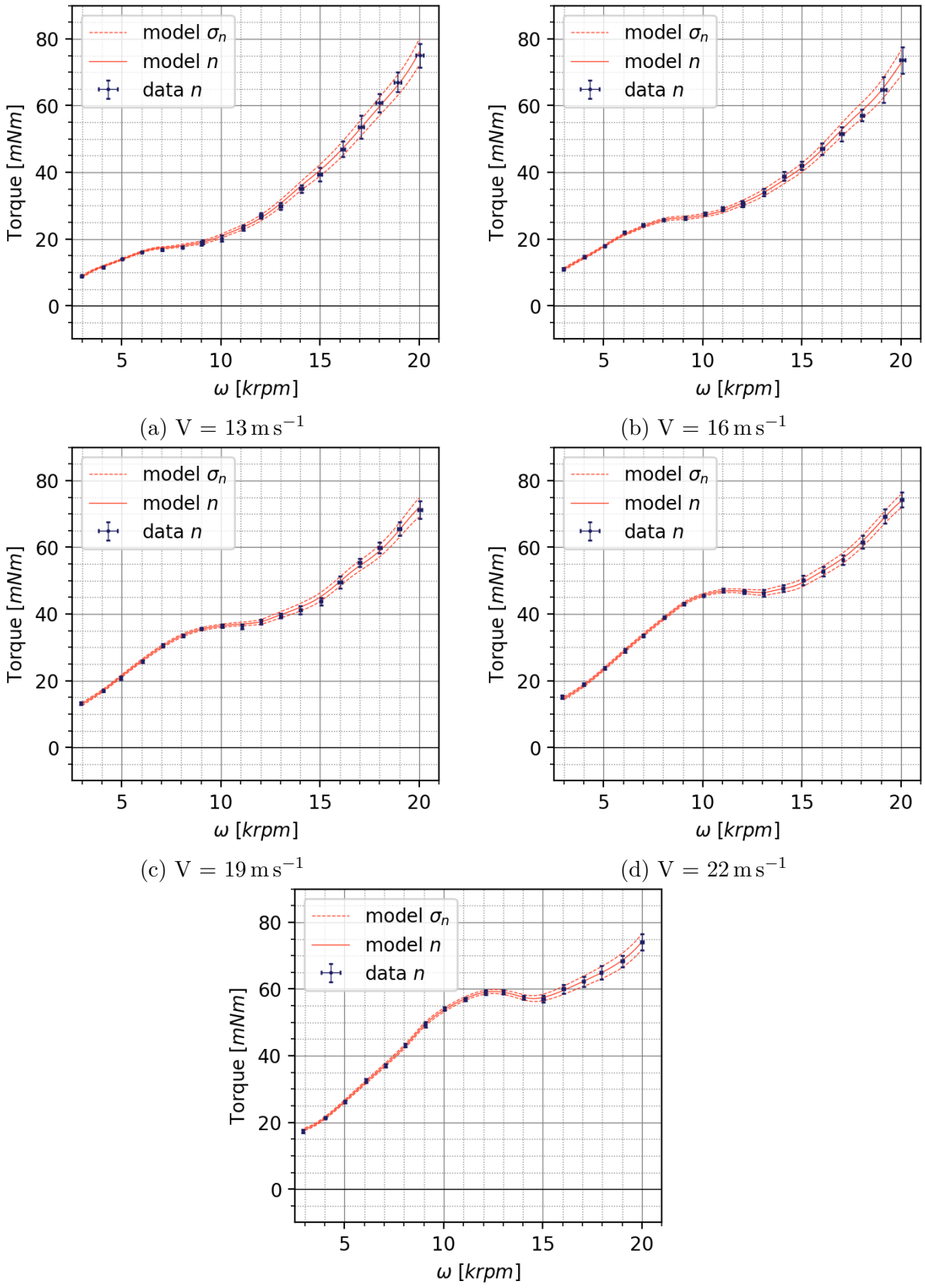

(a) V = 13 m s^{-1}

(b) V = 16 m s^{-1}

(c) V = 19 m s^{-1}

(d) V = 22 m s^{-1}

(e) V = 25 m s^{-1}

Figure A.9: Moment-rpm curves for the 5x4.5x3 rotor (13 m s^{-1} to 25 m s^{-1}).

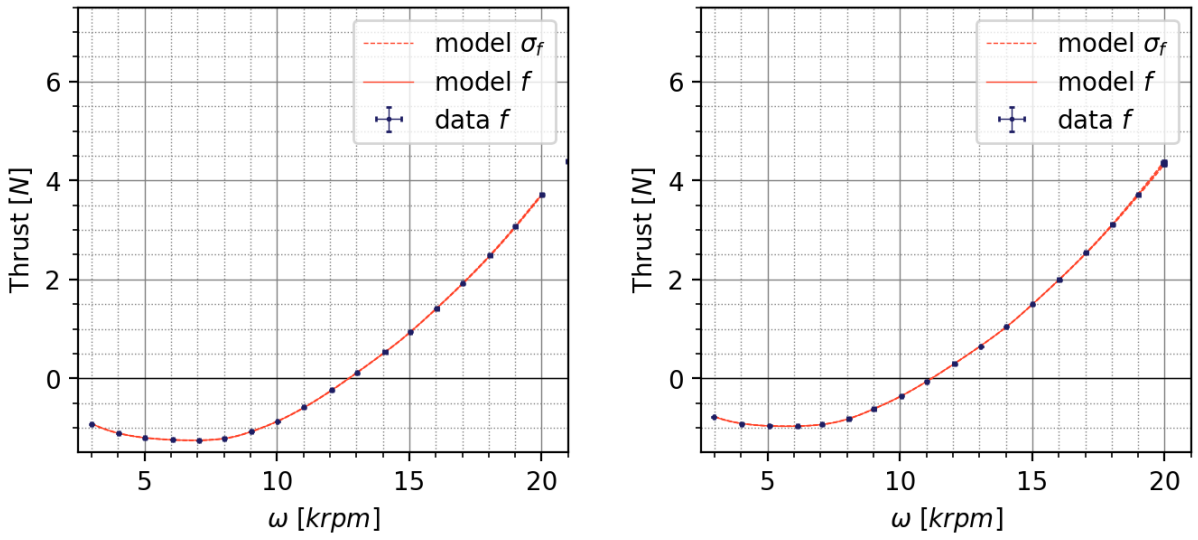

(a) V $= -25\,\mathrm{m\,s^{-1}}$

(b) V $= -22\,\mathrm{m\,s^{-1}}$

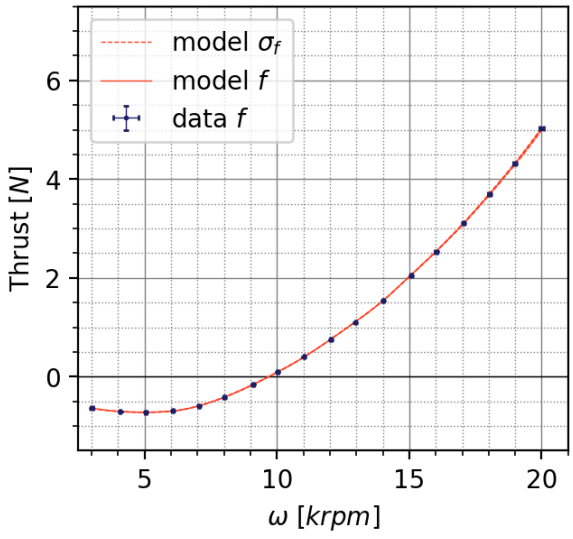

(c) V $= -19\,\mathrm{m\,s^{-1}}$

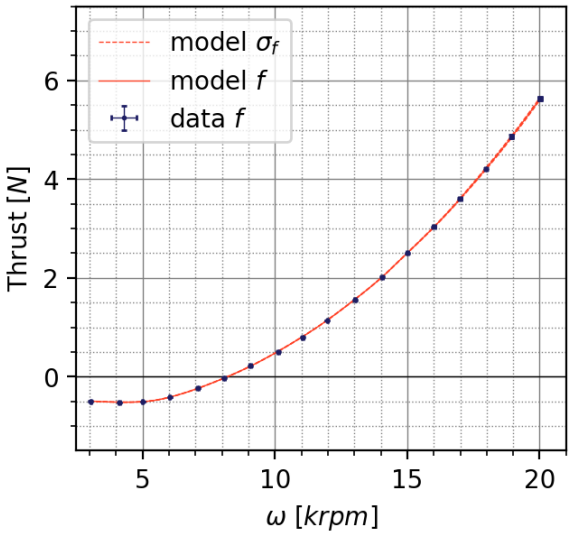

(d) V $= -16\,\mathrm{m\,s^{-1}}$

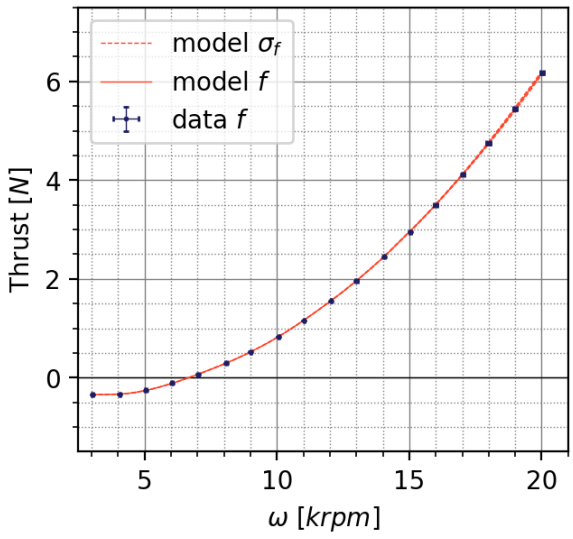

(e) V $= -13\,\mathrm{m\,s^{-1}}$

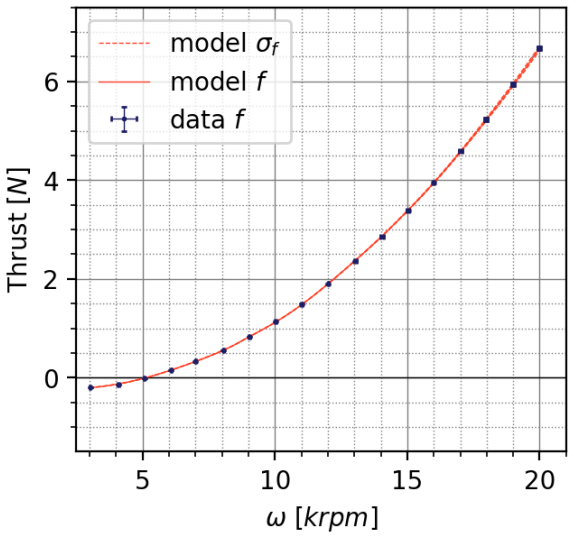

(f) V $= -10\,\mathrm{m\,s^{-1}}$

Figure A.10: Thrust-rpm curves for the 5x5x3 rotor ($-25\,\mathrm{m\,s^{-1}}$ to $-10\,\mathrm{m\,s^{-1}}$).

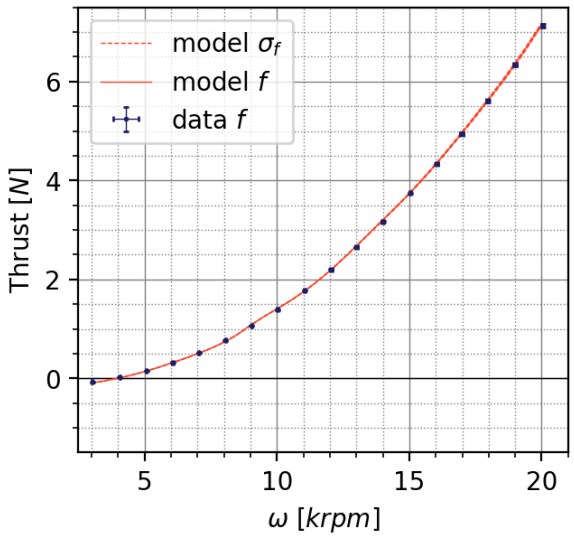

(a) V = $-7\,\mathrm{m\,s^{-1}}$

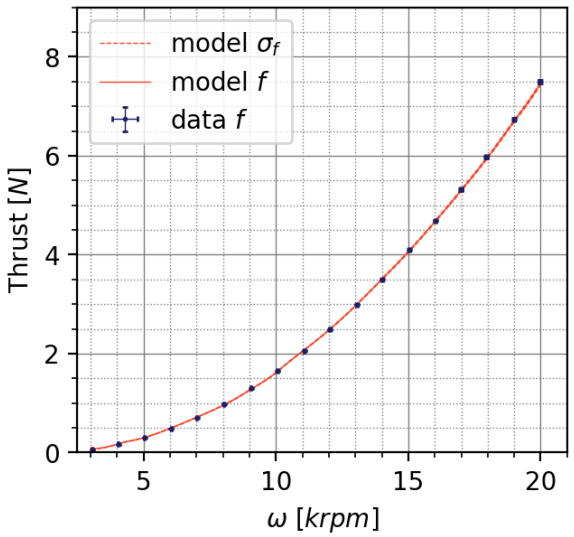

(b) V = $-4\,\mathrm{m\,s^{-1}}$

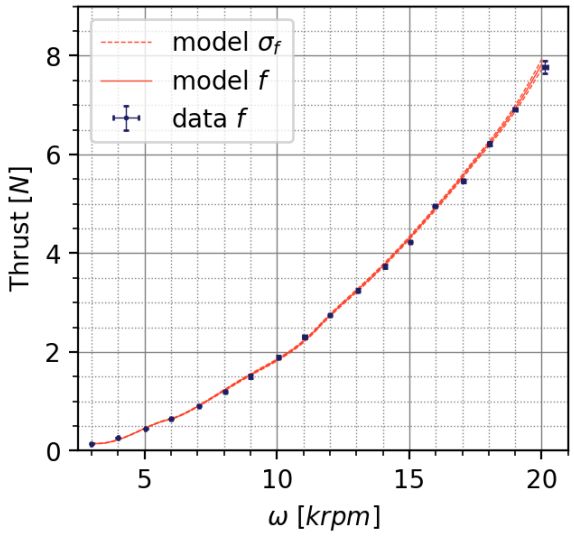

(c) V = $0\,\mathrm{m\,s^{-1}}$

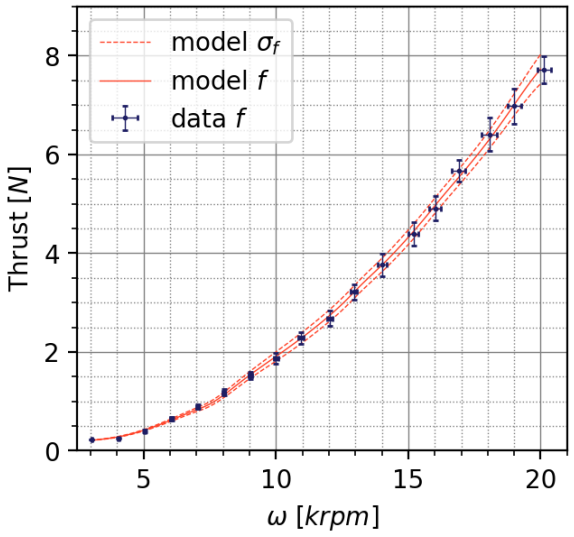

(d) V = $4\,\mathrm{m\,s^{-1}}$

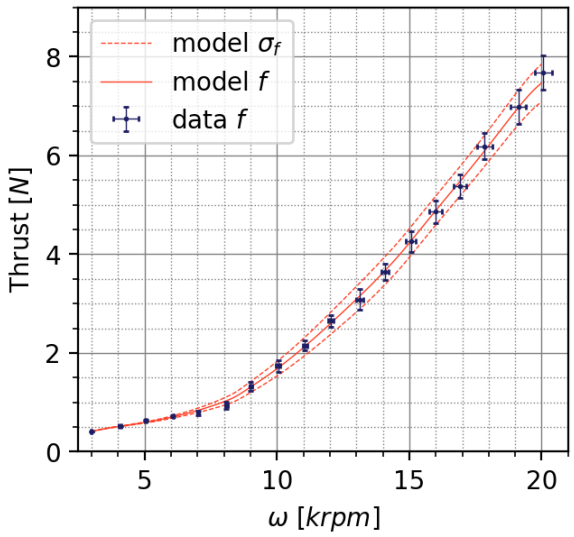

(e) V = $7\,\mathrm{m\,s^{-1}}$

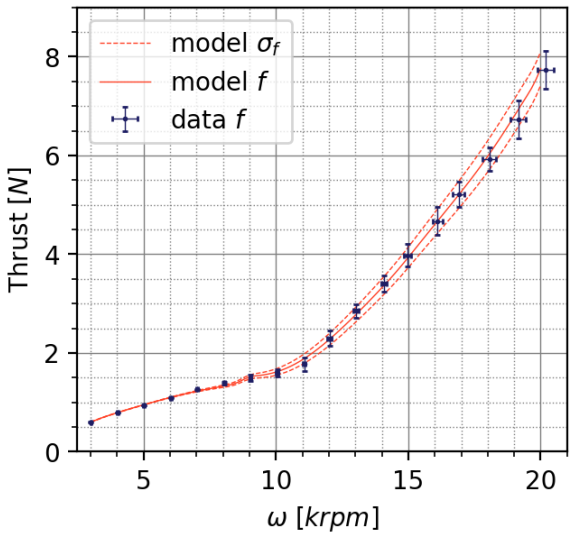

(f) V = $10\,\mathrm{m\,s^{-1}}$

Figure A.11: Thrust-rpm curves for the 5x5x3 rotor ($-7\,\mathrm{m\,s^{-1}}$ to $10\,\mathrm{m\,s^{-1}}$).

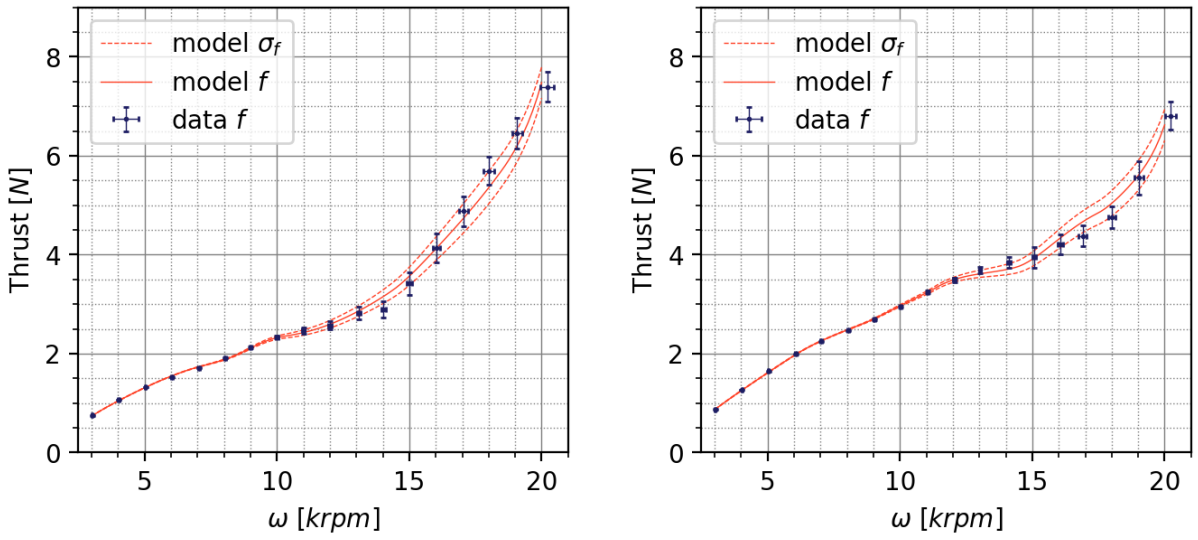

(a) V = 13 m s^{-1}

(b) V = 16 m s^{-1}

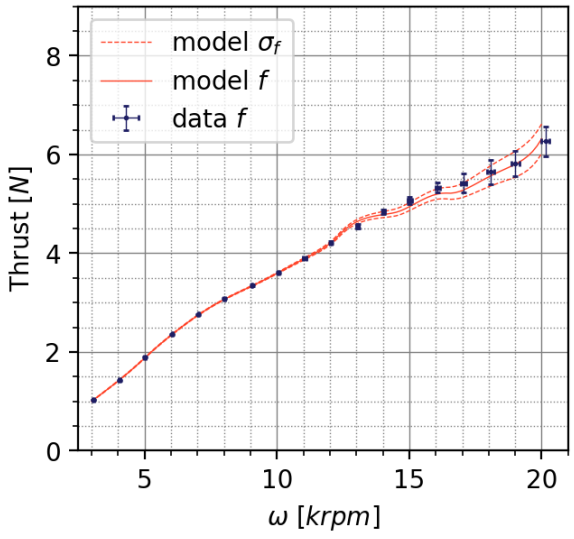

(c) V = 19 m s^{-1}

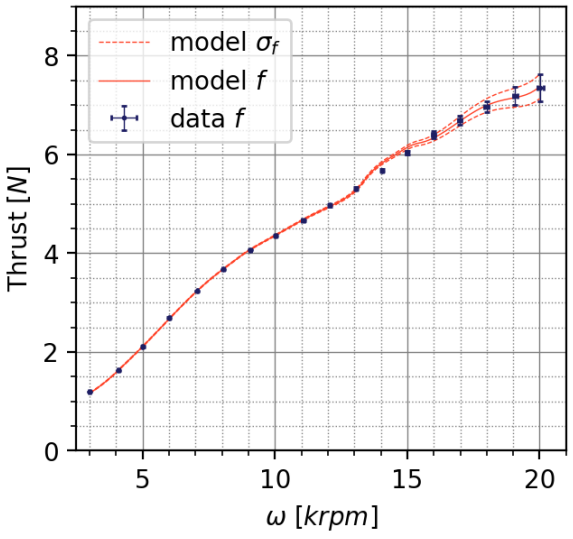

(d) V = 22 m s^{-1}

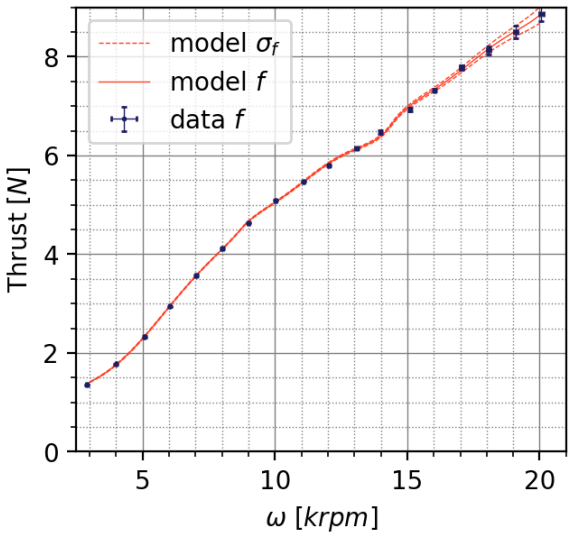

(e) V = 25 m s^{-1}

Figure A.12: Thrust-rpm curves for the 5x5x3 rotor (13 m s^{-1} to 25 m s^{-1}).

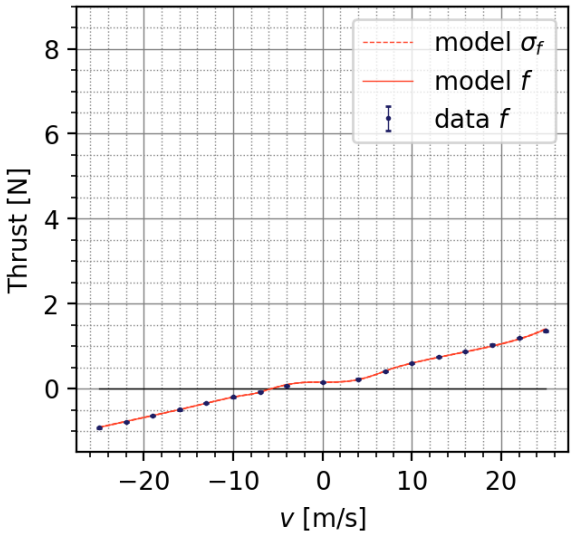

(a) $\omega = 3000\,\text{rpm}$

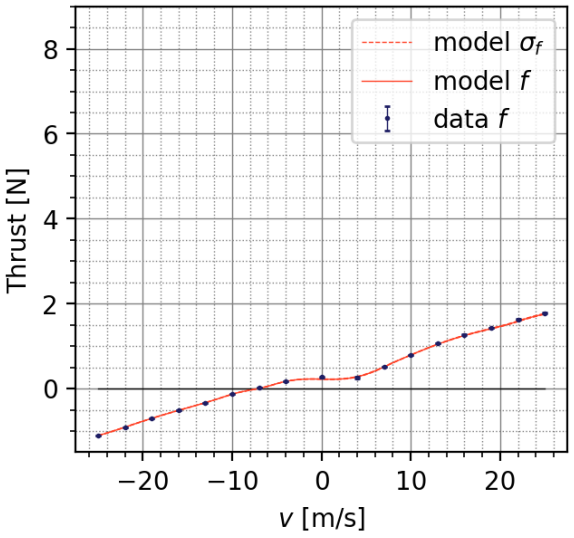

(b) $\omega = 4000\,\text{rpm}$

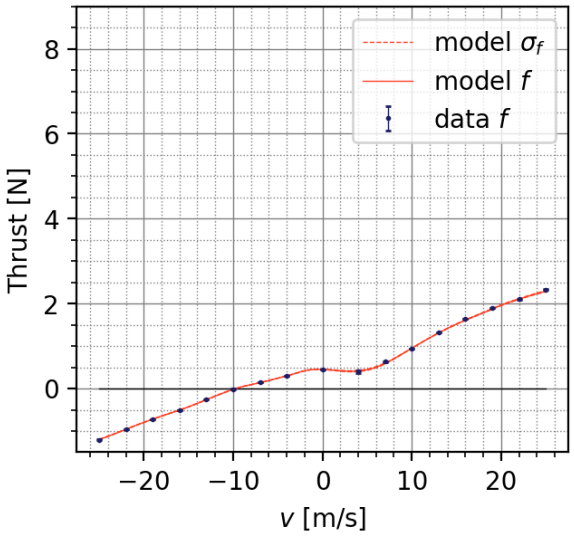

(c) $\omega = 5000\,\text{rpm}$

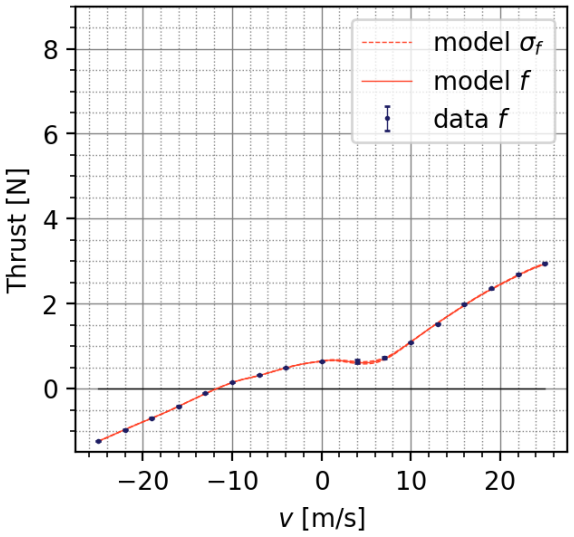

(d) $\omega = 6000\,\text{rpm}$

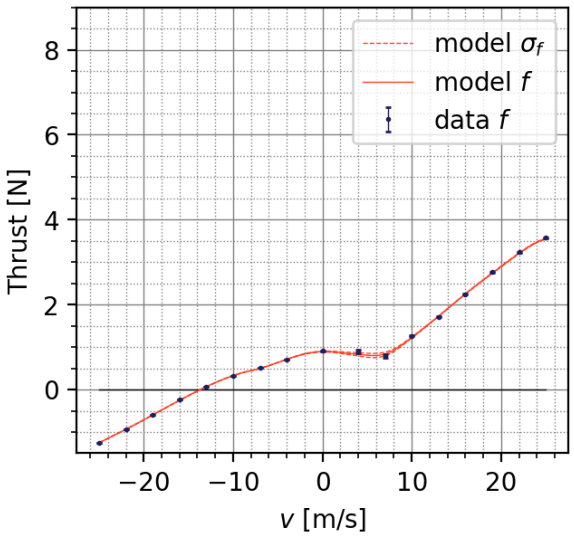

(e) $\omega = 7000\,\text{rpm}$

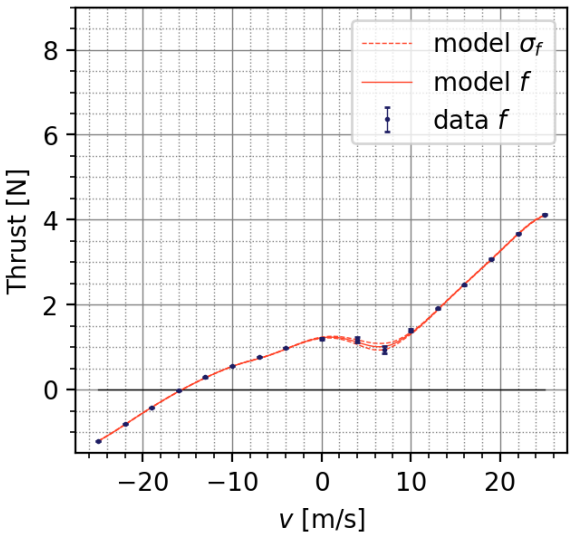

(f) $\omega = 8000\,\text{rpm}$

Figure A.13: Thrust-speed curves for the 5x5x3 rotor (3 krpm to 8 krpm).

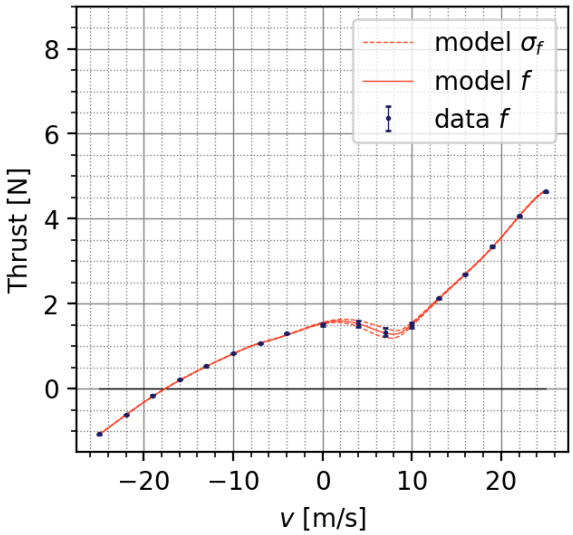

(a) $\omega = 9000\,\text{rpm}$

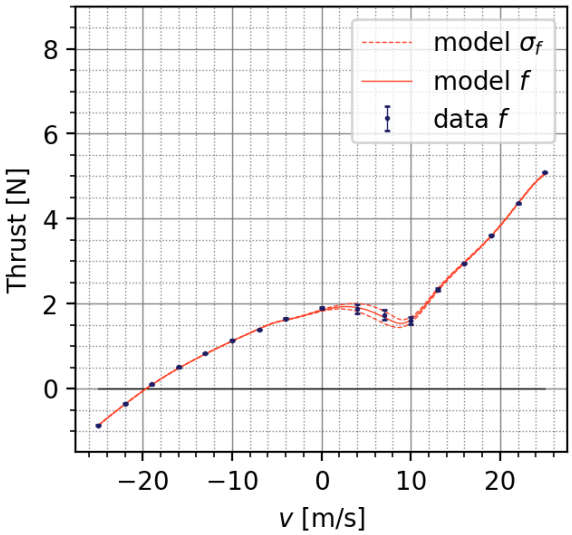

(b) $\omega = 10\,000\,\text{rpm}$

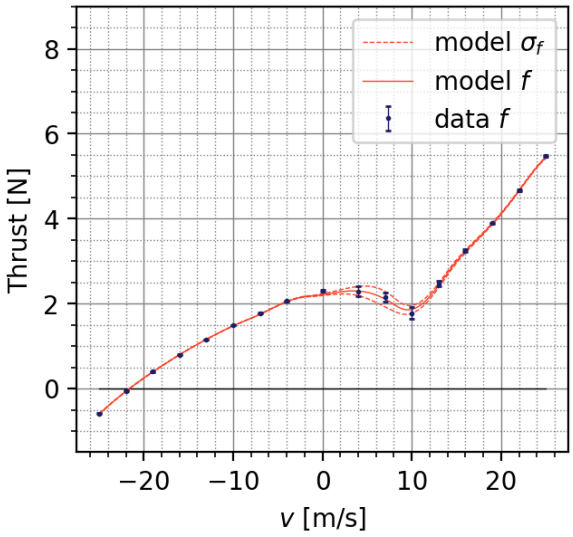

(c) $\omega = 11\,000\,\text{rpm}$

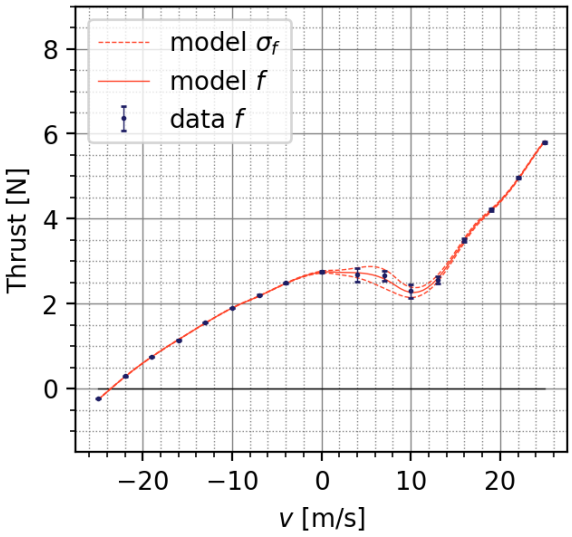

(d) $\omega = 12\,000\,\text{rpm}$

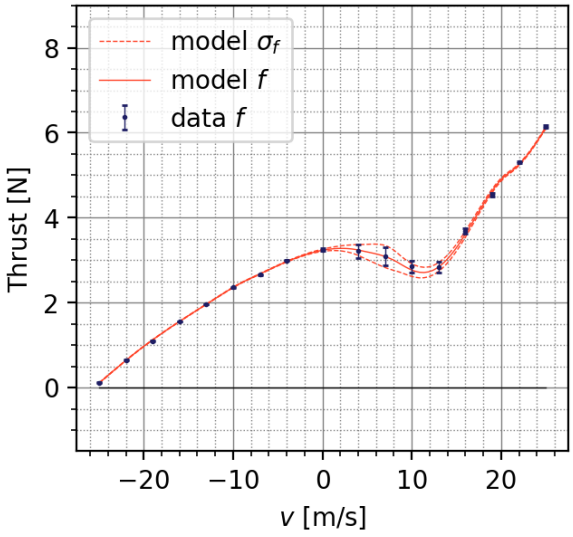

(e) $\omega = 13\,000\,\text{rpm}$

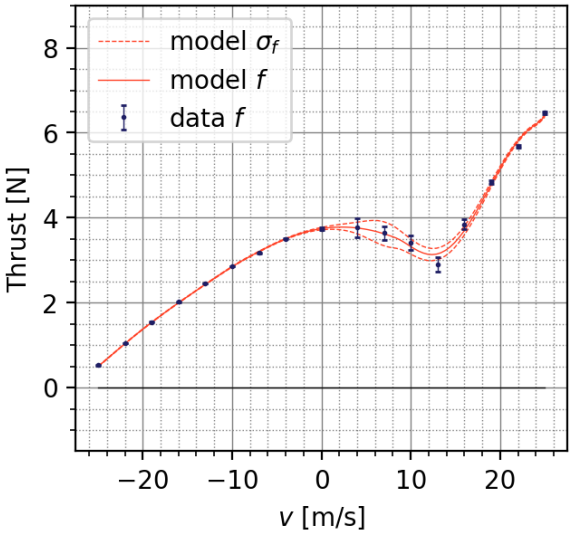

(f) $\omega = 14\,000\,\text{rpm}$

Figure A.14: Thrust-speed curves for the 5x5x3 rotor (9 krpm to 14 krpm).

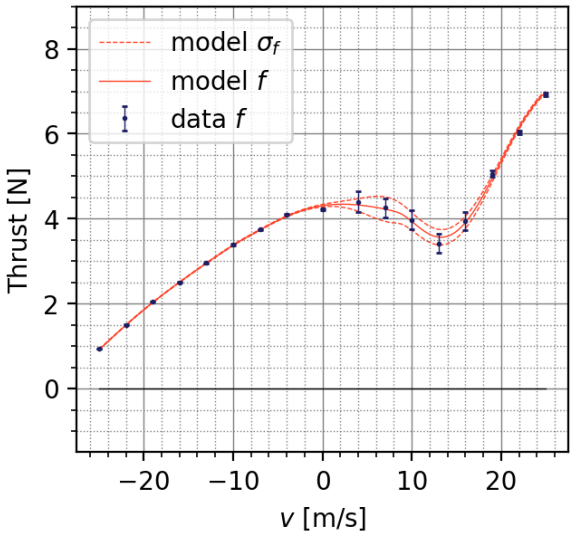

(a) $\omega = 15\,000\,\text{rpm}$

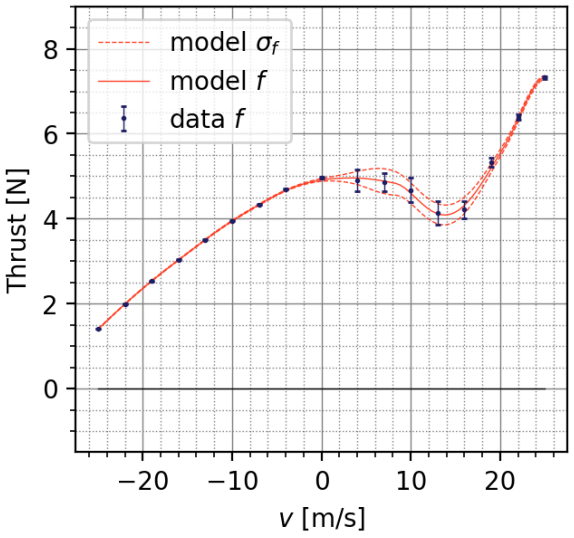

(b) $\omega = 16\,000\,\text{rpm}$

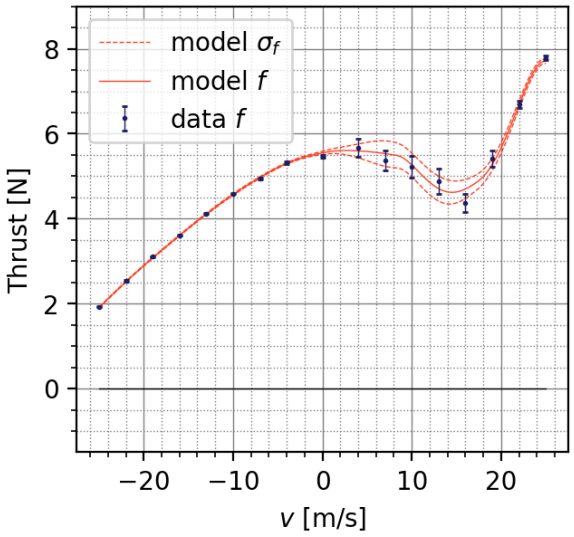

(c) $\omega = 17\,000\,\text{rpm}$

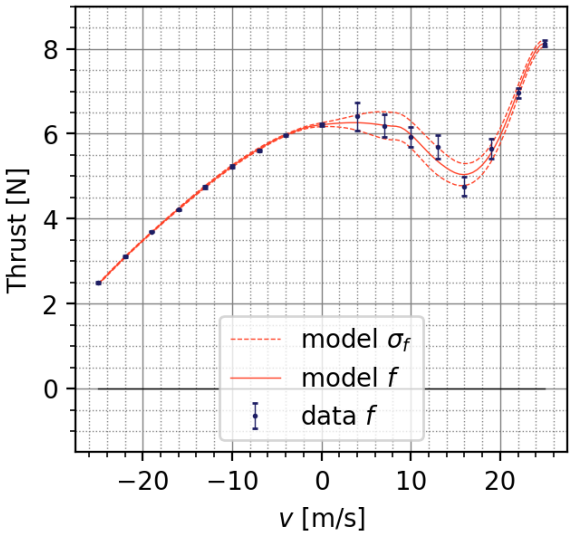

(d) $\omega = 18\,000\,\text{rpm}$

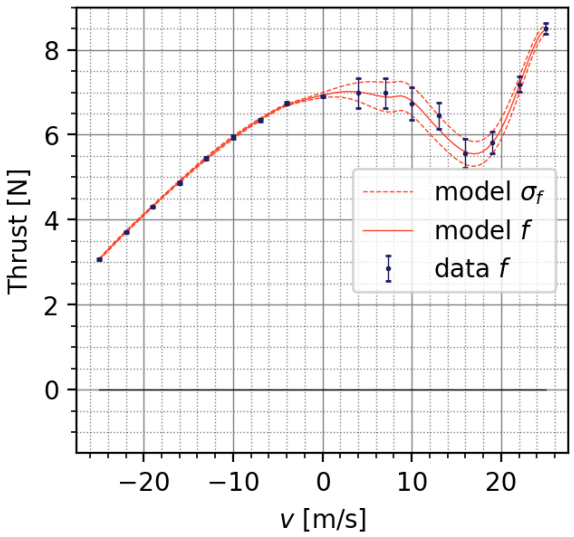

(e) $\omega = 19\,000\,\text{rpm}$

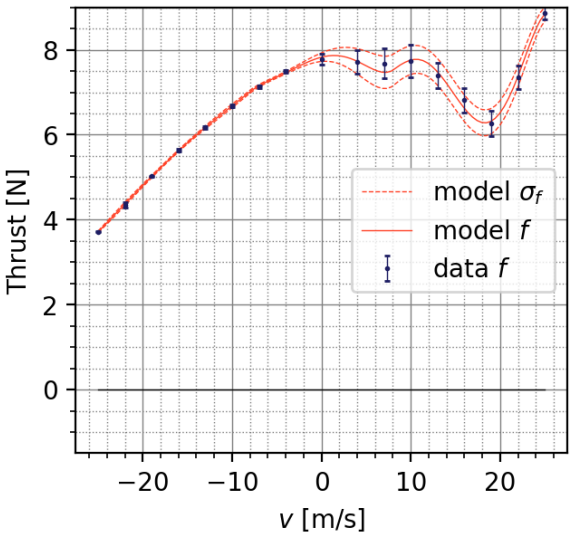

(f) $\omega = 20\,000\,\text{rpm}$

Figure A.15: Thrust-speed curves for the 5x5x3 rotor (15 krpm to 20 krpm).

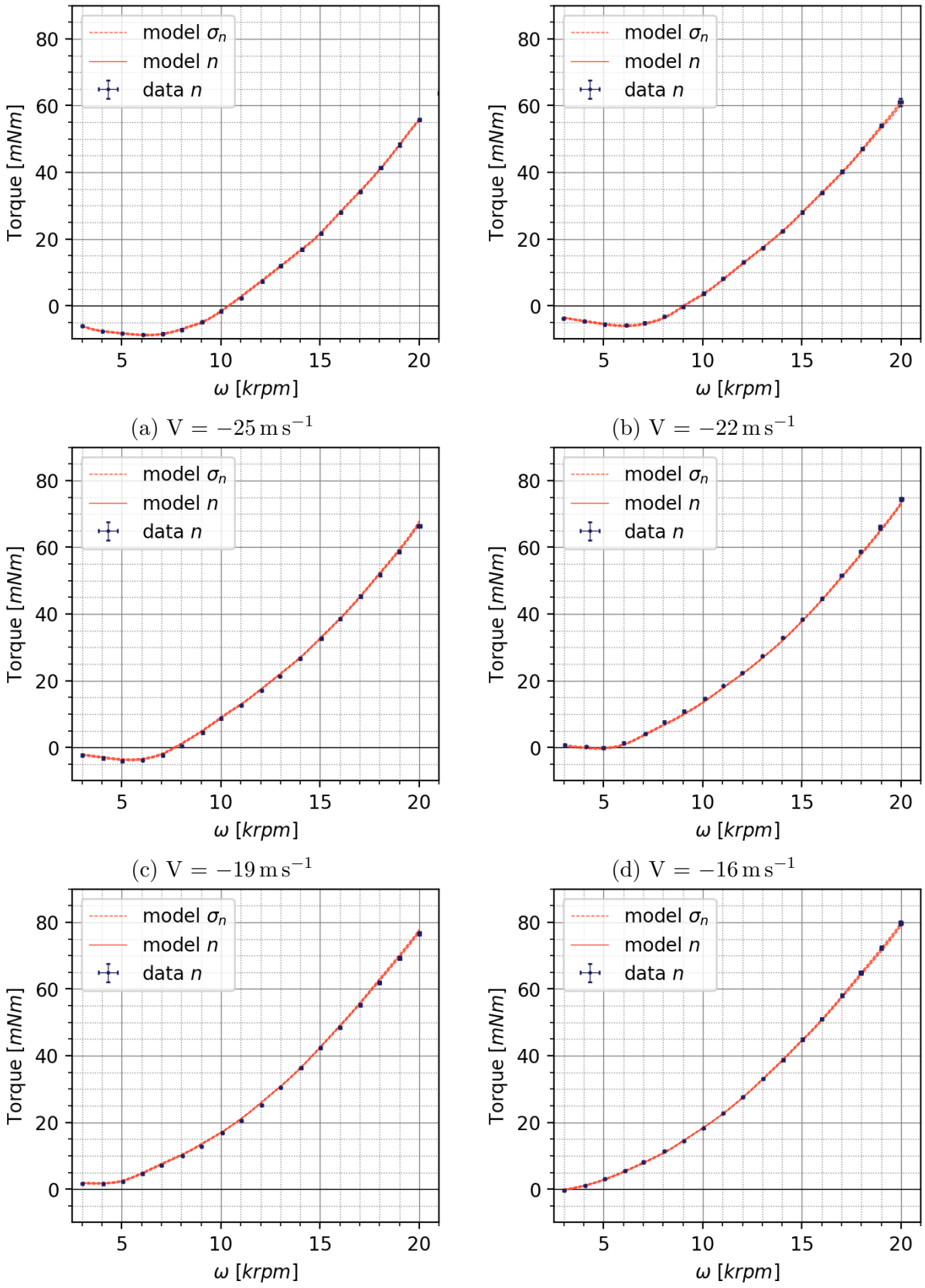

(a) V $= -25\,\mathrm{m\,s^{-1}}$

(b) V $= -22\,\mathrm{m\,s^{-1}}$

(c) V $= -19\,\mathrm{m\,s^{-1}}$

(d) V $= -16\,\mathrm{m\,s^{-1}}$

(e) V $= -13\,\mathrm{m\,s^{-1}}$

(f) V $= -10\,\mathrm{m\,s^{-1}}$

Figure A.16: Moment-rpm curves for the 5x5x3 rotor ($-25\,\mathrm{m\,s^{-1}}$ to $-10\,\mathrm{m\,s^{-1}}$).

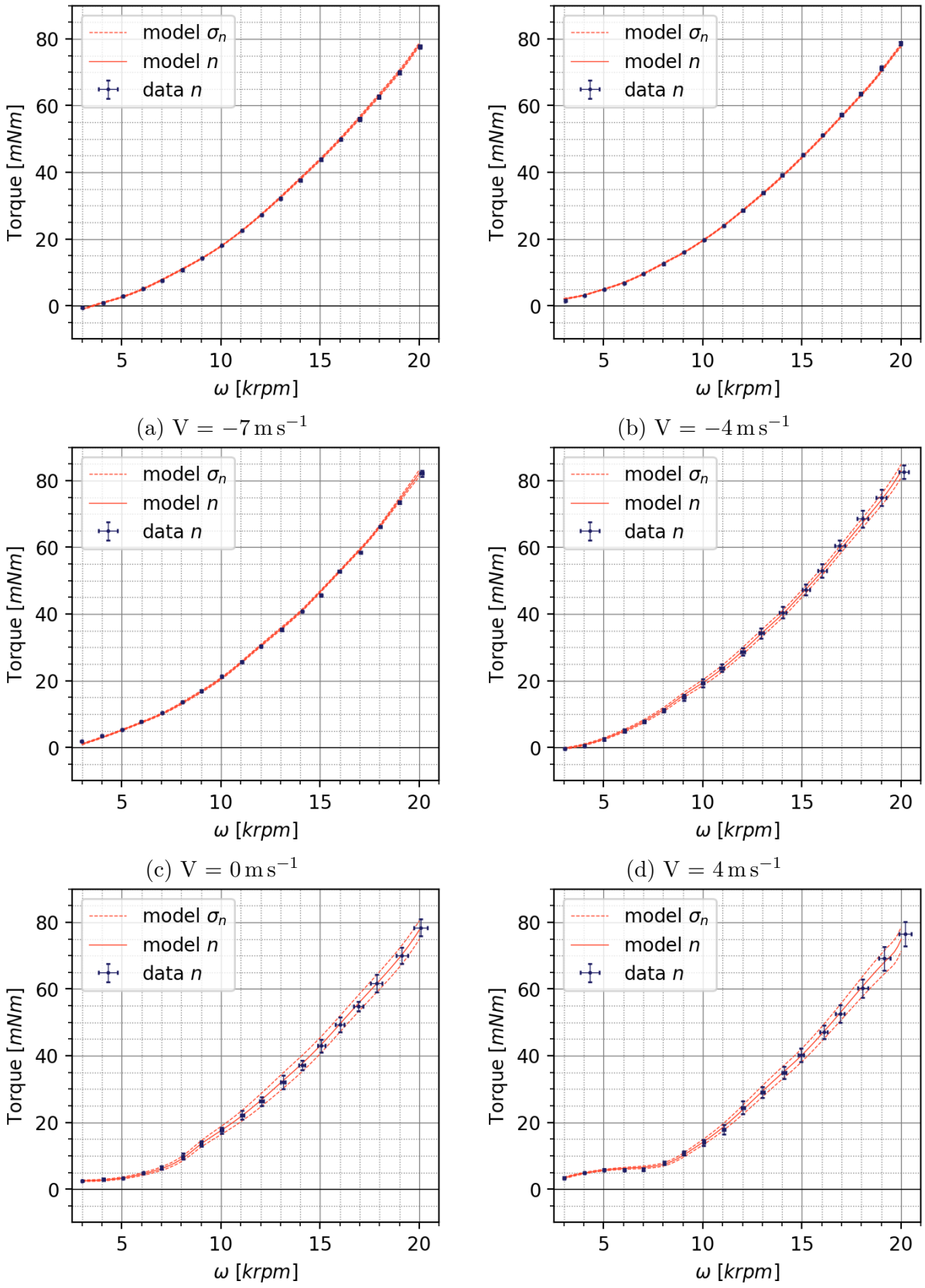

(a) V $= -7\,\mathrm{m\,s^{-1}}$ (b) V $= -4\,\mathrm{m\,s^{-1}}$

(c) V $= 0\,\mathrm{m\,s^{-1}}$ (d) V $= 4\,\mathrm{m\,s^{-1}}$

(e) V $= 7\,\mathrm{m\,s^{-1}}$ (f) V $= 10\,\mathrm{m\,s^{-1}}$

Figure A.17: Moment-rpm curves for the 5x5x3 rotor ($-7\,\mathrm{m\,s^{-1}}$ to $10\,\mathrm{m\,s^{-1}}$).

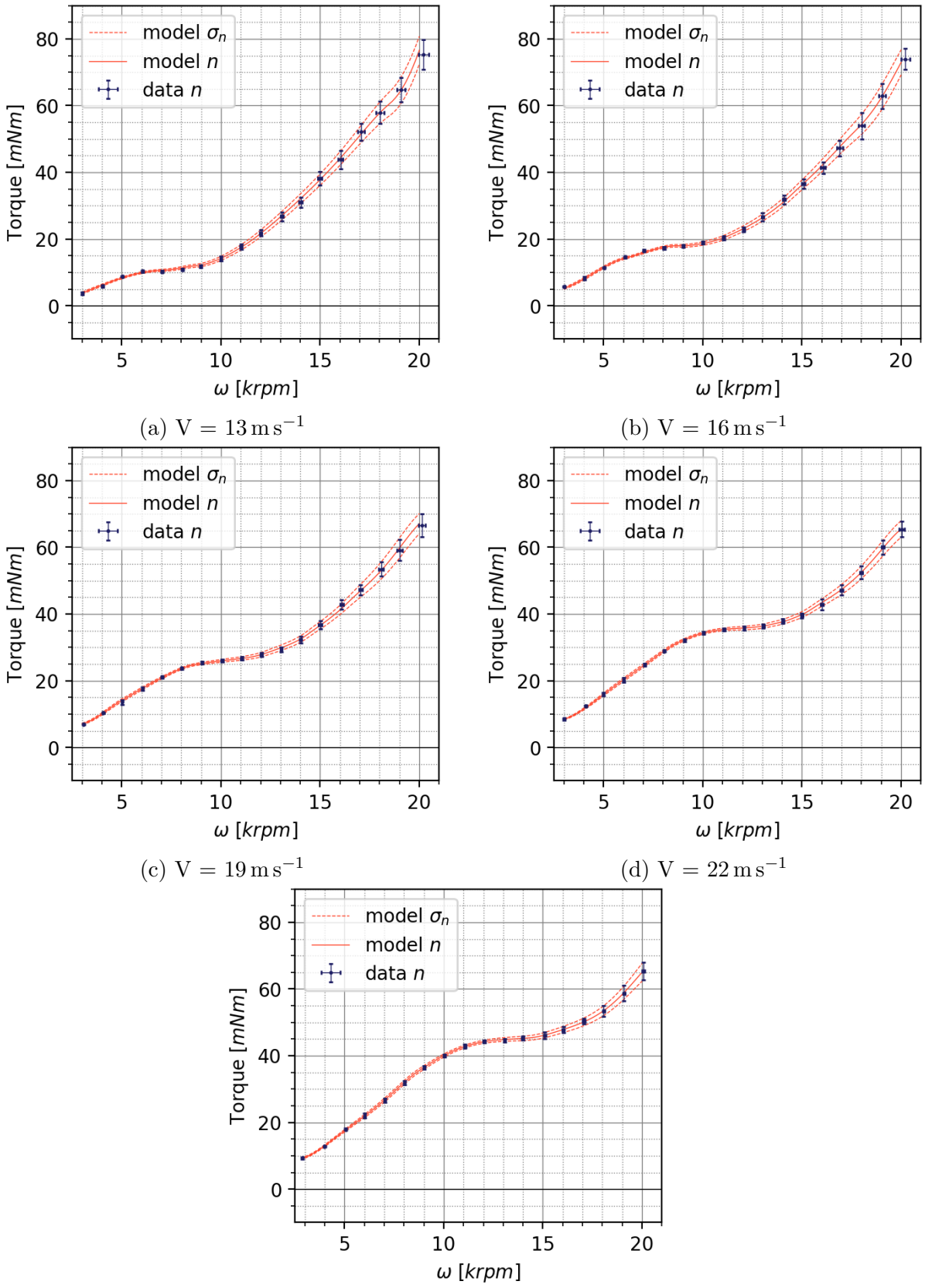

(a) V = 13 m s^{-1}

(b) V = 16 m s^{-1}

(c) V = 19 m s^{-1}

(d) V = 22 m s^{-1}

(e) V = 25 m s^{-1}

Figure A.18: Moment-rpm curves for the 5x5x3 rotor (13 m s^{-1} to 25 m s^{-1}).

Bibliography

[1] E. J. Smeur, Q. Chu, and G. C. D. Croon, "Adaptive incremental nonlinear dynamic inversion for attitude control of micro air vehicles," *Journal of Guidance, Control, and Dynamics*, vol. 39, pp. 450–461, 2016.

[2] J. K. Stolaroff, C. Samaras, E. R. O'Neill, A. Lubers, A. S. Mitchell, and D. Ceperley, "Energy use and life cycle greenhouse gas emissions of drones for commercial package delivery," *Nature Communications*, vol. 9, 12 2018.

[3] J. Verbeke and J. D. Schutter, "Experimental maneuverability and agility quantification for rotary unmanned aerial vehicle," *International Journal of Micro Air Vehicles*, vol. 10, pp. 3–11, 3 2018.

[4] G. M. Hoffmann, H. Huang, S. L. Waslander, and C. J. Tomlin, "Quadrotor helicopter flight dynamics and control: Theory and experiment," in *AIAA Guidance, Navigation and Control Conference and Exhibit*, 2007.

[5] M. Ayamga, B. Tekinerdogan, A. Kassahun, and G. Rambaldi, "Developing a policy framework for adoption and management of drones for agriculture in africa," *Technology Analysis and Strategic Management*, vol. 33, pp. 970–987, 2021.

[6] J. Ye, J. Wang, T. Song, Z. Wu, and P. Tang, "Nonlinear modeling the quadcopter considering the aerodynamic interaction," *IEEE Access*, vol. 9, pp. 134716–134732, 2021.

[7] J. Y. Hwang, M. K. Jung, and O. J. Kwon, "Numerical study of aerodynamic performance of a multirotor unmanned-aerial-vehicle configuration," *Journal of Aircraft*, vol. 52, pp. 839–846, 2015.

[8] M. Misiorowski, F. Gandhi, and A. A. Oberai, "Computational study on rotor interactional effects for a quadcopter in edgewise flight," *AIAA Journal*, vol. 57, pp. 5309–5319, 2019.

[9] D. P. Witkowski, A. K. Lee, and J. P. Sullivan, "Aerodynamic interaction between propellers and wings," *Journal of Aircraft*, vol. 26, pp. 829–836, 1989.

[10] J. Seddon, *Basic Helicopter Aerodynamics*. BSP Professional Books, 1990.

[11] W. Johnson, *Helicopter Theory*. Dover Publications, Inc, 1980.

[12] A. Talaeizadeh, D. Antunes, H. N. Pishkenari, and A. Alasty, "Optimal-time quadcopter descent trajectories avoiding the vortex ring and autorotation states," *Mechatronics*, vol. 68, 6 2020.

[13] A. Talaeizadeh, H. N. Pishkenari, and A. Alasty, "Quadcopter fast pure descent maneuver avoiding vortex ring state using yaw-rate control scheme," *IEEE Robotics and Automation Letters*, vol. 6, pp. 927–934, 4 2021.

[14] A. Taghizad, J. Jiminez, L. Binet, and D. Heuze, "Experimental and theoretical investigations to develop a model of rotor aerodynamics adapted to steep descents," *Proc. American Helicopter Society 58th Annual Forum*, 2002.

[15] L. Chenglong, F. Zhou, W. Jiafang, and Z. Xiang, "A vortex-ring-state-avoiding descending control strategy for multi-rotor uavs," in *Proceedings of the 34th Chinese Control Conference*, 2015.

[16] G. Throneberry, A. Takeshita, C. M. Hocut, F. Shu, and A. Abdelkefi, "Multi-rotor wake characterization and visualization in ascending and descending flight," *Experiments in Fluids*, vol. 63, 6 2022.

[17] S. Chae, S. Lee, and J. Kim, "Effects of rotor-rotor interaction on the wake characteristics of twin rotors in axial descent," *Journal of Fluid Mechanics*, vol. 952, 12 2022.

[18] M. Veismann, C. Dougherty, and M. Gharib, "Effects of rotor separation on the axial descent performance of dual-rotor configurations," *Flow*, vol. 3, 2 2023.

[19] A. Hughes, *Electric Motors and Drives*. Elsevier Ltd, third ed., 2006.

[20] C. C. de Visser, Q. P. Chu, and J. A. Mulder, "A new approach to linear regression with multivariate splines," *Automatica*, vol. 45, pp. 2903–2909, 12 2009.

[21] C. C. D. Visser, Q. P. Chu, and J. A. Mulder, "Differential constraints for bounded recursive identification with multivariate splines," *Automatica*, vol. 47, pp. 2059–2066, 9 2011.

[22] B. Widrow and M.-C. Liu, "Statistical theory of quantization," *IEEE Transactions on Instrumentation and Measurement*, vol. 45, p. 353, 1996.

[23] E. J. Smeur, G. C. de Croon, and Q. Chu, "Cascaded incremental nonlinear dynamic inversion for mav disturbance rejection," *Control Engineering Practice*, vol. 73, pp. 79–90, 4 2018.

[24] M. Saad, C. Rajhans, and S. Kannaiyan, "Application of pid and sliding mode control on quadcopter for autonomous optimized flight," in *2021 IEEE 18th India Council International Conference (INDICON)*, pp. 1–6, IEEE, 12 2021.

[25] E. Tal and S. Karaman, "Accurate tracking of aggressive quadrotor trajectories using incremental nonlinear dynamic inversion and differential flatness," *IEEE Transactions on Control Systems Technology*, vol. 29, pp. 1203–1218, 5 2021.

[26] S. Yoon, V. P. Diaz, D. D. B. Jr, W. M. Chan, and C. R. Theodore, "Computational aerodynamic modeling of small quadcopter vehicles," *American Helicopter Society (AHS) 73rd Annual Forum Fort Worth*, 2017.

[27] H. Jeon, J. Song, H. Lee, and Y. Eun, "Modeling quadrotor dynamics in a wind field," *IEEE/ASME Transactions on Mechatronics*, vol. 26, pp. 1401–1411, 6 2021.

[28] A. Bousquet, *The Eye of War: Military Perception From the Telescope to the Drone*. U of Minnesota Press, 2018.

[29] J. Kim, S. A. Gadsden, and S. A. Wilkerson, "A comprehensive survey of control strategies for autonomous quadrotors," *Canadian Journal of Electrical and Computer Engineering*, vol. 43, 5 2020.

[30] E. D. Sontag, "Stability and feedback stabilization," tech. rep., Rutgers University, 2009.

[31] T. P. Nascimento and M. Saska, "Position and attitude control of multi-rotor aerial vehicles: A survey," *Annual Reviews in Control*, vol. 48, pp. 129–146, 1 2019.

[32] S. Bouabdallah, P. Murrieri, and R. Siegwart, "Design and control of an indoor micro quadrotor," in *Proceedings - IEEE International Conference on Robotics and Automation*, vol. 2004, pp. 4393–4398, Institute of Electrical and Electronics Engineers Inc., 2004.

[33] D. Hanover, P. Foehn, S. Sun, E. Kaufmann, and D. Scaramuzza, "Performance, precision, and payloads: Adaptive nonlinear mpc for quadrotors," *IEEE Robotics and Automation Letters*, vol. 7, 9 2021.

[34] "Global commercial drones market 2021-2025." https://www.researchandmarkets.com/reports/4894489/global-commercial-drones-market-2021-2025. Accessed: 10-jan-2022.

[35] A. S. Saeed, A. B. Younes, C. Cai, and G. Cai, "A survey of hybrid unmanned aerial vehicles," *Progress in Aerospace Sciences*, vol. 98, pp. 91–105, 4 2018.

[36] "Dji mavic 3 specs." https://www.dji.com/nl/mavic-3/specs. Accessed: 10-jan-2022.

[37] S. Sabikan and S. Nawawi, "Open-source project (osps) platform for outdoor quadcopter optimization view project," *Journal of Advanced Research Design*, 2016.

[38] H. Lim, J. Park, D. Lee, and H. J. Kim, "Build your own quadrotor: Open-source projects on unmanned aerial vehicles," *IEEE Robotics and Automation Magazine*, vol. 19, pp. 33–45, 2012.

[39] E. Ebeid, M. Skriver, and J. Jin, "A survey on open-source flight control platforms of unmanned aerial vehicle," in *Proceedings - 20th Euromicro Conference on Digital System Design, DSD 2017*, pp. 396–402, Institute of Electrical and Electronics Engineers Inc., 9 2017.

[40] S. Sun, X. Wang, Q. Chu, and C. C. de Visser, "Incremental nonlinear fault-tolerant control of a quadrotor with complete loss of two opposing rotors," *IEEE Transactions on Robotics*, vol. 37, pp. 116–130, 2 2021.

[41] Z. Liu, C. Yuan, and Y. Zhang, "Adaptive fault-tolerant control of unmanned quadrotor helicopter using linear parameter varying control technique," in *2016 International Conference on Unmanned Aircraft Systems, ICUAS 2016*, pp. 980–985, Institute of Electrical and Electronics Engineers Inc., 6 2016.

[42] E. Ebeid, M. Skriver, K. H. Terkildsen, K. Jensen, and U. P. Schultz, "A survey of open-source uav flight controllers and flight simulators," *Microprocessors and Microsystems*, vol. 61, pp. 11–20, 9 2018.

[43] C. Dim, F. Nabor, G. Santos, M. Schoeler, and A. Chua, "Novel experiment design for unmanned aerial vehicle controller performance testing," in *IOP Conference Series: Materials Science and Engineering*, vol. 533, Institute of Physics Publishing, 2019.

[44] "Px4 user guide." https://docs.px4.io/master/. Accessed: 10-jan-2022.

[45] "Ardupilot documentation." https://ardupilot.org/ardupilot/. Accessed: 10-jan-2022.

[46] R. Niemiec and F. Gandhi, "Multirotor controls, trim, and autonomous flight dynamics of plus- and cross-quadcopters," *Journal of Aircraft*, vol. 54, pp. 1910–1920, 9 2017.

[47] S. Sun, "Quadrotor fault tolerant flight control and aerodynamic model identification," tech. rep., Delft University of Technology, 2020.

[48] C. Powers, D. Mellinger, A. Kushleyev, B. Kothmann, and V. Kumar, "Influence of aerodynamics and proximity effects in quadrotor flight," *Experimental Robotics*, pp. 289–302, 2013.

[49] H. Huang, G. M. Hoffmann, S. L. Waslander, and C. J. Tomlin, "Aerodynamics and control of autonomous quadrotor helicopters in aggressive maneuvering," in *IEEE International Conference on Robotics and Automation*, [IEEE], 2009.

[50] D. Serrano, M. Ren, A. J. Qureshi, and S. Ghaemi, "Effect of disk angle-of-attack on aerodynamic performance of small propellers," *Aerospace Science and Technology*, vol. 92, pp. 901–914, 9 2019.

[51] X. Fei, B. L. Litherland, and B. J. German, "Development of an unsteady vortex lattice method to model propellers at incidence," *AIAA Journal*, pp. 1–13, 9 2021.

[52] O. R. Shetty and M. S. Selig, "Small-scale propellers operating in the vortex ring state," in *49th AIAA Aerospace Sciences Meeting including the New Horizons Forum and Aerospace Exposition*, 2011.

[53] S. Sun, R. J. Schilder, and C. C. D. Visser, "Identification of quadrotor aerodynamic model from high speed flight data," in *AIAA Atmospheric Flight Mechanics Conference, 2018*, vol. 0, American Institute of Aeronautics and Astronautics Inc, AIAA, 2018.

[54] S. Sun and C. C. D. Visser, "Aerodynamic model identification of a quadrotor subjected to rotor failures in the high-speed flight regime," *IEEE Robotics and Automation Letters*, 2019.

[55] H. J. Kim and D. H. Shim, "A flight control system for aerial robots: Algorithms and experiments," *Control Engineering Practice*, vol. 11, pp. 1389–1400, 2003.

[56] E. Altuğ, J. P. Ostrowski, and C. J. Taylor, "Control of a quadrotor helicopter using dual camera visual feedback," *International Journal of Robotics Research*, vol. 24, pp. 329–341, 5 2005.

[57] S. Sun, A. Romero, P. Foehn, E. Kaufmann, and D. Scaramuzza, "A comparative study of nonlinear mpc and differential-flatness-based control for quadrotor agile flight," *arXiv*, 9 2021.

[58] A. Narasimhan, C. de Visser, C. de Wagter, and M. Rischmueller, "Fault tolerant control of multirotor uav for piloted outdoor flights," *ArXiv*, 11 2020.

[59] C. K. Jones, *Geometric Singular Perturbation Theory*, vol. 1609. Springer, Berlin, Heidelberg, 1995.

[60] J.-J. E. Slotine and W. Li, *Applied nonlinear control*. Prentice Hall, 1991.

[61] D. J. Leith and W. E. Leithead, "Survey of gain-scheduling analysis and design," *International Journal of Control*, vol. 73, pp. 1001–1025, 7 2000.

[62] J. Mohammadpour and C. W. Scherer, *Control of Linear Parameter Varying Systems with Applications*. Springer Science & Business Media, 2012.

[63] J. Shah, M. Okasha, and W. Faris, "Gain scheduled integral linear quadratic control for quadcopter," *International Journal of Engineering and Technology(UAE)*, vol. 7, pp. 81–85, 2018.

[64] J. S. Shamma, "Analyses and design of gain scheduled control systems," tech. rep., Massachusetts Institute of Technology, 1988.

[65] L. R. Samarathunga and J. F. Whidborne, "Linear parameter varying control of a quadrotor," in *International Conference on Industrial and Information Systems*, 2011.

[66] H. Pham, D. Ichalal, and S. Mammar, "Lpv unknown input observer for attitude of a mass-varying quadcopter," in *16th IEEE International Conference on Control, Automation, Robotics and Vision, ICARCV 2020*, pp. 917–924, Institute of Electrical and Electronics Engineers Inc., 12 2020.

[67] Y. Ameho, F. Niel, F. Defay, J.-M. Biannic, and C. Berard, "Adaptive control for quadrotors," in *International Conference on Robotics and Automation*, 2013.

[68] J. Stephan, L. Schmitt, and W. Fichter, "Linear parameter-varying control for quadrotors in case of complete actuator loss," *Journal of Guidance, Control, and Dynamics*, vol. 41, pp. 2232–2246, 2018.

[69] H. K. Khalil, *Nonlinear systems*. Prentice Hall, 2002.

[70] I. Khan, H. Zeeshan, J. Rajput, and J. Riaz, "A robust nonlinear dynamic inversion control of a class of multicopters," *International Bhurban Conference on Applied Sciences & Technology*, 2020.

[71] P. R. Smith, "A simplified approach to nonlinear dynamic inversion based flight control," in *23rd Atmospheric Flight Mechanics Conference*, pp. 762–770, American Institute of Aeronautics and Astronautics Inc, AIAA, 1998.

[72] S. Sun, M. Baert, B. A. S. van Schijndel, and C. de Visser, "Upset recovery control for quadrotors subjected to a complete rotor failure from large initial disturbances," *ArXiv*, 2 2020.

[73] X. Wang, S. Sun, E. J. van Kampen, and Q. Chu, "Quadrotor fault tolerant incremental sliding mode control driven by sliding mode disturbance observers," *Aerospace Science and Technology*, vol. 87, pp. 417–430, 4 2019.

[74] X. Wang, E. J. V. Kampen, Q. Chu, and P. Lu, "Stability analysis for incremental nonlinear dynamic inversion control," in *AIAA Guidance, Navigation, and Control Conference, 2018*, American Institute of Aeronautics and Astronautics Inc, AIAA, 1 2018.

[75] E. Fresk and G. Nikolakopous, "Full quaternion based attitude control for a quadrotor," in *European Control Conference*, p. 4615, 2013.

[76] A. M. Lyapunov, "The general problem of the stability of motion," *International Journal of Control*, vol. 55, pp. 531–534, 1992.

[77] N. Xuan-Mung, S. K. Hong, N. P. Nguyen, L. N. N. T. Ha, and T. L. Le, "Autonomous quadcopter precision landing onto a heaving platform: New method and experiment," *IEEE Access*, vol. 8, pp. 167192–167202, 2020.

[78] P. V. Kokotović, "The joy of feedback: Nonlinear and adaptive," *IEEE Control Systems*, vol. 12, pp. 7–17, 1992.

[79] A. A. Mian and W. Daobo, "Modeling and backstepping-based nonlinear control strategy for a 6 dof quadrotor helicopter," tech. rep., Nanjing University of Aeronautics and Astronautics, 2008.

[80] W. Xie, D. Cabecinhas, R. Cunha, and C. Silvestre, "Adaptive backstepping control of a quadcopter with uncertain vehicle mass, moment of inertia, and disturbances," *IEEE Transactions on Industrial Electronics*, vol. 69, pp. 549–559, 1 2022.

[81] A. K. Bhatia, J. Jiang, Z. Zhen, N. Ahmed, and A. Rohra, "Projection modification based robust adaptive backstepping control for multipurpose quadcopter uav," *IEEE Access*, vol. 7, pp. 154121–154130, 2019.

[82] Z. Huang, R. Bauer, and Y. J. Pan, "Closed-loop identification and real-time control of a micro quadcopter," *IEEE Transactions on Industrial Electronics*, vol. 69, pp. 2855–2863, 3 2022.

[83] V. I. Utkin, "Survey paper: Variable structure systems with sliding modes," *IEEE Transactions on Automatic Control*, vol. 22, pp. 212–222, 1977.

[84] R. A. Decarlo, S. H. Zak, and G. P. Matthews, "Variable structure control of nonlinear multivariate systems: A tutorial," *Proceedings of the IEEE*, vol. 76, pp. 212–232, 1988.

[85] R. Zhang, Q. Quan, and K. Y. Cai, "Attitude control of a quadrotor aircraft subject to a class of time-varying disturbances," *IET Control Theory and Applications*, vol. 5, pp. 1140–1146, 6 2011.

[86] T. H. Chiew, H. E. Lee, Y. K. Lee, K. M. Chang, J. J. Ong, and K. S. Eu, "Second order sliding mode controller for altitude and yaw control of quadcopter," in *Proceedings - 2021 11th IEEE International Conference on Control System, Computing and Engineering, ICCSCE 2021*, pp. 97–102, Institute of Electrical and Electronics Engineers Inc., 8 2021.

[87] A. Eltayeb, M. F. ad Rahmat, M. A. M. Basri, M. A. Eltoum, and S. El-Ferik, "An improved design of an adaptive sliding mode controller for chattering attenuation and trajectory tracking of the quadcopter uav," *IEEE Access*, vol. 8, pp. 205968–205979, 2020.

[88] S. J. K. Kersbergen, "Quantifying loss-of-control of quadrotors," tech. rep., Delft University of Technology, 2018.

[89] A. Baldini, "Estimation of actuator faults in quadrotor vehicles: from theory to validation with experimental flight data," *IEEE*, 2020.

[90] G. Ortiz-Torres, P. Castillo, F. D. Sorcia-Vázquez, J. Y. Rumbo-Morales, J. A. Brizuela-Mendoza, J. D. L. Cruz-Soto, and M. Martínez-García, "Fault estimation and fault tolerant control strategies applied to vtol aerial vehicles with soft and aggressive actuator faults," *IEEE Access*, vol. 8, pp. 10649–10661, 2020.

[91] X. Nian, W. Chen, X. Chu, and Z. Xu, "Robust adaptive fault estimation and fault tolerant control for quadrotor attitude systems," *International Journal of Control*, vol. 93, pp. 725–737, 3 2020.

[92] Y. Song, L. He, D. Zhang, J. Qian, and J. Fu, "Neuroadaptive fault-tolerant control of quadrotor uavs: A more affordable solution," *IEEE Transactions on Neural Networks and Learning Systems*, vol. 30, pp. 1975–1983, 7 2019.

[93] B. S. van Schijndel, S. Sun, and C. de Visser, "Fast fault detection on a quadrotor using onboard sensors and a kalman filter approach," *ArXiv*, 2 2021.

[94] Z. Hou, P. Lu, and Z. Tu, "Nonsingular terminal sliding mode control for a quadrotor uav with a total rotor failure," *Aerospace Science and Technology*, vol. 98, 3 2020.

[95] W. Zhang, M. W. Mueller, and R. D'Andrea, "A controllable flying vehicle with a single moving part," in *Proceedings - IEEE International Conference on Robotics and Automation*, vol. 2016-June, pp. 3275–3281, Institute of Electrical and Electronics Engineers Inc., 6 2016.

[96] J. Jiang and X. Yu, "Fault-tolerant control systems: A comparative study between active and passive approaches," *Annual Reviews in Control*, vol. 36, pp. 60–72, 2012.

[97] J. Svacha, G. Loianno, and V. Kumar, "Inertial yaw-independent velocity and attitude estimation for high-speed quadrotor flight," *IEEE Robotics and Automation Letters*, vol. 4, pp. 1109–1116, 4 2019.

[98] S. Li, C. D. Wagter, C. C. de Visser, Q. P. Chu, and G. C. de Croon, "In-flight model parameter and state estimation using gradient descent for high-speed flight," *International Journal of Micro Air Vehicles*, vol. 11, 3 2019.

[99] Y. Li, S. Zahran, Y. Zhuang, Z. Gao, Y. Luo, Z. He, L. Pei, R. Chen, and N. El-Sheimy, "Imu/magnetometer/barometer/mass-flow sensor integrated indoor quadrotor uav localization with robust velocity updates," *Remote Sensing*, vol. 11, 4 2019.

[100] P. F. Yaggy and K. W. Mort, "Wind-tunnel test of two vtol propellers in decent," tech. rep., NASA, 1963.